# Investigation into the Rapid Manufacture of Investment Casting Moulds through Accelerated Drying

By

Elliot Douse

A thesis submitted to the
University of Birmingham
for the degree of
DOCTOR OF ENGINEERING

School of Chemical Engineering
College of Engineering and Physical Sciences
University of Birmingham
April 2020

UNIVERSITY OF
BIRMINGHAM

## University of Birmingham Research Archive

### e-theses repository

This unpublished thesis/dissertation is copyright of the author and/or third parties. The intellectual property rights of the author or third parties in respect of this work are as defined by The Copyright Designs and Patents Act 1988 or as modified by any successor legislation.

Any use made of information contained in this thesis/dissertation must be in accordance with that legislation and must be properly acknowledged. Further distribution or reproduction in any format is prohibited without the permission of the copyright holder.

# Abstract

The manufacture of ceramic moulds for investment casting turbine blades is time consuming due to the accumulation of successive periods of drying between layers. Each layer is composed of a ceramic slurry onto which ceramic grains are deposited. Substitution of conventional non-porous ceramic grains for porous ceramic grains containing up to 60 vol% pore volume was conducted which reduced the amount of time required to dry a layer by up to 50%. After firing to casting temperature, moulds containing porous stucco display flexural deformation and an increase in flexural strength of up to 20%, both of which can cause casting defects. Through selective thermo-mechanical analysis of materials comprised within the ceramic mould, it was identified that defects originated primarily from large volumetric contraction of porous grains at casting temperature. To counteract this, composite ceramic materials were developed containing a porous and non-porous component to produce a material capable of absorbing water from the slurry upon contact but remain dimensionally stable at casting temperature. An alternative solution was also evaluated which minimised defect formation by constraining contraction within the layers containing porous grains. Both of these solutions successfully produced a reduction in drying time whilst maintaining the integral properties of the ceramic mould. The mechanism of accelerated drying when utilising porous ceramic grains was also investigated and it was hypothesised that a rate limited step prevents the utilisation of the complete pore volume of the porous grain.

# Acknowledgements

I would like to express my sincerest gratitude to Professor Stuart Blackburn for his support and encouragement as well as his invaluable advice and guidance in technical discussions throughout my postgraduate venture. I would also like to thank Dr. Richard Greenwood for his technical advice and continuous support for the welfare of the EngD students. I would also like to acknowledge Dr. Stewart Welch, Dr. Jeffery Knight and Mr. Steve Irwin for their constructive feedback and suggestions throughout the project. It has been a pleasure working with all of you. I would like to kindly acknowledge the EPSRC and Rolls-Royce plc for funding this project.

I would like to extend my gratitude to Grant Holt, John Wedderburn and Katy Lewis for their practical and organisational support in the laboratory. I would also like to thank all my friends on the EngD scheme for their personal support which has made the process all the more enjoyable and meaningful. I am very grateful to my close family and friends who have supported me every step of the way through this journey.

# Contents

Abstract ..... i
Acknowledgements ..... ii
Contents ..... iii
List of Figures ..... ix
List of Tables ..... xix
Abbreviations ..... xxii
Symbols ..... xxiv
1. Introduction ..... 1
1.1 Introduction ..... 1
1.2 Project Aims and Objectives ..... 2
1.3 Thesis Outline ..... 3
2. Literature Review ..... 4
2.1 The Gas Turbine Engine ..... 4
2.2 Turbine Blade Composition ..... 4
2.3 Investment Casting ..... 5
2.3.1 Overview ..... 5
2.3.2 Casting Techniques ..... 7
2.3.3 Investment Casting Mould Requirements ..... 10
2.3.4 Mould Materials ..... 10
2.3.4.1 Colloidal Silica Binder ..... 10
2.3.4.2 Zircon ..... 12
2.3.4.3 Alumina ..... 13
2.3.4.3.1 Tabular Alumina ..... 13
2.3.4.3.2 Fused Alumina ..... 13
2.3.4.4 Additives ..... 14
2.4 Drying ..... 14
2.4.1 Drying Theory ..... 14
2.4.1.1 Equilibrium Period (EP) ..... 15
2.4.1.2 Constant Rate Period (CRP) ..... 16

2.4.1.2.1 Solid Suspensions....18
2.4.1.3 Falling Rate Period (FRP)....18
2.4.1.3.1 Diffusion Controlled Mass Transfer....19
2.4.1.3.2 Capillary Controlled Mass Transfer....20
2.4.2 Simulation and Modelling of Drying Behaviour....23
2.4.3 Contact-Sorption Drying....24
2.4.4 Drying Materials with Variable Pore Sizes....25
2.4.5 Drying of Investment Casting Moulds....26
2.4.5.1 Effect of Air Flow....26
2.4.5.2 Effect of Relative Humidity....26
2.4.5.3 Effect of Temperature....26
2.4.6 Accelerated Drying of Investment Casting Moulds....27
2.4.6.1 Cyclone Drying....27
2.4.6.2 Microwave Drying....27
2.4.6.3 Contact Sorption Drying....27
2.4.6.3.1 Super Absorbent Polymer....28
2.4.6.3.2 Super Absorbent Polymer....28
2.5 Accelerated Manufacture of Investment Casting Moulds....29
2.5.1 Sterolithography (SLA)....29
2.5.2 Direct Laser Sintering....30
2.6 Synthesis of Porous Ceramics....30
2.6.1 Macro-porous Ceramic Synthesis....30
2.6.1.1 Partial Sintering....30
2.6.1.2 Replica Template....31
2.6.1.3 Direct Foaming....31
2.6.1.4 Sacrificial Fugitives....32
2.6.2 Micro/Meso-porous Ceramic Synthesis....33
2.6.2.1 Alumina....33
2.6.2.1.1 Boehmite Processing....34
2.6.2.2 Silica....35
2.7 High Temperature Processing....36
2.7.1 Sintering....36
2.7.1.1 Solid State Sintering....36

2.7.1.2 Liquid Phase Sintering....38
2.7.1.3 Viscous Sintering....39
2.7.2 Creep....39
3. Materials and Methods....41
3.1 Methods....41
3.1.1 Material Characterisation....41
3.1.1.1 X-ray Diffraction (XRD)....41
3.1.1.2 Particle Size Distribution (PSD)....41
3.1.1.3 Nitrogen Adsorption....42
3.1.1.4 Helium Pycnometer....47
3.1.1.5 Dynamic Vapour Sorption (DVS)....48
3.1.1.6 Thermomechanical Analysis (TMA)....48
3.1.1.7 Scanning Electron Microscopy (SEM)....49
3.1.1.8 Archimedes' Method....50
3.1.2 Slurry Preparation and Maintenance....51
3.1.3 Shell Manufacture....52
3.1.4 In-line Characterisation....54
3.1.4.1 Coat Weight....54
3.1.5 Drying Characterisation....55
3.1.5.1 Monitoring Weight Loss....55
3.1.5.2 Monitoring Colour Change....55
3.1.6 Shell Characterisation....57
3.1.6.1 Mechanical Testing....57
3.1.6.2 Horizontal Dilatometer....59
3.1.6.3 Cyclic Loading Dilatometry....59
3.1.6.4 Three Point Bend Thermomechanical Analysis....62
3.1.6.5 3D Structured Light Scanner....63
3.1.6.6 Photography....64
3.2 Materials....65
3.2.1 Silica Binder....65
3.2.2 Alumina Binder....65
3.2.3 Zircon Powder....65
3.2.4 Alumina Powder....65

3.2.5 Boehmite Powder ..... 65
3.2.6 Stucco ..... 66
4. Application of Monolithic Porous Stucco ..... 69
4.1 Introduction ..... 69
4.2 Stucco Characterisation ..... 69
4.2.1 X-ray Diffraction (XRD) ..... 69
4.2.2 Particle Size Distribution (PSD) ..... 70
4.2.3 Nitrogen Adsorption ..... 72
4.2.4 Particle Density and Porosity ..... 75
4.2.5 Dynamic Vapour sorption (DVS) ..... 77
4.2.6 Thermomechanical Analysis (TMA) ..... 79
4.3 Shell Build ..... 87
4.3.1 Analysing Surface Coverage after Stucco Deposition ..... 87
4.3.2 Coat Weight ..... 92
4.4 Shell Characterisation ..... 97
4.4.1 Scanning Electron Microscopy (SEM) ..... 97
4.4.2 Archimedes' Porosity ..... 103
4.4.3 Flexural Strength ..... 106
4.4.4 Observation of Deformation ..... 108
4.4.5 Reducing Drying Times ..... 110
4.4.5.1 Photography Analysis ..... 110
4.4.5.2 Flexural Strength ..... 112
4.5 Conclusions ..... 114
5. Investigation into Flexural Deformation ..... 116
5.1 Introduction ..... 116
5.2 Thermal Expansion/Contraction of Shell Components ..... 116
5.3 Thermal Expansion/Contraction of Shell Layers ..... 120
5.4 Predicting Flexural Deformation ..... 130
5.5 Predicting Stress ..... 139
5.6 Measuring Flexural Deformation in-situ ..... 142
5.7 3D Structured Light Analysis ..... 151
5.8 Comparison between Methods ..... 154
5.9 Effect of Flexural Deformation on Casting ..... 155

5.10 Conclusions....157
6. Solutions to Flexural Deformation....158
6.1 Introduction....158
6.2 Composite Stucco....158
6.2.1 Synthesis of α-$Al_2O_3$ Framework....159
6.2.2 Characterisation of α-$Al_2O_3$ Framework....159
6.2.2.1 Scanning Electron Microscopy (SEM)....159
6.2.2.2 Archimedes' Porosity....161
6.2.3 Synthesis of α-$Al_2O_3$ Framework Composite....162
6.2.3.1 Formulation and Process Optimisation....163
6.2.4 Characterisation of α-$Al_2O_3$ Framework Composite....172
6.2.4.1 X-ray Diffraction (XRD)....172
6.2.4.2 Nitrogen Adsorption....173
6.2.4.3 Analysis of Internal Structure....174
6.2.4.4 Dynamic Vapour Sorption (DVS)....175
6.2.4.5 Thermomechanical Analysis (TMA)....176
6.2.4.6 Particle Size Distribution (PSD)....177
6.2.4.7 Particle Density and Porosity....178
6.2.5 Shell Build....179
6.2.5.1 Analysing Surface Coverage after Stucco Deposition....179
6.2.6 Shell Characterisation....181
6.2.6.1 Scanning Electron Microscopy (SEM)....181
6.2.6.2 Mechanical Strength....183
6.2.6.3 Thermal Expansion/Contraction of Shell Layers....184
6.2.6.4 Predicting Flexural Deformation....186
6.2.6.5 Measuring Flexural Deformation in-situ....188
6.2.6.6 Reduced Drying Times....191
6.2.7 Closing Comments....192
6.3 Introduction of the Tertiary Layer....193
6.3.1 Shell Build....193
6.3.2 Shell Characterisation....194
6.3.2.1 Scanning Electron Microscopy (SEM)....194
6.3.2.2 Mechanical Strength....196

6.3.2.3 Measuring Flexural Deformation in-situ....197
6.3.3 Closing Comments....199
6.4 Conclusions....200
7. Drying Behaviour....201
7.1 Introduction....201
7.2 Monitoring Weight Loss....201
7.2.1 Introduction....201
7.2.2 Recording Weight Loss....202
7.2.3 Mass Balance....204
7.2.4 Percentage Weight Loss....205
7.2.4 Rate of Weight Loss....205
7.3 Monitoring Colour Change....212
7.3.1 Introduction....212
7.3.2 Method....212
7.3.3 Results....215
7.4 Conclusions....221
8. Conclusions and Future Work....222
8.1 Summary of Conclusions....222
8.2 Future Work....224
9. Appendices....227
10. References....230

# List of Figures

**Figure 1** – Step by step process of investment casting for a simplified turbine blade design..5

**Figure 2** – Turbine blades in (a) equiaxed, (b) columnar and (c) single crystal from © 2012 Belan J. Published in [9] under CC by 3.0 license. Available from: http://dx.doi.org/10.5772/37254.....8

**Figure 3** – Schematic of directional solidification casting techniques to produce a) columnar crystal components or b) single crystal components. Reproduced from [11] .....9

**Figure 4** – Polymerisation behaviour of aqueous silica showing growth via Ostwald ripening in basic conditions or aggregation in acidic conditions. Reproduced from [18] .....11

**Figure 5** – Schematic of an electric double layer surrounding a negatively charged particle 12

**Figure 6** – Typical drying curves displaying either one falling rate period (a) or two falling rate periods (b) initiating at a critical moisture content ($X_c$). Each curve displays an equilibrium period (EP), constant rate period (CRP) and falling rate period (FRP). In case (b) the falling rate period is divided into the 1$^{st}$ falling rate period (FRP1) and 2$^{nd}$ falling rate period (FRP2). Adapted from [34] .....15

**Figure 7** – Replica template method of synthesising macro-porous ceramics .....31

**Figure 8** – Direct foaming method of synthesising macro-porous ceramics.....32

**Figure 9** – Sacrificial fugitives method of synthesising porous ceramics .....32

**Figure 10** – Thermal transformation sequence of AlOOH and $Al(OH)_3$ minerals. Reproduced from [85] .....34

**Figure 11** – Mass transport mechanisms in sintering leading to densification where (1) is grain boundary diffusion, (2) is lattice diffusion from a grain boundary and (3) is plastic flow .....37

**Figure 12** – Mass transport mechanisms in sintering leading to coarsening where (4) is surface diffusion, (5) is lattice diffusion from the surface and (6) is vapour transport .....37

**Figure 13** – Microstructural development occurring during liquid phase sintering. Reproduced from [102] .....39

**Figure 14** – Shape evolution of two equally sized glassy particles coalescing via viscous sintering. Reproduced from [108] .....39

**Figure 15** – Typical stages of creep exhibited when a material is subject to stress over a prolonged period of time at elevated temperature ..... 40
**Figure 16** – BET plot showing calculation of gradient ($M_{BET}$) and intercept ($i_{BET}$) ..... 43
**Figure 17** – Nitrogen adsorption isotherms identified by IUPAC. Reproduced from [119] ..... 46
**Figure 18** – Hysteresis loops identified by IUPAC for nitrogen adsorption. Reproduced from [119] ..... 47
**Figure 19** – TMA setup showing analysis of BD-$Al_2O_3$ (left) and SGB127 (right) ..... 49
**Figure 20** – Annotated setup of beaker coated in Indicating slurry and Tab-$Al_2O_3$ stucco ..... 56
**Figure 21** – 3 Point bend schematic identifying the thickness of sample ($T$), width of sample ($W$) and span length ($L_{Span}$) ..... 58
**Figure 22** – Horizontal dilatometer setup ..... 59
**Figure 23** – Linear strain under free sintering conditions ($F_0$) and under different loads ($F_1$, $F_2$ and $F_3$). Shaded regions represent the period where load takes place, outside this regions minimal stress is applied. Interpreted from [127] ..... 60
**Figure 24** – Linear strain rate under free sintering conditions ($F_0$) and under applied load ($F_1$). Shaded regions represent the period where loading takes place, outside this regions minimal stress is applied. The free sintering strain rate ($\varepsilon_F$) and strain rate under load ($\varepsilon_L$) are labelled for temperature $T_1$. Interpreted from [127] ..... 60
**Figure 25** – Plot of strain rate against true stress to calculate uniaxial viscosity at temperature $T_{1\text{-}8}$. Interpreted from [127] ..... 61
**Figure 26** – 3 point bend TMA setup ..... 63
**Figure 27** – Pre-fired shell sample fired vertically as part of the process to observe dimensional change taking place after the simulated casting cycle. The sample is highlighted with a red arrow ..... 64
**Figure 28** – XRD traces with labels identifying main peaks for each phase (B = boehmite, γ = γ-$Al_2O_3$ and α = α-$Al_2O_3$). The intensity is shifted by 1 for each sample for clarification ..... 70
**Figure 29** – Particle size distribution of stucco grains analysed under aero dispersion method ..... 71
**Figure 30** – Particle size distribution of stucco grains analysed under hydro dispersion method ..... 72
**Figure 31** – Representative example of nitrogen adsorption and desorption isotherm of each stucco material. Arrows indicate axis used for each plot ..... 73

**Figure 32** – Representative example of t-plot analysis on each stucco material. Arrows indicate axis used for each plot .....74
**Figure 33** – Representative example of incremental pore volume calculated by BJH method plotted against pore diameter for each porous stucco material .....74
**Figure 34** – Representative example of cumulative pore volume calculated by BJH method plotted against pore diameter for each porous stucco material .....75
**Figure 35** – Dynamic vapour sorption and desorption plots for porous stucco materials.....77
**Figure 36** – Expansion/contraction plot of BD-$Al_2O_3$ analysed throughout the simulated casting cycle conducted by TMA.....80
**Figure 37** – Diagram showing the three behavioural regions of expansion/contraction for BD-$Al_2O_3$ broadly described as A (thermal expansion), B (sintering and phase transition) and C (sintering).....80
**Figure 38** – Expansion/contraction plot of SGB127 analysed throughout the simulated casting cycle conducted by TMA.....82
**Figure 39** – Diagram showing four behavioural regions of expansion/contraction for SGB127 upon heating broadly described as I (primarily weight loss), II (shrinkage proportional to weight loss), III (primarily shrinkage) and depending on the heating rate IV (foaming).....83
**Figure 40** – Dehydration of silanol groups occurring within silica gel [135] .....84
**Figure 41** – Polycondensation reactions occurring within silica gel [135] .....85
**Figure 42** – Comparison of surface coverage when depositing BD-$Al_2O_3$ stucco (left) and Tab-$Al_2O_3$ stucco (right) on Secondary slurry. Poor adhesion between the slurry and stucco is demonstrated when depositing BD-$Al_2O_3$ as particles are removed from the surface when lightly brushed whereas Tab-$Al_2O_3$ particles remain in place under the same treatment .....87
**Figure 43** – Surface coverage of BD-$Al_2O_3$ stucco blends deposited onto Secondary slurry ..88
**Figure 44** – Surface coverage of SGB127 stucco blends deposited onto Secondary slurry ....89
**Figure 45** – Surface coverage of Tab-$Al_2O_3$ stucco deposited onto Secondary slurry.....89
**Figure 46** – Stucco mass and corresponding volume deposited during shell build .....93
**Figure 47** – Cumulative mass recorded after dipping partially complete shell moulds in Secondary slurry during shell build.....94
**Figure 48** – Proposed mechanism of cake growth surrounding porous particles embedded in the mould resulting from water transfer from the slurry to the porous stucco.....95

**Figure 49** – Proposed mechanism of porosity generation in shells containing porous stucco resulting from slurry unsuccessfully penetrating into inter-particle voids .....95
**Figure 50** – BD-$Al_2O_3$ stucco grains embedded in shell displaying behaviour characteristic of slurry drying before penetrating between inter-particle voids. B = BD-$Al_2O_3$ particles, T = Tab-$Al_2O_3$ particles .....96
**Figure 51** – SEM analysis of Shell (Tab-$Al_2O_3$) displaying the shell cross-section with the slurry applied in each layer identified. Typical stucco particles in the shell and particle microstructure are shown at greater magnification. T = Individual Tab-$Al_2O_3$ particles .....98
**Figure 52** – SEM analysis of Shell (BD-$Al_2O_3$) displaying the shell cross-section with the slurry applied in each layer identified. Typical stucco particles in the shell and particle microstructure are shown at greater magnification. B = BD-$Al_2O_3$ particles, T = Tab-$Al_2O_3$ particles.....99
**Figure 53** – SEM analysis of Shell (SGB127) displaying the shell cross-section with the slurry applied in each layer identified. Typical stucco particles in the shell and particle microstructure are shown at greater magnification. SGB = SGB127 particles, T = Tab-$Al_2O_3$ particles.....100
**Figure 54** – Evidence of foaming in Shell (SGB127) in fired condition .....103
**Figure 55** – Bulk density of shells in pre-fired and fired condition .....104
**Figure 56** – Open porosity of shells in pre-fired and fired condition .....105
**Figure 57** – Flexural strength of Shell (Tab-$Al_2O_3$), Shell (BD-$Al_2O_3$) and Shell (SGB127) in green, pre-fired and fired condition tested in ambient conditions.....106
**Figure 58** – Observation of a greater magnitude of flexural deformation in shells containing porous stucco than non-porous stucco following the simulated casting cycle. Dashed lines indicate the side of the shell coated with Primary slurry and highlight the curved nature of the shells .....109
**Figure 59** – Shells containing 100 vol% Tab-$Al_2O_3$ in secondary layers showing the formation of cracks when reducing the drying time between Secondary slurry dips from 2 hours to 0.5 hours. Reducing the drying time between dips below 2 hours causes failure.....110
**Figure 60** – Shells containing 60 vol% blended BD-$Al_2O_3$ stucco in secondary layers showing the formation of cracks when reducing the drying time between Secondary slurry dips from 2 hours to 0.5 hours. Reducing the drying time between dips below 1 hour causes failure111

**Figure 61** – Shells containing 60 vol% blended SGB127 stucco in secondary layers showing the formation of cracks when reducing the drying time between Secondary slurry dips. Reducing the drying time between dips below 1 hour causes failure .....112
**Figure 62** – Flexural strength of shell bars in green state after varying the drying time in secondary layers tested in ambient conditions.....113
**Figure 63** – Thermal expansion/contraction of slurry components analysed throughout the simulated casting cycle conducted by TMA.....117
**Figure 64** – Adaptation of complete shell into bi-layered ceramic containing a primary section ($Section_P$) and secondary section ($Section_S$) .....120
**Figure 65** – Sample Secondary (Tab-$Al_2O_3$) with arrows indicating the direction in which thermal expansion/contraction was measured.....122
**Figure 66** – SEM cross-sections of shell samples replicating $Section_P$ or $Section_S$ used for dilatometer analysis. The initial layer applied to the wax pattern is displayed on the right side for each sample .....123
**Figure 67** – SEM image of Secondary slurry cross-section used for dilatometer analysis ....123
**Figure 68** – Expansion/contraction plots of shell samples replicating $Section_P$ or $Section_S$ analysed throughout the simulated casting cycle conducted by dilatometer analysis .....124
**Figure 69** – Proposed mechanism for greater shrinkage in shell containing porous stucco in comparison to shell containing non-porous stucco during the simulated casting cycle .....127
**Figure 70** – Adaptation of a multi-layered shell into a bi-layered ceramic composed of $Section_P$ (P) thickness equal to $T_1$ and $Section_S$ (S) thickness equal to $T_2$. The original length of the sample is labelled $L_0$ .....130
**Figure 71** – Radius of curvature ($\rho$), deflection from normal ($\delta$) and length of arc ($L_{arc}$) of a bi-layered ceramic where $Section_S$ (S) has contracted to a greater degree than $Section_P$ (P) .....130
**Figure 72** – Method of quantifying section thickness by SEM analysis using the scale bar for reference. Displaying $Section_P$ (P) and $Section_S$ (S) of Shell (Tab-$Al_2O_3$) in pre-fired condition .....134
**Figure 73** – Cyclic loading dilatometry undertaken on sample Secondary (BD-$Al_2O_3$) with varied stresses applied under load. Shaded regions represent the period where loading takes place at the stated stress, outside this region a stress of 4 kPa is applied.....135

**Figure 74** – Cyclic loading dilatometry undertaken on sample Secondary (-) with varied stresses applied under load. Shaded regions represent the period where loading takes place at the stated stress, outside this region a stress of 4 kPa is applied. .....136
**Figure 75** – Positive deflection (left) and negative deflection (right).....136
**Figure 76** – Normalised curvature predicted from thermal expansion/contraction of shell samples replicating $Section_P$ and $Section_S$ throughout the simulated casting cycle.....137
**Figure 77** – Stress distribution in a bi-layered ceramic resulting from $Section_S$ (S) contracting at a faster rate than $Section_P$ (P) causing a mismatch stress, the result of which produces curvature. Reproduced from [173].....140
**Figure 78** – Mismatched strain rate between $Section_P$ and $Section_S$ of complete shell samples calculated from thermal expansion/contraction obtained by dilatometer.....141
**Figure 79** – TMA schematic identifying isotropic thermal expansion results in push rod movement downwards (+d$T/T_0$) and isotropic thermal contraction results in push rod movement upwards (-d$T/T_0$) over a specified span length .....142
**Figure 80** – $Primary_{DOWN}$ (left) and $Primary_{UP}$ (right) orientations used for 3 point bend TMA labelled depending on orientation of $Section_P$ (P) and $Section_S$ (S).....142
**Figure 81** – 3 point bend TMA of complete shells tested in $Primary_{UP}$ and $Primary_{DOWN}$ orientation throughout the simulated casting cycle. Each sample is separated by 4 % at the origin for clarification.....147
**Figure 82** – Normalised curvature predicted from thermal expansion/contraction of $Section_P$ and $Section_S$ analysed by dilatometer (full lines) compared to normalised curvature measured from 3 point bend TMA method (dashed lines) throughout the simulated casting cycle .....149
**Figure 83** – 3D structured light analysis showing dimensional change from pre-fired to fired condition .....151
**Figure 84** – Defining X and Y plane for cross-section analysis as shown on sample Shell (SGB127) .....152
**Figure 85** – Cross-section analysis of Shell (SGB127) in X plane showing pre-fired cross-section in black and fired cross-section in red. Shown on the diagram is original thickness in pre-fired condition ($T_0$), length of arc ($L_{arc}$) and deflection from normal after firing ($\delta$)....152
**Figure 86** – Diagram illustrating the unknown deflection from normal for an arc length equal to 20 mm ($\delta_{unknown}$) calculated from deflection for a known arc length ($\delta_{known}$) .....153

**Figure 87** – Normalised curvature following the complete simulated casting cycle characterised by three methods.....155
**Figure 88** – Cross-section of pre-fired shell exhibiting curvature following the simulated casting cycle with a magnified image showing development of tensile and compressive stresses concentrated in the edge regions.....156
**Figure 89** – Examples of failure in Shell (BD-$Al_2O_3$) following the simulated casting cycle indicative of fracture early in the firing cycle.....156
**Figure 90** – Cross-section of the proposed composite material displaying interconnected porosity throughout the structure.....158
**Figure 91** – Synthesis route for α-$Al_2O_3$ framework denoted αFrame.....159
**Figure 92** – SEM image of αFrame particles at 90X magnification showing porosity in the grains and the angular nature of the particles resulting from the grinding process.....160
**Figure 93** – SEM image of αFrame particle at 400X magnification.....160
**Figure 94** – SEM image of αFrame particle at 1500X magnification showing particle-particle necking.....161
**Figure 95** – Schematic of synthesis route for production of α-$Al_2O_3$ framework composite162
**Figure 96** – Volume fraction of pores in αFrame saturated with $BD^I$-$Al_2O_3$ ($\tau$) following a given number of vacuum impregnation steps calculated from surface area or pore volume data.....167
**Figure 97** – SEM image of αFrame-$Impreg_8$ particles showing external coverage of $BD^I$-$Al_2O_3$ as highlighted by red arrows.....169
**Figure 98** – αFrame-$Impreg_8$-Clean particles showing minimal external coverage of $BD^I$-$Al_2O_3$ as highlighted by the red arrow.....169
**Figure 99** – Volume fraction of αFrame saturated with $BD^I$-$Al_2O_3$ ($\tau$) for αFrame-$Impreg_8$ and αFrame-$Impreg_8$-Clean calculated from surface area or pore volume data.....171
**Figure 100** – XRD traces with labels identifying main peaks for each phase (γ = γ-$Al_2O_3$ and α = α-$Al_2O_3$). The intensity is shifted by 1 for each sample for clarification.....172
**Figure 101** – Representative example of incremental pore volume calculated by BJH method plotted against pore diameter for αFrame-$Impreg_8$-Clean and $BD^I$-$Al_2O_3$.....173
**Figure 102** – SEM image of internal structure of αFrame-$Impreg_4$ at 400X magnification (left) and 800X magnification (right).....174

**Figure 103** – SEM image of internal structure of αFrame-Impreg$_8$ at 400X magnification (left) and 800X magnification (right) .....174
**Figure 104** – Dynamic vapour sorption plot for αFrame-Impreg$_8$-Clean material .....175
**Figure 105** – Expansion/contraction of αFrame-Impreg$_8$-Clean, αFrame and BD-$Al_2O_3$ throughout the simulated casting cycle conducted by TMA. Samples are separated by 1 % for clarification .....176
**Figure 106** – Particle size distribution of stucco grains analysed under aero dispersion method .....178
**Figure 107** – Surface coverage of αFrame-Impreg$_8$-Clean stucco blends deposited onto Secondary slurry .....180
**Figure 108** – SEM analysis of Shell (αFrame-I$_8$-C) displaying the shell cross-section with slurry applied in each layer identified. Typical stucco particles are shown at greater magnification. A = Individual αFrame-Impreg$_8$-Clean particles .....182
**Figure 109** – Flexural strength of Shell (Tab-$Al_2O_3$) and Shell (αFrame-I$_8$-C) in green, pre-fired and fired condition tested in ambient conditions .....183
**Figure 110** – Expansion/contraction of shell samples replicating Section$_S$ analysed throughout the simulated casting cycle conducted by dilatometer analysis .....184
**Figure 111** – Normalised curvature predicted from thermal expansion/contraction of shell samples replicating Section$_P$ and Section$_S$ throughout the simulated casting cycle .....187
**Figure 112** – 3 point bend TMA of complete shells tested in Primary$_{UP}$ and Primary$_{DOWN}$ orientation throughout the firing cycle. Each sample is separated by 4 % at the origin for clarification .....188
**Figure 113** – Normalised curvature measured from 3 point bend TMA method throughout the simulated casting cycle .....189
**Figure 114** – Shells containing 100 vol% αFrame-Impreg$_8$-Clean in secondary layers showing the formation of cracks when reducing the drying time between Secondary slurry dips from 2 hours to 0.5 hours. Reducing the drying time between dips below 1.25 hours causes failure .....191
**Figure 115** – Flexural strength of shell bars in green state after varying the drying time in secondary layers tested in ambient condition .....192
**Figure 116** – Shell composed of a primary section (Section$_P$), secondary section (Section$_S$) and tertiary section (Section$_T$) .....193

**Figure 117** – SEM analysis of Shell (Tert Tab-$Al_2O_3$) displaying the shell cross-section with slurry applied in each layer identified. The red arrow identifies a transverse crack .....195
**Figure 118** – SEM analysis of Shell (Tert Fused-$Al_2O_3$) displaying the shell cross-section with slurry applied in each layer identified. The red arrows identify transverse cracks.....195
**Figure 119** – Flexural strength measured by 3 point bend loading on shell samples containing a tertiary section in comparison to the standard shell.....196
**Figure 120** – 3 point bend TMA of shells containing a tertiary section in both $Primary_{UP}$ and $Primary_{DOWN}$ orientation in comparison to Shell (Tab-$Al_2O_3$) and Shell (BD-$Al_2O_3$) throughout the simulated casting cycle. Samples are separated by 4 % for clarification.....197
**Figure 121** – Normalised curvature measured from 3 point bend TMA method throughout the simulated casting cycle.....198
**Figure 122** – Recorded weight loss over time for drying experiments conducted on samples coated in slurry and stucco.....202
**Figure 123** – Percentage weight loss over time for drying experiments conducted on samples coated in slurry and stucco.....205
**Figure 124** – Rate of weight loss against time for drying experiments conducted on samples coated in slurry and stucco. Samples are separated by 0.1 g $min^{-1}$ at the origin for clarification .....206
**Figure 125** – Rate of weight loss against moisture content for drying experiments conducted on samples coated in slurry and stucco. Samples are separated by 0.1 g $min^{-1}$ at the origin for clarification.....206
**Figure 126** – Schematic proposed to describe the evaporation of liquid from both the slurry and porous stucco surfaces throughout the drying period upon contact.....209
**Figure 127** – Example of possible mechanisms in which the rate of evaporation in the system remains equal when applying porous or non-porous stucco despite porous stucco absorbing water from the slurry. Full lines represent the porous stucco absorbing water until the slurry is completely dry. Dotted lines represent the porous stucco absorbing until liquid transport becomes limited. Dashed lines represent the porous stucco absorbing water until becoming saturated, a constant rate of evaporation occurs at the stucco surface as pores in the porous stucco are replenished with liquid from the slurry as evaporation takes place until the slurry is completely dry.....211

**Figure 128** – Typical image recorded during experiment of a glass beaker coated in Indicating slurry and Tab-$Al_2O_3$ stucco at the initial point of the drying.....212
**Figure 129** – Average red, blue or green colour component values over time for images taken of a glass beaker coated in Indicating slurry and Tab-$Al_2O_3$ stucco .....213
**Figure 130** – Annotated diagram of blue colour component values over time for images taken of a glass beaker coated in Indicating slurry and Tab-$Al_2O_3$ stucco. The time taken to dry is identified in addition to the blue colour component values equal to 0 % and 100 % dry .....214
**Figure 131** – Typical examples of moisture content progression over time when applying different stucco compositions. Each plot displays the recorded moisture content until the sample is determined to be dry in addition to the 10 minutes proceeding this.....215
**Figure 132** – Moisture content at 10 minute intervals when applying different stucco compositions. Once all 3 repeat analyses per stucco composition have been identified as dry the moisture content is taken as 100 % dry with no variability. .....216
**Figure 133** – Time taken for each stucco composition to dry the Indicating slurry.....216
**Figure 134** – Difference between the blue colour component value defined as 0 % dry and the blue colour component value defined as 100 % dry when applying different stucco compositions to Indicating slurry .....218

# List of Tables

**Table 1** – Refractive index of materials used for PSD characterisation .....41
**Table 2** – SEM polishing stages.....50
**Table 3** – Slurry composition and specification.....52
**Table 4** – Identification of ceramic mould layer defined by the slurry applied, stucco composition deposited and drying time.....53
**Table 5** – Colour changing slurry composition and specifications .....56
**Table 6** – Dominant XRD peaks identified for each crystalline phase. Peaks identified from [128] and [93].....70
**Table 7** – Surface and pore characteristics obtained by nitrogen adsorption .....73
**Table 8** – True density attained by helium pycnometer analysis in addition to bulk density and volumetric porosity calculated using pore volume and true density data.....76
**Table 9** – Description of adhesive strength between stucco and slurry based on the force required to remove particles embedded in the slurry by passing a brush over the surface ..90
**Table 10** – Adhesive strength of stucco compositions characterised by the magnitude of force required to remove embedded particles as described in Table 9.....90
**Table 11** – Composition of complete shells containing non-porous or porous stucco blends labelled Shell (Tab-$Al_2O_3$), Shell (BD-$Al_2O_3$) and Shell (SGB127).....91
**Table 12** – Linear shrinkage of samples following the entire simulated casting cycle and linear thermal expansion coefficients measured from 50 – 700 °C conducted by TMA .....117
**Table 13** – Sintering onset temperatures for shell components conducted by TMA .....118
**Table 14** – Composition of shells replicating $Section_P$ and $Section_S$ of complete shell samples .....121
**Table 15** – Linear shrinkage of samples following the simulated casting cycle and linear thermal expansion coefficients measured from 50 – 700 °C by dilatometer analysis .....124
**Table 16** – First and second sintering onset temperatures for shell samples conducted by dilatometer analysis.....125
**Table 17** – Notation of complete shells composed of a specified $Section_P$ and $Section_S$ .....132
**Table 18** – Average thicknesses for $Section_P$ ($T1$) and $Section_S$ ($T2$) in pre-fired condition measured by SEM analysis.....134

**Table 19** – Average original thickness ($T0$) and thickness ratio ($a$) values for each shell ....134

**Table 20** – Normalised curvature following the complete simulated casting cycle predicted from thermal expansion/contraction of shell samples replicating $Section_P$ and $Section_S$....139

**Table 21** – Average push rod movement of complete shell samples analysed by 3 point bend TMA in $Primary_{UP}$ and $Primary_{DOWN}$ orientation following the complete firing cycle .....148

**Table 22** – Normalised curvature following the complete simulated casting cycle measured from 3 point bend TMA method for complete shell samples .....150

**Table 23** – Dimensional analysis of cross-sections in X and Y plane .....153

**Table 24** – Normalised curvature following the complete firing cycle measured by 3D structured light imaging method for complete shell samples.....154

**Table 25** – Bulk density, true density and porosity of αFrame material calculated by Archimedes method.....161

**Table 26** – Average surface area of composite materials and their constituent materials analysed by nitrogen adsorption .....163

**Table 27** – Average pore volume of composite materials and their constituent materials analysed by nitrogen adsorption .....164

**Table 28** – True density of $BD^{I}$-$Al_2O_3$ calculated from helium pycnometer analysis and bulk density of $BD^{I}$-$Al_2O_3$ calculated from helium pycnometer and nitrogen adsorption data....166

**Table 29** – Mass and volume fractions of $BD^{I}$-$Al_2O_3$ in composite materials following a given number of vacuum impregnation steps calculated from surface area or pore volume of each material with the accompanying percentage saturation of pores in each material.....167

**Table 30** – Average pore volume and surface area of αFrame-$Impreg_8$-Clean analysed by nitrogen adsorption .....170

**Table 31** – Mass and volume fractions of $BD^{I}$-$Al_2O_3$ in αFrame-$Impreg_8$-Clean calculated from surface area or pore volume of each material with the accompanying saturation of pores in the material.....170

**Table 32** – Surface and pore characteristics of composite stucco and mesoporous component of composite stucco obtained by nitrogen adsorption.....173

**Table 33** – Linear shrinkage of αFrame-$Impreg_8$-Clean, αFrame and BD-$Al_2O_3$ following the simulated casting cycle measured by TMA.....177

**Table 34** – True density of αFrame attained by helium pycnometer method.....179

**Table 35** – Composition of shell containing αFrame-Impreg$_8$-Clean stucco labelled Shell (αFrame-I$_8$-C).....181
**Table 36** – Composition of shell replicating Section$_S$ of Shell (α-Frame-I$_8$-C) .....184
**Table 37** – Linear shrinkage of shell samples following the simulated casting cycle and thermal expansion coefficients measured from 50 – 700 °C by dilatometer analysis .....185
**Table 38** – First and second sintering onset temperatures for shell samples conducted by dilatometer analysis.....185
**Table 39** – Average thickness for Section$_P$ and Section$_S$ measured by SEM analysis.....186
**Table 40** – Average original thickness ($T0$) and thickness ratio ($a$) for each shell.....186
**Table 41** – Normalised curvature following the complete simulated casting cycle predicted from thermal expansion/contraction of shell samples replicating Section$_P$ and Section$_S$....187
**Table 42** – Average push rod movement of complete shell samples analysed by 3 point bend TMA in Primary$_{UP}$ and Primary$_{DOWN}$ orientation following the simulated casting cycle .....188
**Table 43** – Normalised curvature following the complete simulated casting cycle measured from 3 point bend TMA method for complete shell samples .....190
**Table 44** – Composition of shells containing a tertiary section labelled Shell (Tert Tab-$Al_2O_3$) and Shell (Tert Fused-$Al_2O_3$) .....194
**Table 45** – Average push rod movement of complete shell samples analysed by 3 point bend TMA in Primary$_{UP}$ and Primary$_{DOWN}$ orientation following the simulated casting cycle .....197
**Table 46** – Normalised curvature following the complete simulated casting cycle measured from 3 point bend TMA method for complete shell samples .....199
**Table 47** – Classification of each drying experiment labelled depending on the condition of the wax pattern dipped in slurry and the stucco composition applied.....202
**Table 48** – Average weight loss for each drying experiment after 6 hours .....203
**Table 49** – Identifying labels for various stucco compositions.....215

# Abbreviations

| | |
|---|---|
| αFrame | Macroporous α-$Al_2O_3$ |
| αFrame-$Impreg_8$ | Macroporous α-$Al_2O_3$/mesoporous alumina composite stucco |
| αFrame-$Impreg_8$-clean | Macroporous α-$Al_2O_3$/mesoporous alumina composite stucco |
| BD-$Al_2O_3$ | Synthesised boehmite derived mesoporous alumina stucco |
| BD'-$Al_2O_3$ | Commercial boehmite derived mesoporous alumina |
| BET | Brunauer–Emmett–Teller |
| BJH | Barrett–Joyner–Halenda |
| CX | Columnar crystal |
| CRP | Constant rate period |
| DVS | Dynamic vapour sorption |
| EP | Equilibrium period |
| EQ | Equiaxed crystal |
| FRP | Falling rate period |
| FRP1 | 1$^{st}$ falling rate period |
| FRP2 | 2$^{nd}$ falling rate period |
| Fused-$Al_2O_3$ | Fused alumina stucco |
| IUPAC | International Union of Pure and Applied Chemistry |
| LTD | Lenton Thermal Designs |
| NMR | Nuclear magnetic resonance |
| $Primary_{DOWN}$ | Orientation of shell bar with primary layers facing downwards |
| $Primary_{UP}$ | Orientation of shell bar with primary layers facing upwards |
| PSD | Particle size distribution |
| SAP | Super absorbent polymer |
| $Section_P$ | Primary section |
| $Section_S$ | Secondary section |
| $Section_T$ | Tertiary section |
| SEM | Scanning electron microscope |
| SGB127 | Silica gel stucco |
| SLA | Sterolithography |

| | |
|---|---|
| STP | Standard temperature pressure |
| SX | Single crystal |
| TMA | Thermomechanical analysis |
| Tab-$Al_2O_3$ | Tabular alumina stucco |
| vol% | Volume percent |
| wt% | Weight percent |
| XRD | X-ray diffraction |

# Symbols

| | |
|---|---|
| $A$ | Area of interface for mass transfer ($m^2$) |
| $A_{cs}$ | Molecular cross section of adsorbate molecule ($m^2$) |
| $a$ | Ratio of thickness between layer 1 and 2 (-) |
| $B$ | Constant ($m^2\ s^{-1}$) |
| $b$ | Ratio of uniaxial viscosity between layer 1 and 2 (-) |
| $b_e$ | Ratio of elastic modulus between layer 1 and 2 (-) |
| $b_J$ | Burges vector (m) |
| $C$ | Dimensionless constant (-) |
| $D$ | Permeability ($m^2$) |
| $D_L$ | Liquid diffusivity coefficient ($m^2\ s^{-1}$) |
| $D_{mould}$ | Permeability of mould ($m^2$) |
| $d$ | Mean pore size (m) |
| $d_{grain}$ | Grain size (m) |
| $E$ | Young's modulus ($N\ m^{-2}$) |
| $F$ | Max load (N) |
| $F_{mass(\alpha Frame)}$ | Mass fraction of αFrame (-) |
| $F_{mass(BD^{I}-Al_2O_3)}$ | Mass fraction of $BD^{I}$-$Al_2O_3$ (-) |
| $F_{vol(\alpha Frame)}$ | Volume fraction of solid in αFrame (-) |
| $F_{vol(BD^{I}-Al_2O_3)}$ | Volume fraction $BD^{I}$-$Al_2O_3$ (-) |
| $F_{vol(pore)}$ | Volume fraction of pores in αFrame (-) |
| $G$ | Shear modulus (Pa) |
| $h$ | Cake thickness (m) |
| $h_s$ | Suction potential (m) |
| $h_t$ | Heat transfer coefficient ($J\ m^{-2}\ s^{-1}\ K^{-1}$) |
| $I$ | Intensity (-) |
| $I_0$ | Background intensity (-) |
| $J$ | Flux ($m\ s^{-1}$) |
| $K$ | Boltzmann constant ($J\ K^{-1}$) |

| | |
|---|---|
| $k$ | Diffusion coefficient ($m^2\ s^{-1}$) |
| $k_g$ | Mass transfer coefficient ($kg\ m^{-2}\ s^{-1}\ Pa^{-1}$) |
| $L$ | Length of sample (m) |
| $L_0$ | Original length of sample (m) |
| $L_{span}$ | Length of span (m) |
| $L_{arc}$ | Length of arc (m) |
| $M$ | Molecular mass ($g\ mol^{-1}$) |
| $m$ | Mass of sample (g) |
| $m_{ads}$ | Mass of gas adsorbed at specified pressure (g) |
| $m_{dry}$ | Dry mass (g) |
| $m_{mono}$ | Mass of adsorbed gas to produce monolayer at STP (g) |
| $m_{sat}$ | Saturated mass (g) |
| $m_{sub}$ | Submerged mass (g) |
| $N$ | Avogadro's constant ($6.023 \times 10^{23}\ mol^{-1}$) |
| $n$ | Fraction of porous stucco in blend (-) |
| $n_\sigma$ | Stress exponent (-) |
| $P$ | Equilibrium vapour pressure of adsorbate gas (Pa) |
| $P_0$ | Saturated pressure of adsorbate gas (Pa) |
| $P_{\alpha Frame}$ | Pore volume of αFrame ($cm^3\ g^{-1}$) |
| $P_{BD^{I}-Al_2O_3}$ | Pore volume of $BD^{I}$-$Al_2O_3$ ($cm^3\ g^{-1}$) |
| $P_c$ | Capillary pressure (Pa) |
| $P_{composite}$ | Pore volume of composite material ($cm^3\ g^{-1}$) |
| $P_s$ | Partial pressure of vapour at the surface (Pa) |
| $P_{suc}$ | Suction potential (m) |
| $P_w$ | Partial pressure of vapour in the air stream (Pa) |
| $P_{ws}$ | Saturation pressure of vapour in the air stream (Pa) |
| $p$ | Exponent of inverse grain size (-) |
| $\nabla P_L$ | Pressure gradient in liquid ($Pa\ m^{-1}$) |
| $R$ | Gas constant ($8.314\ J\ K^{-1}\ mol^{-1}$) |
| $R_C$ | Rate of moisture loss during capillary controlled mass transfer ($kg\ m^{-2}\ s^{-1}$) |
| $R_{CRP}$ | Rate of moisture loss during constant rate period ($kg\ m^{-2}\ s^{-1}$) |

| | |
|---|---|
| $R_D$ | Rate of moisture loss during diffusion controlled mass transfer (kg $m^2$ $s^{-1}$) |
| $R_H$ | Relative humidity (-) |
| $R_{NP(slurry)}$ | Rate of moisture loss resulting from evaporation at slurry-air interface in system containing only non-porous stucco (kg $m^{-2}$ $s^{-1}$) |
| $R_{NP(system)}$ | Rate of moisture loss from system containing only non-porous stucco (kg $m^{-2}$ $s^{-1}$) |
| $R_{P(BD-Al_2O_3)}$ | Rate of moisture loss resulting from evaporation at BD-$Al_2O_3$-air interface in system containing porous stucco (kg $m^{-2}$ $s^{-1}$) |
| $R_{P(slurry)}$ | Rate of moisture loss resulting from evaporation at slurry-air interface in system containing porous stucco (kg $m^{-2}$ $s^{-1}$) |
| $R_{P(system)}$ | Rate of moisture loss in system containing porous stucco (kg $m^{-2}$ $s^{-1}$) |
| $r$ | Radius of sphere (m) |
| $r_c$ | Radius of core (m) |
| $S$ | Specific surface area ($m^2$ $g^{-1}$) |
| $S_{\alpha Frame}$ | Surface area of αFrame ($m^2$ $g^{-1}$) |
| $S_{BD^I-Al_2O_3}$ | Surface area of $BD^I$-$Al_2O_3$ ($m^2$ $g^{-1}$) |
| $S_{composite}$ | Surface area of composite material ($m^2$ $g^{-1}$) |
| $S_{tot}$ | Total surface area ($m^2$) |
| $T$ | Thickness of sample (m) |
| $T_0$ | Original thickness of sample (m) |
| $T_1$ | Thickness of layer 1 (m) |
| $T_2$ | Thickness of layer 2 (m) |
| $T_s$ | Temperature of vapour in air at surface (K) |
| $T_w$ | Temperature of vapour in the air stream (K) |
| $t$ | Time (s) |
| $t_{stat}$ | Statistical thickness of adsorbed phase on non-porous surface (nm) |
| $V_{bulk}$ | Volume of material including pores ($cm^3$) |
| $V_{mono}$ | Volume of adsorbed gas to produce monolayer at STP (g) |
| $V_{MP}$ | Volume of micropores ($cm^3$ $g^{-1}$) |
| $V_{true}$ | Volume of material excluding pores ($cm^3$) |
| $W$ | Width of sample (m) |

| | |
|---|---|
| $w$ | Dimensionless constant (-) |
| $X$ | Free moisture content ($kg_{moisture}$ $kg^{-1}_{dry\ solid}$) |
| $X_0$ | Initial free moisture content ($kg_{moisture}$ $kg^{-1}_{dry\ solid}$) |
| $X_c$ | Critical moisture content ($kg_{moisture}$ $kg^{-1}_{dry\ solid}$) |
| $x$ | Distance in the solid (m) |
| $x_T$ | Total thickness of slab if drying occurs from one face (m) |
| $x_{PF}$ | Packing factor (-) |
| $z$ | Surface energy (J $m^{-2}$) |

Greek

| | |
|---|---|
| $\gamma$ | Surface tension (N $m^{-1}$) |
| $\delta$ | Deflection from normal (m) |
| $\delta_t$ | Push rod displacement resulting from differential shrinkage of sections at time $t$ (m) |
| $\varepsilon$ | Strain (-) |
| $\varepsilon_{eng}$ | Engineering strain (-) |
| $\dot{\varepsilon}$ | Strain rate ($s^{-1}$) |
| $\dot{\varepsilon_F}$ | Free sintering strain rate ($s^{-1}$) |
| $\dot{\varepsilon_L}$ | Strain rate under load ($s^{-1}$) |
| $\eta$ | Uniaxial viscosity (Pa s) |
| $\eta_1$ | Uniaxial viscosity of layer 1 (Pa s) |
| $\eta_2$ | Uniaxial viscosity of layer 2 (Pa s) |
| $\eta_{fast}$ | Uniaxial viscosity of section contracting fastest (Pa s) |
| $\eta_{slow}$ | Uniaxial viscosity of section contracting slowest (Pa s) |
| $\eta_f$ | Viscosity of filtrate (Pa s) |
| $\eta_l$ | Viscosity of liquid (Pa s) |
| $\theta$ | Contact angle (°) |
| $\lambda$ | Latent heat of evaporation (J $kg^{-1}$) |
| $\rho$ | Radius of curvature (m) |

| | |
|---|---|
| $\rho_{\alpha Frame}$ | Bulk density of αFrame (g $cm^{-3}$) |
| $\rho_{BD^{I}-Al_2O_3}$ | Bulk density of $BD^{I}$-$Al_2O_3$ (g $cm^{-3}$) |
| $\rho_{bulk}$ | Bulk density (g $cm^{-3}$) |
| $\rho_C$ | Radius of curvature of liquid in capillary (m) |
| $\rho_l$ | Density of liquid (kg $m^{-3}$) |
| $\rho_{np}$ | Bulk density of non-porous stucco (g $cm^{-3}$) |
| $\rho_p$ | Bulk density of porous stucco (g $cm^{-3}$) |
| $\rho_{true}$ | True density (g $cm^{-3}$) |
| $\sigma$ | Applied stress (Pa) |
| $\sigma_{flexural}$ | Flexural strength (Pa) |
| $\sigma_0$ | Initial stress (Pa) |
| $\sigma_{fast}^{max}$ | Maximum tensile stress in section contracting fastest (Pa) |
| $\sigma_{slow}^{max}$ | Maximum tensile stress in section contracting slowest (Pa) |
| $\sigma_t$ | True stress (Pa) |
| $\mathbb{T}$ | Absolute temperature (K) |
| $\tau$ | Volume fraction of pores in αFrame saturated with $BD^{I}$-$Al_2O_3$ (-) |
| $\upsilon$ | Poisson's ratio (-) |
| $\varphi_t$ | Push rod movement resulting from expansion/contraction through thickness at time $t$ (m) |
| $\omega_t$ | Push rod movement resulting from creep at time $t$ (m) |

Other

| | |
|---|---|
| $\epsilon_{s\cdot cake}$ | Volume fraction of solids in cake (-) |
| $\epsilon_{s\cdot slurry}$ | Volume fraction of solids in slurry (-) |
| $\epsilon_{l\cdot mould}$ | Volume fraction of filtrate in wetted part of mould (-) |
| $\Phi_{open}$ | Open porosity ($cm^3_{pore}$ $cm^{-3}_{bulk}$) |

# 1. Introduction

## 1.1 Introduction

Rolls-Royce plc supply jet propulsion engines for the civil aerospace sector. To produce greater fuel efficiency the engine is required to run at a higher temperature to produce a greater amount of thrust for the same amount of fuel. However, to achieve higher operational temperatures the components of the engine must be able to withstand these demanding conditions. This is most notable in the turbine region which experiences the highest temperature during operation. As such, continuous research into the development of turbine blades has been carried out through development of creep resistant alloys; casting methods; thermal barrier coatings; internal cooling passages and blade geometry optimisation.

Turbine blades are manufactured by the investment casting process which produces near net shape castings which requires minimal cutting and finishing steps to complete the component. The investment casting process utilises a ceramic mould which is produced by sequentially dipping a wax pattern in ceramic slurry and depositing coarse grains called stucco onto the surface before drying is undertaken. Drying the ceramic slurry is time consuming and comprises the majority of time in manufacturing the ceramic mould and a significant portion of time in producing the final cast component. As such, developing a process whereby the drying time is decreased can reduce lead time for producing cast components and optimise processing conditions.

## 1.2 Project Aims and Objectives

The aim of the project was to develop a process to minimise the drying time when manufacturing investment casting moulds to accelerate manufacture of single crystal turbine blades. The avenue chosen for achieving this goal was to substitute conventional refractory stucco grains with porous ceramic stucco grains in an attempt to absorb water from the slurry upon contact; thus reducing the amount of time required to dry the mould via convection.

Numerous advantages can result from an accelerated manufacturing process:

Reduction in lead time

Accelerated manufacturing allows rapid prototyping of new products by reducing the time from design to manufacture. This allows a greater number of iterations to be tested in a given time period, allowing optimisation and commercialisation of products more quickly. This can provide a business with an advantage over competitors as new technology can be developed in-house more rapidly than other external businesses.

Reduced energy consumption

By reducing the time taken to dry a mould, the energy associated with controlling temperature, humidity and airflow is also reduced.

Increased output

As drying is a rate limiting step in the manufacturing of investment casting moulds, an accelerated drying process will allow a greater output of moulds to be manufactured over a given time period if required.

Reduced business expenses

Reducing the manufacturing time of a process will produce an associated reduction in labour. In addition, periods of downtime may result as moulds are produced at a greater rate than they can be consumed.

To achieve the aims of the project, a range of materials were evaluated to substitute conventional refractory stucco grains with porous stucco grains. To successfully adopt this technology, the integral properties of the mould must be maintained as specified by Rolls-Royce. The requirements include:

- Capable of sustaining casting temperatures between 1475 – 1575°C without deformation, distortion or fracture.
- Maintain acceptable flexural strength to prevent fracture during processing and handling.
- Cause minimal metallurgical defects to the cast component.
- Cause minimal dimensional defects to the cast component.
- Contain materials compliant with modern health and safety standards.

## 1.3 Thesis Outline

This chapter has discussed the business case and objectives for the project with reasoning as to why the research was conducted. Chapter 2 discusses relevant literature on investment casting with emphasis on the properties of the constituent materials of the ceramic mould and theory related to the drying of such materials. Also discussed in Chapter 2 is literature surrounding the synthesis of porous materials and the theory of sintering. Chapter 3 discusses the methods used to characterise the physical, mechanical and thermomechanical properties of the materials in addition to methods used to characterise drying behaviour. Also discussed in Chapter 3 are the material specifications and processes used to manufacture investment casting moulds. Chapter 4 evaluates the substitution of refractory stucco for monolithic porous stucco to accelerate drying in investment casting moulds. Within Chapter 4 it is shown that flexural deformation of the mould occurs when heating to casting temperatures when monolithic porous stucco is present in the mould. Chapter 5 uses various thermomechanical analysis methods to evaluate the reason for this flexural deformation occurring and in Chapter 6 methods are implemented to reduce the extent of this defect taking place. Chapter 7 focuses on characterising the mechanism of accelerated drying when depositing porous stucco onto ceramic slurry. A summary of conclusions and future work are detailed in Chapter 8.

# 2. Literature Review

## 2.1 The Gas Turbine Engine

The gas turbine engine generates thrust by accelerating air as it passes through the engine. This is produced as cool air is pulled into the engine by the compressor blades, mixing the air with fuel and igniting the mixture to expel high pressure, high temperature exhaust gases that produce thrust. The turbine blades extract energy from the exhaust gasses to drive the compressor blades at the front of the engine, subsequently drawing a larger volume of air into the engine and allowing more fuel to burn, producing a higher energy output. There is a drive for operation at higher temperatures as the hotter the fuel burns the more efficient the engine, thus less fuel is required per quantity of thrust. However, this requires temperature resistant materials that remain dimensionally stable at the extreme conditions experienced inside the gas turbine engine. This is most notable in the turbine region where the environment can reach temperatures 85 – 90 % of the turbine blade melting temperature [1]; this is made possible by internal cooling passages and thermal barrier coatings to ensure the stability of the component at high temperature. Additionally, the turbine blades must be able to withstand large centrifugal loads with a small turbine blade weighing only two ounces exerting a force over two tonnes at top speed [2].

## 2.2 Turbine Blade Composition

In order for the turbine blades to remain dimensionally stable at operational temperatures, great consideration must be taken to prevent creep and failure. In search of materials suitable for such applications, nickel-based superalloys are used due to their high temperature oxidation and creep resistance. Nickel-based superalloys are composed of a face centred cubic (FCC) nickel matrix (γ phase) with a precipitated γ’ phase of $Ni_3Al$. The formation of the precipitated γ’ phase inhibits the movement of dislocations in the γ phase matrix, which are a source of weakness at high temperature [3]. Numerous elements such as Mo, W, Nb and Re can be added to strengthen the γ phase through solid-solution strengthening whilst Ti, Ta and Nb can contribute to the formation and strengthening of the γ’ phase. The addition of B, C, Hf and Zr result in the formation of borides and carbides at

grain boundaries which further enhances creep resistant properties as grain boundaries are a source of weakness at high temperature [1, 3].

## 2.3 Investment Casting

### 2.3.1 Overview

The process through which turbine blades are manufactured is called the investment casting process or lost wax casting. This process can produce near net shape components with excellent surface finish qualities whilst requiring a minimum number of machining and finishing stages to complete the component [4]. The manufacture of a simplified turbine blade by investment casting is outlined in Figure 1. As shown, the completed blade has internal cooling passages formed by the removal of a ceramic core.

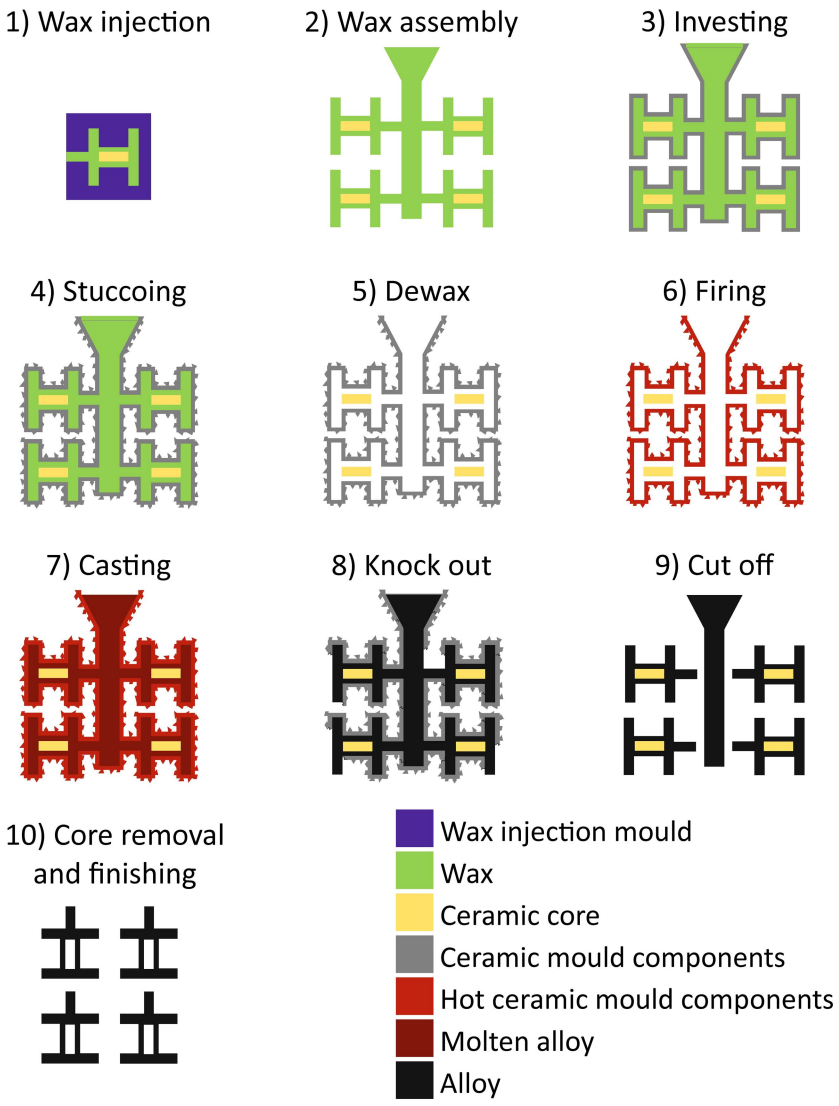



**Figure 1** – Step by step process of investment casting for a simplified turbine blade design

1. A ceramic core which defines the internal cooling passages of the turbine blades is held inside a metal mould, the void between the two is injected with molten wax to form a wax part the same shape as the required component, encapsulating the ceramic core.
2. Once the molten wax has cooled, the wax parts are typically joined together with the use of a runner system (also made from wax) to form a tree, this allows more than one component to be cast at once.
3. The wax assembly is dipped into a slurry typically composed of colloidal silica binder and refractory powder. The wax assembly is then removed from the slurry and allowed to drain until the coating becomes smooth and even with no drips falling off the surface.
4. Coarse ceramic particles called “stucco” are applied to the surface of the slurry, typically through the use of a rainfall sander or fluidised bed. Stucco grains are typically composed of alumina, fused silica or other refractory grain. The slurry coated wax assembly is rotated throughout the application of stucco until the slurry has been completely covered in stucco. Next, the assembly is placed in a temperature and humidity controlled environment for 1.5 – 6 hours [5] to dry the slurry. Once dry, steps three and four are repeated to build up the thickness of the mould in layers until the required number of layers are applied. The application of stucco builds up the thickness of the mould and minimises drying stresses by presenting many stress concentration centres [6]. Additionally, the stucco provides a rough surface for the next coating of slurry, facilitating a good adhesion between the two contacting surfaces.
5. The wax constituent is removed by rapidly heating the entire assembly. This causes the wax to quickly melt and subsequently drain due to gravity without imparting significant stress due to differential thermal expansion coefficients between the wax and the ceramic. This is typically conducted in a pressurised steam vessel called an autoclave. Once the wax is removed, a hollow “mould” or “shell” is formed with smooth internal passages containing the suspended ceramic core.
6. The shell is fired to remove residual wax and give the mould strength.
7. Molten alloy is poured into the mould to cast the component.
8. Once the metal has cooled the ceramic mould is broken to release the cast component.
9. The individual cast components are separated from the runner system by machining and cutting processes.

10. The ceramic core is removed by the use of chemical leaching to expose the channels used for cooling during operation. Finally, finishing, polishing and inspection stages are undertaken to complete the cast component.

It should be noted that the layers of the ceramic mould are typically not identical in composition. The slurry initially applied to the wax assembly is usually more viscous to produce a smooth and complete coverage on the wax surface [7]. This is important as the surface finish produced at the wax-slurry interface is transferred to the cast component. Subsequently applied layers require a lower viscosity slurry as the slurry easily bonds to the previously dried layer. The particle size distribution of stucco is also formulated to ensure a smooth surface finish at the wax-slurry interface, whilst coarser particles are used in subsequent layers to build up the thickness of the shell more quickly per layer.

### 2.3.2 Casting Techniques

To improve the creep resistance properties of the turbine blade, the microstructure can be tailored to remove grain boundaries by modification to the casting method. Traditional casting methods produce an equiaxed (EQ) grain structure resulting from nucleation of the molten alloy at the mould surface propagating into the bulk. However, by implementing directional solidification (DS) casting techniques, transverse grains can be removed to produce a columnar crystal (CX) structure or grain boundaries can be removed completely by adding a grain selector to the wax pattern to produce a single crystal (SX) component. The removal of grain boundaries prevents dislocation slip occurring at high temperature [8]. This extends the service lifetime of the component before elongation resulting from creep occurs to an unacceptable amount and the component must be replaced [2]. The microstructure of turbine blades with an EQ, CX or SX crystal structure is shown in Figure 2.

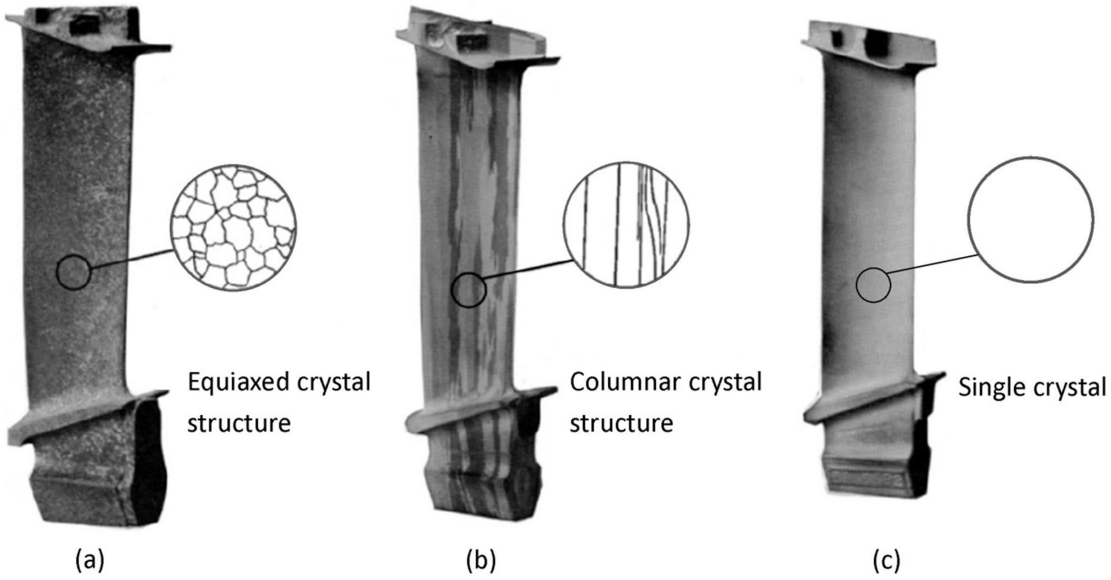



**Figure 2** – Turbine blades in (a) equiaxed, (b) columnar and (c) single crystal from © 2012 Belan J. Published in [9] under CC by 3.0 license. Available from: http://dx.doi.org/10.5772/37254

The production of components with a CX structure takes place by constricting nucleation sites to a chill plate and allowing those grains to propagate by withdrawing the mould at a few millimetres per hour through a temperature gradient. The addition of a helical grain selector allows only a single grain to propagate from the chill plate to the component which produces components with a SX structure [10]. The temperature gradient is produced by extracting heat energy from the chill plate with water or liquid metal cooling whilst the hot section of the mould remains in the furnace. As the mould passes through the temperature gradient (under vacuum) the molten alloy solidifies until the entire casting is solid. A schematic of directional solidification casting is shown in Figure 3 to yield components with a CX or SX structure.

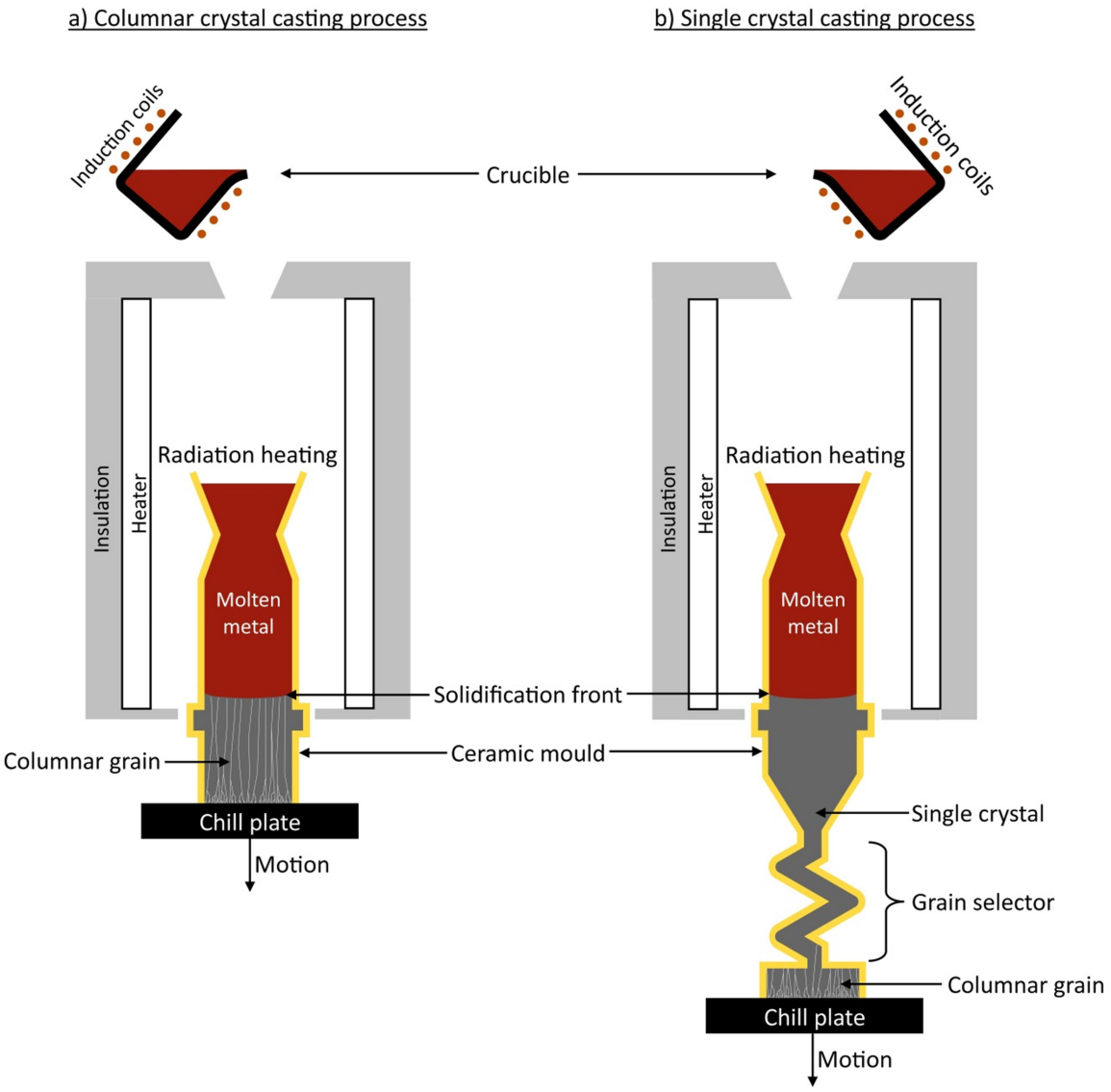



**Figure 3** – Schematic of directional solidification casting techniques to produce a) columnar crystal components or b) single crystal components. Reproduced from [11]

### 2.3.3 Investment Casting Mould Requirements

In order for an investment casting mould to successfully cast a component it must avoid fracture and deformation during both manufacture and casting. Firstly the mould must attain sufficient green strength to withstand the forces imposed upon the shell walls during the dewaxing process in the autoclave [12]. Secondly, the mould must have high thermal shock resistance to prevent fracture upon transition through the temperature gradient during casting. Furthermore, the mould must support the weight of the molten alloy during the casting process and be resistant to creep at high temperature. As such, the mould must remain dimensionally stable and not fracture or deform from the point the metal is poured, through to the max temperature when the mould is heated by the contained molten alloy [13] and throughout the slow withdrawal process until solidification is complete. This, however, must be achieved without excess shell strength which can cause hot tears and strain induced recrystallisation of the alloy upon cooling [14]. High chemical stability is also required to prevent reaction between the mould and the molten alloy. A smooth inner surface finish is also required [7].

### 2.3.4 Mould Materials

The composition of the mould used to cast turbine blades comprises materials from both the slurry and stucco. The standard investment casting slurry formulation utilised by Rolls-Royce for single crystal casting comprises colloidal silica filled with zircon ($ZrSiO_4$) powder in addition to wetting agents. The stucco deposited on the surface of the slurry after each slurry dip is either fused or tabular alumina depending on the specific layer applied.

#### 2.3.4.1 Colloidal Silica Binder

Commercial colloidal silica is composed of a stable dispersion of spherical amorphous $SiO_2$ particles typically stabilised by electrostatic repulsion. Each silica particle is typically between 5 – 100 nm in size with each particle following Brownian motion. Typical colloidal silica dispersions are capable of remaining stable for multiple years [3]. Synthesis methods for the production of colloidal silica are vast, employing either a gaseous or liquid route [15]. Typical liquid sol-gel synthesis routes involve the hydrolysis of metal alkoxides ($Si(OR)_4$) or inorganic metal salts such as sodium silicate with acid or base catalyst to form silicic acid ($Si(OH)_4$) [16]. These monomeric silicic acid molecules undergo condensation reactions to form dimeric, cyclic and polymeric species which can be grown by Ostwald ripening at pH 7-

10 or agglomerated below pH 7 to form a gel network as illustrated in Figure 4. As particles increase in size and decrease in number at low pH the solubility reduces and particle growth stops; thus a stable sol is produced. To increase particle size further the solubility of silica species can be increased by raising the temperature; thus growth continues once more via Ostwald ripening [17].

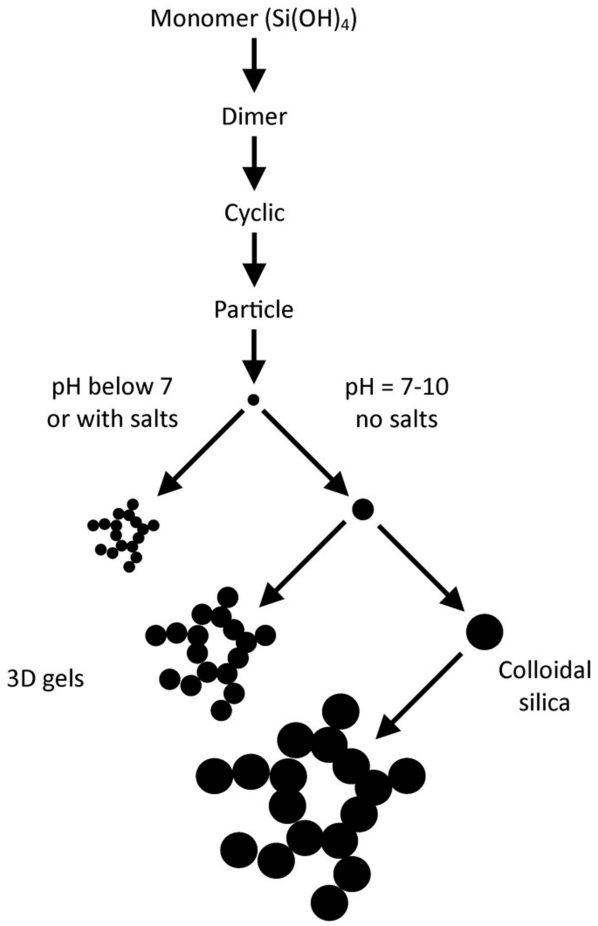



**Figure 4** – Polymerisation behaviour of aqueous silica showing growth via Ostwald ripening in basic conditions or aggregation in acidic conditions. Reproduced from [18]

Colloidal silica particles remain stable due to the formation of an electric double layer on the surface of each particle which repels neighbouring particles when they come into close proximity, opposing Van der Waal forces. This occurs as counter-ions in the solution are attracted to the charged silica surface forming a layer of counter-ions called the Stern layer in which the concentration of counter-ions decreases linearly with distance. Past the Stern layer the concentration of counter-ions decreases exponentially, this region is called the

diffuse layer. The stability of the suspension can be measured by determining the zeta potential at the shear plane, a high magnitude indicates a stable suspension where particles remain dispersed [19]. A diagram of the electric double layer is shown in Figure 5.

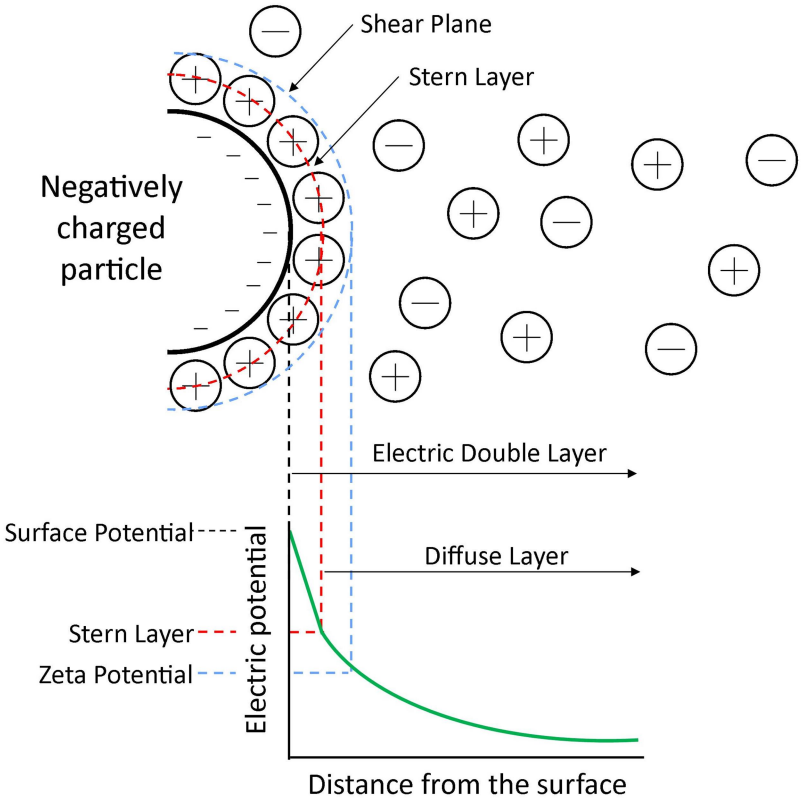



**Figure 5** – Schematic of an electric double layer surrounding a negatively charged particle

The stability of colloidal suspensions is described by DLVO theory [20] which outlines the interaction of attractive and repulsive forces between colloidal particles. This theory details that colloidal species remain stable in solution if the repulsive effect of overlapping electric double layers between particles is sufficiently larger than the attractive Van der Waals forces pulling particles together. Depending on the balance of attractive and repulsive forces, particles can reversibly aggregate (flocculate), irreversibly coagulate or remain stable.

#### 2.3.4.2 Zircon

Zirconium silicate ($ZrSiO_4$) with the mineral name zircon is chosen for use in casting due to its high refractoriness and ability to resist creep at high temperatures [21] which prevents mould distortion during the firing cycle. Zircon is also chosen due to its low wettability and low reactivity to molten metal preventing penetration of the molten alloy into the fine

pores in the ceramic mould, thus maintaining a good surface finish of the component [22]. Additionally, a low thermal expansion coefficient [23], high melting temperature [24] and lack of phase dissociation up until 1500 °C [25] allows accurate control of dimensions when casting. However, zircon is a natural mineral and thus has inherent compositional variation depending on the source the mineral is mined and the processing route through which it is refined.

#### 2.3.4.3 Alumina

##### 2.3.4.3.1 Tabular Alumina

Tabular alumina is a high purity synthetic mineral formed by sintering calcined α-$Al_2O_3$ powder produced from the Bayer process. This is typically conducted by pelletising α-$Al_2O_3$ powder into balls with a diameter of approximately 25 mm (often without the aid of additives or binders) before transferring the balls to a vertical shaft kiln where they are fired between 1800 – 1900 °C [26]. Once the balls are cooled the material is crushed and ball milled before being screened to give a range of particle sizes. As the process of manufacturing tabular alumina is a continuous one, the material properties and distribution of impurities such as $Na_2O$ remain uniform throughout the entirety of the material [27].

Tabular alumina has a characteristic microstructure with small closed spherical pores which are the result of entrapped air present from the pelletisation process which persists after sintering. The spherical nature of the pores helps prevent cracks propagating through the material as stress is distributed into a large area when a crack penetrates into a pore. This mechanism produces high crush strength after thermal shock and superior resistance to thermal spalling [27].

##### 2.3.4.3.2 Fused Alumina

Fused alumina is available in a range of different grades such as brown, white, pink, ruby and black depending on the raw materials used for synthesis and impurities present. White fused alumina (the grade of stucco utilised in the Rolls-Royce formulation for investment casting moulds) is produced in a batch melting process where calcined α-$Al_2O_3$ powder from the Bayer process is heated in an electric arc furnace to temperatures in excess of 2000 °C to form a molten mass which is then cooled and solidified. As the molten mass solidifies the outer segment cools quicker than the insulated inner section producing an inhomogeneous

crystal size throughout the material leading to different properties between the inner and outer section of the solid. Within the solidified mass a segment of β-alumina ($Na_2O$-11 $Al_2O_3$) is present which is separated to reduce impurities. The remaining fused alumina is crushed and screened to give a range of particle sizes. However, chemical variation occurs throughout the grades as the residual β-alumina has a lower hardness than α-alumina and is thus more prone to fracture during crushing. This results in a larger portion of $Na_2O$ impurities in the finer grades of alumina which can be as high as 1.08 % in fine grains (>120 mesh) and 0.31 % in coarse grains (>14 mesh) [27]. Fused alumina has a characteristic microstructure with interconnecting pores which can be greater than 1 mm in length. Due to this type of porosity, fused alumina displays low thermal shock resistance [27].

2.3.4.4 Additives

It is commonplace to add wetting agents to the slurry that initially coats the wax pattern to promote adhesion between the hydrophilic slurry and the hydrophobic wax surface. Typical wetting agents include non-ionic surfactants which reduce surface tension and decrease the propensity for the slurry to form a high contact angle on the surface of the wax. In addition, antifoam agents are also used to supress the formation of bubbles and air gaps in the slurry which would lead to a poor surface coverage. These are typically silicone emulsions or liquid fatty alcohols [28].

Due to the inherently low unfired strength of the ceramic mould the addition of polymer [29], fibre [30, 31] or needles [32] to enhance the green strength is often carried out. These modifiers aid in the prevention of autoclave cracking by increasing green strength, but also increase the porosity of the mould upon firing as organic material decomposes during the firing cycle. This has been shown to reduce the flexural strength of the mould and increase the magnitude of shrinkage after firing [5].

## 2.4 Drying

### 2.4.1 Drying Theory

When drying a material containing a solid phase and a liquid phase, moisture loss occurs in stages in which the rate of moisture loss differs. These stages are broken down into an equilibrium period (EP) in which a constant temperature at the surface is established; a constant rate period (CRP) in which the rate of evaporation is similar to that of an

equivalent area of liquid phase [33] and a falling rate period (FRP) initiating at a critical moisture content ($X_c$) in which the rate of evaporation decreases with moisture content. Depending on the material and drying conditions one or two falling rate periods can be observed as shown in Figure 6.

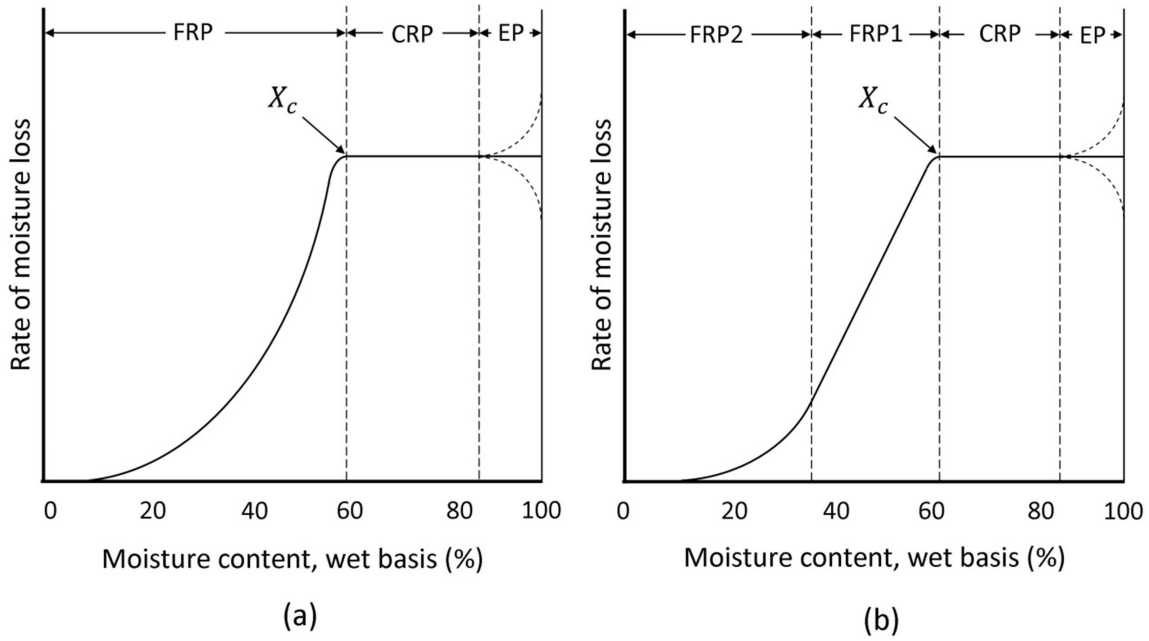



**Figure 6** – Typical drying curves displaying either one falling rate period (a) or two falling rate periods (b) initiating at a critical moisture content ($X_c$). Each curve displays an equilibrium period (EP), constant rate period (CRP) and falling rate period (FRP). In case (b) the falling rate period is divided into the 1st falling rate period (FRP1) and 2nd falling rate period (FRP2). Adapted from [34]

2.4.1.1 Equilibrium Period (EP)

Initially, as moisture loss takes place the exterior surface cools due to the latent heat of evaporation. Simultaneously, thermal energy is transferred between the drying body and the carrier gas to either heat or cool the surface of the drying body. Once an equilibrium temperature is established at the exterior surface (approximately the same as the wet bulb temperature [35]) a constant rate of evaporation is observed [36].

2.4.1.2 Constant Rate Period (CRP)

The rate of moisture loss in the CRP is dependent on how fast liquid can be removed from the surface as liquid is present as a continuous film on the surface acting independently of the solid phase [37].

The rate of water loss during the CRP can be calculated by either mass transfer or heat transfer [38] as shown by Equations 1 and 2 respectively.

$$R_{CRP} = -\frac{M_s}{A}\frac{dX}{dt} = k_g(P_s - P_w) \qquad \text{eq.1}$$

$R_{CRP}$ Rate of moisture loss during constant rate period (kg $m^{-2}$ $s^{-1}$)

$M_s$ Mass of dry solid (kg)

$A$ Area of interface for mass transfer ($m^2$)

$X$ Free moisture content ($kg_{moisture}$ $kg^{-1}_{dry\ solid}$)

$t$ Time (s)

$k_g$ Mass transfer coefficient (kg $m^{-2}$ $s^{-1}$ $Pa^{-1}$)

$P_s$ Partial pressure of vapour at the surface (Pa)

$P_w$ Partial pressure of vapour in the air stream (Pa)

$$R_{CRP} = -\frac{M_s}{A}\frac{dX}{dt} = \frac{h_t(T_s - T_w)}{\lambda} \qquad \text{eq.2}$$

$h_t$ Heat transfer coefficient (J $m^{-2}$ $s^{-1}$ $K^{-1}$)

$T_s$ Temperature of vapour at the surface (K)

$T_w$ Temperature of vapour in the air stream (K)

$\lambda$ Latent heat of evaporation (J $kg^{-1}$)

As shown in Equation 1, the rate of moisture loss for a given exposed area is dependent on the difference in partial pressure between the vapour in the air stream ($P_w$) and vapour pressure at the surface ($P_s$). The partial pressure of vapour in the air stream is related to the relative humidity ($R_H$) by Equation 3.

$$R_H = \frac{P_w}{P_{ws}} \qquad \text{eq.3}$$

$R_H$ Relative humidity (-)

$P_{ws}$ Saturation pressure of vapour in the air stream (Pa)

By modifying the $R_H$ of the gas stream a greater concentration gradient of moisture can be achieved at the liquid-gas interface. This produces a greater driving force for moisture loss as a higher volume of vapour can diffuse into the moving air stream. As such, a greater rate of moisture loss is attained by reducing the $R_H$ of the carrier gas. To attain the maximum rate of moisture loss, humid air produced at the liquid-gas interface must be replaced with dry air to maintain the initial vapour pressure in the air stream before moisture loss. Humid air is typically dried and recycled using a dehumidifier.

As shown in Equation 2, the rate of moisture loss for a given exposed area is dependent on the difference in temperature between the vapour in the air stream ($T_w$) and at the surface ($T_s$). Increasing the temperature of the gas stream raises the temperature of the drying body which provides more kinetic energy to the liquid, this results in a greater number of molecules transitioning to the gas phase. In addition, the saturation pressure of vapour in the gas stream is increased as warm air has the capacity to retain more moisture [39]. Both of these factors increase the rate of moisture loss when the temperature is increased.

2.4.1.2.1 Solid Suspensions

During the CRP a solid suspension transitions from a fluid to a gel as neighbouring particles are brought into closer proximity and form a 3D network. As drying progresses, particles form higher coordination numbers as the concentration of solids increases resulting in the structure stiffening with decreasing moisture content.

As moisture is evaporated, the drying body shrinks due to compressive forces acting on the solid phase due to capillary tension in the liquid arising from a curved meniscus at the surface of the drying body [36]. As the drying body shrinks, the meniscus remains at the surface. This creates a film of liquid on the surface of the drying body. As the moisture content decreases particles rearrange to higher packing fractions as shrinkage continues until a critical moisture content ($X_c$) is reached at which point the menisci begins to retreat into the bulk of the material and shrinkage virtually stops [36] initiating the beginning of the FRP.

2.4.1.3 Falling Rate Period (FRP)

During the FRP the rate of moisture loss decreases as there is insufficient moisture to maintain a continuous film of liquid at the surface. In this period the rate of moisture loss is dependent on the transport mechanism controlling liquid migrating from the bulk to the surface. Mass transport of liquid from the bulk to the surface can occur by either diffusion of vapour or capillary action of liquid depending on the characteristics of the material being dried. Typically, diffusion controlled drying behaviour exhibits a profile similar to Figure 6 (a) whereas typical capillary controlled drying behaviour exhibits a profile similar to Figure 6 (b) [35].

In capillary controlled mass transfer the transition from FRP1 to FRP2 marks a change in mechanism to diffusion controlled mass transfer as the drying front recedes below the surface into the bulk and liquid can no longer flow to the surface. In some cases a gradual discontinuity from first order rate loss kinetics are observed at the transition from FRP1 to FRP2 [40] and in other cases no FRP2 is observed [41].

2.4.1.3.1 Diffusion Controlled Mass Transfer

In diffusion controlled mass transfer the rate determining step in moisture loss is moisture transport from the bulk to the surface as vapour evaporating from the surface is rapid in comparison to vapour migration from the bulk to the surface. The diffusion of vapour in solids occurring within the FRP conforms to Fick's 2nd Law of diffusivity. This unsteady state equation typically applies to vapour transport in non-porous solids with a single phase such as soap, paste and glue. Diffusion controlled mass transfer occurs by redistribution of water molecules by random motion of gas phases into one another forming a concentration gradient. The change in concentration gradient with time is dependent on the 2nd derivative of this concentration gradient as shown by Equation 4 [35].

$$\frac{dX}{dt} = D_L\left(\frac{d^2X}{dx^2}\right) \qquad \text{eq.4}$$

$D_L$ Liquid diffusivity coefficient ($m^2\ s^{-1}$)

$x$ Distance in the solid (m)

A solution to Equation 4 was proposed by Sherwood [42] assuming a uniform initial moisture content and zero liquid concentration at the surface once drying has begun as shown by Equation 5. For long periods of drying only the first term is significant.

$$\frac{X}{X_0} = \frac{8}{\pi^2}\left[e^{-D_L t\left(\frac{\pi}{2x_T}\right)^2} + \frac{1}{9}e^{-D_L t\left(\frac{\pi}{2x_T}\right)^2} + \frac{1}{25}e^{-D_L t\left(\frac{\pi}{2x_T}\right)^2} + \cdots\right] \qquad \text{eq.5}$$

$X_0$ Initial free moisture content ($kg_{moisture}\ kg^{-1}_{dry\ solid}$)

$x_T$ Total thickness of slab if drying occurs from one face (m)

Rearranging Equation 5 to make $t$ the subject gives Equation 6.

$$t = \frac{4x_T^2}{\pi^2 D_L} \ln\left(\frac{8X_0}{\pi^2 X}\right) \quad \text{eq.6}$$

Assuming that the diffusion limited behaviour starts at $X = X_c$ then $X_0 = X_c$. Differentiating Equation 6 with respect to time and rearranging gives Equation 7.

$$R_D = -\frac{M_s}{A}\frac{dX}{dt} = \frac{\pi^2 M_s D_L}{4x_T^2 A} X \quad \text{eq.7}$$

$X_c$ Critical free moisture content ($kg_{moisture}$ $kg^{-1}_{dry\ solid}$)

$R_D$ Rate of moisture loss during diffusion controlled mass transfer (kg $m^2$ $s^{-1}$)

As shown by Equation 7, when internal diffusion controls evaporation from the surface, the rate of moisture loss ($R_D$) is proportional to the free moisture content ($X$) and liquid diffusivity ($D_L$). This, however, is often not the case as the liquid diffusivity coefficient decreases as drying proceeds [35] leading to the rate of moisture loss becoming non-linear with respect to moisture content as displayed in the FRP of Figure 6 (a) . Additionally, the drying rate is inversely proportional to the thickness squared; meaning doubling the thickness will quarter the drying rate. It is also noted that during diffusion limited evaporation the drying rate is independent of gas velocity and relative humidity and as such modification to these terms will not affect drying time [35].

2.4.1.3.2 Capillary Controlled Mass Transfer

The mechanism of liquid transport in granular materials such as clays, pigments, minerals and colloidal suspensions [43, 44] typically occurs by capillary action. The critical moisture content ($X_c$) at which the CRP transitions into the FRP1 is dependent on the particle size of the material. Typically, a higher $X_c$ is observed for smaller particles as liquid cannot be

supplied from the bulk to the surface to maintain a film of liquid on the surface due to internal friction effects [34].

Flow of liquid through porous mediums is described by Darcy's law [45] shown by Equation 8. This equation describes the mass transport of liquid in porous mediums towards regions of negative pressure. Consequently, as evaporation occurs at the surface of the porous body, liquid is pumped out of the largest capillary into smaller capillaries resulting in smaller capillaries remaining saturated preferentially over larger ones [36]. This leads to the surface forming a progressively decreasing wetted area as moisture content reduces [46].

$$J = -\frac{D}{\eta_l}\nabla P_L \qquad \text{eq.8}$$

$J$ Flux (m $s^{-1}$)

$D$ Permeability ($m^2$)

$\eta_l$ Viscosity of liquid (Pa s)

$\nabla P_L$ Pressure gradient in liquid (Pa $m^{-1}$)

Capillary pressure arises in a liquid due to the formation of a curved meniscus as high energy liquid-gas interfaces are minimised in preference for liquid-solid interfaces [36]. The pressure difference over an interface between two immiscible fluids for a thin cylindral capillary is described by the Young-Laplace equation shown by Equation 9 [47, 48]. This equation describes that a smaller radius of curvature produces a greater pressure difference across the interface.

$$P_c = \frac{2\gamma}{\rho_c} \qquad \text{eq.9}$$

$P_c$ Capillary pressure (Pa)

$\gamma$ Surface tension (N $m^{-1}$)

$\rho_c$ Radius of curvature of liquid in capillary (m)

Describing a drying porous body as a packed bed of non-porous spheres of identical diameter the maximum height liquid can be drawn from the bulk to the surface due to capillary action can be calculated by assuming either an open (cubical) or closest (rhombohedral) arrangement. This value is described as the suction potential ($P_{suc}$) which can be calculated by Equation 10 [41]. As such, porous materials with fine pores can draw water from deep cavities.

$$P_{suc} = \frac{\gamma x_{PF}}{r g \rho_l} \qquad \text{eq.10}$$

$P_{suc}$ Suction potential (m)

$x_{PF}$ Packing factor (12.9 for rhombohedral packing 4.82 for cubical packing) (-)

$r$ Radius of sphere (m)

$g$ Acceleration due to gravity (m $s^{-2}$)

$\rho_l$ Density of liquid (kg $m^{-3}$)

During the region of capillary controlled mass transport, evaporation of moisture occurs via the same mechanism as is observed during the CRP [35]. As such, variables such as gas velocity, gas temperature and relative humidity will affect the rate of evaporation [35]. During this period the rate of moisture loss ($R_C$) follows first order kinetics with respect to moisture content as represented by the FRP1 in Figure 6 (b). Therefore, the rate of moisture loss is a linear function of the free moisture content ($X$) and therefore the rate can be calculated from the initial drying rate during the CRP using the Equation 11 [35].

$$R_C = -\frac{M_s}{A}\frac{dX}{dt} = R_{CRP}\frac{X}{X_c} \qquad \text{eq.11}$$

$R_C$ Rate of moisture loss during capillary controlled mass transfer (kg $m^{-2}$ $s^{-1}$)

During the FRP1 liquid is present within the pores in a funicular state allowing flow to the surface through a contiguous pathway of liquid. Capillary controlled mass transfer is sustained until capillary action cannot supply liquid to the surface and the continuity of liquid to the surface breaks. This causes the drying front to recede below the surface as isolated pockets of liquid begin to form near the surface in a pendular state. This initiates the FRP2 as shown in Figure 6 (b) in which a further reduction in rate of moisture loss is observed, subsequently becoming non-linear with respect to moisture content. In the FRP2 vapour is transported to the surface via diffusion of vapour through the dry section of the solid as moisture can no longer flow via capillary action to the surface [36].

### 2.4.2 Simulation and Modelling of Drying Behaviour

Simulating drying in capillary porous media via modelling is a useful tool for predicting drying behaviour under a range of different conditions. Such tools can be used in industrial settings to optimise drying conditions with a minimal number of experimental trials required. Modelling is generally conducted by visualising the pore structure of a material (as characterised by mercury intrusion porosimetry) as a large number of interconnecting pores in an array with specified dimensional characteristics [49]. The transport phenomena occurring within the network is defined by the Young-Laplace equation (Equation 9) which describes favourable liquid migration towards regions of lower pressure. The evaporation of liquid from a capillary is approximated by mass transfer (Equation 6) or heat transfer (Equation 7). Other parameters can be included in the model to account for liquid viscosity, friction, gravitational effects and latent heat of evaporation to name a few. Models describing drying behaviour in porous media accurately predict both constant rate period and falling rate period characteristics [50], in addition to temperature profiles [51] when compared to experimental data.

Modelling provides the ability to investigate behaviour in complex systems with varying pore size distribution [52], bi-modal pore size distributions [50], directional pores [50] and even with the presence of non-porous inclusions [53]. Such tools can be useful for understanding phenomena in complex systems for which experimental results provide little information. However, as the complexity of the model grows, more computing power is

required to run the simulation. As such, many models in literature display a limited area of coverage which may not be representative of the real life system.

### 2.4.3 Contact-Sorption Drying

Contact between a desiccated (dry) porous particle and a wet substance containing solids results in liquid transfer from the wet substance to the dry particle by capillary action as liquid migrates towards regions of negative pressure as described earlier by Equation 8. This procedure is typically described as contact-sorption drying [54]. This procedure has shown promise in drying materials such as coal [55] and agricultural products [56] in addition to heat sensitive biomaterials [57] as drying can be conducted without depressing the surface temperature which occurs in convection drying due to the latent heat of evaporation.

Liquid transfer between the two materials will only occur if the dry particle has an unsaturated pore smaller in diameter than a saturated pore in the wet substance. This produces a greater suction potential in the dry particle resulting in liquid transfer. In addition, liquid in the wet substance must be able to flow to the dry particle. As such, liquid cannot migrate from a wet substance displaying diffusion controlled mass transfer as the drying front has receded into the bulk and liquid cannot flow to the interface between the two materials.

As liquid migrates from the wet substance to the dry particle, liquid is rearranged within the particle to fill pores further from the contact surface. Simultaneously, liquid is rearranged within the wet substance to replenish drained pores with liquid from the bulk. After a given length of time, equilibrium will be established between the two materials and there will be no net movement of water [54] assuming evaporation does not occur.

The scenario described is closely related to slip casting in which the surface of the dry porous particle represents the porous mould and the wet substance represents a solid suspension called the slip. The two scenarios differ in that the dry particle can only absorb a finite volume of water from the suspension before it becomes saturated, whereas a slip casting mould typically remains unsaturated during use due to its large volume relative to the volume of liquid in the slurry. In addition, slip casting provides a complete contact surface from which moisture is drawn, whereas the application of desiccated particles onto

the surface of a wet substance produces a broken layer of contact, allowing evaporation to occur from any exposed surface.

Equations describing the build-up of dried slip (typically called cake in the slip casting industry) can be related to the length of time the slip remains in contact with the mould. As such, the thickness of cake is proportional to the square root of the contact time [58, 59] as shown in Equation 12 .This has proven to be accurate for a range of ceramic slips [60].

$$h^2 = \frac{2tP_{mould}/\eta_f}{(\epsilon_{s\cdot cake}/\epsilon_{s\cdot slurry})\left(\frac{1}{D_{mould}} + \frac{(\epsilon_{s\cdot cake}/\epsilon_{s\cdot slurry} - 1)}{\epsilon_{l\cdot mould} \times D_{mould}}\right)} = Bt \qquad \text{eq.12}$$

| | |
|---|---|
| $h$ | Cake thickness (m) |
| $P_{mould}$ | Mould suction pressure (Pa) |
| $\eta_f$ | Viscosity of filtrate (Pa s) |
| $\epsilon_{s\cdot\text{cake}}$ | Volume fraction of solids in cake (-) |
| $\epsilon_{s\cdot\text{slurry}}$ | Volume fraction of solids in slurry (-) |
| $D_{mould}$ | Permeability of mould ($m^2$) |
| $\epsilon_{l\cdot\text{mould}}$ | Volume fraction of filtrate in wetted part of mould (-) |
| $B$ | Constant ($m^2\ s^{-1}$) |

As described by Equation 12, the magnitude of $B$ is dependent on the properties of the porous mould; namely the permeability ($D_{mould}$) and suction pressure ($P_{mould}$) which are both dependent on the pore size of the mould. The suction pressure can be increased by lowering the pore size within the mould, however this reduces the permeability. The highest magnitude of $B$ is found when the particle size in the slurry is equal to the particle size in the mould for identically sized spherical particles in a close packing arrangement [59].

### 2.4.4 Drying Materials with Variable Pore Sizes

As a result of capillary action, moisture loss occurring at the surface of a material containing interconnected pores of variable size results in wide pores draining preferentially to narrow pores. This takes place as liquid is pumped from wide capillaries into narrow capillaries to

reduce solid-gas interfaces as moisture content decreases [52]. Subsequently, in a situation where moisture is lost from two connected materials of different pore size distributions (such as contact-sorption drying) the distribution of liquid between the two materials may vary as the total moisture content reduces.

### 2.4.5 Drying of Investment Casting Moulds

Investment casting moulds are dried successively during manufacture after each layer is applied. This takes place in a chamber with controlled airflow, temperature and humidity ensuring the deepest cavities are dry before the mould is redipped in slurry. Attaining optimum drying conditions is important to both reduce the lead time during manufacture and ensure the mould does not crack. As such, to minimise failure, investment casting moulds are typically dried under mild conditions close to STP. Each time a partially built mould is submerged in slurry a wetback effect occurs whereby the previously dried layers absorb liquid from the subsequent layer of slurry. As a result, the greater number of layers applied the larger volume of moisture retained in the partially built mould. Consequently, a longer period of time is required to fully dry the mould after each additional layer added [37]. It is important to note that if the rate of water removal is too extreme the magnitude of the latent heat of evaporation can be so large that the mould cracks due to differential thermal expansion coefficients between the wax pattern and the ceramic mould [37].

#### 2.4.5.1 Effect of Air Flow

The effect of air velocity has been found to increase the rate moisture loss for investment casting slurrys with 6 m $s^{-1}$ improving drying times over 3 m $s^{-1}$. However, increasing the air velocity above 6 m $s^{-1}$ yielded no better drying rate with possible damage to the mould taking place at these high velocities [37].

#### 2.4.5.2 Effect of Relative Humidity

Despite the tendency to increase the rate of moisture loss with a low $R_H$, a $R_H$ of between 50 – 90 % is typical in shell drying. This has been shown to improve flexural strength as particles have longer to pack and thus a denser layer is formed with greater strength [61].

#### 2.4.5.3 Effect of Temperature

Raising the temperature from 20 °C to 40 °C has been shown to significantly increase the rate of moisture loss for investment casting slurries [62]. However, drying the mould too

quickly through increasing temperature and reducing $R_H$ can lead to the formation of an impervious outer layer of skin which prevents liquid migrating to the surface [61]. This can lead to cracking as the entrapped liquid in the bulk cannot permeate through this dense layer and expands causing failure.

### 2.4.6 Accelerated Drying of Investment Casting Moulds

Due to longevity of drying the ceramic mould by traditional convection methods, alternative processes have been developed where drying stages are reduced or eliminated. Such processes address the challenge of maximising water loss without depressing the temperature of the slurry resulting from the latent heat of evaporation. This prevents fracture resulting from differential thermal expansion coefficients between the ceramic slurry and the wax pattern.

#### 2.4.6.1 Cyclone Drying

Crack free accelerated drying can be achieved by combining high rates of turbulent airflow (12 m $s^{-1}$), dry conditions (10-15% RH) and temperature control through the use of medium wavelength infra-red bulbs to offset the cooling effect from the latent heat of evaporation [63]. This system is commercially available from MK systems which state a layer can be dried in as little as 30 minutes.

#### 2.4.6.2 Microwave Drying

Crack free accelerated drying can be achieved by implementing microwave heaters to offset the cooling effect from the latent heat of evaporation. Such systems are commercially available from SHELL-O-MATIC stating a drying time per layer of as little as 30 minutes is possible.

#### 2.4.6.3 Contact Sorption Drying

Utilising a capillary porous material as stucco to absorb water from the slurry upon contact results in a reduction in drying time allowing the next layer to be applied more quickly; reducing the time taken to produce a ceramic mould. Examples of materials used for this technique are outlined in the following Sections.

2.4.6.3.1 Super Absorbent Polymer

The use of super absorbent polymer (SAP) has shown a degree of success at reducing the drying time of investment casting moulds. As described in a European [64] and United States of America [65] patent, a combination of milling and drying processes can be undertaken to deposit a thin layer of polyacrylamide on the surface of standard stucco particles. Through this method a substantial reduction in drying time can be achieved, requiring only 2 % the time in comparison to air drying. However, the longevity of this process is limited as the weak polymeric coating is degraded by the abrasive nature of the stucco in the rainfall sander and a problematic dust is created as the coating degrades. In addition to this, the particles swell immensely upon absorption. Tailoring of copolymer and crosslinker quantities can lead to absorption of liquid in excess of 100X the original weight of the material [66]. This high degree of swelling has been shown to produce bulging and delamination of layers [5] which occur during slurry dipping and in the autoclave. Furthermore, a reduction of between 30 – 40 % in flexural strength was observed utilising this method with large voids present once the polymer was burnt out in the firing cycle [5]. Overall this method works extremely well at reducing the drying time; however, the problems encountered make the process impractical in its current state and work must be undertaken to implement this method into industry without degrading shell properties.

2.4.6.3.2 Super Absorbent Polymer

A United States of America patent [67] describes the use of capillary porous ceramic materials to reduce the drying time of investment casting moulds. However, minimal public research is available on this topic. This technique describes the use of various desiccant materials such as silica gel, activated alumina and zeolite possessing a surface area in excess of 100 $m^2 g^{-1}$ blended with standard refractory stucco at a weight ratio no less than 1 %. One of the advantages of this method over use of SAP is the harder nature of ceramic material in comparison to SAP. This property may allow the porous ceramic to withstand the harsh environment in the rainfall sander and avoid the problems associated with degradation of the material during use observed with SAP. Additionally, capillary porous materials remain dimensionally stable when absorbing water as the liquid is drawn into the pores rather than causing swelling as seen with SAP. This property may eliminate the bulging and delamination of layers observed when using SAP. However, desiccant materials have a lower

water absorption capacity in comparison to SAP with porous ceramics typically attaining volumetric porosity values of 0.4 – 0.9 $cm^3_{pore}$ $cm^{-3}_{bulk}$ [68, 69, 70].

## 2.5 Accelerated Manufacture of Investment Casting Moulds

Other additive manufacturing processes are available for producing bespoke monolithic ceramic articles. Such techniques typically build layers sequentially to form a 3 dimensional shape which is subsequently processed to produce the ceramic article. Numerous techniques are currently available [71] including sterolithography 3D printing, binder jetting, extrusion and laser fusion. The dimensional resolution, scale up capability and material compatibility for each technique varies drastically so choosing the correct technique for the application is key. Examples of the techniques covered in literature detailing the manufacture of investment casting moulds are outlined in the following Sections.

### 2.5.1 Sterolithography (SLA)

Stereolithography is a technique that involves the use of a slurry containing photocuring resin which is selectively cured with the use of a high resolution projector or screen. By sequentially building multiple layers of cured resin a 3D structure is produced which often requires supports to build complex shapes. Once the structure is built, the uncured resin is removed by use of solvents. If the slurry is filled with a high loading of ceramic powder a ceramic preform is made which can undergo debinding and firing stages to produce a ceramic component.

Utilising a slurry containing silica powder, Bae et al. demonstrated the possibility of manufacturing an integrally cored mould whereby the mould and core are built simultaneously together [72]. Successful application of such a technique in industry would remove many stages of the investment casting process including wax pattern and ceramic core manufacture. However, this technique would require the mould and core to be made from the same composition which may not simultaneously provide suitable creep resistance in the shell and suitable leachability in the core.

Utilising a sacrificial polymeric component manufactured by SLA, ceramic moulds with cores embedded can be produced by gelcasting [73]. The advantage of this technique is the level of complexity that can be built into the system as the composition of the mould and core

can be varied whilst eliminating the need for a wax pattern and drying/autoclave processing.

### 2.5.2 Direct Laser Sintering

Direct laser sintering involves utilising a high energy laser to selectively bond regions of ceramic powder to form a ceramic article. By successively depositing thin layers of ceramic powder (10-100um) with a doctor blade and sintering selected regions, a 3 dimensional shape is formed which attains high theoretical density in excess of 90% [74]. As described by Klocke et al. investment casting moulds can be manufactured via direct laser sintering using zircon powder as feedstock [75]. The advantage of this process is that the mould doesn't require post-processing treatment, eliminating costs associated with drying, firing and autoclave processing. The disadvantage however is the dimensional resolution is poor and removal of feedstock powder from narrow internal cavities is difficult.

## 2.6 Synthesis of Porous Ceramics

Porous materials are characterised by the International Union of Pure and Applied Chemistry (IUPAC) into three categories depending on the mean pore size ($d$) of the material: macro-porous ($d$ >50 nm), meso-porous (50 nm > $d$ > 2 nm) and micro-porous ($d$ <2 nm) [76]. Fabrication of ceramics in each category requires a different method of synthesis as the formation of large micrometre sized voids requires a different processing route to producing a material with smaller pores capable of molecular filtration for example.

### 2.6.1 Macro-porous Ceramic Synthesis

The synthesis of macro-porous ceramics is undertaken through partial sintering, replica templates, direct foaming or sacrificial fugitive methods [77]. Each method favours a particular pore size, with some methods achieving higher porosities than others due to the process by which pores are produced in the material.

#### 2.6.1.1 Partial Sintering

Partial sintering of powder compacts produces a homogeneous distribution of pores typically attaining a low porosity of less than 60 % [78]. Partial sintering involves firing powder compacts at a temperature or duration below that capable of fully densifying the

ceramic. As a result of this processing route the porous bodies are generally not stable at high temperature and continue to shrink if exposed to high temperature. This was observed in thermal insulators which showed shrinkage after prolonged use [79].

#### 2.6.1.2 Replica Template

The replica template method involves impregnating a degradable porous structure (replica) with a solid suspension. The suspension is then dried and the replica is removed via combustion to yield a green body which can be fired to form a sintered porous body as shown in Figure 7. As the replica structure is typically made of a plastic or wax it is possible to create complex components through 3D printing to manufacture bespoke bio-scaffolds or other desirable components [79]. This method is best utilised for designing specific pore geometries and microstructures, an example of which is exploiting the microcellular properties of pine-wood to produce a template through which long thin pores are generated [80].

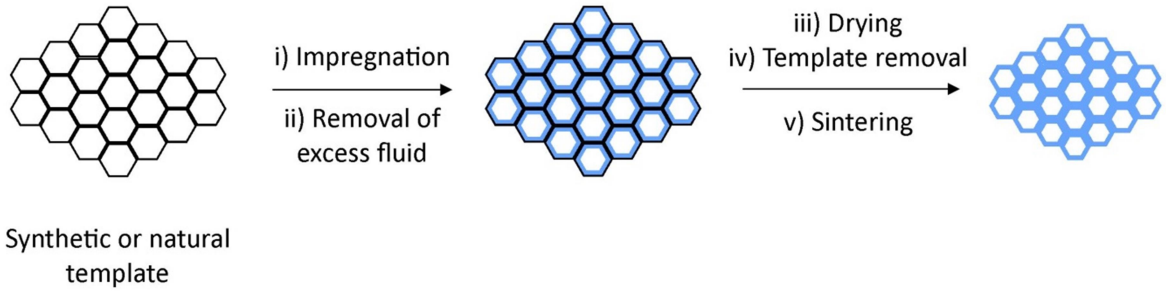



**Figure 7** – Replica template method of synthesising macro-porous ceramics

#### 2.6.1.3 Direct Foaming

Direct foaming is an effective method at producing macro-porous ceramics with large voids through the incorporation of air into a solid suspension containing surfactants to produce foam. This structure is then hardened to form a porous green body which can be subsequently fired and sintered as shown in Figure 8. Typically, the porosity of the green body is determined by the quantity of gas added to the suspension while the pore size is determined by the stability of the wet foam before the structure is hardened. As a result of drainage from gravity the foam can be non-homogeneous as liquid settles which forms a concentration gradient of pores [78].

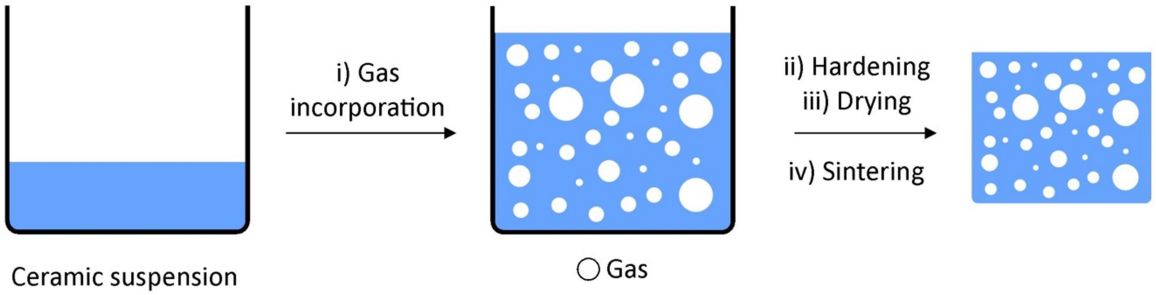



**Figure 8** – Direct foaming method of synthesising macro-porous ceramics

2.6.1.4 Sacrificial Fugitives

Dispersion of a combustible substance (sacrificial fugitive) in a solid suspension produces a slurry which when dried and fired produces a porous ceramic as shown in Figure 9. This method is extremely versatile with numerous sacrificial fugitives available including flour [81], polystyrene microspheres [82] and cotton fibres [83]. As the pore size is determined by the sacrificial fugitive a broad range of pore sizes can be produced by adding the specified particle size to the ceramic suspension. Limitations to this method include the large volume of gas produced upon combustion which needs to permeate through the structure without fracturing the material; this can require a long and slow burnout period in the furnace to achieve. This process can make synthesising bulky structures difficult as the gas generated from the bulk must migrate to the surface without exerting excessive force resulting in fracture. In addition, the environmental impact of burning out combustible material needs to be considered.

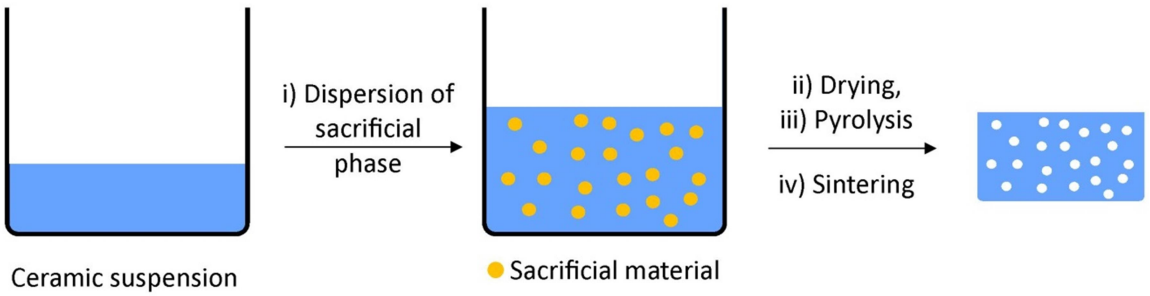



**Figure 9** – Sacrificial fugitives method of synthesising porous ceramics

### 2.6.2 Micro/Meso-porous Ceramic Synthesis

Synthesis of ceramic materials with a mean pore size less than 50 nm can be conducted via three methods [76]:

1) The formation of intracrystalline pores within a crystal lattice. Examples of which include zeolitic frameworks [84] the pore shape and size of which can be tailored depending on the application.
2) The formation of pores between hard particles. This method is typically conducted by removing the liquid component of a colloidal suspension either via evaporation to produce a xerogel or via supercritical drying to produce an aerogel [17]. Once dry, the structure of the material has a network of pores found between interparticle voids.
3) The selective removal of species in a material to generate pores. This method is typically conducted via thermal decomposition of metal hydroxides [85], hydrides [86], carbonates [87] or oxalates [88]. Alternatively, pores can be generated by chemical leaching of a single phase within a multiphase material [89].

Micro/meso-porous materials typically have a high surface area resulting from the fine microstructure of the material. This property is often exploited for use in catalysts [90] and dehumidifying agents [91] as a high volume of gas can adsorb onto the surface of the material. Other uses include molecular filtration of gas/liquid to selectively absorb specific molecules by tailoring the pore size of the material [92].

#### 2.6.2.1 Alumina

The meso-porous transition phases of alumina comprise gamma alumina (γ-$Al_2O_3$), delta alumina (δ-$Al_2O_3$), theta alumina (θ-$Al_2O_3$), kappa alumina (κ-$Al_2O_3$), eta alumina (η-$Al_2O_3$) and chi alumina (χ-$Al_2O_3$). These materials can be synthesised following the thermal decomposition of aluminium oxide hydride (AlOOH) or aluminium trihydrate ($Al(OH)_3$) species. The decomposition reaction of AlOOH and $Al(OH)_3$ is given in Equation 13 and 14 respectively [85].

$$2AlOOH \rightarrow Al_2O_3 + H_2O \qquad \text{eq.13}$$

$$2Al(OH)_3 \rightarrow Al_2O_3 + 3H_2O \qquad \text{eq.14}$$

The transition phase of alumina formed during the thermal decomposition process is dependent on the initial phase of the mineral composed of either AlOOH or $Al(OH)_3$. For some mineral phases, successive phase transformation occurs following thermal decomposition if the temperature is increased further. The thermal transformation sequence for different phases of minerals composed of AlOOH and $Al(OH)_3$ is given in Figure 10 displaying the approximate temperature each phase begins to from. Typically, any transition phase of alumina exposed to temperatures in excess of 1000 ˚C produces α-$Al_2O_3$ which is accompanied by the collapse of the meso-pore structure [93]. Phase transition involves the atomic rearrangement of the crystal lattice to produce a different arrangement of atoms.

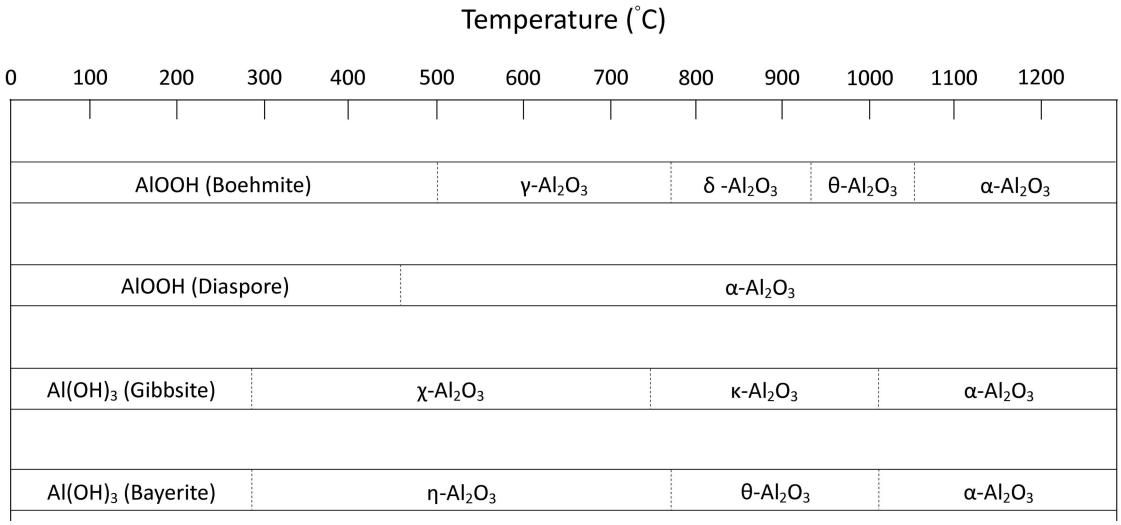



**Figure 10** – Thermal transformation sequence of AlOOH and $Al(OH)_3$ minerals. Reproduced from [85]

2.6.2.1.1 Boehmite Processing

Producing monolithic alumina components from boehmite powder via dry pressing is generally unsuccessful due to the combination of hard agglomerates in the powder and the large volume changes associated with phase transition and sintering [94]. As such, the

production of alumina components from boehmite is typically undertaken via a sol-gel processing route [95] or peptization (deagglomeration) [96]. This yields a colloidal dispersion of AlOOH which is subsequently gelled and dried to form a xerogel which is then fired to produce the required phase of alumina [97].

Peptization is the formation of an electrostatically stabilised colloidal suspension by dispersing agglomerated species to a sufficiently small size to remain suspended in solution [98]. Peptization of boehmite powder composed of agglomerated AlOOH species is typically carried out by adding powder to an acidic medium, whereby the molar acid ratio of the solution determines the volume at which the solution begins to gel during drying. A molar acid ratio of $[H^+/Al] = 0.07$ is known as the "minimum gel volume" whereby any deviation from this value results in gelation below the maximum possible solids loading when drying. This subsequently leads to excess shrinkage often accompanied with cracking as drying nears completion [99].

The addition of boehmite powder to an acidic medium causes agglomerates to break down into their primary, dimeric and polymeric species identified as between 5 – 80 nm in length [100]. These primary species have been identified by $Al^{27}$ NMR as the monomer $[Al(H_2O)_6]^{3+}$ and its hydrolysed counterpart $[Al(H_2O)_5(OH)]^{2+}$. Dimeric species have been identified as $[(H_2O)_4Al_2(OH)_2(H_2O)_4]^{4+}$ and $[Al_3O_2(OH)_4(H_2O)_8]^{+}$ [101].

2.6.2.2 Silica

Silica gel is prepared via a similar processing route to the production of colloidal silica described in Section 2.3.4.1, whereby silica particles are grown in alkaline conditions from the monomer silicic acid. The colloidal suspension is then acidified causing particles to flocculate together to form a three dimensional network. This is followed by a washing step in which the impurities formed in the reaction are removed with fresh water to produce optimum absorption properties [91]. The gel is then dried to form a xerogel containing micropores within each cluster of primary particles and mesopores between these clusters [17]. $CoCl_2$, $FeCl_3$ and methyl violet are often incorporated into silica gel when used as a desiccant material which act as a water content indicator. These species transition from one colour to another to identify if that material is wet or dry.

## 2.7 High Temperature Processing

### 2.7.1 Sintering

The redistribution of mass to form bonds between particles at a temperature below the melting point of the solid is called sintering. The driving force behind this process is the reduction in surface energy via the formation of solid-solid interfaces from solid-vapour ones [99]. This typically results in densification as neighbouring particles form grain boundaries with each other resulting in the removal of porosity. However, to ensure the optimum performance of a sintered component the raw material and processing route must be controlled to limit grain/pore growth. This can be achieved by tailoring the particle size distribution of powder or altering the firing cycle. The mechanism of sintering depends on the crystallinity of the material, whereby crystalline ceramics sinter via solid state sintering unless a lower melting point solid (sintering aid) is present. On the other hand, amorphous ceramics sinter through viscous sintering.

#### 2.7.1.1 Solid State Sintering

Solid state sintering occurs in high purity crystalline materials at temperatures typically above 50 % of a material's melting temperature. Once particles fuse, a range of mass transport mechanisms occur leading to either densification or coarsening. In order for densification to occur, mass is transported from the grain boundary to the necked area, widening the neck and pulling particle centres closer together. Listed in Figure 11 are the mass transport mechanisms leading to densification; it has been identified that the main mechanisms leading to densification in polycrystalline ceramic materials are grain boundary diffusion and lattice diffusion [102]. The rate of sintering is dependent on the mechanism via which sintering occurs [99].

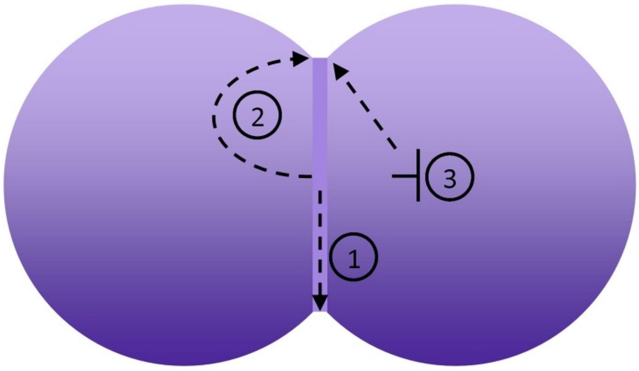



**Figure 11** – Mass transport mechanisms in sintering leading to densification where (1) is grain boundary diffusion, (2) is lattice diffusion from a grain boundary and (3) is plastic flow

Coarsening is the process of mass transport from high surface energy particles to low surface energy particles resulting in grain coalescence to produce a smaller number of larger particles [103]. As a result of this mechanism densification is hindered leading to porosity remaining in the structure. This behaviour typically reduces the strength of components due to the formation of a reduced load bearing cross-section and the development of stress concentration regions [104]. The mass transport mechanisms leading to coarsening are displayed in Figure 12.

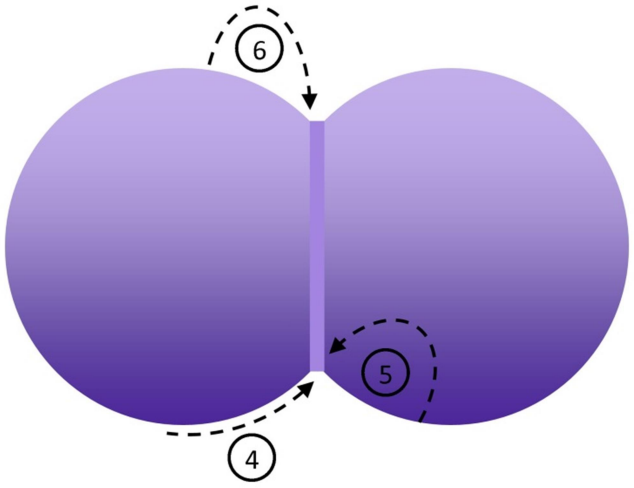



**Figure 12** – Mass transport mechanisms in sintering leading to coarsening where (4) is surface diffusion, (5) is lattice diffusion from the surface and (6) is vapour transport

2.7.1.2 Liquid Phase Sintering

The addition of a lower melting point solid (sintering aid) homogeneously dispersed at low concentrations (typically of a few weight percent) in a green body can lead to enhanced sintering behaviour. Subsequently, porosity can be removed through a more efficient, less energy intensive densification route requiring a lower sintering temperature or duration. The sintering aid chosen for each ceramic system varies. However, a successful sintering aid should encourage particle rearrangement arising from capillary forces due to good wetting and solution re-precipitation arising from a high solubility of the powder medium in the liquid phase. As such, a suitable liquid phase sintering aid will form a low contact angle on the surface of the required powder medium and have sufficient solubility of the powder when in the liquid phase [105].

During the heating stage the liquid phase begins to melt and wet out on the powder medium. This acts as a lubricant allowing particle movement and rearrangement which is encouraged due to capillary forces acting on particles due to curved liquid menisci. This encourages packing into dense arrangements over the random packing present in the green phase [106]. As density increases, physical restrictions prevent rearrangements to closer packing fractions and unless a high volume of liquid phase (approximately 25 – 35 vol%) is present densification cannot be completed via rearrangement alone [107].

In addition to solid state sintering (as described in Section 2.6.1.1) a secondary sintering mechanism called solution reprecipitation begins to occur at higher packing fractions when particles come into close proximity. This mechanism allows mass transport through dissolution from energetic regions of the grain such as areas under compression, convex points and apexes into the liquid where the dissolved solid is deposited onto less energetic regions such as areas under tension and concave areas [105]. As solution reprecipitation continues the particles become more rounded in nature and densification continues leading to the removal of porosity. During the final stages of densification interconnected pores begin to close leading to the formation of closed porosity containing gaseous species present in the sintering environment and vapour from the liquid. At this stage the rate of densification is dependent on the rate of gas diffusion into the atmosphere [107]. The microstructure development throughout the liquid phase sintering process is shown in Figure 13.

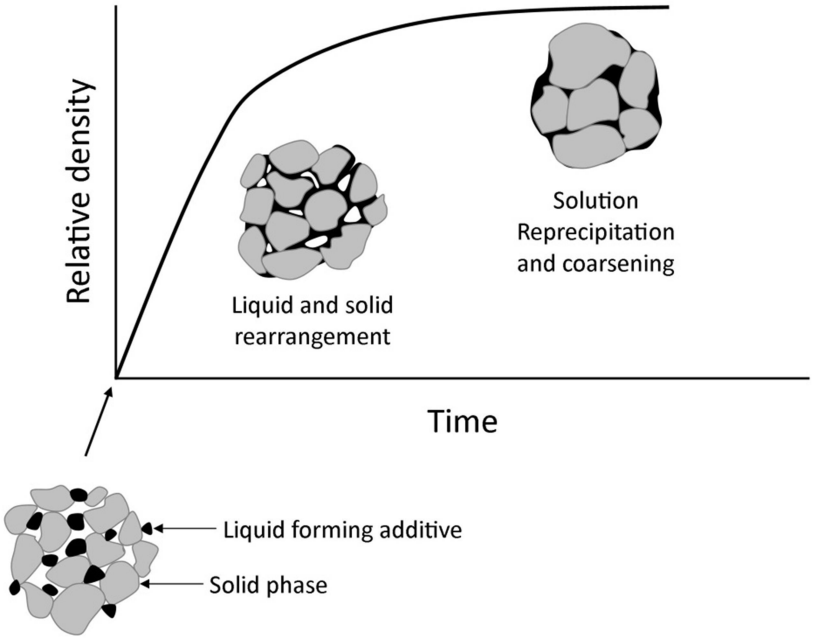



**Figure 13** – Microstructural development occurring during liquid phase sintering. Reproduced from [102]

2.7.1.3 Viscous Sintering

Viscous sintering occurs in amorphous solids (glasses) which flow under pressure if the viscosity is lowered sufficiently with thermal energy. For a silicate material the viscosity is highly dependent on temperature with viscosity changing by an order of magnitude every 20 – 40 °C during the glass transition region [17]. Due to the effects of surface tension, solid-gas interfaces are reduced due to the formation of necks between particles which grow to densify the material over time [108] as shown in Figure 14.

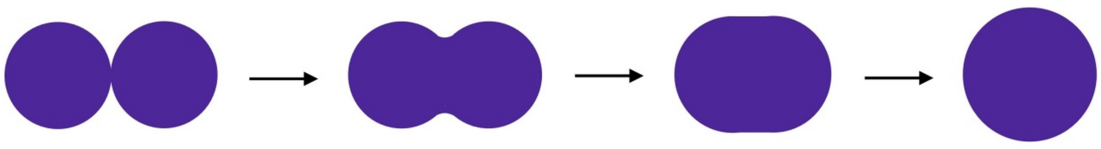


**Figure 14** – Shape evolution of two equally sized glassy particles coalescing via viscous sintering. Reproduced from [108]

### 2.7.2 Creep

Creep is the slow deformation of a material subject to stress at elevated temperature. Typical creep behaviour of a material subject to stress over time displays three stages of

creep consisting of a primary stage, secondary (steady state) stage and a tertiary stage before failure [109] as show in Figure 15.

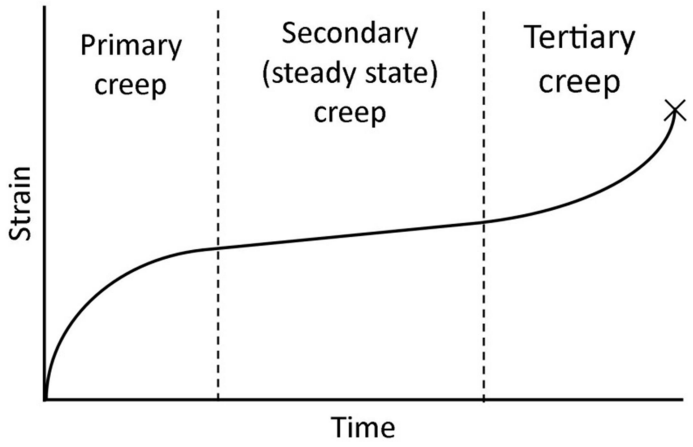



**Figure 15** – Typical stages of creep exhibited when a material is subject to stress over a prolonged period of time at elevated temperature

Creep can result from either intergranular or intragranular deformation typically via bulk diffusion, grain boundary diffusion or dislocation glide. To identify the mechanism of deformation occurring for a specific material, the dependency of grain size and stress on the strain rate is measured at various temperatures [110].

# 3. Materials and Methods

## 3.1 Methods

In this Section the analysis methods used to characterise the properties of ceramic moulds and their constituent components are detailed. Where necessary, the terms BD-$Al_2O_3$, SGB127, Tab-$Al_2O_3$, αFrame and αFrame-$Impreg_8$-Clean are used to describe different stucco materials the synthesis route and composition of which is detailed in Section 3.2.6.

### 3.1.1 Material Characterisation

3.1.1.1 X-ray Diffraction (XRD)

The crystal structure of an experimental material was characterised by XRD using an Equinox 3000 X-Ray diffractometer manufactured by INEL. The instrument uses a copper X-Ray tube powered to 35 kV and 25 mA to generate Cu Kα radiation and uses a germanium monochromator and a nickel filter to remove the kβ radiation. Samples were prepared for analysis by grinding approximately 1.0 g of material in an agate pestle and mortar and sieving the material through a 50 μm sieve before conducting analysis on the fine fraction.

3.1.1.2 Particle Size Distribution (PSD)

A Malvern Mastersizer 3000 implementing Mie theory [111] was used to analyse the PSD of stucco grains by interpreting laser scattering data. For each analysis a red light source was used which was realigned after each test. A background measurement was performed to reduce error before analysing the material five times. Granular stucco material was analysed by both hydro and aero dispersion methods as necessary, requiring approximately 5 $cm^3$ of material for each analysis. Listed in Table 1 is the refractive index of each material used by the instrument to calculate PSD [112]. It should be noted that the refractive index of composite ceramic materials was averaged equally between each component.

**Table 1** – Refractive index of materials used for PSD characterisation

| Material | Material label | Refractive index |
|---|---|---|
| Silica | SGB127 | 1.54 |
| α-$Al_2O_3$ | αFrame | 1.77 |
| Mesoporous alumina | BD-$Al_2O_3$ | 1.70 |
| α-$Al_2O_3$/mesoporous $Al_2O_3$ composite | αFrame-$Impreg_8$-Clean | 1.735 |

3.1.1.3 Nitrogen Adsorption

Nitrogen adsorption analysis is a useful technique to acquire structural information on ceramic materials. This technique works by increasing the partial pressure of nitrogen and observing the quantity of gas physisorbed onto a surface at equilibrium. By incrementally varying the partial pressure of nitrogen the quantity of gas adsorbed can be calculated. This data can be interpreted to provide information about the surface area and pore distribution of a material.

The surface area of a material is calculated by a method described by Brunauer, Emmett and Teller [113] (abbreviated to BET) in which the quantity of gas adsorbed at low partial pressures (before monolayer coverage is achieved) is used to calculate the surface area as shown by Equation 15.

$$\frac{1}{m_{ads}((P_0/P)-1)} = \frac{C-1}{m_{mono}C}\frac{P}{P_0} + \frac{1}{m_{mono}C} \qquad \text{eq.15}$$

| | |
|---|---|
| $m_{ads}$ | Mass of gas adsorbed at specified pressure (g) |
| $P_0$ | Saturated pressure of adsorbed gas (Pa) |
| $P$ | Equilibrium vapour pressure of adsorbent gas (Pa) |
| $m_{mono}$ | Mass of adsorbed gas to produce monolayer at STP (g) |
| $C$ | Dimensionless constant (-) |

Utilising Equation 15, a plot of $\frac{1}{m_{ads}((P_0/P)-1)}$ against $\frac{P}{P_0}$ can be used to calculate the gradient $M_{BET}$ equal to $\left(\frac{C-1}{m_{mono}C}\right)$ and intercept $i_{BET}$ equal to $\left(\frac{1}{m_{mono}C}\right)$ as shown in Figure 16.

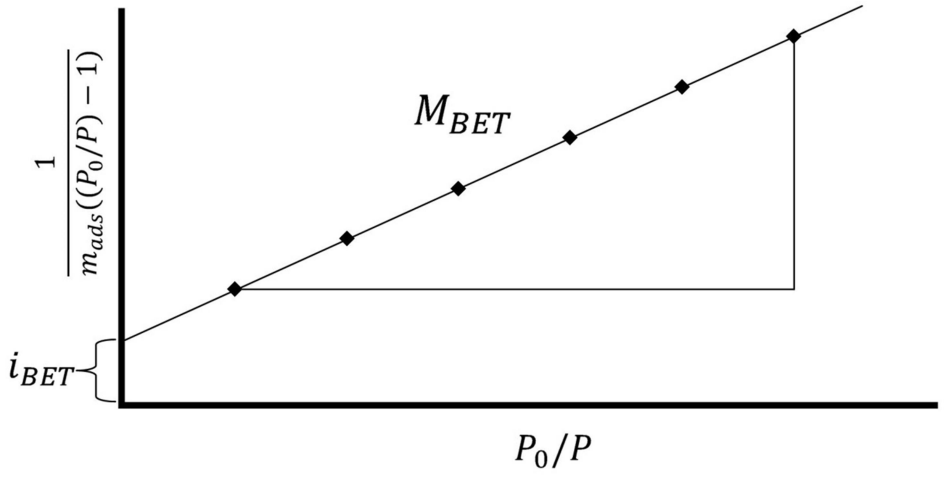



**Figure 16** – BET plot showing calculation of gradient ($M_{BET}$) and intercept ($i_{BET}$)

Once $M_{BET}$ and $i_{BET}$ have been calculated $m_{mono}$ can be calculated from Equation 16.

$$m_{mono} = \frac{1}{M_{BET} + i_{BET}} \qquad \text{eq.16}$$

The total surface area of the material being analysed can be calculated as shown by Equation 17.

$$S_{tot} = \frac{m_{mono}\, N\, A_{cs}}{M} \qquad \text{eq.17}$$

$S_{tot}$ Total surface area ($m^2$)

$N$ Avogadro's constant (6.023 x$10^{23}$ $mol^{-1}$)

$A_{cs}$ Molecular cross section of adsorbate molecule ($m^2$)

$M$ Molecular mass (g $mol^{-1}$)

Finally the specific surface area ($S$) is calculated using Equation 18.

$$S = \frac{S_{tot}}{m} \qquad \text{eq.18}$$

$S$ Specific surface area ($m^2\ g^{-1}$)

$m$ Mass of sample (g)

The pore size distribution of a material can also be analysed using a method developed by Barrett, Joyner and Halenda [114] (abbreviated to BJH). This method is based on the Kelvin equation adapted to correct for multilayer thickness on pore walls and is labelled Equation 19 [115]. The equation describes that capillary condensation will occur in pores at a given relative pressure rather than formation of multi-layers. BJH analysis is carried out in the capillary condensation region $P/P_0$>0.4 where increasing pressure causes thicker multilayers of adsorbate to form on the pore walls resulting in a reduction in the diameter of the pore. Assuming either a slit or cylindral pore geometry allows calculation of the contribution of the film thickness to the volume adsorbed to calculate core volume. From this information the radius of the core of the pore is calculated and related back to the original pore dimensions and volume. This method is only reliable for small meso-pores and large micro-pores with a diameter of 2 – 50 nm [116].

$$\ln\left(\frac{P}{P_0}\right) = \frac{-(2\,\gamma\,V_{mono}\cos\theta)}{R\,\mathbb{T}\,r_c} \qquad \text{eq.19}$$

$V_{mono}$ Volume of adsorbed gas to produce monolayer at STP (g)

$\theta$ Contact angle (°)

$R$ Gas constant (8.314 $J\ K^{-1}\ mol^{-1}$)

$\mathbb{T}$ Absolute temperature (K)

$r_c$ Radius of core (m)

To assess a material's micropore volume a t-plot analysis can be conducted. This allows differentiation between the internal (micropore volume) and external (non-micropore volume) surface area. The statistical thickness ($t_{stat}$) of an adsorbed layer at a given pressure can be calculated from Equation 20 as proposed by Harkins and Jura [117].

$$t_{stat} = \left[\frac{13.99}{0.034 - log_{10}\left(\frac{p_0}{p}\right)}\right]^{0.5} \quad \text{eq.20}$$

$t_{stat}$ Statistical thickness of adsorbed phase on non-porous surface (nm)

By plotting $t_{stat}$ against adsorbed volume ($V$) the micropore volume can be calculated using the intercept ($i_{MP}$) as shown by equation 21 [118]. This results from micropores filling rapidly at low pressures followed by adsorption onto the external surface at higher pressures.

$$V_{MP} = 0.001547 \times i_{MP} \quad \text{eq.21}$$

$V_{MP}$ Volume of micropores ($cm^3\ g^{-1}$)

Depending on the surface and pore properties of a material, a range of different isotherms can be observed. These are classified by the International Union of Pure and Applied Chemistry (IUPAC) as isotherms I to VI [119] as shown in Figure 17.

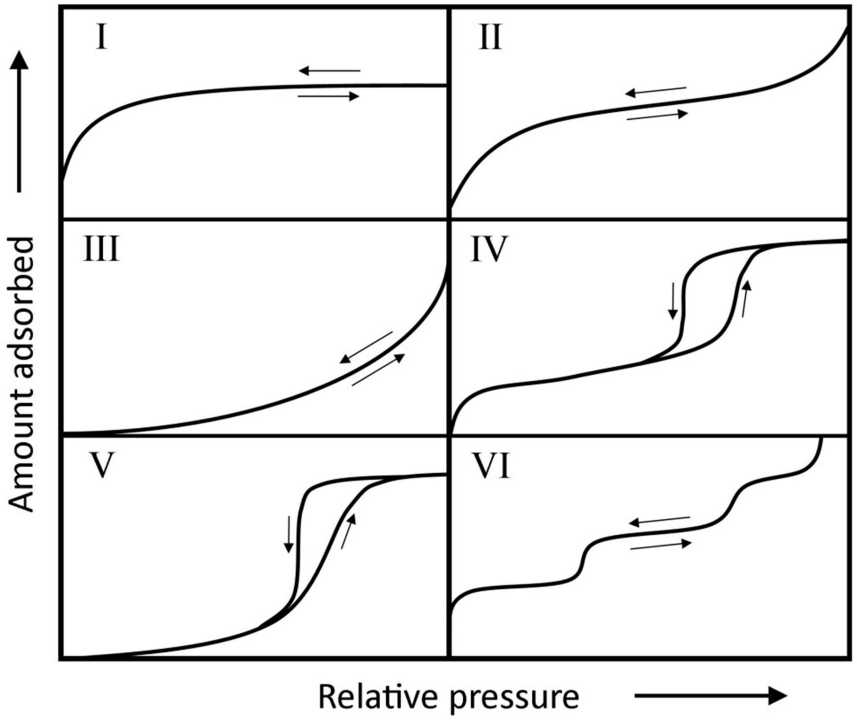



**Figure 17** – Nitrogen adsorption isotherms identified by IUPAC. Reproduced from [119]

In addition, capillary condensation can occur within pores arising due to the formation of a lower energy state when species are in close proximity between the walls of a pore. As pressure is reduced the stable molecules remain within the pores and a higher pressure gradient is required to remove them. As such, a difference in the adsorption and desorption isotherm is observed which is classified by IUPAC as hysteresis loops H1 to H4 [119] as shown in Figure 18.

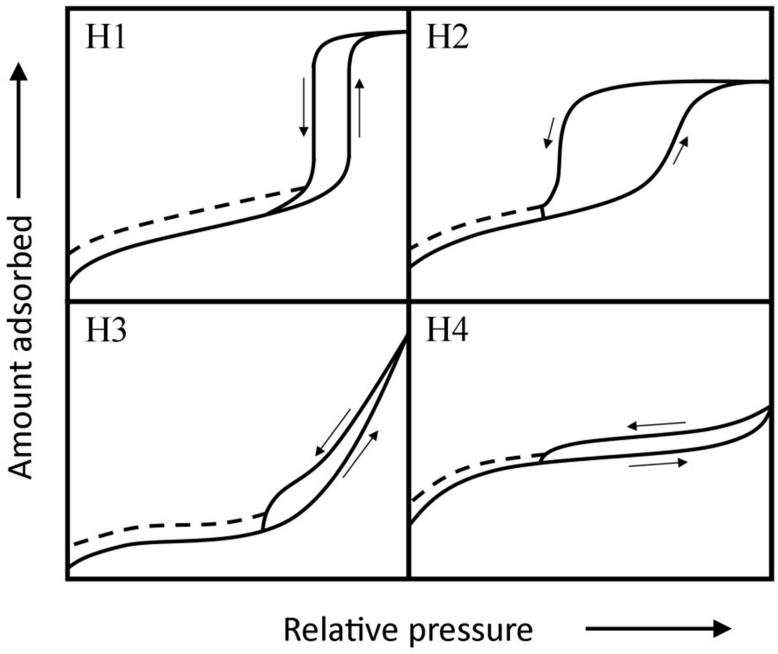



**Figure 18** – Hysteresis loops identified by IUPAC for nitrogen adsorption. Reproduced from [119]

Nitrogen adsorption analysis was undertaken on a Micromeritics 3 flex physisorption instrument with samples cooled with liquid nitrogen to 77 K. Prior to analysis all samples were dehydrated in a Heraeus Kelvitron oven at 100 °C for an hour to remove as much moisture as possible before evacuation at 200 °C for 4 hours on a Micromeritics VacPrep 061. Approximately 1.0 g of sample was used for each analysis, measured on an Sartorius BP300s balance accurate to four decimal places. Analysis was conducted using a 40 point adsorption/desorption cycle for BD-$Al_2O_3$, SGB127 and Tab-$Al_2O_3$. Analysis was conducted using a 20 point adsorption/desorption cycle for composite ceramics and their substituent components for more rapid processing. Each material was analysed in granular form, screening material between a 200 and 600 µm sieve before conducting analysis with three repeats conducted per material. Analysis was validated by running a porous ceramic standard to ensure the reported pore size, pore volume and surface area were within the required specification limits of the material.

3.1.1.4 Helium Pycnometer

The true density of a material was attained utilising a Micromeritics pycnometer 1340 using helium gas. Prior to analysis all samples were dehydrated in a Heraeus Kelvitron oven at 100 °C for an hour to remove as much moisture as possible before evacuation at 200 °C for 4

hours on a Micromeritics VacPrep 061. Each sample was then purged 10 times with helium before analysis was conducted five times on the sample. For each test the sample holder was filled approximately half full with material before recording the mass on a Sartorius BP300s balance accurate to four decimal places. Error can occur if the sample holder is dirty or if an insufficient seal is formed. As such, before each test the sample holder was cleaned with water to remove dirt and dried in an oven at 50 °C for an hour. The helium pycnometer instrument is calibrated monthly with a reference volume to ensure accuracy and reliability.

3.1.1.5 Dynamic Vapour Sorption (DVS)

In order to characterise the sorption of water onto the exposed surfaces of a porous material a controlled humidity and temperature environment was used to measure the change in weight when varying the relative humidity ($R_H$) of the environment.

DVS analysis was undertaken on a Surface Measurement Systems DVS RLSM01501 using an environmental chamber stabilised at 25 °C with approximately 20 mg of material used per analysis. Initially, the experimental material was dried at 0 % $R_H$ for an hour to remove moisture; the mass was then recorded to give an initial dry mass. Next, the $R_H$ of the environment was increased to 10 %. When a gravimetric equilibrium of $\pm$ 0.02 mg min$^{-1}$ was measured the mass was recorded once more. The $R_H$ was increased repeatedly in 10 % increments to 90 % $R_H$ measuring the mass after a gravimetric equilibrium of $\pm$ 0.02 mg min$^{-1}$ was recorded at each step. The $R_H$ was then decreased repeatedly in 10 % increments to 0 % $R_H$ measuring the mass after a gravimetric equilibrium of $\pm$ 0.02 mg min$^{-1}$ was recorded at each step. The mass at equilibrium was then calculated as a percentage of the initial dry mass at each $R_H$ increment.

3.1.1.6 Thermomechanical Analysis (TMA)

A NETZSCH TMA 402 F1 Hyperion utilising SiC elements was used to measure the expansion/contraction behaviour of an experimental material throughout a specified firing cycle. For each analysis, alumina push rods were utilised which continuously applied 0.3 N to the sample. A reference run was completed on a polycrystalline alumina cylinder of dimensions 5 mm in length and 6 mm in diameter. The expansion/contraction data gathered for the reference run was used to determine the expansion/contraction of each experimental material throughout the firing cycle. The firing cycle chosen for analysis

replicates the thermal conditions experienced by the shell components during casting as detailed later in Section 3.1.3. The "simulated casting cycle" starts at room temperature and heats to 1500 °C at 10 °C $min^{-1}$, the temperature is held at 1500 °C for 1 hour then the temperature is reduced to room temperature at 10 °C $min^{-1}$. To analyse BD-$Al_2O_3$, αFrame and αFrame-$Impreg_8$-Clean each material was cut into the approximate dimensions of the reference cylinder using a Voche mini rotary drill then input into the instrument as shown in Figure 19. To analyse spherical SGB127 material the material was loaded into the instrument unmodified as shown in Figure 19. Three repeat analysis runs were undertaken for each sample.

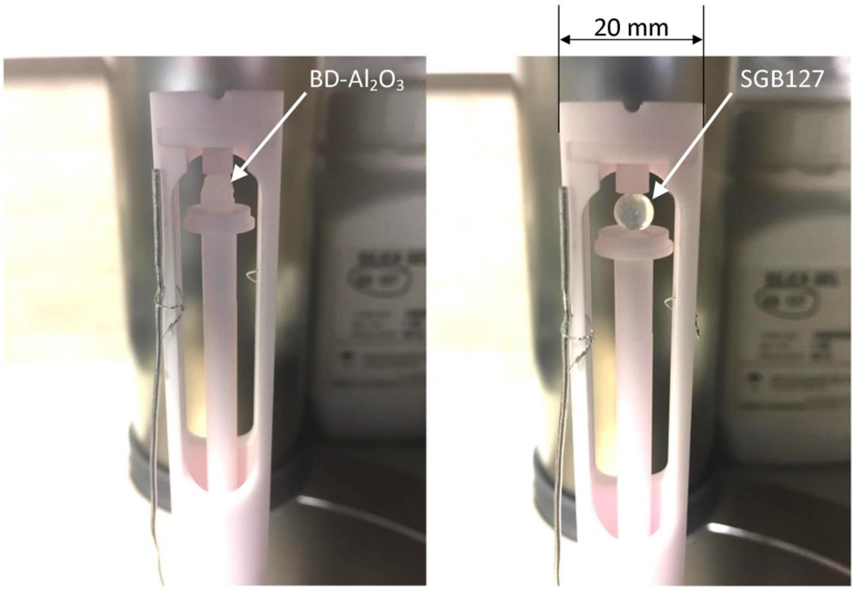



**Figure 19** – TMA setup showing analysis of BD-$Al_2O_3$ (left) and SGB127 (right)

3.1.1.7 Scanning Electron Microscopy (SEM)

Scanning electron microscopy was undertaken on the JOEL 6060 at 20 kV using the secondary electron detector to analyse material embedded in epoxy resin polished to produce a clean flat surface.

To mount a sample in epoxy, firstly the experimental material was dried in a fan oven at 150 °C for 2 hours before placing the material into a silicone rubber mould. The mould was then placed into a vacuum chamber alongside a cup of Easy Composites infusion epoxy resin premixed with hardener. The chamber was then evacuated for around 20 minutes to remove bubbles from the epoxy mixture. The resin was then poured into the silicone mould (still under vacuum) impregnating the sample. The vacuum was held for around 10 minutes

after which time the chamber was opened and the mould was placed in a Heraeus Kelvitron oven at 40 °C for 6 hours. The cured resin was then released from the silicone mould producing a cylinder 40 mm in diameter and approximately 20 mm in height with the sample embedded. The cylinder was then subject to grinding and polishing steps as detailed in Table 2. The cylinder was then platinum coated and a side was coated with silver dag paint to promote conductivity.

**Table 2** – SEM polishing stages

| Disc | Solution | Time (minutes) |
|---|---|---|
| MD-Piano 220 | Water | 10 |
| MD-Allegro | 9 µm diamond | 10 |
| MD-Largo | 3 µm diamond | 10 |
| MD-Nap | 1 µm diamond | 5 |

3.1.1.8 Archimedes' Method

Calculating the true density, bulk density and porosity of a material was undertaken through Archimedes' method utilising an Sartorius BP300s balance accurate to four decimal places. Samples were analysed in accordance with ASTM C373 – 14 [120] where approximately 20 g of material was dehydrated in a Heraeus Kelvitron oven at 150 °C for 24 hours then weighed to give a "dry mass" ($m_{dry}$). The dried material was then submerged in boiling distilled water in a 500 ml beaker for four hours to saturate the pores with water. The contents of the beaker was then cooled to room temperature before weighing the material submerged to give a "submerged mass" ($m_{sub}$), being sure to account for the weight of the sample holder. The material was then removed from the liquid and dried on a paper towel to give a "saturated mass" ($m_{sat}$) where large pores have drained but finer pores remain saturated. Three repeats were conducted per sample. Equations 22 and 23 were used to calculate bulk volume ($V_{bulk}$) and true volume respectively ($V_{true}$) using the assumption that 1 g of water is equal to 1 $cm^3$. Equations 24, 25 and 26 were used to calculate the true density ($\rho_{true}$), bulk density ($\rho_{bulk}$) and porosity ($\Phi_{open}$) respectively.

$$V_{bulk} = m_{sat} - m_{sub} \quad \text{eq.22}$$

$$V_{true} = m_{dry} - m_{sub} \quad \text{eq.23}$$

$$\rho_{true} = \frac{m_{dry}}{V_{true}} \quad \text{eq.24}$$

$$\rho_{bulk} = \frac{m_{dry}}{V_{bulk}} \quad \text{eq.25}$$

$$\Phi_{open} = \frac{m_{sat} - m_{dry}}{V_{bulk}} \quad \text{eq.26}$$

| | |
|---|---|
| $V_{bulk}$ | Volume of material including pores ($cm^3$) |
| $V_{true}$ | Volume of material excluding pores ($cm^3$) |
| $m_{sat}$ | Saturated mass (g) |
| $m_{sub}$ | Submerged mass (g) |
| $m_{dry}$ | Dry mass (g) |
| $\rho_{true}$ | True density ($g\ cm^{-3}$) |
| $\rho_{bulk}$ | Bulk density ($g\ cm^{-3}$) |
| $\Phi_{open}$ | Open porosity ($cm^3_{pore}\ cm^{-3}_{bulk}$) |

### 3.1.2 Slurry Preparation and Maintenance

Three slurries were utilised in the production of ceramic moulds labelled Primary, Primary +1 and Secondary as defined in Table 3. Each slurry was held in a tank approximately 0.1 $m^3$ in volume with the viscosity being maintained within a given range by dilution with distilled water. The viscosity was measured using a standard Ford flow cup in accordance with ASTM D1200 -10 [121] utilising a stop watch to record the time taken to drain the slurry from the cup. It should be noted that commercial wetting and anti-foaming agents were added to both the Primary and Primary +1 slurries. The use of wetting agents in the Primary and Primary+1 slurries reduces the surface tension of the fluid and provides greater adhesion between the hydrophilic slurry and the hydrophobic wax pattern.

**Table 3** – Slurry composition and specification

| Slurry identifier | Silica binder | Zircon filler | Flow cup viscosity |
|---|---|---|---|
| Primary | Binder P | Commercially available 200 mesh zircon | B5 (70 ml) controlled at set point +/- 2 seconds (most viscous) |
| Primary +1 | Binder P | Commercially available 200 mesh zircon | B4 controlled at set point +/- 1.5 seconds (least viscous) |
| Secondary | Binder S | Commercially available 200 mesh zircon | B4 controlled 12.5 seconds above Primary +1 slurry +/- 2.5 seconds |

### 3.1.3 Shell Manufacture

Shell production was undertaken on a rectangular wax pattern of dimensions 130 x 100 x 20 mm. Each pattern was created on a MPI model 55 injection moulding machine utilising 30 % filled commercial wax. The wax was injected into a mould containing a metal hook for ease of handling in later processes. The molten wax was injected at 75 $^{\circ}$C with a pack pressure of 2 MPa and a volumetric flow rate of 0.18 x $10^{-3}$ $m^3$ $s^{-1}$. Once the wax pattern has cooled to room temperature, the pattern was washed in Trisol 60 plus solution for 30 seconds to increase adhesion between the wax and the first slurry coat applied to the wax surface in later stages. Patterns were then washed in deionised water to remove the Trisol 60 plus solution from the surface. The patterns were then placed in a drying chamber to remove surface moisture and acclimatise to the environment. This environment was maintained at 21 $^{\circ}$C and 50 % relative humidity with constant air movement of 0.4 m $s^{-1}$.

The ceramic mould was built around the rectangular wax pattern by sequentially applying layers which are composed of a specified slurry and stucco composition dried for a specific length of time. The composition of each layer is defined in Table 4. Each layer was applied by submerging the wax pattern (or partially built shell) in the required slurry for 30 seconds before withdrawing from the slurry tank and removing the excess slurry by rotating around each axis until an even surface was produced with no drips falling from the surface. The required stucco was then deposited by hand using an 1000 µm sieve to produce an even, complete coverage of particles. The partially built mould was then placed in the drying

chamber described earlier in this Section for the required length of time. Typical moulds (in order of application) are composed of one layer utilising a Primary slurry, one layer utilising a Primary +1 slurry, five layers utilising a Secondary slurry and a seal coat. The phrase "primary layers" describes the section of the mould comprising Primary and Primary +1 slurrys, "secondary layers" describes the section of the mould comprising Secondary slurry.

**Table 4** – Identification of ceramic mould layer defined by the slurry applied, stucco composition deposited and drying time

| **Layer identifier** | **Slurry applied** | **Stucco composition deposited** | **Drying time (hr)** |
|---|---|---|---|
| P (Fused-$Al_2O_3$)$_t$ | Primary | 100 vol% Fused-$Al_2O_3$ | t |
| P+1 (Fused-$Al_2O_3$)$_t$ | Primary +1 | 100 vol% Fused-$Al_2O_3$ | t |
| S (Tab-$Al_2O_3$)$_t$ | Secondary | 100 vol% Tab-$Al_2O_3$ | t |
| S (n BD-$Al_2O_3$)$_t$ | Secondary | n vol% BD-$Al_2O_3$<br>(100-n) vol% Tab-$Al_2O_3$ | t |
| S (n SGB127)$_t$ | Secondary | n vol% SGB127<br>(100-n) vol% Tab-$Al_2O_3$ | t |
| S (n αFrame-Impreg$_8$-Clean)$_t$ | Secondary | n vol% αFrame-Impreg$_8$-Clean<br>(100-n) vol% Tab-$Al_2O_3$ | t |
| Seal (Primary +1) | Primary +1 | None | 24+ |
| Seal (Secondary) | Secondary | None | 24+ |

Once the seal coat has been applied the complete shell was left to dry for at least 24 hours before removing a side of the rectangular prism with a Vitrex bridge saw equipped with a diamond cutting wheel, exposing the wax. Shells were then placed into an LBBC (Leeds and Bradford Boiler Company) Quicklock boilerclave with the exposed wax facing down. The autoclaving process was conducted at 8 bar (approximately 175 °C) for 4 minutes before slow depressurisation to atmospheric pressure over 20 minutes. This process removed the bulk of the wax to form a hollow mould. In this condition the mould is described as green.

The mould was then cut into two tiles approximately 100 x 125 x 5 mm on a Vitrex bridge saw equipped with a diamond cutting wheel with further size reduction being carried out as required. When necessary, shell samples in green condition were fired primary layer in contact with the furnace floor in an Elite Thermal Systems BSF 12/30 furnace with extraction. Shell samples were heated from room temperature to 800 °C at 10 °C $min^{-1}$, before holding at temperature for an hour then cooled to room temperature at 10 °C $min^{-1}$. Following this procedure the shells are classified as being pre-fired.

When necessary, shell samples in pre-fired condition were fired primary layer in contact with the furnace floor in a Lenton Thermal Designs (LTD) 1700 furnace. Shell samples were heated from room temperature to 1500 °C at 10 °C $min^{-1}$, before holding at temperature for an hour then cooled to room temperature at 10 °C $min^{-1}$. Following this procedure the shell is classified as being fired. It should be noted that this firing cycle is designed to replicate the conditions experienced by the shell during the casting of single crystal components, thus it is labelled the "simulated casting cycle". Monitoring the behaviour of the shell or shell components throughout or after this thermal cycle provides a reasonable assessment of the shell properties developed during casting.

### 3.1.4 In-line Characterisation

#### 3.1.4.1 Coat Weight

The mass of Secondary slurry and stucco was measured during shell build when applying the final ($5^{th}$) secondary layer using a PCE Instruments PCE-BT 2000 balance accurate to two decimal places. This was undertaken to observe if the underlying stucco composition affected the quantity of slurry deposited in the subsequent layer and to measure the quantity of stucco deposited on the slurry. Initially, a partially built shell encasing a wax pattern 130 x 100 x 20 mm was tared on the underside of the balance using a hook. The partially built shell was then dipped into the Secondary slurry for 30 seconds before removing from the tank and draining to form an even coating with no drips falling off the surface. The partially built shell was then taken to the balance to record the change in mass resulting from dipping. Next, the required stucco composition was deposited onto the slurry surface and the mass was recorded once more to determine the mass of stucco deposited

onto the slurry. It should be noted that the final secondary layer was chosen for analysing coat weight to pronounce the effect of the underlying stucco composition.

### 3.1.5 Drying Characterisation

#### 3.1.5.1 Monitoring Weight Loss

Adapting methods developed by S. Leyland et al. [37, 122], the weight loss resulting from moisture evaporation was recorded after submerging a wax pattern or partially completed shell in Secondary slurry, removing from the tank and depositing the required stucco composition. Weight loss was recorded at second intervals in a drying chamber (described in Section 3.1.3) using a PCE Instruments PCE-BT 2000 analytical balance accurate to two decimal places connected to a computer utilising Procell software. Three repeat analyses were conducted per condition.

#### 3.1.5.2 Monitoring Colour Change

An additional method used to measure the drying behaviour of the slurry involved the use of a dye dispersed in the slurry which changes colour as moisture is lost from the slurry. The Ransom and Randolph Primecote binder with ReDip$^{TM}$ indicator has been specifically developed for this purpose containing a potassium based fluorescein dye in a colloidal silica binder that changes colour subject to the moisture content of the solution. In order to quantify the moisture content of the slurry through this method, the colour change progression was monitored over time. This was undertaken by dipping a 1 L clear glass beaker in slurry containing Primecote binder with ReDip$^{TM}$ indicator for 30 seconds and rotating the beaker to remove excess slurry. Next the required stucco composition was deposited onto the slurry surface. The composition of the slurry containing Primecote binder with ReDip$^{TM}$ indicator (labelled Indicating slurry) is detailed in Table 5. It should be noted the slurry was designed to imitate the properties of the Secondary slurry whilst maintaining a slightly higher viscosity to promote adhesion to the glass surface. Approximately two litres of slurry was prepared and agitated on a roller table to prevent sedimentation.

**Table 5** – Colour changing slurry composition and specifications

| Slurry identifier | Silica binder | Zircon filler | Flow cup viscosity |
|---|---|---|---|
| Indicating | Ransom and Randolph Primecote binder with ReDip™ indicator | Commercially available 200 mesh zircon | B4 controlled 7.5 seconds above Primary +1 slurry +/- 2.5 seconds |

Next, the beaker coated in Indicating slurry and stucco was placed inside a box as shown in Figure 20, aligning the camera and beaker. The box was designed to minimise error and increase reproducibility when monitoring the colour change of slurry. Some of the attributes of the box include:

-Preventing reflections from the glass beaker being recorded by the camera to ensure a greater area of the image captured by the camera can observe the colour change.

-Aligning the camera and beaker during each experiment.

-Setting the distance between the camera and beaker during each experiment.

-Limiting light exposure allowing long exposure pictures to be taken. This reduces the effect of shadows caused by other lab users moving around the lab.

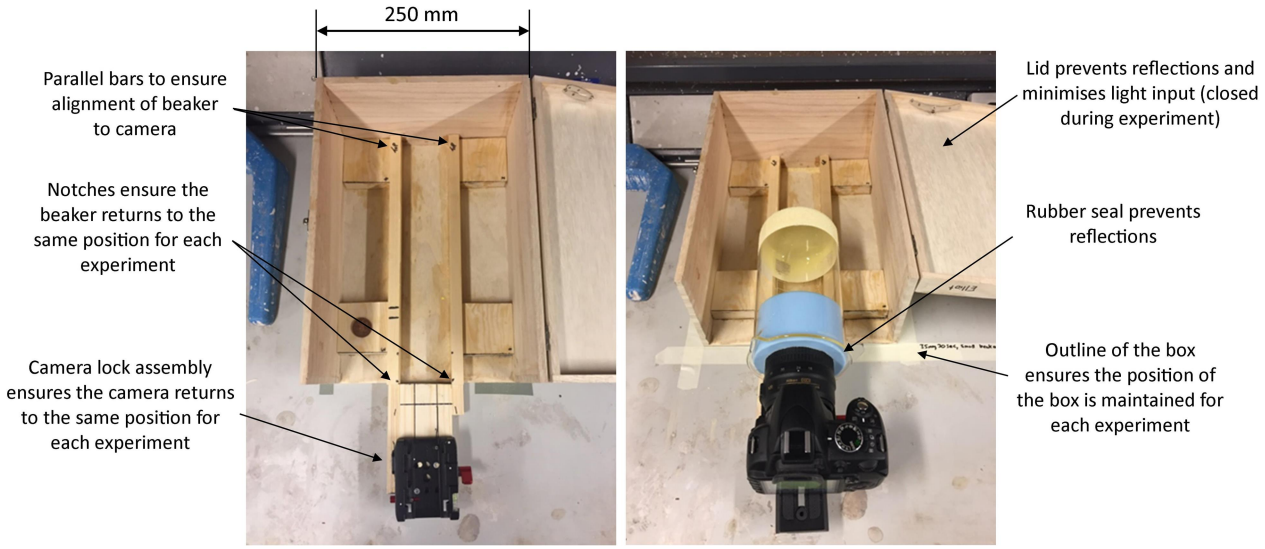



**Figure 20** – Annotated setup of beaker coated in Indicating slurry and Tab-$Al_2O_3$ stucco

Once the camera and beaker had been aligned inside the box the lid was closed and the Nikon D3100 DSLR camera was set to take 60 second long exposure pictures. An ISO of 100 was chosen and an aperture of F22 to minimise the light input. The experiment was conducted in the drying chamber described in Section 3.1.3. Three repeat tests were conducted per stucco composition with each experiment lasting approximately 1 hour.

Limitations to this method include:

-Minimal airflow inside the box.

-The unrepresentative nature of the experiment in comparison to typical drying conditions for ceramic moulds. Therefore results obtained in this experiment may not translate to the same result in real life conditions.

### 3.1.6 Shell Characterisation

#### 3.1.6.1 Mechanical Testing

Due to the brittle nature of investment casting ceramics, evaluating mechanical strength is predominantly evaluated in a 3 point bend flexural test. This is carried out due to difficulty in testing ceramic test pieces in traditional tensile loading apparatuses which leads to failure at the grips as a result of localised contact stresses exceeding the fracture strength [123]. It has been demonstrated that the use of 4 point bend gives more reliable strength measurements due to the formation of a large uniform stress concentration area in comparison to 3 point bend where stress is localised directly below the loading point. This leads to 4 point bend measuring a more representative largest flaw (weakest link) in the shell [124]. Despite this, flexural strength of shell is typically conducted in 3 point bend due to the availability of equipment and ease of comparison to other historical data gathered on shell strength. It has also been observed by Jolly et al. that the orientation of the shell bar gives rise to different flexural strength measurements resulting in up to 40 % difference between testing in primary layer up orientation and primary layer down orientation [5].

Flexural strength analysis was conducted in 3 point bend mode using shell bars approximately 100 x 20 x 5 mm facing primary layer down as shown in Figure 21. Flexural strength was calculated from Equation 27 which calculates the highest stress experienced by the sample before failure [125].

$$\sigma_{flexural} = \frac{3FL_{span}}{2WT^2} \quad \text{eq.27}$$

| | |
|---|---|
| $\sigma_{flexural}$ | Flexural strength (Pa) |
| $F$ | Max load (N) |
| $L_{span}$ | Span length (m) |
| $W$ | Width of sample (m) |
| $T$ | Thickness of sample (m) |

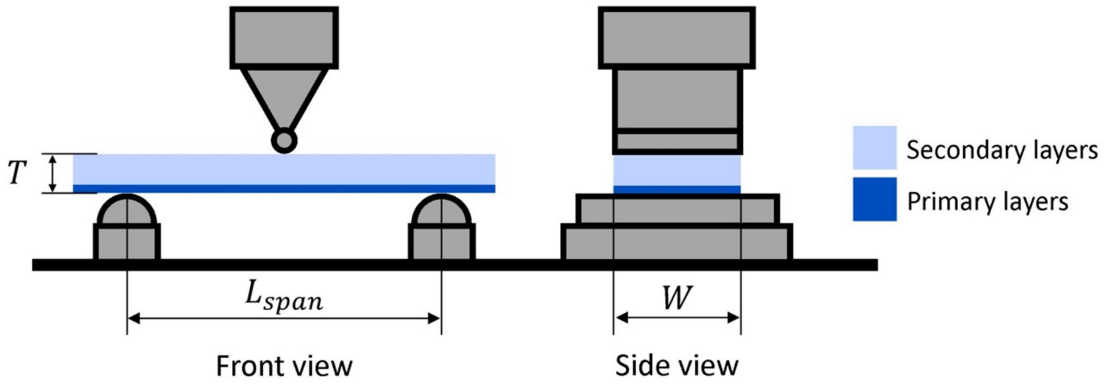



**Figure 21** – 3 Point bend schematic identifying the thickness of sample ($T$), width of sample ($W$) and span length ($L_{span}$)

Flexural strength analysis was conducted using an Instron 4467 universal tester with a 1 kN load cell and span length of 50 mm. The Instron recorded the applied load whilst moving the push rod at a rate of 1 mm $min^{-1}$ until complete fracture. For each shell bar analysed the width ($W$) and thickness ($T$) was recorded using a digital vernier caliper accurate to 0.005 mm; this was conducted three times along the length of the sample to acquire an average value. Shell bars were tested in green, pre-fired and fired condition as required at ambient conditions. A minimum of six repeats were analysed per condition.

3.1.6.2 Horizontal Dilatometer

Dilatometer analysis was undertaken on the NETZSCH DIL 402 E horizontal dilatometer to observe the expansion/contraction behaviour in one dimension of pre-fired shell samples throughout the simulated casting cycle (described in Section 3.1.3). Each shell sample was held between alumina push rods applying 0.5 N throughout the analysis. A reference run was completed on a polycrystalline alumina cylinder 25 mm in length and 6 mm in diameter. The expansion/contraction data gathered for the reference run was used to accurately calculate the expansion/contraction of each shell variant throughout the firing cycle. Three repeat analysis runs were undertaken for each shell variant. A picture of the experimental setup is given in Figure 22. As shown, expansion/contraction was measured through the length of the shell (perpendicular to thickness).

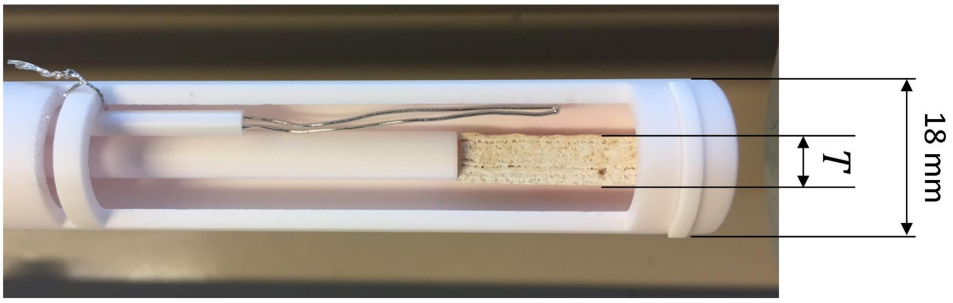



**Figure 22** – Horizontal dilatometer setup

3.1.6.3 Cyclic Loading Dilatometry

Cyclic loading dilatometry is a method developed by Cai et al. to quantify the viscosity of ceramic compacts based on the mechanical response of a material when a specific load is applied periodically throughout a given firing cycle [126]. The magnitude of applied stress in the loading period is varied to evaluate the mechanical response under different loading conditions and compared against the mechanical response when subject to minimal stress. Figure 23 shows a typical example of strain when a material is subject to a constant heating rate under free sintering conditions (minimal force) and under loading conditions. The load free periods are designed to allow the material to relax and resume free sintering behaviour.

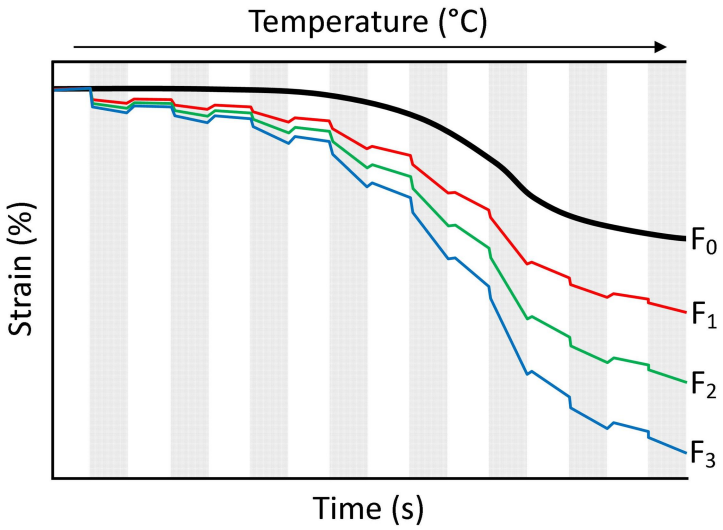



**Figure 23** – Linear strain under free sintering conditions ($F_0$) and under different loads ($F_1$, $F_2$ and $F_3$). Shaded regions represent the period where load takes place, outside this regions minimal stress is applied. Interpreted from [127]

The corresponding strain rate under free sintering conditions and for a single loading condition is shown in Figure 24 displaying the free sintering strain rate ($\dot{\varepsilon}_F$) and strain rate under load ($\dot{\varepsilon}_L$) at a given temperature ($T_{1\text{-}8}$). $\dot{\varepsilon}_F$ and $\dot{\varepsilon}_L$ are recorded at the end of the loading period once a constant strain rate has been established.

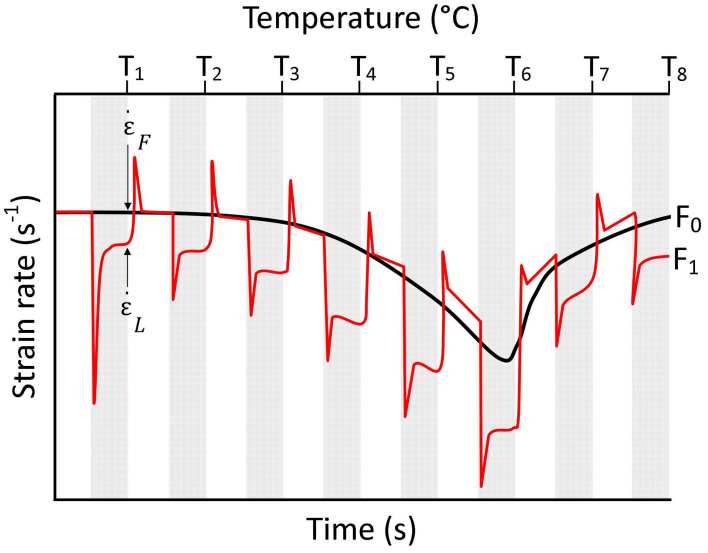



**Figure 24** – Linear strain rate under free sintering conditions ($F_0$) and under applied load ($F_1$). Shaded regions represent the period where loading takes place, outside this regions minimal stress is applied. The free sintering strain rate ($\dot{\varepsilon}_F$) and strain rate under load ($\dot{\varepsilon}_L$) are labelled for temperature $T_1$. Interpreted from [127]

The viscosity of the sintering compact can be calculated from a stress-strain rate relationship as shown by Equation 28, where the stress induced strain rate ($\dot{\varepsilon}$) is calculated from Equation 29. The true stress ($\sigma_t$) is calculated from Equation 30 to account for expansion/shrinkage over the firing cycle.

$$\eta = \frac{\sigma_t}{\dot{\varepsilon}} \qquad \text{eq.28}$$

$\eta$ Uniaxial viscosity (Pa s)

$\sigma_t$ True stress (Pa)

$\dot{\varepsilon}$ Strain rate (stress induced) ($s^{-1}$)

$$\dot{\varepsilon} = \dot{\varepsilon_L} - \dot{\varepsilon_F} \qquad \text{eq.29}$$

$$\sigma_t = \frac{\sigma_0}{(1 + \varepsilon_{eng})} \qquad \text{eq.30}$$

$\sigma_0$ Initial stress (Pa)

$\varepsilon_{eng}$ Engineering strain (-)

By taking a least squares fit through the origin of a plot of $\sigma_t$ against $\dot{\varepsilon}$, the uniaxial viscosity can be calculated at $T_{1\text{-}8}$ as shown by Figure 25.

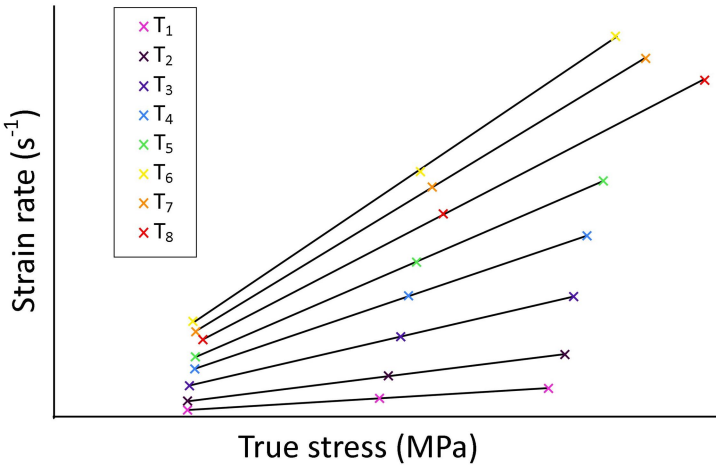



**Figure 25** – Plot of strain rate against true stress to calculate uniaxial viscosity at temperature $T_{1\text{-}8}$. Interpreted from [127]

Cyclic loading dilatometry was carried out to quantify the viscosity of ceramic materials throughout the simulated casting cycle. This was undertaken utilising the NETZCSH TMA 402 F1 Hyperion to apply a force of 0.5, 0.75 or 1.0 N periodically to a material for 5 minutes before the force was reduced to 0.1 N for 5 minutes. This cyclic period of loading and unloading was carried out throughout the entirety of the simulated casting cycle. An additional run was undertaken using a constant force of 0.1 N over the simulated casting cycle to measure free sintering behaviour. Each experimental material analysed was cut to approximately 5 x 5 x 5 mm using a precision diamond saw. When analysing shell samples, analysis was conducted perpendicular to shell thickness in the same manner as horizontal dilatometer analysis in Section 3.1.6.2. For each variant of force applied, a separate reference run was completed on a polycrystalline alumina cylinder 5 mm in length and 6 mm in diameter. The expansion/contraction data gathered for the reference run was used to accurately calculate the expansion/contraction of each shell variant throughout the firing cycle.

3.1.6.4 Three Point Bend Thermomechanical Analysis

A measure of expansion/contraction, flexural deformation and creep was measured utilising a NETZSCH TMA 402 F1 Hyperion in 3 point bend mode throughout the simulated casting cycle. In this setup (shown in Figure 26) a pre-fired shell sample is held in 3 point bend mode with a minimal contact force of 0.1 N being applied throughout the analysis. Shell samples were cut from a bar approximately 25 x 95 x 5 mm into thin bars approximately 25 x 5 x 5 mm using a precision diamond tipped saw and held on alumina push rods supporting a 20 mm span. A reference run was completed on a polycrystalline alumina rectangular prism of dimensions 25 x 5 x 4 mm. The pushrod displacement data gathered for the reference run was used to accurately calculate the pushrod displacement of each shell variant throughout the firing cycle. Three repeat analysis runs were undertaken per condition.

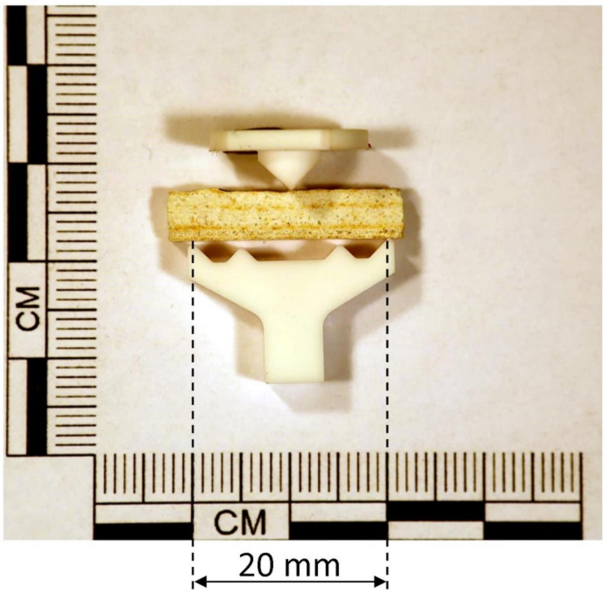



**Figure 26** – 3 point bend TMA setup

3.1.6.5 3D Structured Light Scanner

Rectangular shell samples approximately 125 x 100 x 5 mm were initially analysed on a GOM ATOS 4105 Scanbox utilising a 5M Sensor in pre-fired condition to record the external dimensions of a given shell sample. The shell sample was then fired in the simulated casting cycle in the LTD 1700 furnace, placing the sample upright and lengthways between two alumina crucibles as shown in Figure 27. Once the firing cycle was complete, dimensional analysis was conducted once more on the GOM ATOS 4105. The two scans were then superimposed using GOM ATOS professional software to show the dimensional change occurring from pre-fired condition to fired condition.

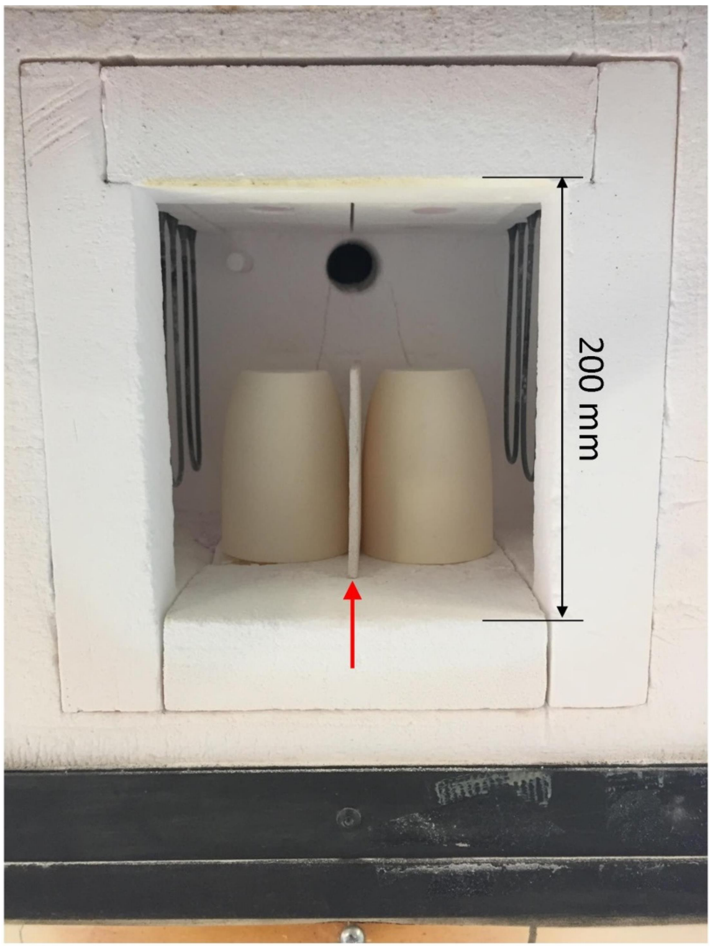



**Figure 27** – Pre-fired shell sample fired vertically as part of the process to observe dimensional change taking place after the simulated casting cycle. The sample is highlighted with a red arrow.

3.1.6.6 Photography

A Canon EOS 6D was used to record shell characteristics optically. The use of a 100 mm digital macro autofocus lens was utilised with an additional 1:1 macro adaptor for use on fine features such as stucco surface coverages.

## 3.2 Materials

The materials used to produce ceramic moulds and their constituent components are listed in the following sections. Material properties and specifications are listed from their respective technical data sheet provided by the manufacturer. For ease of reading, abbreviations are used to easily describe stucco materials. These are displayed in square brackets next to the corresponding material.

### 3.2.1 Silica Binder

Binder P is a commercially available colloidal silica binder with a typical solids loading of 38 wt% stabilised at pH 3.5 – 5.

Binder S is a commercially available colloidal silica binder with a typical solids loading of 30 wt% stabilised at pH 10 – 11.

Primecote binder with premixed ReDip$^{TM}$ indicator from Ransom & Randolph contains silica particles averaging 10 nm in diameter with a solids loading of 30 wt% stabilised at pH 10.6.

### 3.2.2 Alumina Binder

Remal A20 binder from Remet contains boehmite particles averaging 70 nm in diameter with a solids loading of 20 wt% ($Al_2O_3$) stabilised at pH 4.

### 3.2.3 Zircon Powder

A commercially available 200 mesh grade zircon has been used.

### 3.2.4 Alumina Powder

Ground calcined alumina CT 3000 SG was purchased from Almatis containing $\alpha$-$Al_2O_3$ particles averaging 0.4 µm in diameter.

### 3.2.5 Boehmite Powder

Pural SB powder containing 74 wt% $Al_2O_3$ was purchased from Sasol Chemicals.

### 3.2.6 Stucco

Fused alumina – [Fused-$Al_2O_3$]

A commercially available fused alumina grade F80 mesh was used.

Tabular alumina – [Tab-$Al_2O_3$]

A commercially available tabular alumina grade 28 – 48 mesh was used.

Boehmite derived alumina – [BD-$Al_2O_3$]

Colloidal boehmite was prepared in 1 kg batches by peptizing Pural SB powder in distilled water at a weight loading ($g_{Al_2O_3}\, g^{-1}_{H_2O}$) equal to 0.10 with a molar acid ratio ($H^+$/Al) = 0.07. This was undertaken by mixing 4 M nitric acid and distilled water to the required concentration before slowly adding the required amount of Pural SB powder to produce a semi-transparent sol. The sol was mixed for 5 minutes before being transferred to a large basin and dried in a Heraeus Kelvitron oven for 24 hours at 75 $^{\circ}$C. The dried solid was then fired in a LTD 1700 furnace from room temperature to 700 $^{\circ}$C at 10 $^{\circ}$C $min^{-1}$ and held at temperature for 4 hours before cooling at 10 $^{\circ}$C $min^{-1}$ producing hard white flakes approximately 4 – 10 mm in length. The material was then crushed with a pestle and mortar and collected between 200 and 600 µm sieves.

Silica gel – [SGB127]

A non-indicating silica gel was purchased from Grace Chemicals which consisted of spheres 2 – 4 mm in diameter which were crushed with a pestle and mortar and collected between 200 and 600 µm sieves.

Macroporous α-$Al_2O_3$ – [αFrame]

A macroporous alumina was produced from 1 kg batches of 45 wt% alumina slurry prepared from CT 3000 SG alumina powder and distilled water. Additionally, dispersant dispex A4040 was added 12 mg $g^{-1}$ of alumina. The slurry was then ball milled with zirconia balls 5 mm in diameter for 24 hours after which time a 1:1 weight ratio of Sainsbury's plain flour to alumina powder was added to the solution before continuing ball milling for an additional 3 hours. The slurry was then separated from the zirconia balls and moved into a silicone rubber tray and left to dry in an Heraeus Kelvitron oven at 75 °C for 6 hours to form a cream coloured solid. The flour was burnt out the material by firing in an Elite Thermal Systems BSF 12/30 furnace with extraction capabilities from room temperature to 800 °C at 1 °C $min^{-1}$ and held at temperature for 1 hour before cooling to room temperature at 10 °C $min^{-1}$. The material was then fired in a LTD 1700 furnace from room temperature to 1500 °C at 10 °C $min^{-1}$ and held at temperature for 6 hours before cooling at 10 °C $min^{-1}$. The material was ground in a Schutte Buffalo MM-4 hammer mill supporting a 0.84 mm mesh and collected between 200 and 600 µm sieves.

Macroporous α-$Al_2O_3$/mesoporous alumina composite – [αFrame-$Impreg_8$]

Approximately 50 g of αFrame material was held in a 200 ml beaker and evacuated in a vacuum impregnation chamber until an absolute pressure of 0.2 atm was reached. Next, approximately 100 ml of Remasol A20 alumina sol was poured into the container (still under vacuum) and left to impregnate the pores of the material. After 10 minutes the pressure was brought back to atmospheric and the particles were separated from the excess solution using a 200 µm sieve. The particles were then transferred to a large ceramic basin and dried in a Heraeus Kelvitron oven at 175 °C for 20 minutes. This impregnation and drying process was repeated a total of 8 times in attempts to completely fill the macroporous framework with dried alumina sol. The material was then fired in a LTD 1700 furnace from room temperature to 700 °C at 10 °C $min^{-1}$ and held at temperature for 4 hours before cooling to room temperature at 10 °C $min^{-1}$.

Macroporous α-$Al_2O_3$/mesoporous alumina composite – [αFrame-$Impreg_8$-Clean]

To reduce the external mesoporous alumina on the surface of αFrame-$Impreg_8$ the following step was added prior to firing in the LTD 1700 furnace:

Particles were lightly rubbed against each other by hand in a 200 µm sieve for 15 minutes to separate fragile dried alumina sol from the surface of the impregnated αFrame particles.

# 4. Application of Monolithic Porous Stucco

## 4.1 Introduction

This Chapter reports on the use of monolithic porous ceramic materials (BD-$Al_2O_3$ and SGB127) as stucco in substitution for typical non-porous ceramic materials to evaluate the accelerated drying of investment casting shells by contract-sorption drying. This was undertaken only in the secondary layers to maintain the smooth surface finish provided by the primary layers, the roughness of which is transferred to the cast component. Characterisation of each monolithic porous material was conducted alongside the Rolls-Royce standard used in the secondary layers (Tab-$Al_2O_3$) with each material subsequently being utilised as stucco to manufacture moulds suitable for investment casting.

## 4.2 Stucco Characterisation

### 4.2.1 X-ray Diffraction (XRD)

X-ray diffraction was carried out to measure the presence of any crystalline phases present in each stucco material. In addition, the crystallinity of Pural SB boehmite powder was measured to observe if any boehmite phase remained present in BD-$Al_2O_3$ after firing.

Figure 28 displays the XRD traces for each material, identifying crystal phases from literature sources labelled in Table 6. It can be seen that SBG127 attains an amorphous nature showing no identifiable crystalline phases. BD-$Al_2O_3$ on the other hand shows clear peaks identifying the $\gamma$-$Al_2O_3$ phase with no presence of the boehmite precursor. It was also observed that a lack of unique $\delta$-$Al_2O_3$ or $\theta$-$Al_2O_3$ peaks can be seen, leading to the hypothesis that the BD-$Al_2O_3$ material is comprised mostly of $\gamma$-$Al_2O_3$. However, many peaks present in $\delta$-$Al_2O_3$ and $\theta$-$Al_2O_3$ overlap with $\gamma$-$Al_2O_3$ as shown in Table 6, making identification difficult with low resolution apparatus.

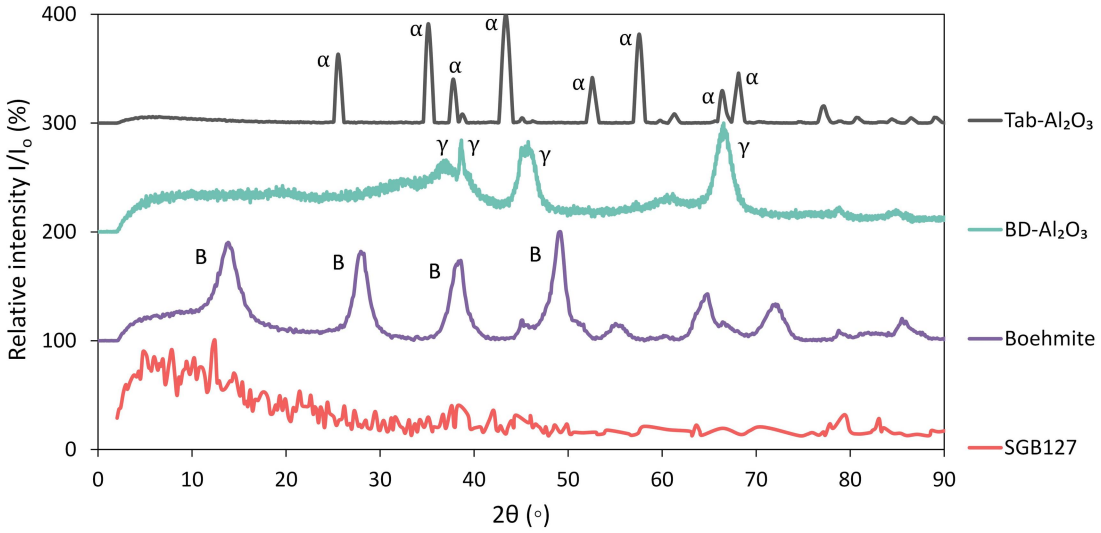



**Figure 28** – XRD traces with labels identifying main peaks for each phase (B = boehmite, γ = γ-$Al_2O_3$ and α = α-$Al_2O_3$). The intensity is shifted by 1 for each sample for clarification

**Table 6** – Dominant XRD peaks identified for each crystalline phase. Peaks identified from [128] and [93]

| **Boehmite** | | **γ-$Al_2O_3$** | | **δ-$Al_2O_3$** | | **θ-$Al_2O_3$** | | **α-$Al_2O_3$** | |
|---|---|---|---|---|---|---|---|---|---|
| 2θ (◦) | $I/I_0$ (%) | 2θ (◦) | $I/I_0$ (%) | 2θ (◦) | $I/I_0$ (%) | 2θ (◦) | $I/I_0$ (%) | 2θ (◦) | $I/I_0$ (%) |
| 14.48 | 100 | 37.6 | 80 | 32.8 | 30 | 31.5 | 80 | 25.6 | 75 |
| 28.17 | 65 | 39.49 | 50 | 34.5 | 25 | 36.7 | 60 | 35.1 | 90 |
| 27.88 | 65 | 45.4 | 100 | 36.5 | 60 | 44.9 | 45 | 37.8 | 40 |
| 38.32 | 55 | 67 | 100 | 45.6 | 75 | 67.4 | 100 | 43.4 | 100 |
| | | | | 46.5 | 40 | | | 52.6 | 45 |
| | | | | 66.9 | 100 | | | 57.5 | 80 |
| | | | | | | | | 66.5 | 30 |
| | | | | | | | | 68.2 | 50 |

### 4.2.2 Particle Size Distribution (PSD)

The PSD of each stucco material was measured in order to ensure the grinding and sieving process conducted in the laboratory produced a grain of similar particle size distribution to the standard stucco used in secondary layers (Tab-$Al_2O_3$). This was to ensure that any property changes observed during shell manufacture were the result of material properties, rather than the grain size.

The PSD of stucco materials analysed via aero dispersion method is shown in Figure 29. From this analysis method, fine particles as small as 50 µm were observed despite the material being collected between 600 – 200 µm sieves. In addition, this method detects that both BD-$Al_2O_3$ and SGB127 materials have approximately 15 vol% of particles below the 200 µm sieve size. This may imply that particles were being deagglomerated during analysis or finer particles were adhering to larger ones preventing separation during sieving.

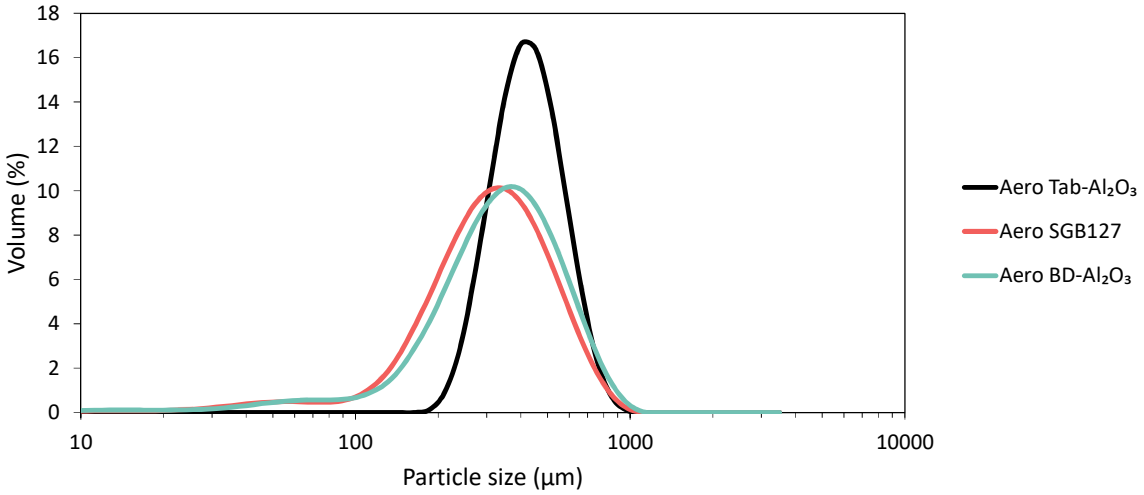



**Figure 29** – Particle size distribution of stucco grains analysed under aero dispersion method

The PSD of stucco materials analysed via hydro dispersion method is shown in Figure 30. It was observed that analysis via this alternative dispersion method produced a PSD much more representative of the sieve sizes used to collect the material. The cumulative volume of particles less than 200 µm for BD-$Al_2O_3$ and SGB127 materials has reduced from approximately 15 vol% via aero dispersion to approximately 1 vol% via hydro dispersion. This contradicts the previous hypothesis that particles become deagglomerated during analysis as the same level of fines would be observed via both dispersion methods. An alternative hypothesis proposed for the observation of fines present via aero dispersion is that weak porous particles facture during analysis. This leads to the production of a finer fraction of particles which are unrepresentative of the original samples loaded into the instrument. This accounts for the shift in PSD from aero to hydro dispersion as a more gentle dispersion technique is employed. In addition, this alternative hypothesis explains why the PSD of Tab-$Al_2O_3$ remains equal when analysed via each dispersion method as the tougher non-porous Tab-$Al_2O_3$ particles remain intact during each dispersion method.

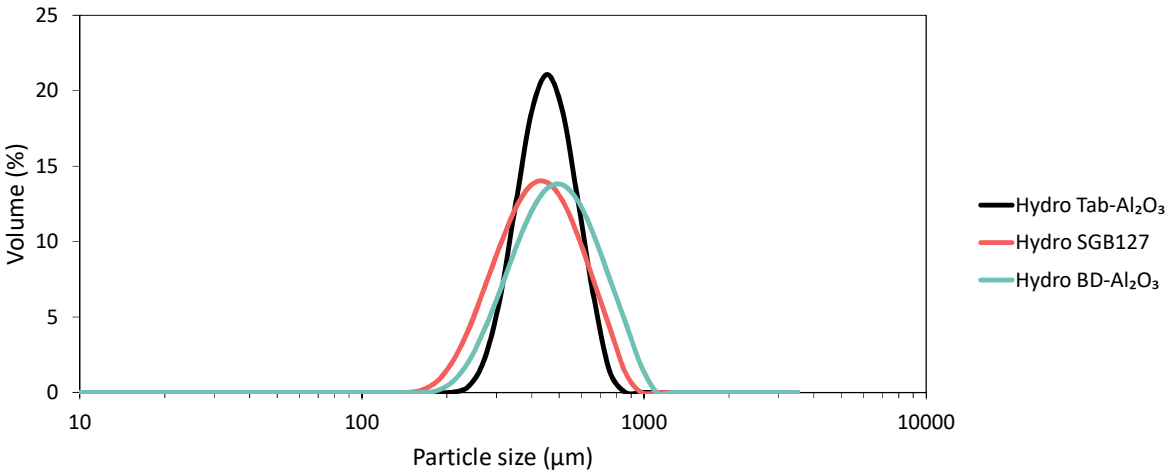



**Figure 30** – Particle size distribution of stucco grains analysed under hydro dispersion method

Overall, both porous stucco materials display a broader range of grain sizes than Tab-$Al_2O_3$. However, an acceptable degree of overlap in PSD is present between the porous grains and Tab-$Al_2O_3$ grains, thus the method of manufacturing porous stucco has successfully produced a material with similar grain size to the standard stucco.

### 4.2.3 Nitrogen Adsorption

Nitrogen adsorption is a useful tool for characterising pore structure and properties; as such a large amount of information can be gathered on BD-$Al_2O_3$ and SGB127. However, due to the dense nature of Tab-$Al_2O_3$ the resulting pore volume is small and often can be seen as negligible. For this reason Tab-$Al_2O_3$ is omitted from pore volume plots.

It can be seen in Table 7 that both BD-$Al_2O_3$ and SGB127 display a high surface area (as calculated by BET method) and pore volume (as calculated by BJH method) resulting from internal open voids in each material. In addition, the synthesised boehmite derived alumina displays properties similar to those found in literature. A typical boehmite derived alumina fired at 700 °C is expected to attain surface area of 100 – 200 $m^2 g^{-1}$; a pore volume of 0.3 – 0.4 $cm^3 g^{-1}$ and an average pore size of 3 – 8 nm [129, 130, 131]. Tab-$Al_2O_3$ on the other hand displays a non-porous nature as although voids are present these too large to be measured via this method.

**Table 7** – Surface and pore characteristics obtained by nitrogen adsorption

| Material | Surface area ($m^2 g^{-1}$) | | Average pore Diameter (nm) | | Total pore volume ($cm^3 g^{-1}$) | | Micropore volume ($cm^3 g^{-1}$) | |
|---|---|---|---|---|---|---|---|---|
| | Average | Standard deviation | Average | Standard deviation | Average | Standard deviation | Average | Standard deviation |
| BD-$Al_2O_3$ | 161 | 3.99 | 9.09 | 0.107 | 0.40 | 0.00734 | - | - |
| SGB127 | 749 | 12.25 | 2.64 | 0.016 | 0.26 | 0.00183 | 0.07 | 0.0002 |
| Tab-$Al_2O_3$ | 0.09 | 0.014 | - | - | - | - | - | - |

Isotherms for BD-$Al_2O_3$, SGB127 and Tab-$Al_2O_3$ are shown in Figure 31. The isotherm plotted for Tab-$Al_2O_3$ displays a type II isotherm with no observed hysteresis indicative of a non-porous or macroporous solid showing monolayer adsorption followed by multi-layered adsorption [132]. The isotherm plotted for BD-$Al_2O_3$ displays a type IV isotherm with a H2 hysteresis loop similar to results obtained by Karouia et al. for similar material [98]. This isotherm profile indicates a large degree of capillary condensation is occurring within the pores, resembling a mesoporous structure. The isotherm of SGB127 displays a profile resembling a type I isotherm due to the sharp increase in adsorption towards lower relative pressures followed by a plateau with a small H2 hysteresis loop. This type of isotherm was observed by Miyazawa et al. whereby a degree of microporosity and mesoporosity coexist in silica gel materials [133].

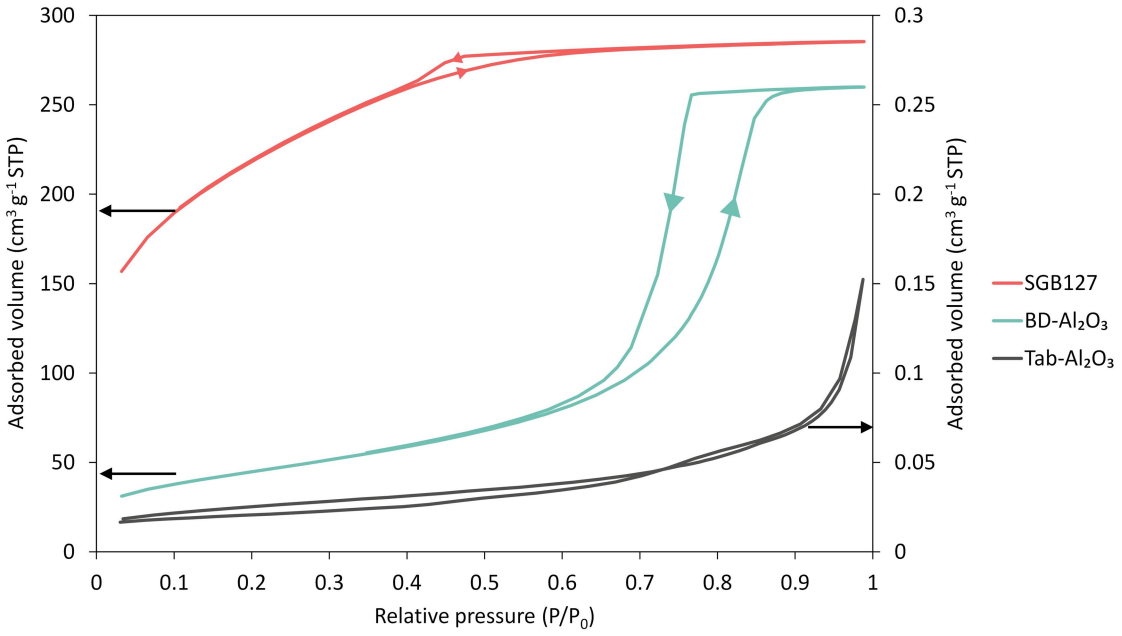



**Figure 31** – Representative example of nitrogen adsorption and desorption isotherm of each stucco material. Arrows indicate axis used for each plot

The t-plot analysis in Figure 32 shows minimal microporosity in both BD-$Al_2O_3$ and Tab-$Al_2O_3$ as shown by the extrapolated line of best fit intersecting the origin. SGB127 on the other hand shows a degree of microporosity which is displayed in Table 7.

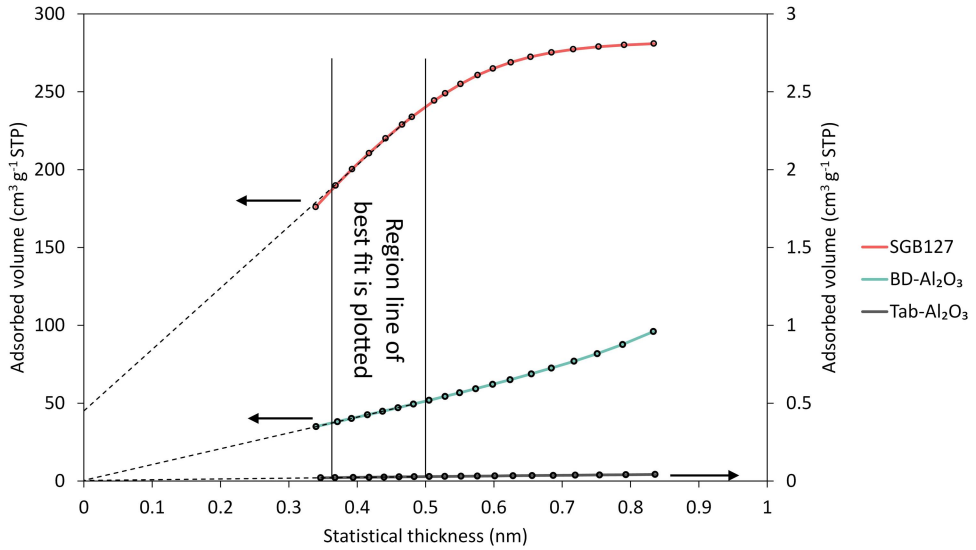



**Figure 32** – Representative example of t-plot analysis on each stucco material. Arrows indicate axis used for each plot

The pore size distribution as calculated by the BJH method on the adsorption plot is shown in Figures 33 and 34 for a representative sample of BD-$Al_2O_3$ and SGB127. It can clearly be seen that the limitations of the BJH method have been reached for SGB127 due to the high degree of porosity below 2 nm. BD-$Al_2O_3$ displays a broad pore size distribution ranging from 2 – 20 nm, whereas SGB127 contains the majority of the porosity below 5 nm.

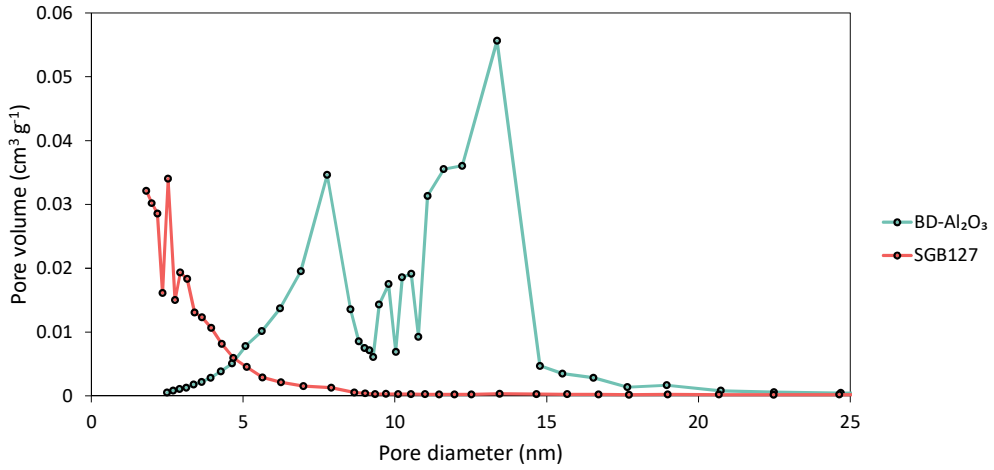



**Figure 33** – Representative example of incremental pore volume calculated by BJH method plotted against pore diameter for each porous stucco material

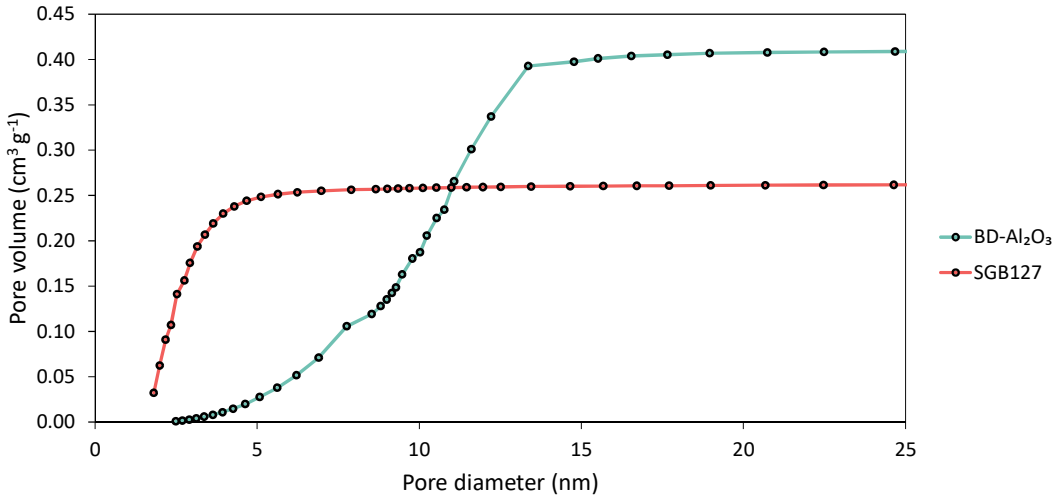



**Figure 34** – Representative example of cumulative pore volume calculated by BJH method plotted against pore diameter for each porous stucco material

### 4.2.4 Particle Density and Porosity

Helium pycnometer analysis was undertaken on BD-$Al_2O_3$, SGB127 and Tab-$Al_2O_3$ to calculate the true density (density of solids only) for each material. This, in combination with results from nitrogen adsorption can be used to calculate the bulk density (density including pores) of each material from Equation 31 by combining Equations 32, 33 and 34. As stated in Section 3.1.1.4, helium pycnometer analysis was conducted after prolonged drying periods to characterise each material in a dehydrated state.

$$Bulk\ density\ (g\ cm^{-3}) = \frac{Mass\ (g)}{Bulk\ volume\ (cm^3)} \qquad \text{eq.31}$$

$$Bulk\ volume\ (cm^3) = Material\ volume\ (cm^3) + Pore\ volume\ (cm^3) \qquad \text{eq.32}$$

$$Material\ volume\ (cm^3) = \frac{Mass(g)}{True\ density\ (g\ cm^{-3})} \qquad \text{eq.33}$$

$$Pore\ volume\ (cm^3) = Mass\ (g) \times Porosity\ (cm^3\ g^{-1}) \qquad \text{eq.34}$$

In addition, it was possible to calculate the porosity of each material in terms of volume from Equation 35. This gives a more illustrative term for porosity.

$$Porosity\left(cm^3_{pore}\, cm^{-3}_{bulk}\right) = \frac{Pore\ volume\ (cm^3)}{Bulk\ volume\ (cm^3)} \qquad \text{eq.35}$$

True density values attained by helium pycnometer method are shown in Table 8 for each material. In addition, the calculated bulk density and volumetric porosity of each material is displayed as calculated from Equation 31 and 35 respectively using BJH porosity data from Table 7 and true density from Table 8.

**Table 8** – True density attained by helium pycnometer analysis in addition to bulk density and volumetric porosity calculated using pore volume and true density data

| Sample | True density (g $cm^{-3}$) | | Bulk density (g $cm^{-3}$) | Porosity ($cm^3_{pore}$ $cm^{-3}_{bulk}$) |
|---|---|---|---|---|
| | Average | Standard deviation | | |
| BD-$Al_2O_3$ | 3.53 | 0.015 | 1.45 | 0.59 |
| SGB127 | 2.25 | 0.032 | 1.42 | 0.37 |
| Tab-$Al_2O_3$ | 3.76 | 0.0004 | 3.76 | 0.00 |

True densities attained for both BD-$Al_2O_3$ and SGB127 match literature values for γ-$Al_2O_3$ = 3.20 g $cm^{-3}$ [134] and amorphous silica 2.27 g $cm^{-3}$ [135]. Additionally, the density of Tab-$Al_2O_3$ closely matches α-$Al_2O_3$ (true density of 3.98 g $cm^{-3}$ [134]) with a minor reduction in the measured density due to the closed porosity present in the structure. From the porosity data it is clear that BD-$Al_2O_3$ has a greater volume of pores per volume of bulk material in comparison to SGB127. However, due to the high surface area and narrow pore size in each material, pores can be filled with water due to the humidity in the atmosphere. This can lead to a lesser degree of porosity present as pores become partially saturated.

### 4.2.5 Dynamic Vapour sorption (DVS)

Dynamic vapour sorption was used to evaluate how water sorbs onto the accessible surfaces of stucco materials over a broad range of humidity environments. This can be used to assess the degree to which pores are filled in porous stucco materials when inside the controlled humidity environment used to dry the investment casting shells. As such, it can be estimated how much free porosity is available to absorb water when the particles are deposited onto the surface of the slurry. It should be noted that due to the lack of hygroscopicity of Tab-$Al_2O_3$ a minimal quantity of mass change was observed and thus the results were not displayed. DVS results for BD-$Al_2O_3$ and SGB127 are displayed in Figure 35.

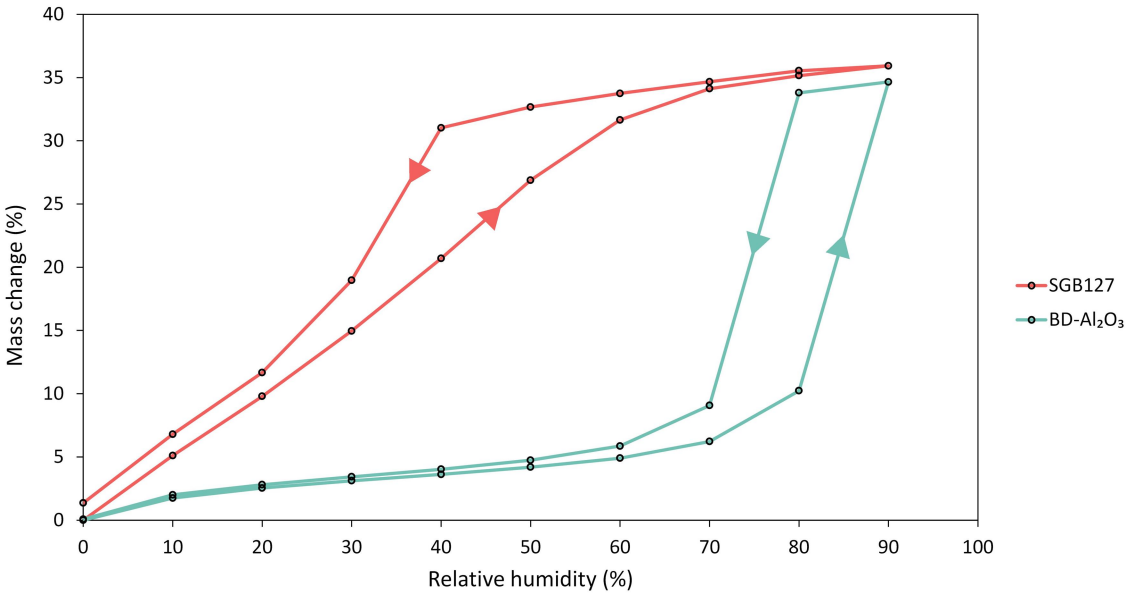



**Figure 35** – Dynamic vapour sorption and desorption plots for porous stucco materials

<u>BD-$Al_2O_3$ analysis</u>

BD-$Al_2O_3$ shows a reversible isotherm which can be identified as type IV with a H2 hysteresis loop. Adsorption of water initially occurs on BD-$Al_2O_3$ in a dehydrated state (after cooling down from firing at 700 ˚C during synthesis) by chemisorption whereby water adsorbed onto the alumina surface dissociates to form hydroxyl groups [136]. This occurs during processing and handling where the material interacts with water species in the atmosphere before DVS analysis was conducted. As such no chemisorption was measured during analysis as identified by the reversible nature of the curve returning to the original mass after

saturation. This behaviour shows water molecules were only physisorbed onto the surface during analysis and can be easily removed, whereas removal of the chemisorbed species requires temperatures nearing 800 K to remove the bound water [136]. The chemisorbed species act as sites for physisorption as the $R_H$ increases which leads to multilayer coverage [137]. As $R_H$ increases further, more water molecules deposit via physisorption and eventually capillary condensation occurs within mesopores and smaller macropores. This leads to a high quantity of sorption occurring as water molecules fill the pore volume. Subsequently, upon desorption a hysteresis loop occurs as a higher relative pressure gradient is required to remove tightly bound water molecules in the pores.

SGB127 analysis

SGB127 shows a type I isotherm with a small H2 hysteresis loop. Sorption of water occurs at the surface hydroxyl groups via physisorption as hydrogen bonds are formed between the surface hydroxyl groups and the water species [138]. As more species adsorb, the water molecules fill mesopores and small macropores via capillary condensation leading to the observed hysteresis loop. A minor degree of chemisorbed water is found as the final point at 0 % $R_H$ is slightly higher than the initial point taken at 0 % $R_H$. This was also observed by Nanono et al. who found that following the initial uptake of water, silica gel does not return to the original mass even after prolonged evacuation for up for 40 hours, indicating the presence of chemisorbed water [138]. As such, only the second adsorption/desorption isotherm yields a reversible trace.

Comparing BD-$Al_2O_3$ and SGB127

The isotherms identified for both BD-$Al_2O_3$ and SGB127 vary considerably. BD-$Al_2O_3$ favours sorption in high $R_H$ environments displaying minimal water uptake at lower $R_H$ values, this leads to a large quantity of unsaturated pores available when stored in atmospheric conditions. SGB127 on the other hand sorbs water at lower $R_H$, resulting in a large quantity of saturated pores when particles are stored in atmospheric conditions. Presuming the shell room accurately maintains a $R_H$ of 50 % and that pores are saturated at 90 % $R_H$ it is found

that SGB127 is 75 % saturated in the shell room environment whereas BD-$Al_2O_3$ is only 12 % saturated. As such, BD-$Al_2O_3$ has a greater capacity for water absorption when utilising the material to uptake water from the investment casting slurry. Assuming the stucco reaches saturation when deposited onto the slurry, pores within SGB127 will remain 90 % saturated while pores within BD-$Al_2O_3$ will remain 14 % saturated as the shell is dried at 50 % $R_H$.

### 4.2.6 Thermomechanical Analysis (TMA)

Thermomechanical analysis was undertaken to predict the shrinkage of stucco materials during the simulated casting cycle. Ideally, experimental material should have the same dimensions as the reference sample to allow for accurate correction of the expansion and contraction of instrument apparatus. However, raw unground BD-$Al_2O_3$ material exists as irregular flakes 4 – 10 mm in length and SGB127 was received as spheres 2 – 4 mm in diameter. As such, grinding and cutting steps were performed on raw unground BD-$Al_2O_3$ material to form a close approximation to the reference cylinder and SGB127 spheres were loaded into the instrument directly as received as shown in Figure 19. Tab-$Al_2O_3$ on the other hand was purchased as grains making the formation of cylinders of appropriate size for TMA impossible and thus the prediction of shrinkage during the simulated casting cycle could not be completed for this material. Each material was analysed three times, recording the expansion/contraction over the simulated casting cycle.

<u>BD-$Al_2O_3$ analysis</u>

The thermal expansion/contraction behaviour exhibited by BD-$Al_2O_3$ throughout the simulated casting cycle is shown in Figure 36. It was observed that following the completion of the firing cycle a high degree of shrinkage has taken place averaging 21.9 linear % which is equivalent to 52.4 volume % assuming isotropic behaviour. Additionally, samples show a high degree of repeatability despite each sample being irregularly shaped. The thermal expansion measured from 50 – 700 °C was calculated to equal 7.1 x $10^{-6}$ $K^{-1}$.

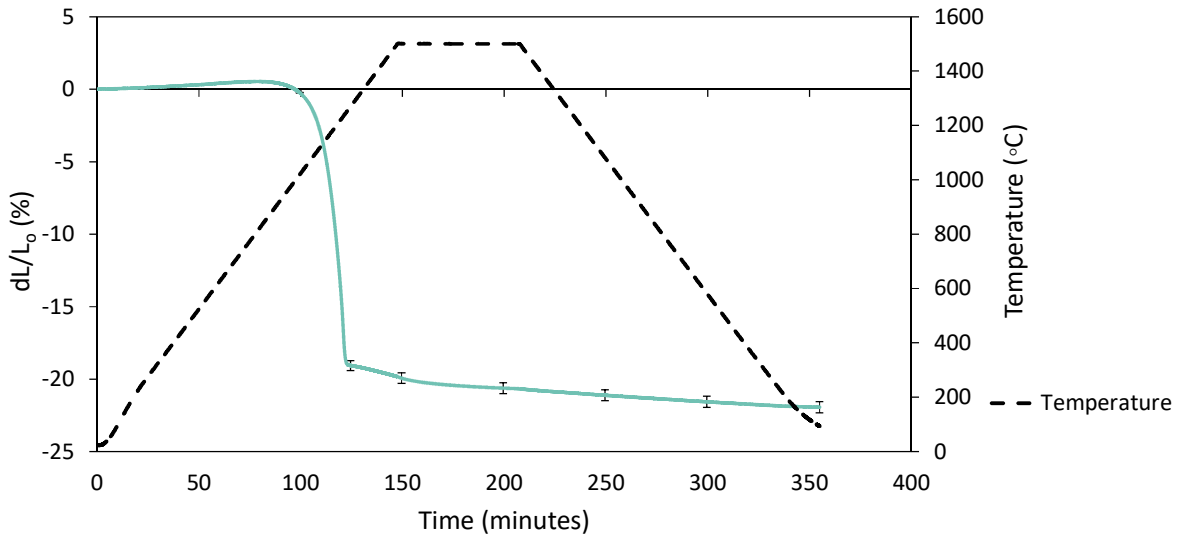



**Figure 36** – Expansion/contraction plot of BD-$Al_2O_3$ analysed throughout the simulated casting cycle conducted by TMA

The thermal expansion/contraction behaviour of BD-$Al_2O_3$ can be broken down into three regions as shown in Figure 37. As the temperature increases, simple thermal expansion is exhibited (region A) until a sufficient temperature is reached at which time phase transition and sintering occur simultaneously (region B). As the temperature increases further, phase transition is complete and sintering continues (region C). After cooling, the end product is a polycrystalline α-$Al_2O_3$ material which has undergone significant shrinkage.

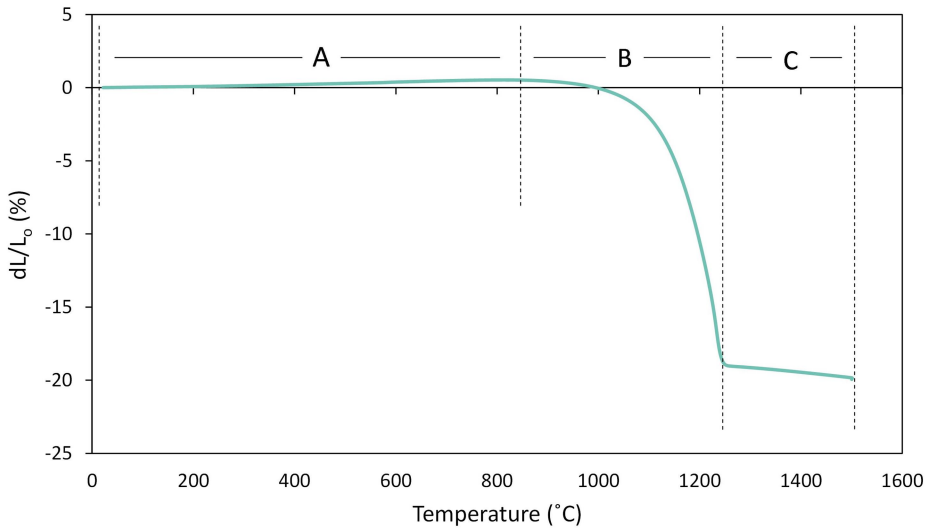



**Figure 37** – Diagram showing the three behavioural regions of expansion/contraction for BD-$Al_2O_3$ broadly described as A (thermal expansion), B (sintering and phase transition) and C (sintering)

Region A

BD-$Al_2O_3$ remains stable showing only thermal expansion up to approximately 850 °C where densification begins. This is similar to results found by Bodisova et al. where densification was also found to initiate at 850 °C [139].

Region B

At 850 °C simultaneous sintering and phase transformation occurs whereby the γ-$Al_2O_3$ phase is converted progressively into δ-$Al_2O_3$, θ-$Al_2O_3$ and α-$Al_2O_3$. Towards 1200 °C all transition phases are depleted and only α-$Al_2O_3$ remains [140]. During the final transition from θ-$Al_2O_3$ to α-$Al_2O_3$ the α phase nucleates and grows at the expense of the θ-$Al_2O_3$ matrix. As a result, considerable redistribution of the pore structure occurs whereby fine pores present in the θ-$Al_2O_3$ matrix are rearranged to form larger ones [140]. This produces elongated or "finger-like" pores propagated from an individual nucleation site which subsequently grow through the matrix as the phase boundary migrates [141]. The α-$Al_2O_3$ phase grows quickly producing single crystal grains up to 100 times larger than the θ-$Al_2O_3$ grains, however large quantities of trapped porosity remain. The resulting microstructure shows a vermicular nature with interconnecting porosity up to 35 % by volume [140]. Thus the conclusion given for such extreme shrinkage is the concurrent rapid densification of the fine θ-$Al_2O_3$ matrix in addition to the volume reduction associated with the phase transition to α-$Al_2O_3$ [142]. As the transformation to α-$Al_2O_3$ nears completion a sudden reduction in shrinkage rate is observed. This results from the larger α-$Al_2O_3$ crystals requiring a much higher temperature to sinter.

Region C

As the temperature increases a greater driving force for sintering occurs and the removal of trapped porosity takes place resulting in further shrinkage.

SGB127 analysis

The thermal expansion/contraction behaviour exhibited by SGB127 throughout the simulated casting cycle is shown in Figure 38. It was observed that following the completion of the firing cycle a high degree of expansion has taken place, averaging 4.9 linear % which is equivalent to 13.0 volume % assuming isotropic behaviour. Samples show an acceptable degree of repeatability.

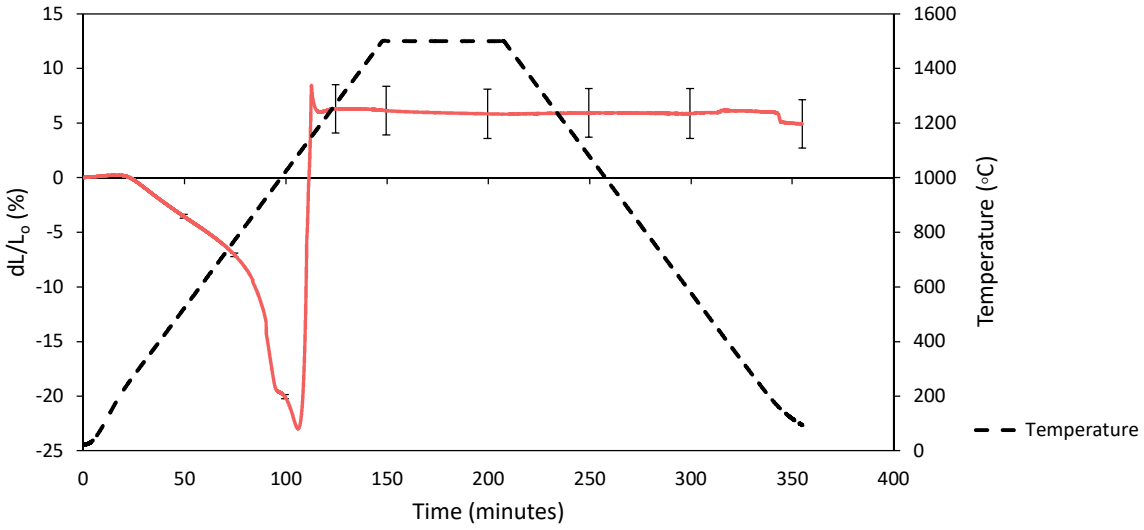



**Figure 38** – Expansion/contraction plot of SGB127 analysed throughout the simulated casting cycle conducted by TMA

The thermal expansion/contraction behaviour of SGB127 can be broken down into four broadly defined regions with a variable pathway dependent on the heating rate as shown in Figure 39. Regions I – III are labelled as defined by Brinker et al. resulting from the removal of water and shrinkage of the material [135]. Region IV is defined based on the hypothesis proposed by Murata et al. that evolution of water from the bulk causes the material to expand if insufficiently diffused [143].

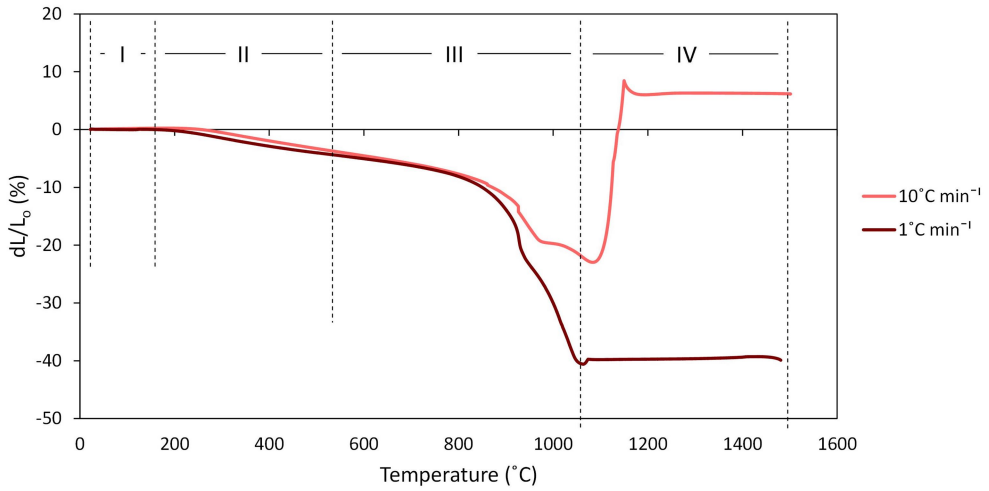



**Figure 39** – Diagram showing four behavioural regions of expansion/contraction for SGB127 upon heating broadly described as I (primarily weight loss), II (shrinkage proportional to weight loss), III (primarily shrinkage) and depending on the heating rate IV (foaming)

The three regions defined by Brinker et al. are: (I) primarily weight loss (25 – 150 ˚C), (II) shrinkage proportional to weight loss (150 – 525 ˚C) and (III) primarily shrinkage (>525 ˚C) [135]. Towards later stages in region III evolved water is still diffusing through the bulk to the surface. However, the material is expected to foam if a build-up of pressure ensues from vapour not diffusing sufficiently, this produces a high degree of expansion [143] as observed in SGB127 material. Whether or not this occurs is dependent on the heating rate and material volume as a controlled release of gas from the internal structure to the external surface is required to prevent the build-up of gas. This leads to a split pathway in region IV dependent on the heating rate of the material as shown in Figure 39. In addition, crystallisation can occur throughout the firing cycle transforming the amorphous silica gel into many possible crystalline phases of silica.

Region I

As the silica gel is heated, physically adsorbed water is removed resulting in a small amount of shrinkage due to an increase in surface energy upon desorption. This increases capillary pressure for which the resulting strain can be calculated from Equation 36 [135, 144].

$$\varepsilon = -\frac{\Delta z(1-\upsilon)S\rho_{true}}{E} \qquad \text{eq.36}$$

$\varepsilon$ Strain (-)

$\upsilon$ Poisson's ratio (-)

$z$ Surface energy (J $m^{-2}$)

$E$ Young's modulus (N $m^{-2}$)

Heat treatments above 150 °C result in dehydration reactions taking place between silanol groups hydrogen bonded to together as shown in Figure 40 [135]. This further increases the surface energy leading to volumetric contraction.

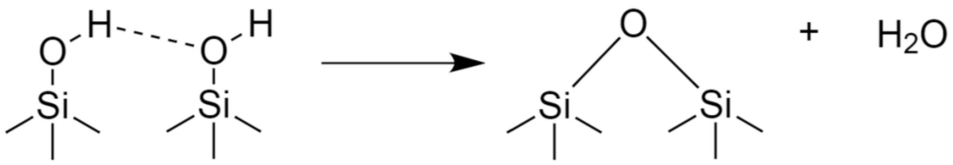



**Figure 40** – Dehydration of silanol groups occurring within silica gel [135]

Region II

In this region, dehydration reactions continue. However, polycondensation reactions taking place within the skeletal structure account for the majority of water loss in this region [135]. An example of a polycondensation reaction occurring in silica gel is shown in Figure 41. This differs from dehydration reactions as silanol groups are not hydrogen bonded.

As temperature increases, silanol groups with weaker hydrogen bonds are combined to evolve water. This occurs as silanol groups attracted by hydrogen bonds have a lower desorption barrier to overcome [145]. Such reactions lead to weight loss from the removal of water as a by-product of the reaction and shrinkage occurring concurrently to densify the structure. As a result, the true density of the structure increases.

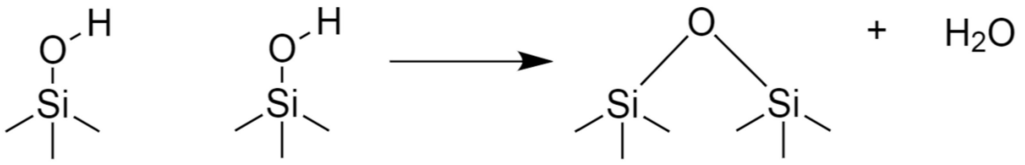



**Figure 41** – Polycondensation reactions occurring within silica gel [135]

The structure is further densified by structural relaxation in which free volume is removed to shrink the matrix isotopically without particles rearranging to higher coordination numbers [135]. This mechanism leads to shrinkage without an associated weight loss, producing a structure characteristic of a metastable liquid upon completion. At this temperature viscous sintering is not taking place as the thermal energy is not sufficient, this was shown by Brinker et al. who observed the reduction in surface area was accounted for due to structural relaxation without any dramatic reduction indicative of sintering [146].

Region III

As temperature increases further the progression of both polycondensation and dehydration reactions near completion and the rate of weight loss begins to decrease. As temperature increases further the material undergoes viscous sintering [135] leading to considerable shrinkage resulting from pore closure and densification. The sintering rate for silica gel is typically high due to the large surface area of the material; this produces a large driving force for sintering.

Region IV

Due to the thermal lag between the external surface and the internal structure a situation can arise whereby water evolved during dehydration and polycondensation reactions are incomplete in the bulk when the surface begins to sinter and remove porosity. As a result of this, the gas evolving in the bulk is required to diffuse through the dense network to the surface. If the gas is not able to diffuse sufficiently it can cause foaming to occur due to a

pressure build up in the bulk if the material is sufficiently viscous [143]. It is possible to reduce this pressure and subsequent expansion by decreasing the heating rate as observed in Figure 39 or alternatively reducing the volume of sample to decrease the thermal gradient in the material allowing gas to escape before surface pores close.

As SGB127 samples were tested as acquired in spherical form ranging from 2 – 4 mm in diameter the volume of material characterised is unrepresentative of the grains used as stucco in the investment casting process. As such, it is possible that SGB127 grains will not experience foaming due to the build-up of gas as the smaller particle size will permit vapour diffusion more efficiently than the SGB127 spheres tested by TMA.

Phase transformation

As temperature increases throughout the firing cycle various crystalline types of silica can form. The formation of β-quartz is possible at fairly low temperatures of approximately 573 ˚C however this transition is favoured by a slow heating rate [147], much less than observed in the investment casting process. Tridymite formation is also possible, but only with mineralisers present [148] which are not typically found in silica gel as impurities are removed during manufacture to optimise absorption properties [91]. The formation of cristobalite on the other hand is favoured and likely represents the majority of phase transition occurring within the silica gel due to the high heating rates favouring this phase transformation [149]. This process begins at approximately 1200 ˚C [150] with nucleation occurring at the surface initially and propagating inwards [151]. As such, the quantity of cristobalite formed in the tested specimen will likely be less than observed in the granular form used as stucco due to a difference in surface area to volume ratio. The expected existence of cristobalite can be observed in SGB127 samples due to the sharp shrinkage observed between 180 – 270 ˚C resulting from the transformation of β-cristobalite to α-cristobalite upon cooling [152].

## 4.3 Shell Build

### 4.3.1 Analysing Surface Coverage after Stucco Deposition

Characterisation of the slurry surface was conducted after application of porous and non-porous stucco materials to observe the surface coverage and adhesion of particles to the slurry once the slurry dried. Initially, a wax pattern of dimensions 130 x 100 x 20 mm was coated in P $(FusedAl)_2$ and P+1 $(FusedAl)_2$ layers (notation defined in Section 3.1.3). The partially completed shell was then dipped in Secondary slurry and after draining the required stucco blend was applied. The mould was then taken to the drying chamber for at least two hours before the surface features were recorded optically, making sure to capture a representative image of the surface being observed.

The result of depositing BD-$Al_2O_3$ stucco on the Secondary slurry is shown in Figure 42 in comparison to Tab-$Al_2O_3$. It was observed that the surface coverage was severely limited when depositing BD-$Al_2O_3$ with a clear reduction in the number of particles per unit area in addition to areas remaining void of particles. In addition, BD-$Al_2O_3$ particles show poor adhesive strength to the dried slurry and require minimal force to remove them completely from the slurry as demonstrated in Figure 42. This effect was not observed for Tab-$Al_2O_3$. Poor adhesion can cause issues when redipping the partially build shell in slurry as the stucco particles can easily be removed due to shear in the slurry tank.




**Figure 42** – Comparison of surface coverage when depositing BD-$Al_2O_3$ stucco (left) and Tab-$Al_2O_3$ stucco (right) on Secondary slurry. Poor adhesion between the slurry and stucco is demonstrated when depositing BD-$Al_2O_3$ as particles are removed from the surface when lightly brushed whereas Tab-$Al_2O_3$ particles remain in place under the same treatment

As a result of this finding, BD-$Al_2O_3$ and SGB127 stucco were blended with Tab-$Al_2O_3$ stucco in attempts to incorporate a high quantity of porous stucco whilst forming a good surface coverage with sufficient adhesion. Blends were produced at 20, 40, 60 and 80 vol% porous stucco with the remaining percentage being equal to the vol% of Tab-$Al_2O_3$ stucco. Blends were produced using bulk density values taken from Table 8 to calculate the correct weight ratio required for each blend. Each stucco material was weighed in the same dehydrated state bulk density data was attained in order for accurate volume ratios to be produced. It should be noted that due to the contrasting bulk densities of porous and non-porous stucco, the denser Tab-$Al_2O_3$ material will preferentially filter through the sieve during application of stucco to a surface. To counteract this, sufficiently large batches of each blend where produced of at least 200 g to fill the sieve when depositing stucco onto the slurry by hand. This ensured that the slurry surface was covered in particles before significant separation within the sieve could occur. The slurry surface after application of either 20, 40, 60, 80 or 100 vol% porous stucco is displayed in Figure 43 for BD-$Al_2O_3$ and Figure 44 for SGB127. Additionally, the surface coverage of 100 vol% Tab-$Al_2O_3$ is given in Figure 45 for comparison to the Rolls-Royce standard stucco used in the secondary layers. Pictures were taken after drying the partially built mould for at least 2 hours.

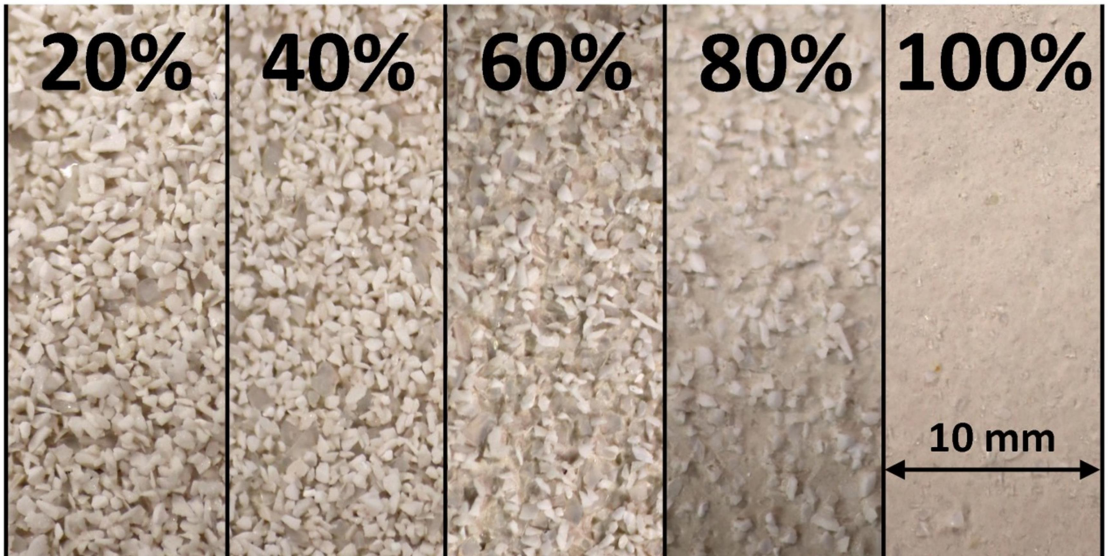



**Figure 43** – Surface coverage of BD-$Al_2O_3$ stucco blends deposited onto Secondary slurry

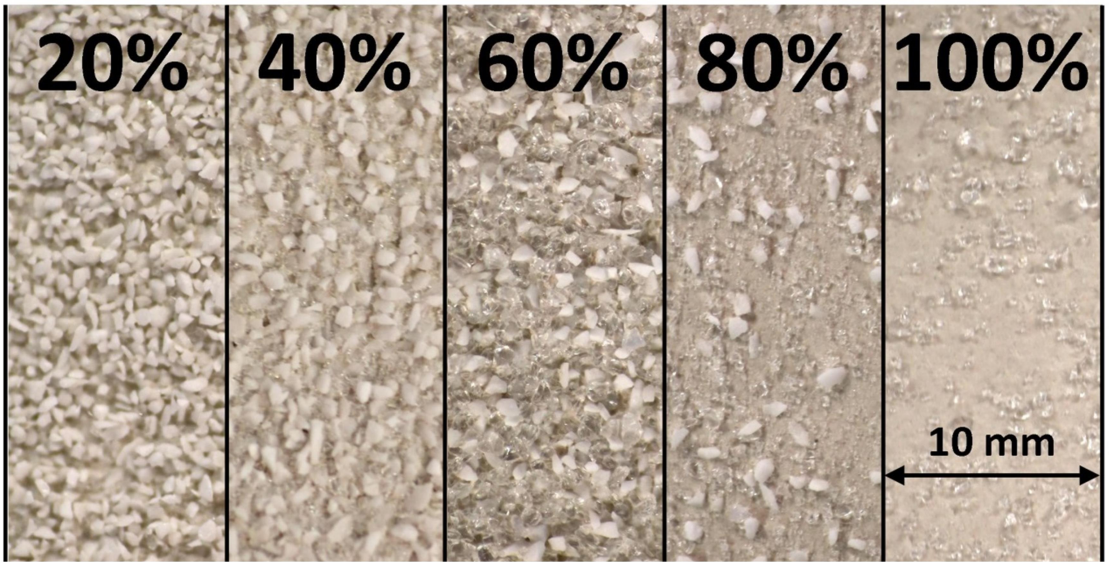



**Figure 44** – Surface coverage of SGB127 stucco blends deposited onto Secondary slurry




**Figure 45** – Surface coverage of Tab-$Al_2O_3$ stucco deposited onto Secondary slurry

It was observed that a higher concentration of porous stucco produces a poorer surface coverage whereby fewer particles are adhered to the surface per unit area. It was hypothesised that this was the result of porous stucco absorbing water from the slurry upon contact, causing the slurry to become more viscous or gel. Subsequently, particles deposited onto the dried slurry surface do not adhere. This hypothesis also explains the low strength of adhesion between the slurry and the stucco particles as the production of a viscous surface on contact will hinder grains on the surface penetrating deeper into the slurry and forming a greater contact area. As a result of the low strength of adhesion, falling particles

can knock weakly bonded particles from the surface and thus further reduce the number of particles bonded to the slurry. This was most prominent when depositing 100 vol% BD-$Al_2O_3$ where some areas of the slurry were void of any particles on the surface. In addition, the lower bulk density of porous material means the stucco particle will hit the slurry with less force, reducing the penetration of stucco into the slurry.

To measure the adhesion between the slurry and stucco after drying, a qualitative method was developed whereby a brush was passed across the surface of the slurry coated in a given stucco composition. The adhesion was ranked based on the magnitude of force required to remove particles from the slurry surface as described in Table 9. The adhesive strength of various stucco compositions as characterised by the description in Table 9 is given in Table 10.

**Table 9** – Description of adhesive strength between stucco and slurry based on the force required to remove particles embedded in the slurry by passing a brush over the surface

| **Number attributed to adhesion strength** | **Description of force required to remove particles embedded in slurry** |
|---|---|
| 1 | Most particles removed by light brushing |
| 2 | Most particles removed by rough brushing |
| 3 | Most particles remain embedded even with rough brushing |

**Table 10** – Adhesive strength of stucco compositions characterised by the magnitude of force required to remove embedded particles as described in Table 9

| **Volume ratio of porous stucco to Tab-$Al_2O_3$** | **Porous stucco composition** | |
|---|---|---|
| | **SGB127** | **BD-$Al_2O_3$** |
| 0:100 | 3 | |
| 20:80 | 3 | 3 |
| 40:60 | 3 | 3 |
| 60:40 | 3 | 3 |
| 80:20 | 2 | 2 |
| 100:0 | 1 | 1 |

As identified in Table 10, the application of porous stucco blends containing 60 vol% or less BD-$Al_2O_3$ or SGB127 produces an adhesive strength equivalent to that measured with 100 vol% Tab-$Al_2O_3$ stucco. As such, a 60 vol% blend of either BD-$Al_2O_3$ or SGB127 was implemented in each secondary layer for further development of investment cast shells utilising porous stucco. This allows the maximum quantity of porous stucco to be introduced into the shell whilst maintaining the adhesive strength of the stucco to the slurry and providing a surface coverage visually similar to depositing Tab-$Al_2O_3$. The composition of shells utilising 60 vol% porous stucco in secondary layers is given in Table 11 in addition to the standard Rolls-Royce formulation utilising Tab-$Al_2O_3$ (using notation from Section 3.1.3 for labelling each layer).

**Table 11** – Composition of complete shells containing non-porous or porous stucco blends labelled Shell (Tab-$Al_2O_3$), Shell (BD-$Al_2O_3$) and Shell (SGB127)

| Complete shell identifier | Layer composition in order of application | Number of layers |
|---|---|---|
| Shell (Tab-$Al_2O_3$) | P $(FusedAl)_2$ | 1 |
| | P+1 $(FusedAl)_2$ | 1 |
| | S (Tab-$Al_2O_3$)$_2$ | 5 |
| | Seal (Secondary) | 1 |
| Shell (BD-$Al_2O_3$) | P $(FusedAl)_2$ | 1 |
| | P+1 $(FusedAl)_2$ | 1 |
| | S (60 BD-$Al_2O_3$)$_2$ | 5 |
| | Seal (Secondary) | 1 |
| Shell (SGB127) | P $(FusedAl)_2$ | 1 |
| | P+1 $(FusedAl)_2$ | 1 |
| | S (60 SGB127)$_2$ | 5 |
| | Seal (Secondary) | 1 |

### 4.3.2 Coat Weight

The quantity of slurry and stucco deposited during shell build was measured when applying secondary layers containing a 60 vol% porous stucco blend or 100 vol% Tab-$Al_2O_3$ to a shell containing previously dried layers as described in Section 3.1.4.1. This was undertaken to observe if the underlying porous stucco would affect the mass of slurry deposited on the following layer and measure the quantity of stucco deposited onto the slurry. When analysing the effect of varying stucco composition in previous layers the mass of slurry cannot be measured independently and is accompanied by the additional mass resulting from the backfill of liquid into previously dried layers. As such, the phrase "cumulative mass" is used to specify the cumulative effect of the mass of the slurry deposited in addition to the mass of the liquid backfilled into previously dried layers.

The volume of stucco deposited in each layer was also quantified by calculating the average bulk density for each stucco blend using Equation 37. This calculation applies a 60:40 volume ratio to bulk density data attained in Table 8. Using the average bulk density of each porous stucco blend the volume of stucco deposited can be estimated from the mass of stucco recorded by the balance using Equation 38. The volume of porous stucco deposited can then be related to the volume of Tab-$Al_2O_3$ deposited over the same area for comparison. It should be noted that the bulk density values were attained in a dehydrated state and thus any additional weight from moisture retained in the porous stucco will over predict the volume deposited.

$$Average\ bulk\ density\ (g\ cm^{-3}) = (n)\rho_P + (1-n)\rho_{np} \qquad \text{eq.37}$$

$n$ Fraction of porous stucco in blend (-)

$\rho_p$ Bulk density of porous stucco (g $cm^{-3}$)

$\rho_{np}$ Bulk density of non-porous stucco (g $cm^{-3}$)

$$Total\ stucco\ volume\ (cm^3) = \frac{Stucco\ mass\ (g)}{Average\ bulk\ density\ (g\ cm^{-3})} \qquad \text{eq.38}$$

As shown in Figure 46, a clear reduction in the mass of stucco deposited can be seen when applying porous stucco blends in comparison to non-porous stucco. This was partly the result of porous stucco having a lower bulk density and thus for the same volume of stucco deposited a reduction in mass was measured. However, a reduction in stucco volume was also calculated when comparing the volume of stucco deposited for both porous stucco blends in comparison to Tab-$Al_2O_3$. The volume of stucco deposited for 60 vol% blends of BD-$Al_2O_3$ and SGB127 was 67 % and 43 % respectively in comparison to Tab-$Al_2O_3$ stucco deposited onto an equivalent area of slurry. This quantifies the reduction in surface coverage observed optically in Section 4.3.1.

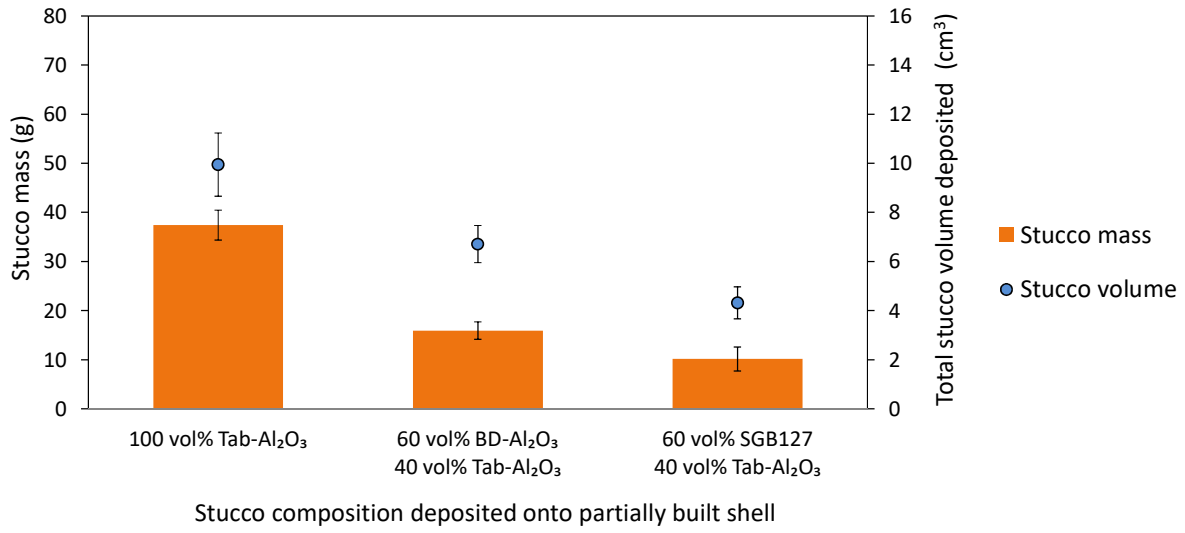



**Figure 46** – Stucco mass and corresponding volume deposited during shell build

As shown in Figure 47, the cumulative mass recorded for shells containing 60 vol% SGB127 and 100 vol% Tab-$Al_2O_3$ show similar values with overlapping error bars. This indicates that the porous silica stucco does not change the quantity of slurry deposited or the amount of liquid backfilled during shell build-up in comparison to Tab-$Al_2O_3$ stucco. However, shells containing 60 vol% BD-$Al_2O_3$ show a significantly higher mean difference in cumulative mass in comparison to shells built with 100 vol% Tab-$Al_2O_3$ when conducting a t-test at 95 % confidence. It was hypothesised that the porous stucco from the previously dried layers absorbs water from the slurry during dipping, increasing the recorded quantity of

cumulative mass. An explanation as to why SGB127 did not behave in a similar manner to BD-$Al_2O_3$ is that after absorbing the water, SGB127 particles remain mostly saturated in the environmental conditions of the drying chamber (as shown by DVS analysis in Section 4.2.5). As such, SGB127 particles are likely unable to absorb water from the subsequent layer of slurry.

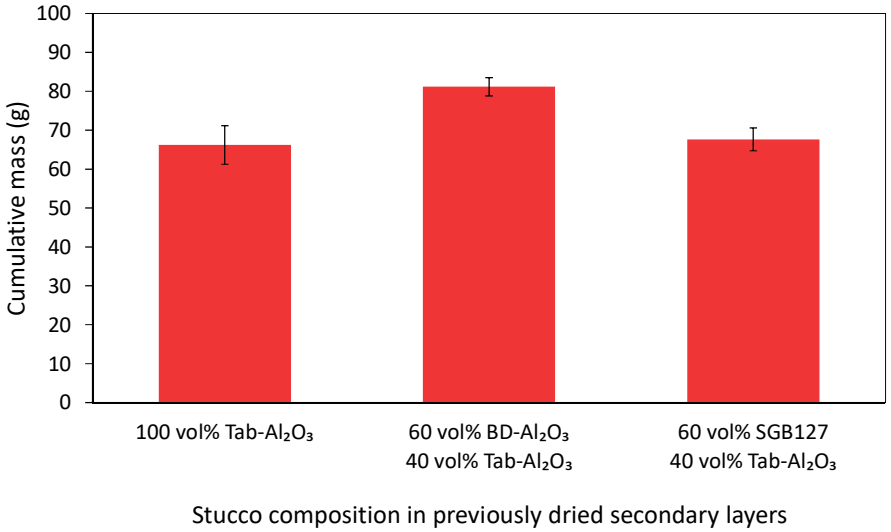



**Figure 47** – Cumulative mass recorded after dipping partially complete shell moulds in Secondary slurry during shell build

The hypothesis that BD-$Al_2O_3$ particles embedded in the mould absorb water from the following layer of Secondary slurry will result in the surrounding slurry becoming drier upon contact. This takes place as water transfers from the slurry to the porous particles. This will form a cake (dried slurry) surrounding the porous particles which would otherwise be absent when utilising non-porous stucco. This mechanism is described in Figure 48 which is similar to the technique slip casting.

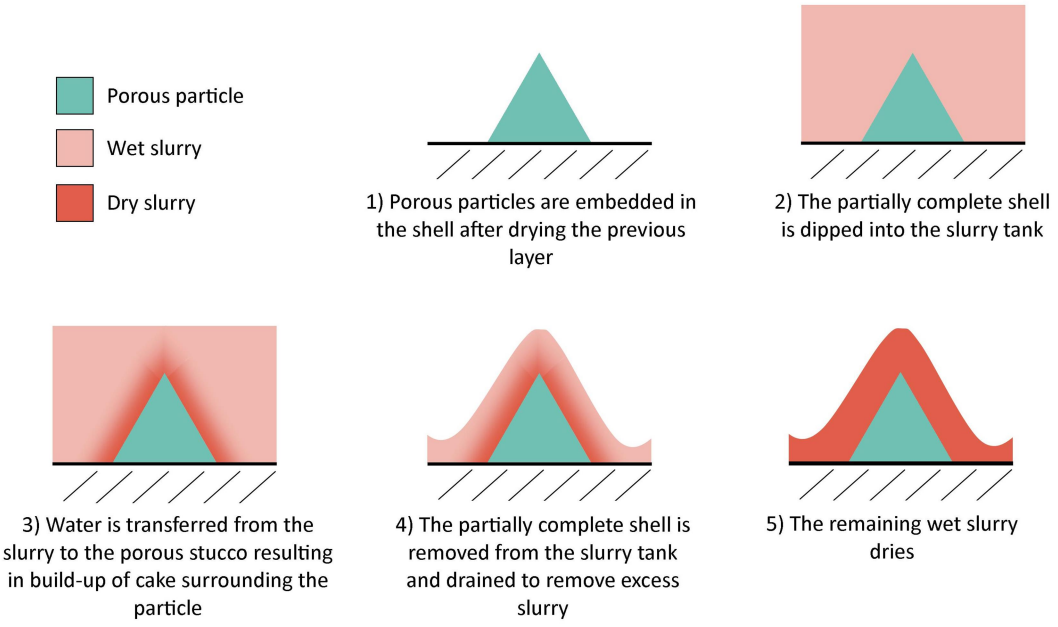



**Figure 48** – Proposed mechanism of cake growth surrounding porous particles embedded in the mould resulting from water transfer from the slurry to the porous stucco

Extrapolating the mechanism described in Figure 48 to include neighbouring porous particles it can be envisaged the porous stucco particles have the capability to dry the slurry before it can penetrate between inter-particle gaps. This mechanism is shown in Figure 49. Evidence of this occurring in Shell (BD-$Al_2O_3$) is shown in Figure 50.

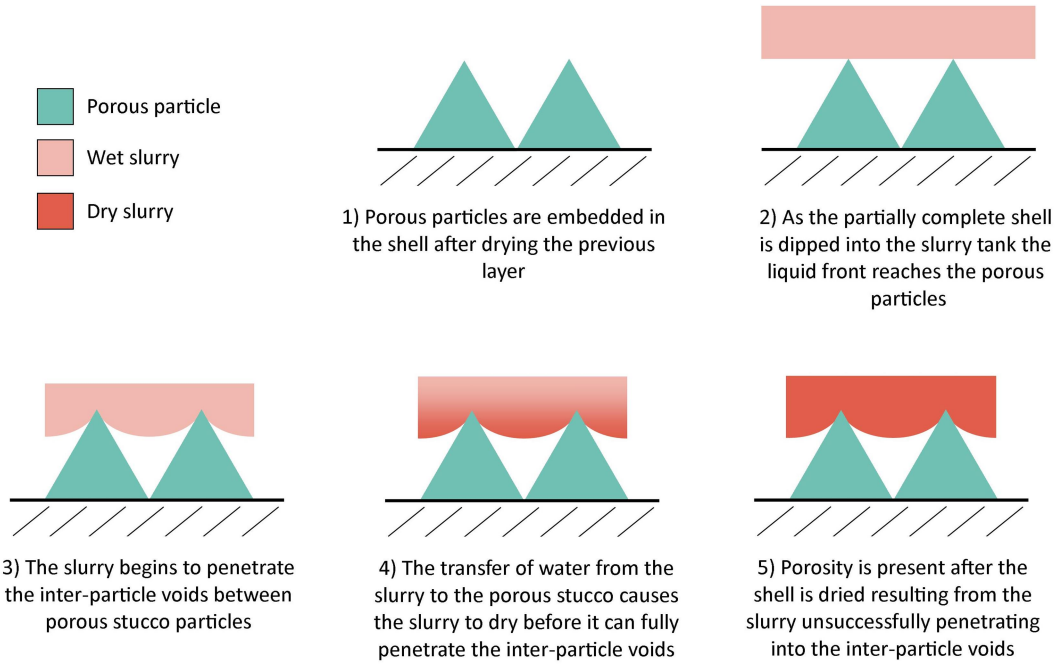



**Figure 49** – Proposed mechanism of porosity generation in shells containing porous stucco resulting from slurry unsuccessfully penetrating into inter-particle voids

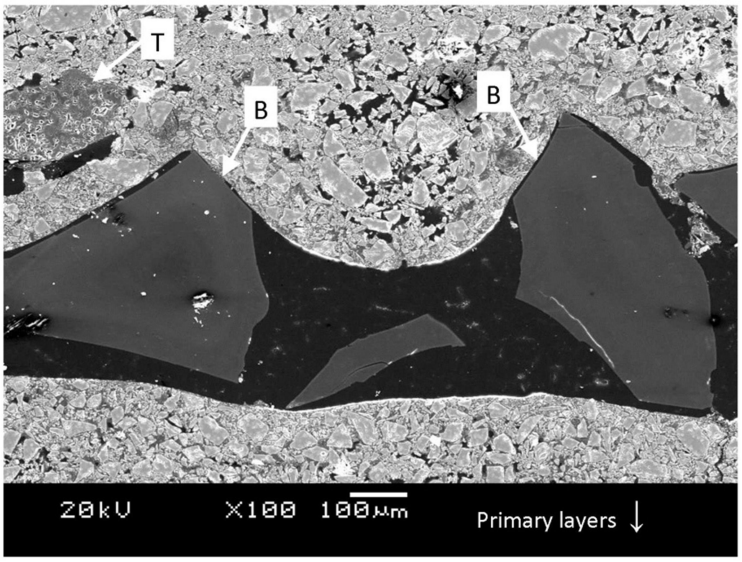



**Figure 50** – BD-$Al_2O_3$ stucco grains embedded in shell displaying behaviour characteristic of slurry drying before penetrating between inter-particle voids. B = BD-$Al_2O_3$ particles, T = Tab-$Al_2O_3$ particles

It is possible the formation of cake surrounding the porous particles (as proposed in Figure 48) contributes to the increase in cumulative mass when redipping the mould in Secondary slurry. This may occur as a thicker layer of slurry is deposited onto the mould resulting from the additional thickness of the cake. However, the formation of porosity between interparticle voids (as proposed in Figure 49) is a competing factor which will result in a reduced cumulative mass. As the cumulative mass measured on a mould containing BD-$Al_2O_3$ was measured to be statistically higher than on a mould containing only Tab-$Al_2O_3$ (Figure 47); it was hypothesised the cumulative effect of the greater volume of slurry and increased water absorption outweighs the effect of porosity generation when coating slurry onto a mould containing BD-$Al_2O_3$.

Consequently, if stucco particles are sufficiently dry in the underlying layers when the mould is redipped in slurry, the slurry may be dried from beneath as water is transferred from the slurry to the unsaturated porous stucco. This conclusion, however, does not necessarily lead to a reduction in drying time as the underlying stucco may become saturated during the dipping process and thus water will not be transferred once the shell is removed from the tank.

## 4.4 Shell Characterisation

### 4.4.1 Scanning Electron Microscopy (SEM)

Scanning electron microscopy was conducted on Shell (Tab-$Al_2O_3$), Shell (BD-$Al_2O_3$) and Shell (SGB127) in both pre-fired and fired condition following the experimental method outlined in Section 3.1.1.7. Analysis was conducted at a range of different magnifications which vary depending on the microstructure being observed.

-All shell cross-sections were taken at 15X magnification.

-Typical particles in the shell were taken at 100X magnification.

-Particle microstructures were taken at:

1000X magnification for both Tab-$Al_2O_3$ and SGB127

1500X magnification for BD-$Al_2O_3$

Each shell cross-section is marked labelling the slurry used within each layer. P represents the Primary slurry, P+1 represents the Primary + 1 slurry and S represents the Secondary slurry. After a greater number of layers are deposited identification becomes more difficult. As such, layer markings are an approximation.

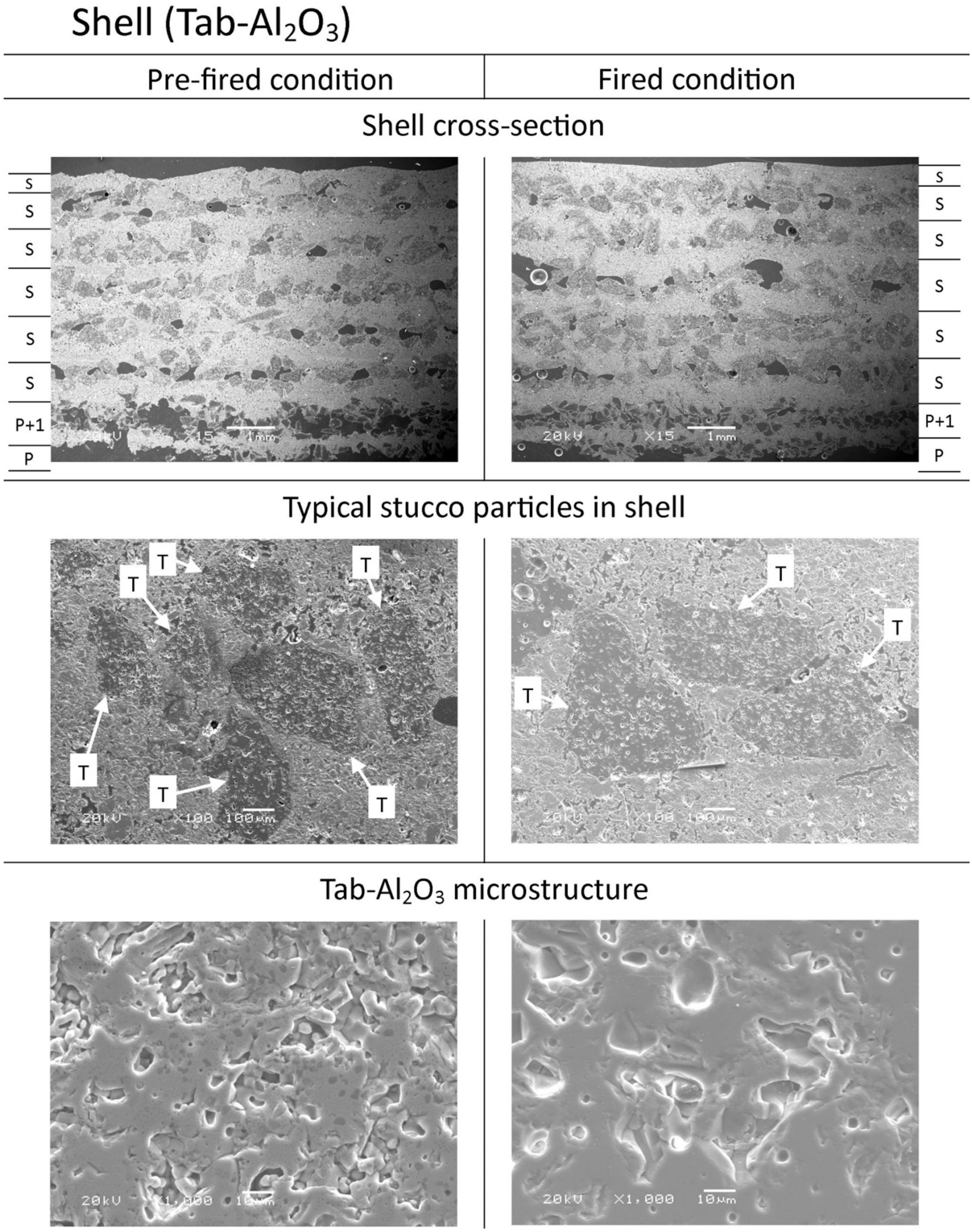



**Figure 51** – SEM analysis of Shell (Tab-$Al_2O_3$) displaying the shell cross-section with the slurry applied in each layer identified. Typical stucco particles in the shell and particle microstructure are shown at greater magnification. T = Individual Tab-$Al_2O_3$ particles

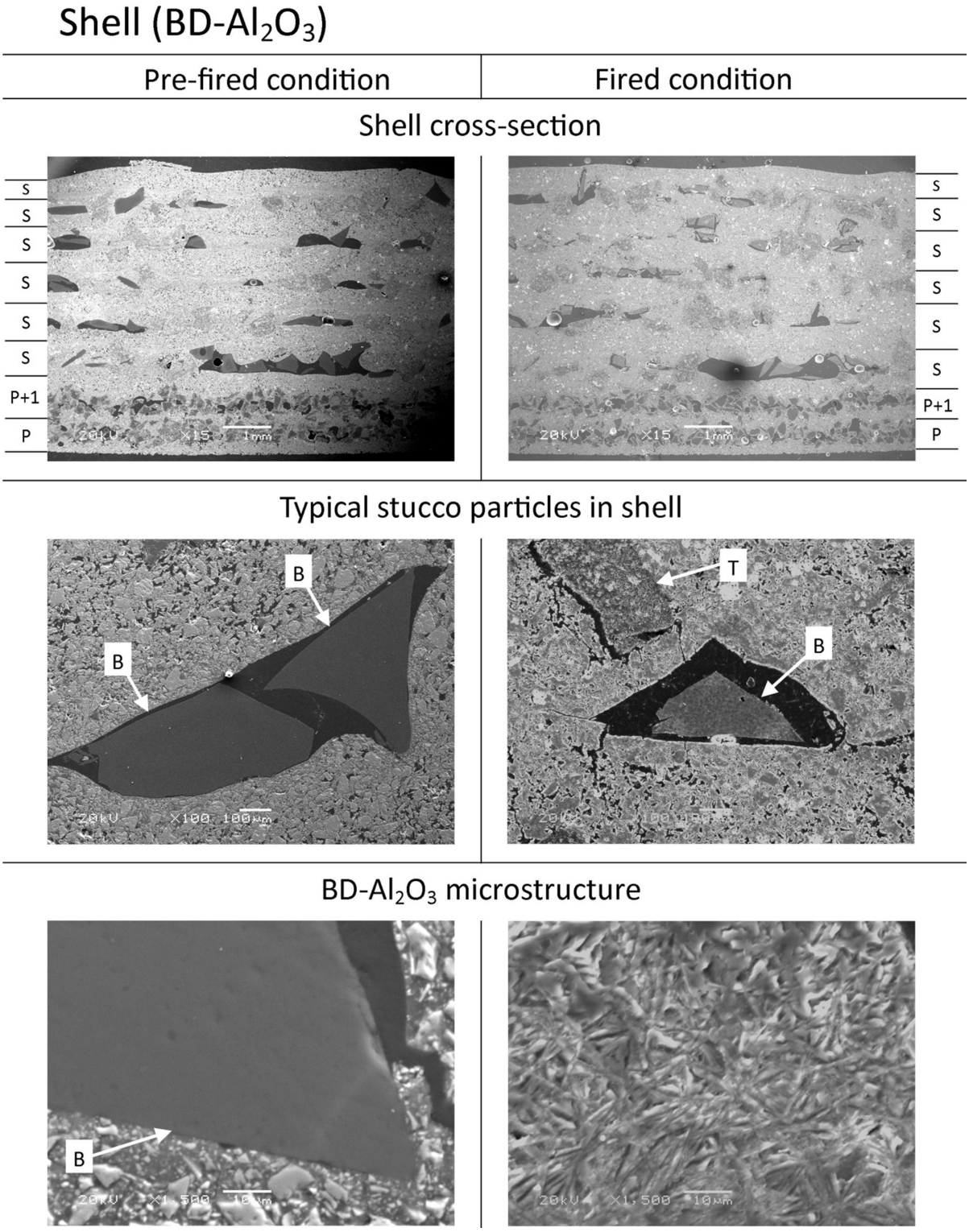



**Figure 52** – SEM analysis of Shell (BD-$Al_2O_3$) displaying the shell cross-section with the slurry applied in each layer identified. Typical stucco particles in the shell and particle microstructure are shown at greater magnification. B = BD-$Al_2O_3$ particles, T = Tab-$Al_2O_3$ particles

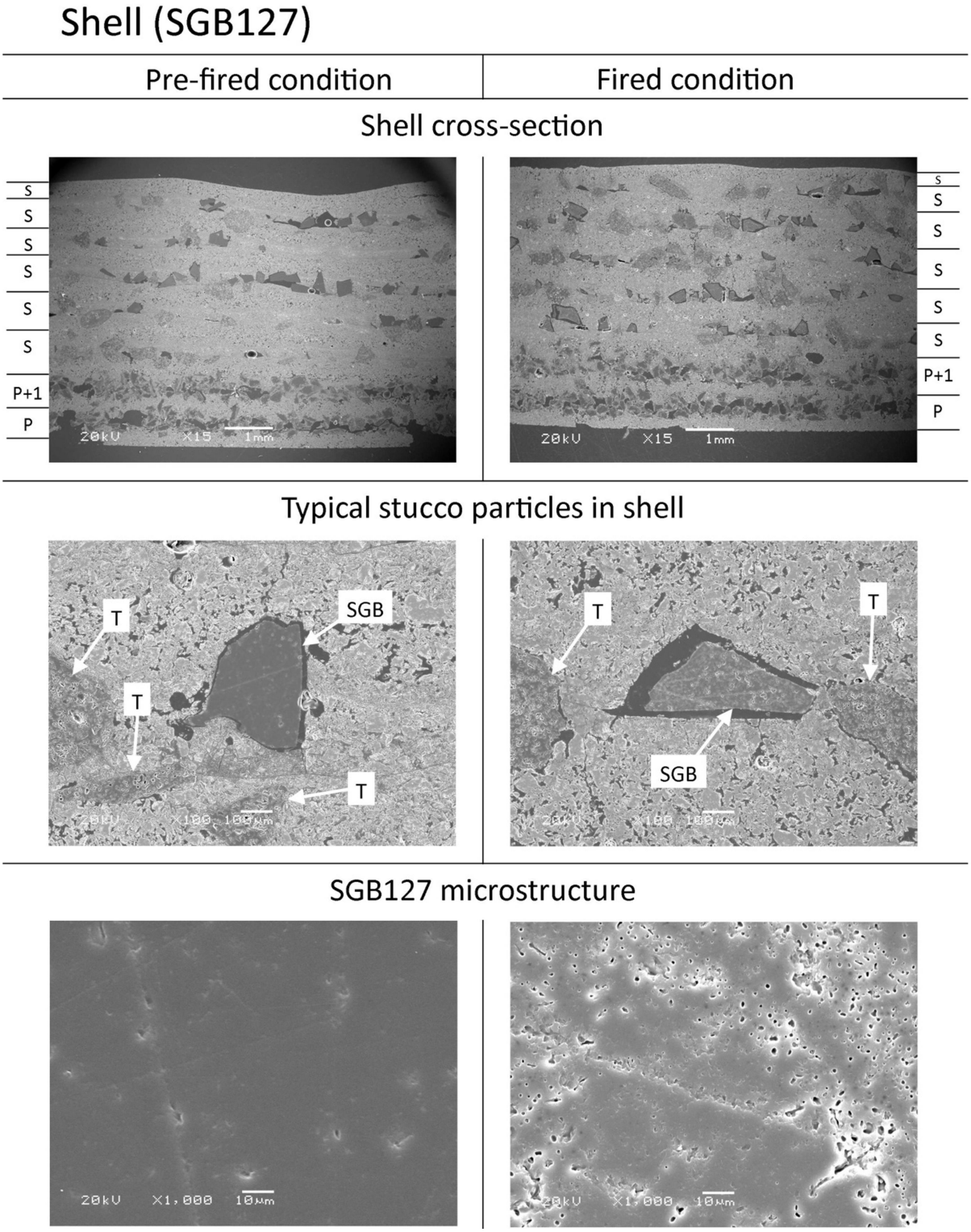



**Figure 53** – SEM analysis of Shell (SGB127) displaying the shell cross-section with the slurry applied in each layer identified. Typical stucco particles in the shell and particle microstructure are shown at greater magnification. SGB = SGB127 particles, T = Tab-$Al_2O_3$ particles

Shell (Tab-$Al_2O_3$) analysis

SEM analysis of Shell (Tab-$Al_2O_3$) is shown in Figure 51. It can be seen that a finer stucco particle size is present in both primary layers in comparison to secondary layers. This can be seen in all shells. Porosity is distributed throughout the shell network with more localised porosity occurring where a multilayer of stucco has been deposited, leading to trapped porosity between grains. The slurry wets out across the stucco particles well, producing a good bond between the slurry and stucco, this results in a high degree of interlocking between neighbouring layers. The bond between the slurry and stucco is maintained following the firing process as the Tab-$Al_2O_3$ particles remain dimensionally stable during the firing cycle.

Shell (BD-$Al_2O_3$) analysis

SEM analysis of Shell (BD-$Al_2O_3$) is shown in Figure 52. BD-$Al_2O_3$ particles can be identified as dark grains with minimal surface features resulting from the fine, porous microstructure that could not be resolved even at 1500X magnification. It can be seen that generally less stucco is present in the secondary layers in comparison to Shell (Tab-$Al_2O_3$) as predicted by analysis of coat weight in Section 4.3.2. It can also be seen that a high degree of porosity typically surrounds the porous particles which results from the slurry drying before it can penetrate between BD-$Al_2O_3$ grains as explained in Section 4.3.2. It could also be argued that as water is absorbed into the BD-$Al_2O_3$ grains during shell manufacture, air is displaced from the material in equal volumes. Consequently, porosity will be produced around the particles if the bubbles cannot permeate to the surface of the slurry during shell manufacture. As a result of both of these mechanisms a poor degree of wetting is present on the surface of BD-$Al_2O_3$ particles which is amplified when a large concentration of such particles exist adjacent to each other. When this occurs, a poor amount of interlocking between neighbouring layers takes place as the slurry seemingly sits on top of the porous stucco. The bond between the BD-$Al_2O_3$ particles and slurry is reduced further upon firing where it can be observed the particles experience high volumetric contraction as observed by TMA in Section 4.2.6. This leads to the BD-$Al_2O_3$ particles pulling away from the slurry matrix leaving a cavity of similar shape and size to the original particle, inside which the densified grain resides. Additionally, the presence of crescent voids can be seen surrounding

Tab-$Al_2O_3$ particles after firing which were not observed in Shell (Tab-$Al_2O_3$). It was hypothesised this defect resulted from the slurry matrix densifying in regions exhibiting less constraint; such regions may develop due to the formation of voids as BD-$Al_2O_3$ particles contract. Alternatively, variation in matrix density prior to firing may explain such defects. This may take place as fine particles filter through coarse particles when liquid is transferred from the slurry to the porous stucco in a mechanism similar to clogging in slip casting of ceramics which leads to inhomogeneous packing [153].

Shell (SGB127) analysis

SEM analysis of Shell (SGB127) is shown in Figure 53. Particles can be identified as dark grains with minimal surface features similar to BD-$Al_2O_3$. A greater level of adhesion between the stucco and slurry can be seen in comparison to Shell (BD-$Al_2O_3$). This was likely due to the pores in SGB127 material remaining saturated after absorbing water from the slurry as predicted by DVS analysis in Section 4.2.5. As such, it would be expected that when depositing slurry the underlying SGB127 stucco will absorb less water than BD-$Al_2O_3$ particles. Consequently, only a small quantity of water would be expected to transfer from the slurry to the underlying stucco, permitting the slurry to penetrate inter-particle voids without drying and producing fewer bubbles from displacement of air with liquid. This explains the greater adhesion between the slurry and SGB127 particles in comparison to BD-$Al_2O_3$ particles.

It was also observed that the presence of foaming in SGB127 material as predicted by TMA in Section 4.2.6 was predominantly absent. This was likely due to the much smaller grain size of the stucco embedded in the shell in comparison to the as received spherical samples analysed by TMA. As such, water evolved from dehydration and condensation reactions in the bulk diffuses more efficiently in the smaller grains leading to densification rather than foaming upon firing. There were, however, a few select grains found which displayed a structure resembling foaming as shown in Figure 54. It can be seen that this grain appears to have expanded into a void forming a flush seam between the particle and the slurry along the top right face. This behaviour was not observed in most SGB127 particles which appear to densify and shrink away from the slurry matrix. In addition, the crescent void defect

observed in Shell (BD-$Al_2O_3$) surrounding Tab-$Al_2O_3$ particles can be seen in Shell (SGB127). This was once again hypothesised to be the result of either densification into regions of less constraint or variation in the density of the slurry matrix prior to firing.

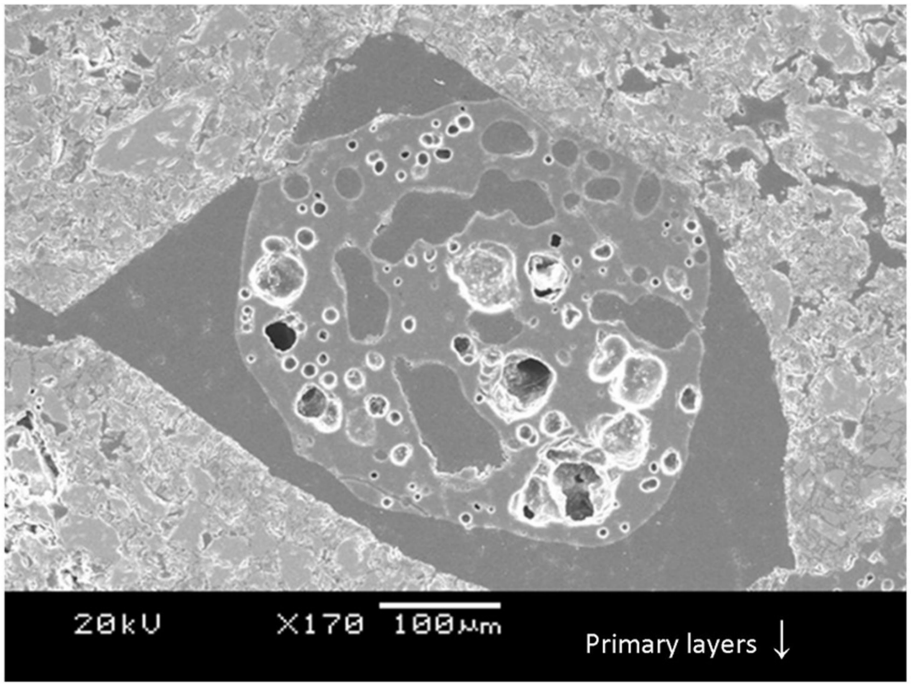



**Figure 54** – Evidence of foaming in Shell (SGB127) in fired condition

### 4.4.2 Archimedes' Porosity

The bulk density and open porosity of each shell in both pre-fired and fired shells was calculated using Archimedes' method as described in Section 3.1.1. This was undertaken to observe the change in material properties when firing shells in the simulated casting cycle. This method is useful for analysing multicomponent samples where a representative value can be attained for a large quantity of material in contrast to other analysis methods such as nitrogen adsorption or mercury porosimetry where small volumes of sample are used. Limitations for this method include gauging how much excess liquid to remove when measuring the saturated weight which can lead to variability between samples. Additionally, larger pores are emptied preferentially in comparison to smaller pores as water is transferred to smaller pores via capillary action. Therefore, the method is effectively measuring the slurry matrix and embedded particles excluding the millimetre sized pores often found around the porous stucco. This method cannot measure closed porosity resulting from trapped pores.

Bulk density

The bulk density of Shell (Tab-$Al_2O_3$), Shell (BD-$Al_2O_3$) and Shell (SGB127) is displayed in Figure 55 for samples in both pre-fired and fired condition. Analysis shows minimal variation between each shell as a result of the large concentration of zircon in each shell dominating the bulk density for each sample. Greater error is present for Shell (BD-$Al_2O_3$) in comparison to Shell (Tab-$Al_2O_3$) and Shell (SGB127) which may result from incomplete draining of large inter-particle voids (as shown in Figure 49). The error in this measurement will be transferred to later calculations for open porosity later in this Section.

It can be see that all shell samples display an increase in bulk density upon firing which results from densification and sintering in the shell matrix and stucco particles. However, samples containing porous stucco show a greater increase in bulk density after firing in comparison to Shell (Tab-$Al_2O_3$). This is likely due to the porous stucco densifying considerably during the firing cycle whilst the Tab-$Al_2O_3$ particles remain unmodified due to the high temperature stability of the material. However, this effect may also be the result of the slurry matrix densifying to a greater degree in Shell (BD-$Al_2O_3$) or Shell (SGB127) in comparison to Shell (Tab-$Al_2O_3$).

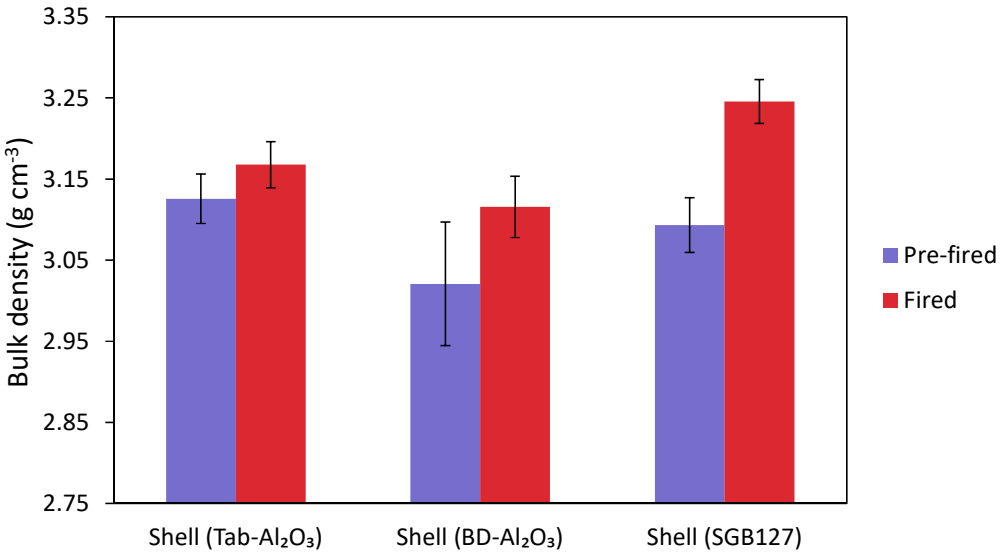



**Figure 55** – Bulk density of shells in pre-fired and fired condition

It was also observed that following the firing process, Shell (SGB127) attains a statistically higher bulk density than Shell (Tab-$Al_2O_3$) when conducting a t-test at 95 % confidence level. This was unexpected following the observation by helium pycnometer analysis in Section 4.2.4 that the true density of SGB127 grains (2.25 g $cm^{-3}$) is less than Tab-$Al_2O_3$ grains (3.76 g $cm^{-3}$). As such, it would be expected that even if the SGB127 grains fully densified in the firing cycle the bulk density of the system would not reach that of Shell (Tab-$Al_2O_3$). One explanation for this phenomenon is the densification of the slurry matrix in Shell (SGB127) leads to an increase in bulk density which outweighs the effect of the less dense stucco present.

Open porosity

The open porosity of Shell (Tab-$Al_2O_3$), Shell (BD-$Al_2O_3$) and Shell (SGB127) is displayed in Figure 56 for samples in both pre-fired and fired condition. It can be seen that a noteworthy decrease in porosity can be seen between pre-fired and fired specimens resulting from sintering and consolidation mechanisms occurring within the slurry matrix and stucco which is more prominent in shells containing porous stucco. However, due to the numerous components in the system it was impossible to determine to what extent the reduction in porosity was the result of stucco or slurry consolidation. Once more, evidence for enhanced slurry densification in Shell (SGB127) can be seen as a statistically lower open porosity in fired condition is present in comparison to Shell (Tab-$Al_2O_3$) when conducting a t-test at 95 %.

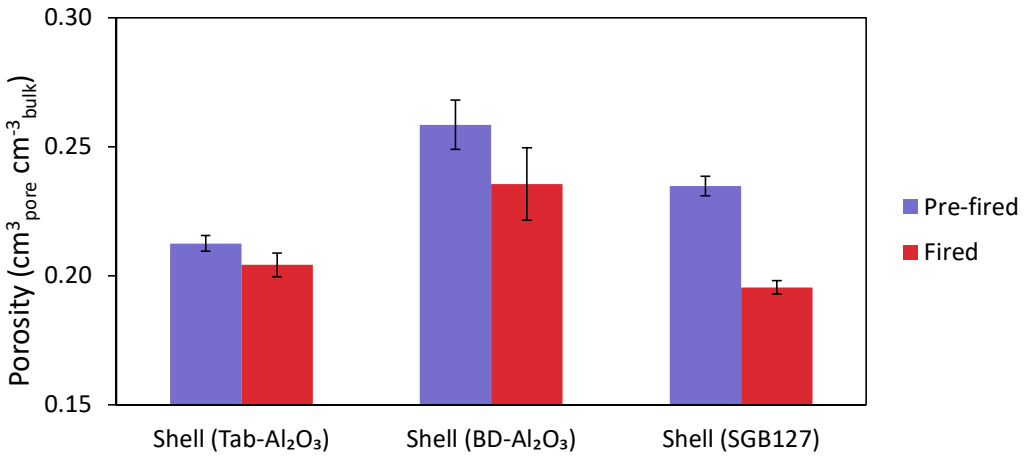



**Figure 56** – Open porosity of shells in pre-fired and fired condition

### 4.4.3 Flexural Strength

The flexural strength of Shell (Tab-$Al_2O_3$), Shell (BD-$Al_2O_3$) and Shell (SGB127) was measured in ambient conditions via 3 point bend loading as described in Section 3.1.6.1. Shells were tested in green, pre-fired and fired condition in ambient conditions to assess the flexural strength observed at different stages of the investment casting process when substituting Tab-$Al_2O_3$ for porous stucco blends.

In the green state, shell bars are reinforced by residual wax which has penetrated into pores as a result of dewaxing the shell in the autoclave. This effect has been shown to give a marginal increase in strength as the wax supports load when tested at ambient temperature [154]. In pre-fired condition the residual wax has been removed along with the reinforcement effect however, polycondensation and dehydration reactions take place between the colloidal silica species strengthening the siloxane network [135]. Firing the shell causes inorganic species to sinter, creating intimate contact and a high degree of adhesion between particles which subsequently raises the strength further. The flexural strength of shells in green, pre-fired and fired condition is shown in Figure 57.

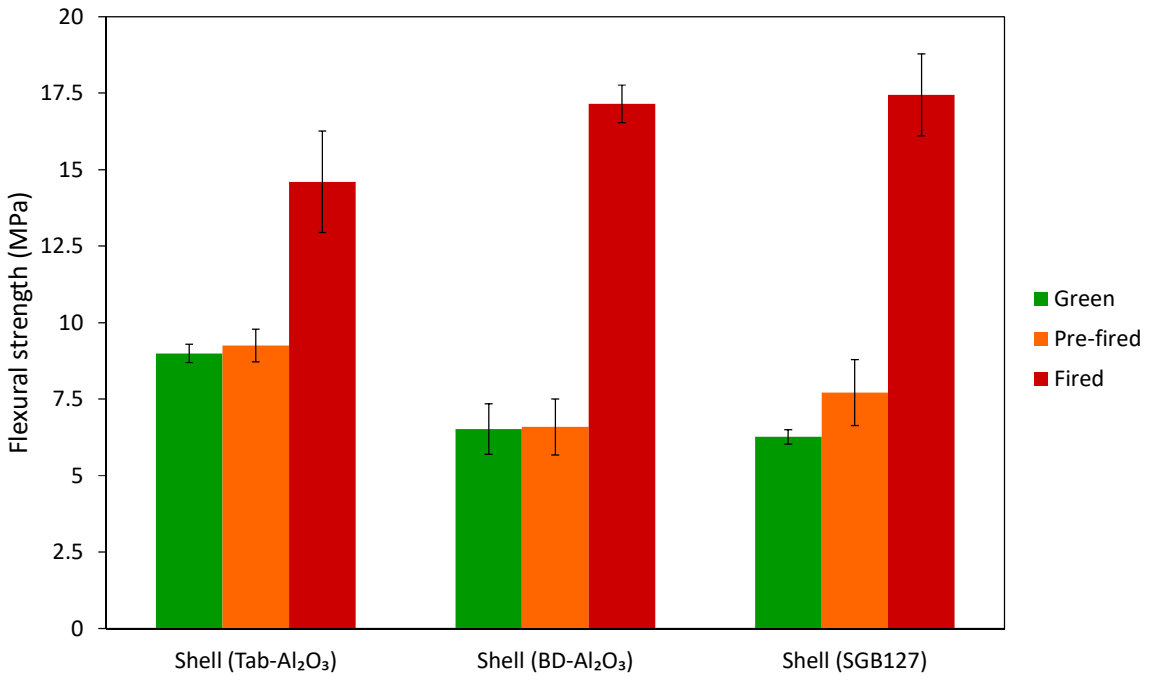



**Figure 57** – Flexural strength of Shell (Tab-$Al_2O_3$), Shell (BD-$Al_2O_3$) and Shell (SGB127) in green, pre-fired and fired condition tested in ambient conditions

Green strength

It can be seen that a reduction in flexural strength occurs in Shell (BD-$Al_2O_3$) and Shell (SGB127) in comparison to Shell (Tab-$Al_2O_3$) which is equal to 28 % and 30 % respectively. The weakening of the shell system was expected due to the high degree of porosity observed in the shells containing porous stucco leading to large volumes in the shell which do not support load and introduce large flaw sizes. The relationship between porosity and flexural strength has been observed in alumina, zirconia and SiC ceramics [155, 156]. Such behaviour was also observed when incorporating nylon fibres [30], needle coke additives [32] and super absorbent polymers [5] into investment casting moulds where a reduction in flexural strength was observed upon burning out organic material due to the increase in porosity.

Pre-fired strength

The flexural strength in pre-fired condition shows similarities to the results obtained for green strength showing a reduction of 29 % and 17 % for Shell (BD-$Al_2O_3$) and Shell (SGB127) respectively in comparison to Shell (Tab-$Al_2O_3$).

Fired strength

Following the simulated firing cycle, porous stucco particles contract as shown by SEM analysis in Section 4.4.1. This leads to the formation of large voids within the slurry matrix. It was therefore expected that the generation of large voids in a shell system already displaying a high degree of porosity would display a further reduction in strength in comparison to Shell (Tab-$Al_2O_3$) upon firing, however, the opposite was observed. Shell (BD-$Al_2O_3$) and Shell (SGB127) show an increase in flexural strength equal to 17 % and 19 % respectively in comparison to Shell (Tab-$Al_2O_3$). Both shells containing porous stucco show a statistically higher mean difference in comparison to Shell (Tab-$Al_2O_3$) when conducting a t-test at 95 % confidence. This indicates that the presence of porous stucco has caused a change in the structure of the shell in such a way as to lead to an increased flexural strength. Unfortunately, an increase in fired flexural strength can lead to strain induced

recrystallisation of the cast component upon cool down from casting temperatures leading to post-solidification grain defects. Strain is induced upon cooling as the metal contracts at a higher rate in comparison to the shell and sections of the cast component that are restricted from contracting due to the component's geometry experience plastic deformation. If this plastic deformation exceeds 1.5 %, recrystallisation occurs within CMSX-4 alloy [14] to relieve internal strain energy following solution heat treatment. This produces a new grain in a different orientation to the single crystal to reduce strain [157]. It has been demonstrated that stiffer shells promote greater plastic strain in the cast component; this results from higher stresses acting on the metal during cooling due to less elastic deformation in the rigid shell [158].

A possible explanation for the increased fired strength is the formation of a denser slurry matrix in the secondary layers resulting from the porous stucco shrinking and allowing the zircon and silica matrix to densify more freely. Evidence for this was proposed in Section 4.4.2 where an increased bulk density and decreased porosity was observed in Shell (SGB127) in comparison to Shell (Tab-$Al_2O_3$). Minor increases in bulk density have been shown to significantly increase mechanical properties as a result of necking and increased coordination number between particles [159].

### 4.4.4 Observation of Deformation

During the shell manufacturing process it was observed that shells containing porous stucco exhibited flexural deformation after the simulated casting cycle when samples were placed primary layers down against the furnace floor. This was not observed in shells containing only non-porous stucco. A representative magnitude of flexural deformation for each shell following the simulated casting cycle is shown in Figure 58. The presence of this deformation translates to unwanted dimensional changes within the mould, leading to the production of a cast component which would be out of specification due to the stringent dimensional tolerances set on turbine blade components.

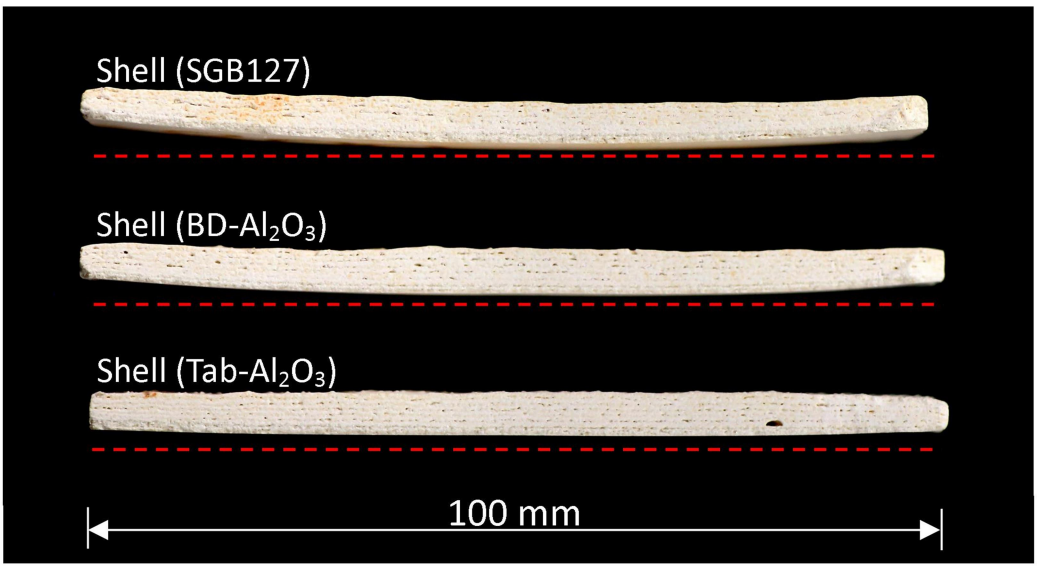



**Figure 58** – Observation of a greater magnitude of flexural deformation in shells containing porous stucco than non-porous stucco following the simulated casting cycle. Dashed lines indicate the side of the shell coated with Primary slurry and highlight the curved nature of the shells

It was proposed that this phenomenon occurs because the shrinkage experienced by the secondary layers containing porous stucco is greater than the primary layers containing non-porous stucco during the firing cycle. This leads to the formation of curvature due to the difference in the degree of thermal contraction between layers following the firing cycle. This phenomenon was not observed in typical shell bars containing only Tab-$Al_2O_3$ in secondary layers presumably because of the similarity in the amounts of shrinkage present in both primary and secondary layers containing non-porous stucco. Evidence for this hypothesis is corroborated by the observation that shells containing porous stucco attain a higher bulk density and fired strength in comparison to shells containing only non-porous stucco as shown in Sections 4.4.2 and 4.4.3 respectively. Both of these observations appear to show densification of the slurry matrix when porous stucco is incorporated. Further evidence for this hypothesis is provided in Chapter 5.

### 4.4.5 Reducing Drying Times

#### 4.4.5.1 Photography Analysis

The effectiveness of 60 vol% porous stucco blends at reducing the drying time between Secondary slurry dips during shell manufacture was compared to Tab-$Al_2O_3$. Shells were prepared on wax patterns of dimensions 130 x 100 x 20 mm coated in P $(FusedAl)_2$ and P+1 $(FusedAl)_2$ layers (notation described in Section 3.1.3) before applying five secondary layers and a seal coat at either 2, 1.5, 1.25, 1.0, 0,75 or 0.5 hours drying time between dips. Once shell manufacture was complete, the shells were left drying for 24 hours before recording the surface of the shell optically.

Tab-$Al_2O_3$ analysis

The effect of reducing the drying time between Secondary slurry dips for shells containing 100 vol% Tab-$Al_2O_3$ in secondary layers is shown in Figure 59. It can be seen that only a slight deviation from the 2 hour drying time results in cracking on the surface. Reducing the drying time between dips below 1 hour produces moulds which display slumping as slurry insufficiently dried in previous layers is removed by the weight of the subsequently applied layer. As such, shells with a drying time of 0.75 or 0.5 hours between dips could not be completed and thus are not shown in Figure 59.

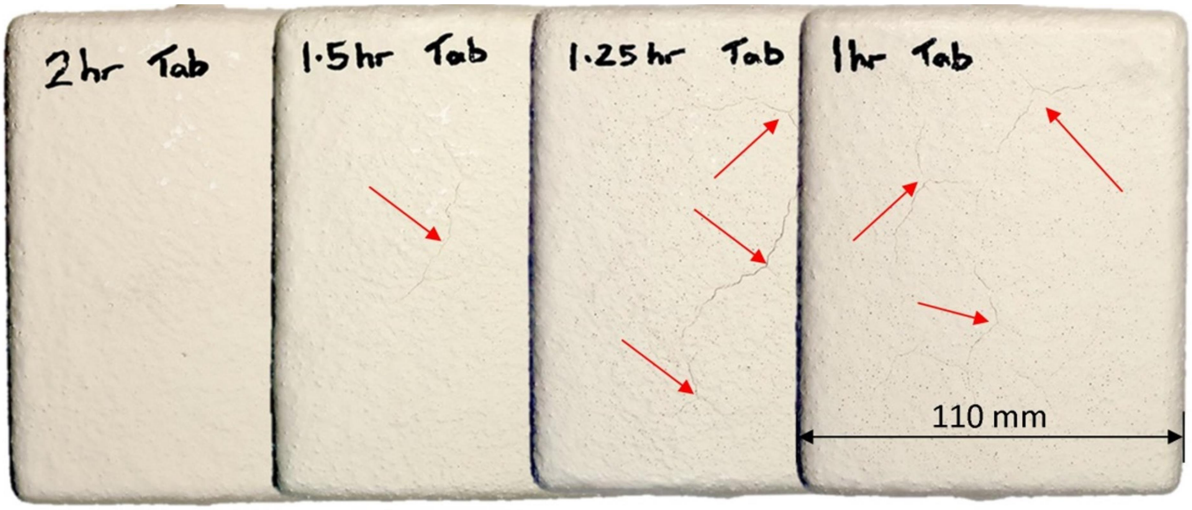



**Figure 59** – Shells containing 100 vol% Tab-$Al_2O_3$ in secondary layers showing the formation of cracks when reducing the drying time between Secondary slurry dips from 2 hours to 0.5 hours. Reducing the drying time between dips below 2 hours causes failure

BD-$Al_2O_3$ analysis

The effect of reducing the drying time between Secondary slurry dips for shells containing 60 vol% BD-$Al_2O_3$ in secondary layers is shown in Figure 60. It was observed that shells remain whole up until the drying time is reduced to 0.75 hours, at which time major cracking was observed. This demonstrates that the porous stucco works effectively at removing water from the slurry and thus the sample requires less water volume to be removed through evaporation. As such, the drying time can be reduced to 1 hour, a 50 % reduction in comparison to using non-porous stucco. This finding however is not as substantial as when applying SAP which can reduce the drying time to 2 % [65]. On the other hand, the use of SAP incurred problems with burnout of organic polymer and required a slower firing rate which was not found to be an issue in this system.

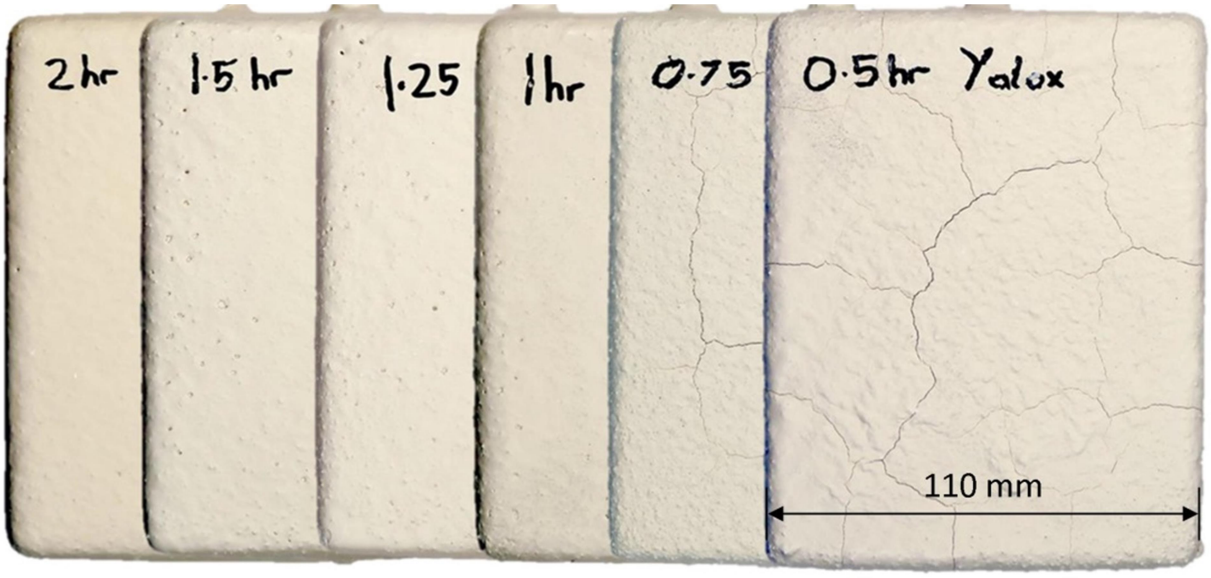



**Figure 60** – Shells containing 60 vol% blended BD-$Al_2O_3$ stucco in secondary layers showing the formation of cracks when reducing the drying time between Secondary slurry dips from 2 hours to 0.5 hours. Reducing the drying time between dips below 1 hour causes failure

SGB127 analysis

The effect of reducing the drying time between Secondary slurry dips for shells containing 60 vol% SGB127 in secondary layers is shown in Figure 61. It can be seen that (in the same manner as shells containing 60 vol% BD-$Al_2O_3$) shells remain whole up until the drying time was reduced to 0.75 hours at which time major cracking is observed. This result was surprising as SGB127 has been characterised to have a lower volumetric porosity with a greater fraction of pores filled with water in the conditions of the shell room in comparison to BD-$Al_2O_3$. As such, it would be expected that shells containing BD-$Al_2O_3$ would enable a greater reduction in drying time in comparison to shells containing SGB127, however, this was not observed. The mechanism of drying is explored in Chapter 7 to provide an explanation to this phenomenon.

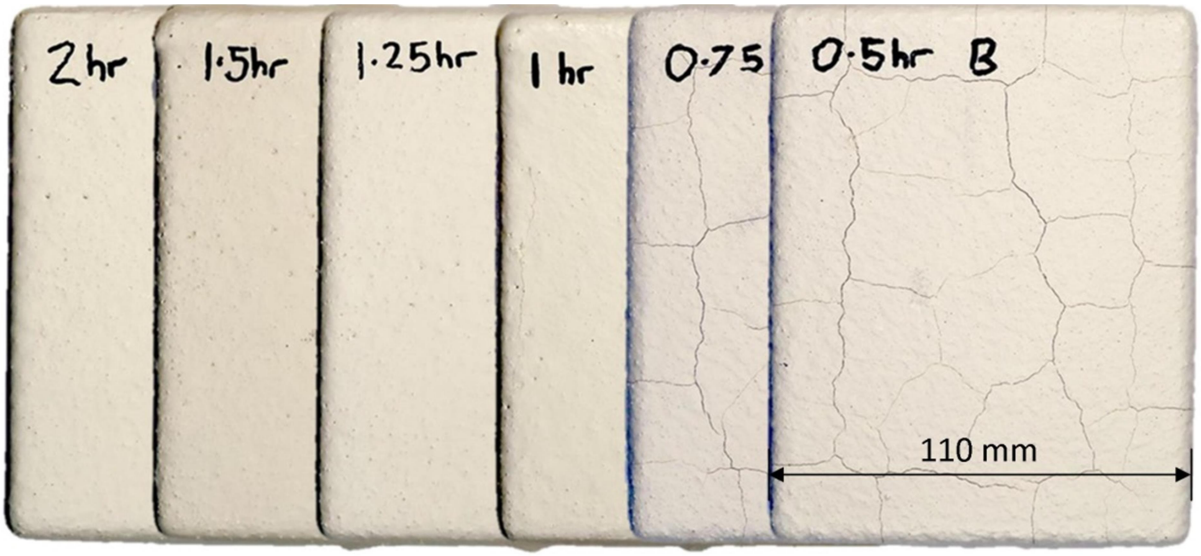



**Figure 61** – Shells containing 60 vol% blended SGB127 stucco in secondary layers showing the formation of cracks when reducing the drying time between Secondary slurry dips. Reducing the drying time between dips below 1 hour causes failure

4.4.5.2 Flexural Strength

Shells which remained whole after reducing the drying time in Section 4.4.5.1 were taken for flexural strength analysis at ambient conditions in the green state. This was undertaken to observe if the strength of the shell was compromised by the accelerated drying process. The results are shown in Figure 62.

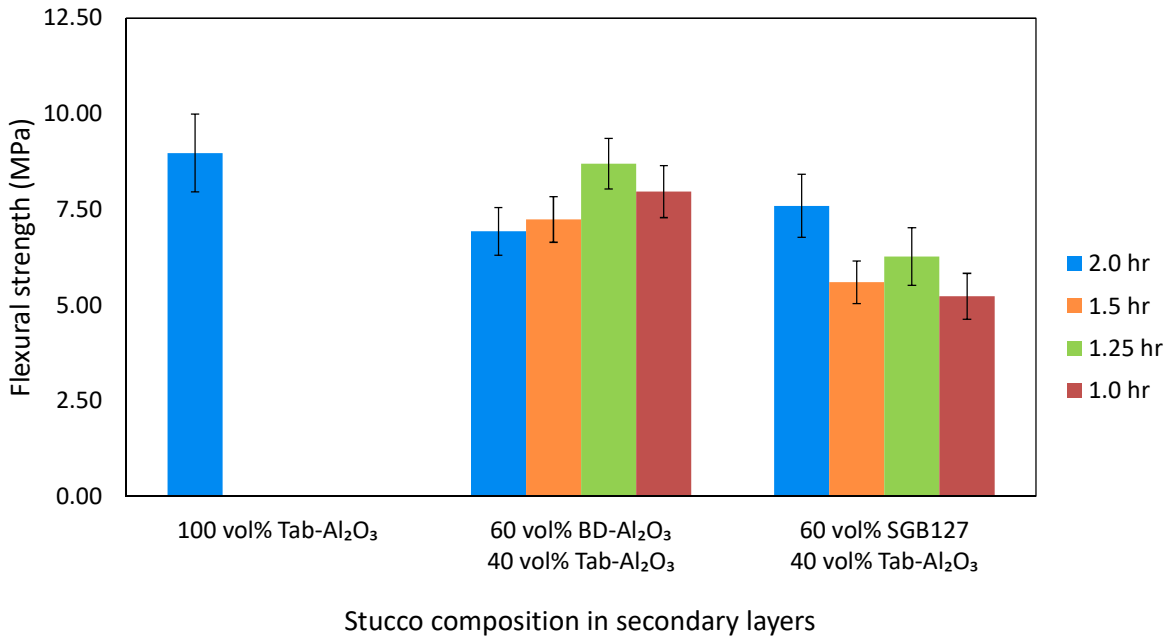



**Figure 62** – Flexural strength of shell bars in green state after varying the drying time in secondary layers tested in ambient conditions

BD-$Al_2O_3$ analysis

It was observed that for shells containing BD-$Al_2O_3$ a potential increase in flexural strength can be gained by reducing the drying time. A possible explanation for this occurrence is that longer drying periods progressively dry out the porous stucco embedded in the shell. The drier the stucco particles are, the more porosity will be introduced to the shell through the formation of bubbles in the slurry as particles absorb water and displace air or alternatively cause the slurry to dry before it can penetrate between inter-particle voids. Therefore, shorter drying periods between dips will introduce less porosity and more adhesion between the slurry and stucco particles explaining the possible increase in green strength observed with shorter drying times

SGB127 analysis

Shells containing SGB127 appear to show an opposite trend in comparison to shells containing BD-$Al_2O_3$ whereby reducing the drying time leads to a reduction in green strength. This can be explained due to the fact that SGB127 particles require a low $R_H$ to

desorb moisture (as shown by DVS in Section 4.2.5) and thus the particles embedded in the mould remain mostly saturated even after extended drying periods in the environmental conditions of the drying chamber. Therefore, the same level of saturation in SGB127 particles was expected at all drying times. Subsequently, the mechanism used to explain the increased flexural strength when using BD-$Al_2O_3$ particles does not apply as the underlying SGB127 particles were expected to remain saturated.

The reduction in strength is likely due to the incomplete drying of layers which contain a greater moisture concentration with further reduction in drying times. This leads to the formation of micro-cracking as contraction of the partially dry layers takes place during the final drying period which reduces the flexural strength of the shell. The 30 – 40 % reduction in green strength observed for shells dried for 1 – 1.5 hours between slurry coats is below the minimum strength requirement for handling in the shell environment.

## 4.5 Conclusions

In this Chapter the use of monolithic porous silica and alumina grains have been successfully implemented as stucco into the manufacture of investment casting moulds without modification to autoclave or procedures. It has been shown that a blend of less than 60 vol% porous stucco needs to be applied in order to form an acceptable coverage with sufficient adhesion between the particles and the slurry surface. Using a 60 vol% blend of porous stucco a reduction in drying time of 50 % can be achieved, halving the time required to dry each layer from two hours to one hour. However, this was attained at the expense of green and pre-fired strength which were reduced significantly. This was attributed to high levels of porosity present in shells containing porous stucco. It was hypothesised that the greater quantity of porosity arises from the slurry drying before it can penetrate inter-particle gaps and the formations of bubbles as water displaces with air from the porous particles embedded in underlying layers upon absorption. Additionally, an increased fired strength was observed in shells containing porous stucco. This has been attributed to the densification of the slurry matrix as a result of the porous stucco shrinking in the firing cycle, allowing the zircon and silica matrix to sinter more freely in the secondary layers. It was hypothesised that as a result of this mechanism, flexural deformation occurs as the

secondary layers shrink to a greater degree than the primary layers. This undesirable deformation cannot be tolerated due to the high dimensional accuracy required for the mould. Consequently, any reduction in drying time attained by using porous stucco is voided by the detrimental effect of deformation which accompanies its use. As such, further investigation was conducted to understand why the flexural deformation occurs upon firing and how to prevent dimensional change for moulds containing porous stucco.

# 5. Investigation into Flexural Deformation

## 5.1 Introduction

In this chapter the magnitude of flexural deformation occurring in investment casting shells is quantified throughout the simulated casting cycle with evidence provided as to why deformation occurs more dominantly in shells containing porous stucco. The aim of this work was to understand the mechanism of deformation in order to find a solution to allow porous stucco to be incorporated into the shell system without causing detrimental deformation to the shell upon firing.

## 5.2 Thermal Expansion/Contraction of Shell Components

In order to better understand the thermal expansion/contraction traces of multicomponent shell samples, the constituent materials of slurry components (zircon powder and silica binder) were analysed individually. Sample preparation of silica binder was carried out by filling a petri dish with liquid binder then leaving the sample to dry at room temperature for four days. After this time period a semi-transparent solid was formed which had cracked in many areas. The material was then removed from the petri-dish and fired in the pre-fire cycle and cut into a shape approximating a cylinder 5 mm in length and 6 mm in diameter. This sample was then analysed in the TMA under the simulated casting cycle.

Sample preparation of zircon powder was carried out by preparing an 80 wt% slurry with deionised water and drying the sample in a petri dish at room temperature for two days. After this time period a solid body was formed which required fracturing to remove from the petri dish. Firing the zircon sample in the pre-firing cycle yielded a weak powder not suitable for TMA and as such the temperature was raised to partially sinter the powder. It was found that the lowest temperature to sufficiently consolidate the powder was 1250 ˚C, holding at temperature for 1 hour with 10 ˚C $min^{-1}$ heating and cooling rates. Following this treatment the sample had sufficient strength to be tested on the TMA, but densification was limited to allow observation of further sintering behaviour. The material was then and cut into a shape approximating a cylinder 5 mm in length and 6 mm in diameter. This sample was then analysed in the TMA under the simulated casting cycle.

The expansion/contraction profile of Binder P, Binder S and zircon analysed throughout the simulated casting cycle is shown in Figure 63, averaged for three repeat samples. The average quantity of shrinkage experienced by each sample following the firing cycle is displayed in Table 12 in addition to the thermal expansion coefficient up to 700 ˚C. Additionally, the sintering onset temperature was measured for each sample by recording the temperature at which the thermal trace deviated from linear thermal expansion. The average sintering onset temperature for each sample is displayed in Table 13.

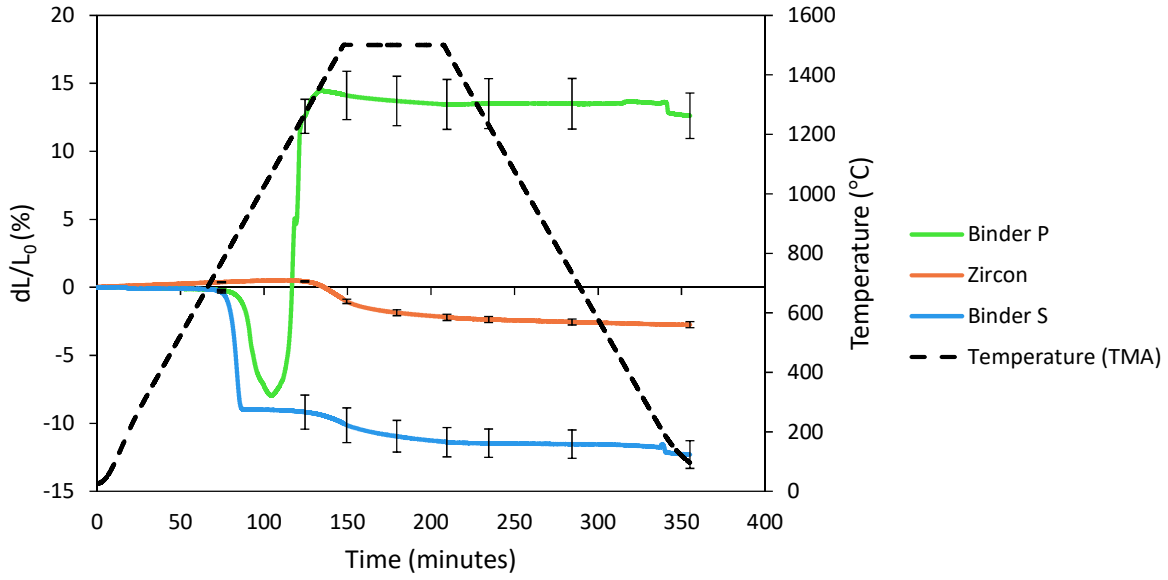



**Figure 63** – Thermal expansion/contraction of slurry components analysed throughout the simulated casting cycle conducted by TMA

**Table 12** – Linear shrinkage of samples following the entire simulated casting cycle and linear thermal expansion coefficients measured from 50 – 700 ˚C conducted by TMA

| Sample | Linear shrinkage (%) | | Linear thermal expansion coefficient from 50 – 700 ˚C ($10^{-6}$ $K^{-1}$) | |
|---|---|---|---|---|
| | Average | Standard deviation | Average | Standard deviation |
| Binder P | -12.62 | 1.67 | -2.23 | 0.297 |
| Binder S | 12.29 | 1.02 | -1.83 | 0.825 |
| Zircon | 2.74 | 0.21 | 4.73 | 0.621 |

**Table 13** – Sintering onset temperatures for shell components conducted by TMA

| Sample | Sintering onset temperature (˚C) | |
|---|---|---|
| | Average | Standard deviation |
| Binder P | 771 | 9.8 |
| Binder S | 724 | 20.8 |
| Zircon | 1039 | 24.3 |

Binder S

Binder S initially shows negative thermal expansion indicative of dehydration and polycondensation reactions taking place. At approximately 720 ˚C substantial shrinkage occurs; as such it was proposed viscous sintering occurs in the amorphous material at this temperature. As the sample reaches 1000 ˚C an abrupt decrease in shrinkage can be seen which is characteristic of the pore structure collapsing as identified by Brinker et al. in silicate glass systems [160]. Raising the temperature further, a secondary contraction can be seen. This may arise from viscous flow as the material softens approaching the melting point of silica (1726 ˚C [161]), aided by the presence of $Na_2O$ stabilising agent in the material which promotes softening at lower temperatures [162]. Alternatively, the secondary contraction may result from devitrification as a volumetric contraction accompanies the phase transition from amorphous silica to cristobalite due to a change in phase density [163]. Upon cool down at approximately 200 ˚C, a sharp shrinkage transition can be seen which is associated with the β to α cristobalite phase change [152].

Binder P

Binder P shows similar thermal expansion/contraction characteristics to Binder S up until approximately 1070 ˚C at which point rapid expansion occurs, similar to foaming observed in SGB127 material by TMA in Section 4.2.6. As such, it was proposed that dehydration and polycondensation reactions occur up until approximately 770 ˚C at which point viscous sintering occurs resulting in substantial shrinkage. This is followed by a rapid expansion resulting from pressure build up in the bulk causing the material to foam as evolving gasses cannot permeate to the surface [143]. As the silica binder is finely distributed within the

slurry matrix it would be expected that foaming behaviour does not occur as the evolving gasses can diffuse to a surface more easily. As such, material properties measured by TMA in excess of 1070 ˚C are likely unrepresentative of the behaviour occurring within the shell.

Zircon

The zircon sample shows positive thermal expansion up until approximately 1040 ˚C. It was proposed that at this temperature solid state sintering occurs in the crystalline material leading to the observed shrinkage. This may be accelerated by impurities located either within the crystal structure or on the surface which act as a liquid phase sintering aid [25]. It can be seen the sintering rate for zircon is much slower than dried colloidal silica. This likely occurs due to the larger particle size and higher melting temperature of zircon powder (approximately 2500 ˚C [24]) in comparison to silica (1726 ˚C [161]). Consequently, it would be expected that fusing zircon particles requires more energy as a smaller driving force for sintering is present with less mobility for mass transport. However, the specific pathway of mass transport also plays a role in the sintering rate and onset temperature [99]. In addition, it has been shown zircon undergoes thermal dissociation to form zirconia and silica at 1500 °C which can hinder the sintering process [25]. Due to the high melting temperature of zircon and minimal force applied during analysis it was expected that the majority of the contraction was the result of sintering as opposed to creep. As contraction can be seen up until the end of the isothermal hold period it was concluded that the zircon sample remains partially sintered after the full firing cycle.

## 5.3 Thermal Expansion/Contraction of Shell Layers

In Section 4.4.4 it was proposed that flexural deformation occurs upon firing more noticeably in shells containing porous stucco in secondary layers due to variation in the degree of shrinkage between secondary layers containing porous stucco and primary layers containing non-porous stucco. To test this hypothesis, the shell was visualised as a bi-layered ceramic containing a primary section ($Section_P$) and secondary section ($Section_S$) the thermal expansion/contraction behaviour of which can be measured independently from one other. The adaptation of a complete shell into a bi-layered ceramic is shown in Figure 64.




**Figure 64** – Adaptation of complete shell into bi-layered ceramic containing a primary section ($Section_P$) and secondary section ($Section_S$)

The shell was grouped this way due to the similarities in the composition of the layers within each section. $Section_P$ is composed of zircon, Binder P and Fused-$Al_2O_3$ stucco. $Section_S$ is composed of zircon, Binder S and the specific stucco applied during shell build. As such, it was expected that the layers contained within each section expand/contract at the same rate during the firing cycle.

In order to measure the thermal expansion/contraction behaviour of either $Section_S$ or $Section_P$ for Shell (Tab-$Al_2O_3$), Shell (BD-$Al_2O_3$) and Shell (SGB127); samples were produced representative of each section and analysed independently by dilatometer analysis. It should be noted that each complete shell comprises an identical $Section_P$ and variation between each complete shell results only from variation in stucco composition within $Section_S$.

Shells representative of $Section_S$ or $Section_P$ were built on a wax pattern of dimensions 130 x 100 x 20 mm by applying slurry and stucco with a drying time representative of the layer imitated until a thickness of approximately 5 mm was achieved. The shell was then dewaxed in an autoclave, cut into test bars approximately 25 x 5 x 5 mm and fired in the pre-fire cycle before being tested in the Netzsch DIL 402 E horizontal dilatometer under the simulated casting cycle as detailed in Section 3.1.6.2. In addition to testing shell samples, the thermal expansion/contraction of the Secondary slurry (labelled Secondary (-)) was also measured. This was produced by drying a sample of Secondary slurry in a petri-dish for two days at room temperature before following the cutting, firing and analysis steps listed above. The composition of each sample is shown below in Table 14 using notation from Section 3.1.3 to label each layer. An example of a sample ready for dilatometer analysis is shown in Figure 65.

**Table 14** – Composition of shells replicating $Section_P$ and $Section_S$ of complete shell samples

| Sample identifier | Layer composition in order of application | Number of layers |
|---|---|---|
| Primary (Fused-$Al_2O_3$) | P $(FusedAl)_2$ | 1 |
| | P+1 $(FusedAl)_2$ | 1 |
| | P $(FusedAl)_2$ | 1 |
| | P+1 $(FusedAl)_2$ | 1 |
| | P $(FusedAl)_2$ | 1 |
| | P+1 $(FusedAl)_2$ | 1 |
| | P $(FusedAl)_2$ | 1 |
| | P+1 $(FusedAl)_2$ | 1 |
| | Seal (Primary +1) | 1 |
| Secondary (Tab-$Al_2O_3$) | S (Tab-$Al_2O_3)_2$ | 7 |
| | Seal (Secondary) | 1 |
| Secondary (BD-$Al_2O_3$) | S (60 BD-$Al_2O_3)_2$ | 7 |
| | Seal(Secondary) | 1 |
| Secondary (SGB127) | S (60 $SGB127)_2$ | 7 |
| | Seal (Secondary) | 1 |

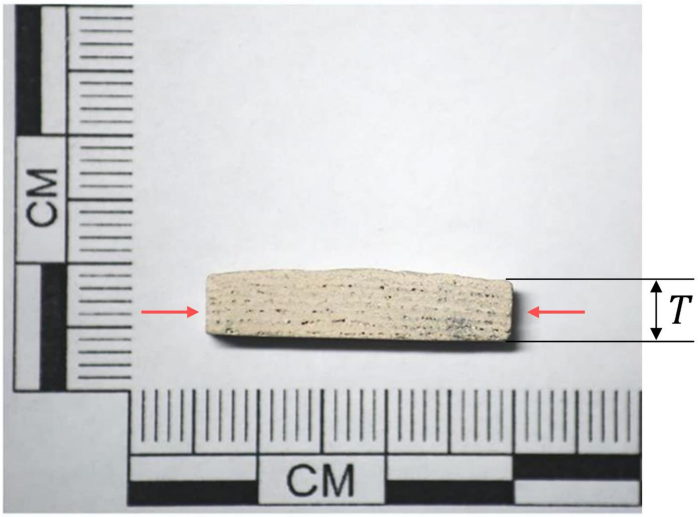



**Figure 65** – Sample Secondary (Tab-$Al_2O_3$) with arrows indicating the direction in which thermal expansion/contraction was measured

The microstructure of each sample was also recorded via SEM as shown in Figures 66 and 67, labelling each layer in the same manner as Section 4.4.1. It was observed that each shell sample displayed the same visual characteristics as the equivalent layer within the complete shell system shown in Section 4.4.2. This provided evidence that the samples listed in Table 14 were representative of the associated $Section_S$ or $Section_P$ within the complete shell and thus likely to show the same degree of thermal expansion/contraction during firing.

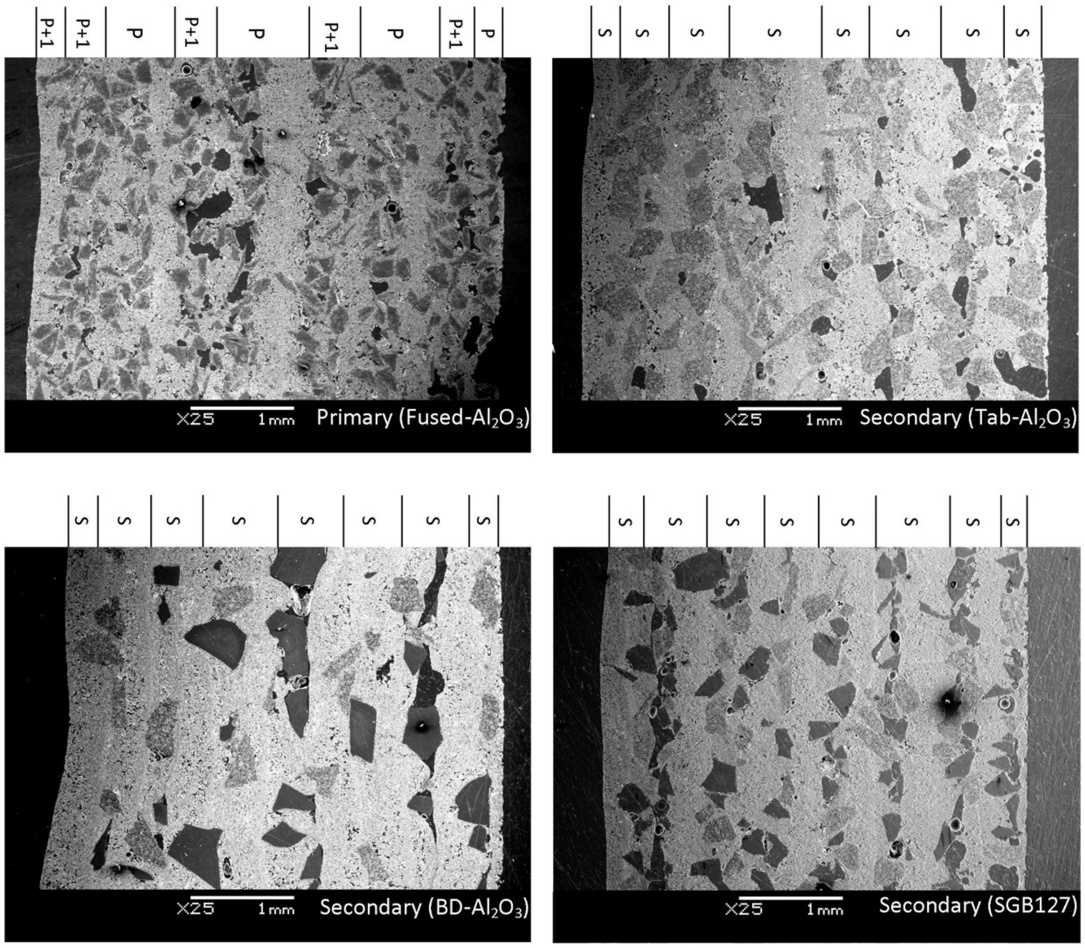



**Figure 66** – SEM cross-sections of shell samples replicating $Section_P$ or $Section_S$ used for dilatometer analysis. The initial layer applied to the wax pattern is displayed on the right side for each sample

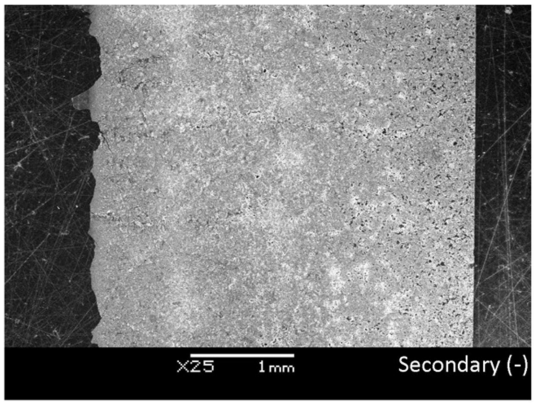



**Figure 67** – SEM image of Secondary slurry cross-section used for dilatometer analysis

Dilatometer analysis was successfully conducted on each sample listed in Table 14 in addition to Secondary (-) with a total of three runs being completed for each sample. The average thermal trace for each sample is shown in Figure 68 with standard error bars

displayed intermittently throughout the firing cycle. The average quantity of shrinkage experienced by each sample following the firing cycle is displayed in Table 15 in addition to the thermal expansion coefficient measured up to 700 °C. The sintering onset temperature was also measured for each sample by recording the temperature at which the thermal trace deviated from linear thermal expansion; this occurred more than once due to the multi-component composition of the samples being investigated. The average sintering onset temperature for each sample is displayed in Table 16. A magnified diagram for each sample is provided in Appendix 1.

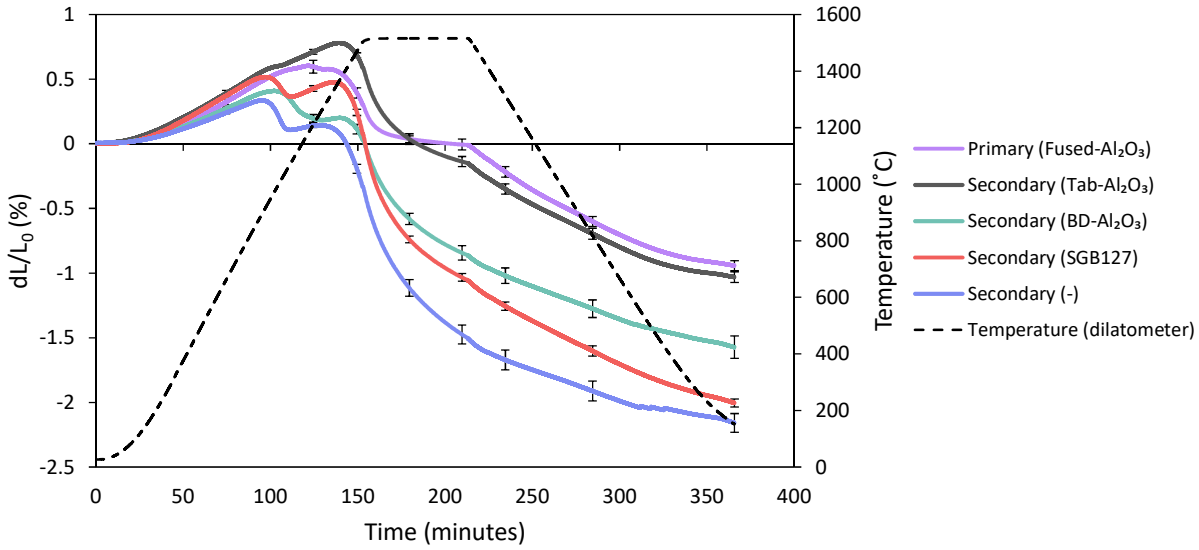



**Figure 68** – Expansion/contraction plots of shell samples replicating $Section_P$ or $Section_S$ analysed throughout the simulated casting cycle conducted by dilatometer analysis

**Table 15** – Linear shrinkage of samples following the simulated casting cycle and linear thermal expansion coefficients measured from 50 – 700 ˚C by dilatometer analysis

| Sample | Linear shrinkage (%) | | Linear thermal expansion coefficient from 50 – 700 ˚C ($10^{-6}$ $K^{-1}$) | |
|---|---|---|---|---|
| | Average | Standard deviation | Average | Standard deviation |
| Primary (Fused-$Al_2O_3$) | 0.94 | 0.038 | 5.20 | 0.276 |
| Secondary (Tab-$Al_2O_3$) | 1.03 | 0.041 | 6.11 | 0.224 |
| Secondary (BD-$Al_2O_3$) | 1.57 | 0.086 | 4.32 | 0.219 |
| Secondary (SGB127) | 2.00 | 0.031 | 5.86 | 0.163 |
| Secondary (-) | 2.16 | 0.072 | 3.84 | 0.066 |

**Table 16** – First and second sintering onset temperatures for shell samples conducted by dilatometer analysis

| Sample | First sintering onset temperature (°C) | | Second sintering onset temperature (°C) | |
|---|---|---|---|---|
| | Average | Standard deviation | Average | Standard deviation |
| Primary (Fused-$Al_2O_3$) | 924 | 3.3 | 1312 | 7.9 |
| Secondary (Tab-$Al_2O_3$) | 902 | 3.1 | 1310 | 20.9 |
| Secondary (BD-$Al_2O_3$) | 895 | 11.3 | 1370 | 9.4 |
| Secondary (SGB127) | 878 | 3.4 | 1299 | 10.8 |
| Secondary (-) | 861 | 3.4 | 1236 | 15.3 |

General analysis

Analysis shows a two stage sintering process is occurring in all samples with each stage varying in magnitude of shrinkage and sintering onset temperature depending on the sample. This effect is most pronounced in sample Secondary (-) where shrinkage begins at approximately 860 °C and again at approximately 1240 °C. The first transition strongly resembles the sintering characteristics of Binder S analysed in Section 5.2 in which the transition begins at approximately 720 °C and is quickly completed. The second transition strongly resembles the sintering characteristics of the zircon sample analysed in Section 5.2 in which the shrinkage transition begins at approximately 1040 °C with the sample displaying a slow densification rate and remaining partially sintered following the complete firing cycle. Due to the similarities in sintering behaviour between the slurry components (Binder S and zircon powder) and the sample Secondary (-) it was proposed that each component sinters sequentially during the firing cycle giving rise to the two stage sintering process. However, there appears to be a degree of interaction between the two components when mixed together resulting in a delayed onset of sintering temperature in the sample Secondary (-) in comparison to the components tested separately. Additionally, the densification of sample Secondary (-) is limited, displaying a lesser degree of shrinkage than either Binder S or zircon when tested independently. This may be explained by the TMA being used to measure both zircon and Binder S whereas the dilatometer was used to measure sample Secondary (-). In hindsight, using a single instrument to measure each sample would have given more comparable data however; every attempt was made to replicate equivalent temperature profiles in each method by using the sample thermocouple to measure the temperature at

the sample surface. Assuming each sample experiences a similar thermal cycle in each instrument, such behaviour can be explained by the zircon particles forming a non-densifying network (above the percolation threshold) within sample Secondary (-). This limits the shrinkage associated with Binder S contraction in the early stages of sintering due to constraint [164]. As temperature increases further, the sintered amorphous silica devitrifies to form cristobalite which is inherently shrinkage resistant [165, 166]. As such, the shrinkage resistant silica network will likely act to hinder the shrinkage of the zircon component, further reducing the shrinkage of Secondary (-) in comparison to the isolated components analysed independently. Therefore, a simple rule of mixtures cannot be applied to predict the sintering profile of the sample Secondary (-) due to the interaction between the two components.

It was also observed that the addition of stucco particles to the Secondary slurry matrix decreases the linear shrinkage in comparison to the slurry matrix analysed independently (Secondary (-)). This occurs most dominantly in sample Secondary (Tab-$Al_2O_3$). It was hypothesised this occurred due to the refractory stucco particles restricting shrinkage by forming of a plane of particles within each layer which remain dimensionally stable throughout the firing cycle. The particles remain stable at high temperature due to the low surface area of coarse alumina particles which are manufactured at temperatures in excess of 1500 ˚C, giving stability at high temperature. With the addition of less refractory stucco particles the mechanism preventing shrinkage reduces in efficiency as shown by the higher magnitude of linear shrinkage observed for samples Secondary (BD-$Al_2O_3$) and Secondary (SGB127). This occurs as the plane of particles which remained dimensionally stable in Shell (Tab-$Al_2O_3$) begins to develop voids as the porous stucco begins to sinter and shrink away from the surrounding slurry matrix as shown by SEM in Section 4.4.1. This produces a shrinkage prone structure in which the matrix can contract without constraint from the plane of dimensionally stable particles. The proposed mechanism is shown visually in Figure 69 for a shell layer containing either densifying or non-densifying particles with equal volumes of slurry and stucco in each scenario (excluding the presence of porosity present prior to firing). This effect will likely be magnified in shells containing porous stucco blends as a greater volumetric ratio of slurry to stucco is present in addition to greater pore volume in comparison to shells containing non-porous stucco.

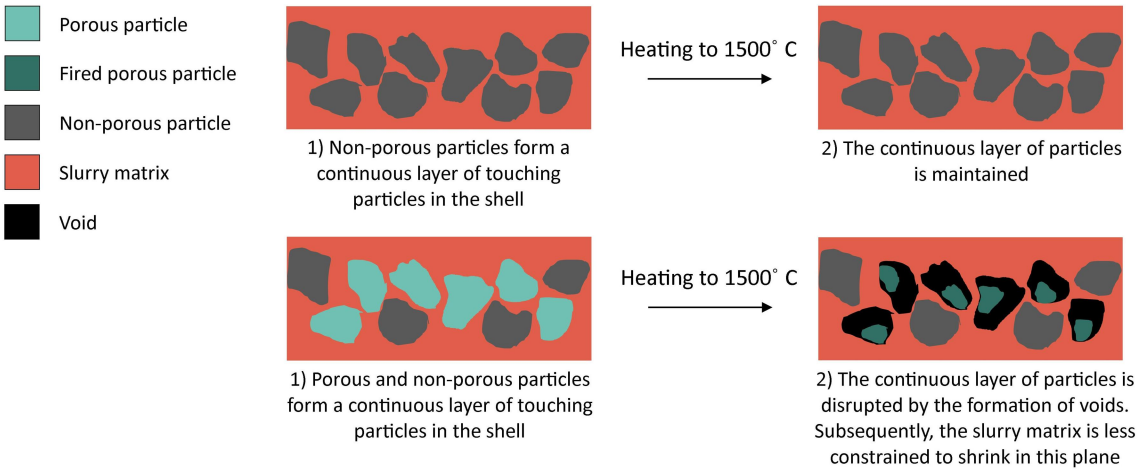



**Figure 69** – Proposed mechanism for greater shrinkage in shell containing porous stucco in comparison to shell containing non-porous stucco during the simulated casting cycle

Furthermore, it was observed that the linear thermal expansion coefficient (measured from 50 – 700 ˚C) for each sample varies between approximately 4.0 – 6.0 x $10^{-6}$ $K^{-1}$. This can be explained as the linear thermal expansion of each sample depends on the thermal expansion of the constituent components [3]. The linear thermal expansion coefficient of sample Secondary (-) (3.84 x $10^{-6}$ $K^{-1}$) is similar to that of the zircon powder sample (4.73 x $10^{-6}$ $K^{-1}$) measured in Section 5.2 with a slight reduction due to the negative contribution of Binder S (-1.83 x $10^{-6}$ $K^{-1}$) also analysed in Section 5.2. The addition of alumina stucco raises the linear thermal expansion coefficient due to the higher linear thermal expansion coefficient of α-alumina (9 x $10^{-6}$ $K^{-1}$ [167]) in comparison to the slurry matrix. Thus a shell containing Tab-$Al_2O_3$ or Fused-$Al_2O_3$ stucco displays a higher thermal expansion coefficient than sample Secondary (-).

Primary (Fused-$Al_2O_3$) analysis

The Primary (Fused-$Al_2O_3$) sample shows the least shrinkage of all samples following the firing cycle. In addition, analysis of the sintering profile shows a peak between the first and second onset of sintering plateaus. This was likely the result of Primary slurry and Primary +1 slurry sintering at slightly different rates producing a multimodal curve as Binder P and

zircon sinter at slightly different temperatures within each alternating layer. This leads to a more complicated sintering profile than other samples containing only the Secondary slurry.

Secondary (Tab-$Al_2O_3$) analysis

The Secondary (Tab-$Al_2O_3$) sample shows a comparable degree of shrinkage to the Primary (Fused-$Al_2O_3$) sample following the firing cycle. It can also be observed that the addition of stucco has lessened the degree of shrinkage associated with silica binder sintering at approximately 900 ˚C when comparing the shrinkage trace to sample Secondary (-). This implies that the added rigidity brought about from the addition of stucco restricts the shrinkage of the shell as the silica sinters and thus only a minor inflection can be observed in the sintering profile.

Secondary (BD-$Al_2O_3$) analysis

The sample Secondary (BD-$Al_2O_3$) shows a significantly higher degree of shrinkage in comparison to Secondary (Tab-$Al_2O_3$) following the firing cycle. This was hypothesised to be the result of porosity within the shell (identified in Sections 4.3.2 and 4.4.1); the shrinkage of BD-$Al_2O_3$ particles above 850 ˚C (identified in Section 4.2.6) and a greater volumetric ratio of slurry to stucco (identified in Section 4.3.2). This consequently gives the slurry network more freedom to contract (as described in Figure 69), giving rise to a sintering profile that looks similar to the sample Secondary (-). It was also observed that the linear thermal expansion coefficient for Secondary (BD-$Al_2O_3$) was lower than expected considering the linear thermal expansion coefficient of BD-$Al_2O_3$ ($7.1 \times 10^{-6}$ $K^{-1}$) measured by TMA in Section 4.2.6 is similar to alpha alumina ($9 \times 10^{-6}$ $K^{-1}$) [167]. Despite this, the linear thermal expansion closely resembles Secondary (-). This may be caused by the high degree of porosity in the sample, coupled with the low adhesion of BD-$Al_2O_3$ particles to the slurry (as observed by SEM in Section 4.4.1). This may result in particles expanding into voids upon heating rather than expanding against the slurry matrix.

Secondary (SGB127) analysis

The sample Secondary (SGB127) shows a significantly higher degree of shrinkage in comparison to Secondary (Tab-$Al_2O_3$) following the firing cycle. Similarly to sample Secondary (BD-$Al_2O_3$), it was hypothesised that the increased shrinkage was the result of porosity within the shell, the shrinkage of BD-$Al_2O_3$ particles above 850 ˚C and a greater volumetric ratio of slurry to stucco. It was also observed that the linear thermal expansion coefficient of Secondary (SGB127) closely resembles Secondary (Tab-$Al_2O_3$) which was surprising considering SGB127 particles were expected to shrink away from the slurry matrix immediately upon firing (as identified by TMA in Section 4.2.6). As such, it was expected that the SGB127 particles do not contribute to the thermal expansion of the sample. It is possible the water evolved from SGB127 material causes the higher than expected thermal expansion coefficient. However, it would be unlikely this effect raises the thermal expansion coefficient past 525 ˚C as dehydration and condensation reactions would be expected to approach completion past this temperature [135].

Relation to flexural deformation

Measuring the thermomechanical properties of shell sections representative of $Section_P$ and $Section_S$ throughout the simulated casting cycle has provided evidence that the flexural deformation observed in complete shell systems (explained in Section 4.4.4) results from variation in the degree of shrinkage between each section. This arises when substituting non-densifying refractory stucco for porous stucco which contract during the firing cycle and subsequently shrink away from the slurry matrix. This produces a large amount of porosity allowing the slurry matrix more freedom to contract. This effect was likely amplified by the fact that shells containing porous stucco have large voids distributed throughout the structure prior to firing and a greater volumetric ratio of slurry to stucco. As such, curvature would be expected in shells containing either BD-$Al_2O_3$ or SGB127 in secondary layers as $Section_S$ contracts to a greater degree than the $Section_P$. However, for shells containing only Tab-$Al_2O_3$, $Section_S$ has a similar degree of shrinkage to $Section_P$ and thus minimal curvature would be expected.

## 5.4 Predicting Flexural Deformation

It was proposed that the thermal expansion/contraction behaviour of shells representative of $\text{Section}_S$ and $\text{Section}_P$ analysed by dilatometer in Section 5.3 can be used to predict the flexural deformation of a complete shell throughout the simulated casting cycle. This requires treating the shell as a bi-layered system with the expansion/contraction behaviour of $\text{Section}_P$ equivalent to sample Primary (Fused-$Al_2O_3$) and the expansion/contraction behaviour of $\text{Section}_S$ equivalent to either Secondary (Tab-$Al_2O_3$), Secondary (BD-$Al_2O_3$) or Secondary (SGB127). This allows the radius of curvature ($\rho$) to be predicted for a complete shell composed of a $\text{Section}_P$ and $\text{Section}_S$ contracting to the magnitude recorded in Section 5.3 throughout the simulated casting cycle using Equation 39 [168]. From this, the deflection from the normal ($\delta$) can also be calculated over a specified length. Shown in Figures 70 and 71 is the proposed adaptation from the multi-layered shell system to a bi-layered ceramic.

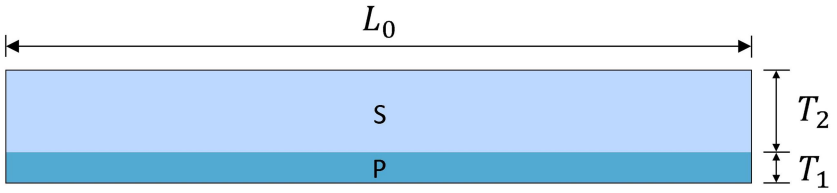



**Figure 70** – Adaptation of a multi-layered shell into a bi-layered ceramic composed of $\text{Section}_P$ (P) thickness equal to $T_1$ and $\text{Section}_S$ (S) thickness equal to $T_2$. The original length of the sample is labelled $L_0$

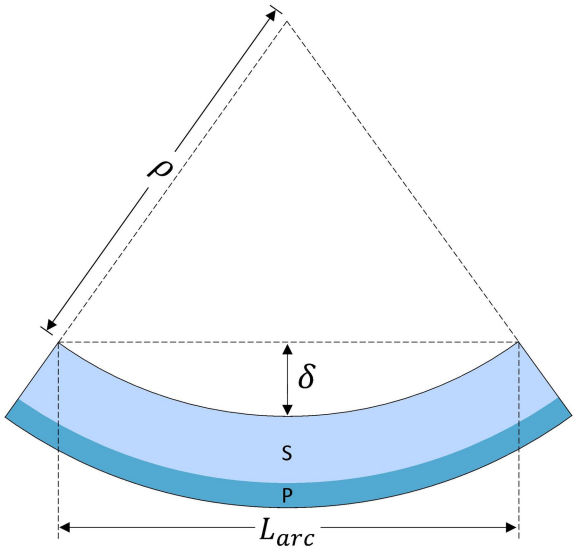



**Figure 71** – Radius of curvature ($\rho$), deflection from normal ($\delta$) and length of arc ($L_{arc}$) of a bi-layered ceramic where $\text{Section}_S$ (S) has contracted to a greater degree than $\text{Section}_P$ (P)

The equation used to calculate the radius of curvature for bi-layered ceramics is labelled Equation 39 [168]. By measuring each parameter throughout the simulated casting cycle the radius of curvature can be predicted over the entire firing cycle.

$$\frac{T_1 + T_2}{\rho} = \left( \frac{6(a+1)^2 ab}{a^4 b^2 + 2ab(2a^2 + 3a + 2) + 1} \right) \Delta\varepsilon \qquad \text{eq.39}$$

$T_1$ Thickness of layer 1 (m)

$T_2$ Thickness of layer 2 (m)

$\rho$ Radius of curvature (m)

$a$ Ratio of thickness between layer 1 and 2 (-)

$b$ Ratio of uniaxial viscosity between layer 1 and 2 (-)

$\Delta\varepsilon$ Mismatch strain (-)

The ratio of thickness ($a$) is defined as:

$$a = \frac{T_1}{T_2} \qquad \text{eq.40}$$

The original thickness of the sample ($T_0$) is defined as:

$$T_0 = T_1 + T_2 \qquad \text{eq.41}$$

The ratio of viscosity ($b$) at a given time is defined as:

$$b = \frac{\eta_1}{\eta_2} \qquad \text{eq.42}$$

$\eta_1$ Uniaxial viscosity of layer 1 (Pa s)

$\eta_2$ Uniaxial viscosity of layer 2 (Pa s)

To convert the radius of curvature calculated from Equation 39 to the deflection from normal, Equation 43 is used given that $\rho >> \delta$ [169]. This remains true for all samples with $\rho$ remaining at least 1000 times greater than $\delta$ throughout the firing cycle. The dependent variable (defection from normal) is used as a metric to describe the magnitude of flexural deformation. The length of arc ($L_{arc}$) is approximated to the original length of sample ($L_0$) for the entire firing cycle as the minor degree of shrinkage and curvature create a close approximation between the two values throughout the firing cycle. A $L_0$ value of 20 mm was used in this method for later comparison to direct methods of measuring $\delta$ over the same length throughout the simulated casting cycle.

$$\delta = \frac{{L_{arc}}^2}{8\rho} \qquad \text{eq.43}$$

$\delta$ Deflection from normal (m)

$L_{arc}$ Length of arc (m)

The list of complete shells for which flexural deformation was predicted is given in Table 17. Each complete shell was composed of a $\text{Section}_P$ and $\text{Section}_S$ which expands/contracts at the average quantity measured by dilatometer method in Section 5.3 over the simulated casting cycle. The mismatched strain required to predict the radius of curvature from Equation 39 was calculated by subtracting the expansion/contraction of $\text{Section}_S$ from the expansion/contraction of $\text{Section}_P$ for each data point analysed throughout the simulated casting cycle.

**Table 17** – Notation of complete shells composed of a specified $\text{Section}_P$ and $\text{Section}_S$

| **Complete shell** | **$\text{Section}_P$** | **$\text{Section}_S$** |
|---|---|---|
| Shell (Tab-$Al_2O_3$) | Primary (Fused-$Al_2O_3$) | Secondary (Tab-$Al_2O_3$) |
| Shell (BD-$Al_2O_3$) | Primary (Fused-$Al_2O_3$) | Secondary (BD-$Al_2O_3$) |
| Shell (SGB127) | Primary (Fused-$Al_2O_3$) | Secondary (SGB127) |

Thickness ratio

The approximate thickness of $Section_S$ and $Section_P$ for each shell outlined in Table 17 was measured by SEM analysis. This was conducted on pre-fired shell samples shown previously in Chapter 4 for which the composition of each shell is shown in Table 11. An example of image analysis is shown in Figure 72 displaying the method of measuring thickness of each section using the scale bar as a reference. Due to the inherent variation in thickness of shell samples, three images were taken with the average thickness of each section being recorded. As the primary and primary +1 layers were deposited before any effect from the secondary stucco could take place, the thickness of $Section_P$ is taken as equal for all samples with the average thickness being calculated from all 9 samples analysed. The average thickness for each section is given in Table 18 alongside the original thickness ($T_0$) and thickness ratio ($a$) in Table 19. When using Equation 39 to calculate the radius of curvature ($\rho$) the thickness of each section is inputted using data in these Tables. These values were taken as constant throughout the entire firing cycle. To predict flexural deformation more accurately the thermal expansion/contraction behaviour of each sample listed in Table 14 could be analysed through thickness to calculate the varying thickness ratio throughout the firing cycle. However, this was deemed unnecessary.

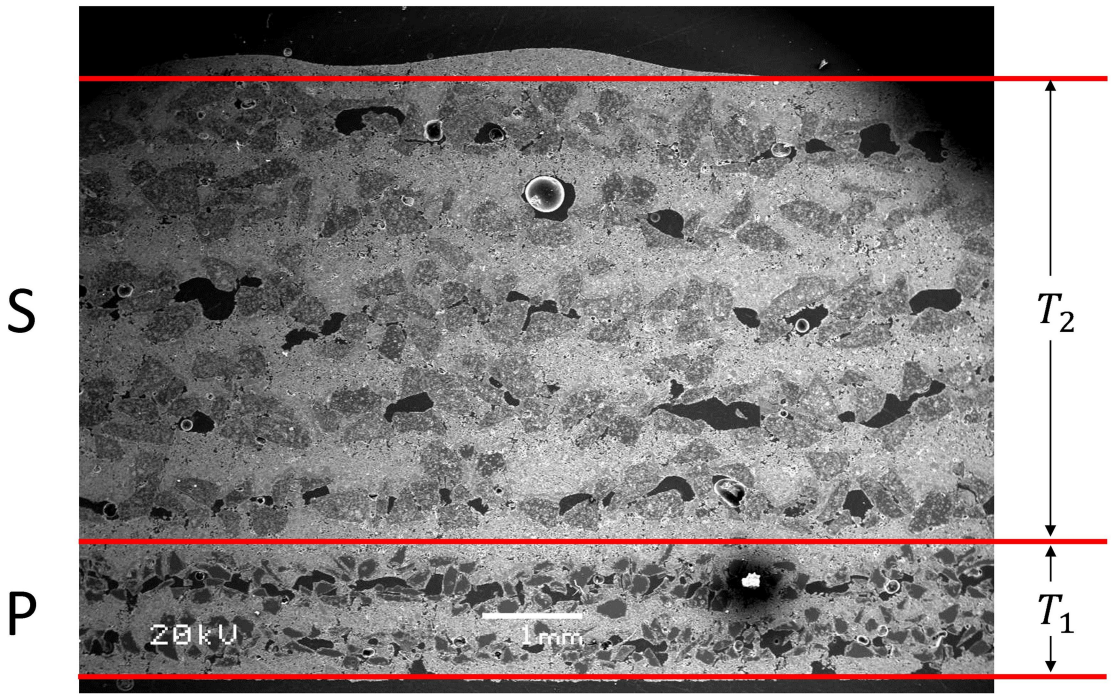



**Figure 72** – Method of quantifying section thickness by SEM analysis using the scale bar for reference. Displaying $Section_P$ (P) and $Section_S$ (S) of Shell (Tab-$Al_2O_3$) in pre-fired condition

**Table 18** – Average thicknesses for $Section_P$ ($T_1$) and $Section_S$ ($T_2$) in pre-fired condition measured by SEM analysis

| **Complete shell** | **Average $Section_P$ thickness (mm)** | | **Average $Section_S$ thickness (mm)** | |
|---|---|---|---|---|
| | **Average** | **Standard deviation** | **Average** | **Standard deviation** |
| Shell (Tab-$Al_2O_3$) | 1.54 | 0.104 | 4.90 | 0.109 |
| Shell (BD-$Al_2O_3$) | | | 4.97 | 0.110 |
| Shell (SGB127) | | | 4.27 | 0.106 |

**Table 19** – Average original thickness ($T_0$) and thickness ratio ($a$) values for each shell

| **Complete shell** | **Original thickness (mm)** | **Thickness ratio (-)** |
|---|---|---|
| Shell (Tab-$Al_2O_3$) | 6.44 | 0.315 |
| Shell (BD-$Al_2O_3$) | 6.51 | 0.310 |
| Shell (SGB127) | 5.81 | 0.362 |

Measuring the viscosity of each layer throughout the simulated casting cycle

The viscosity of each section can be measured using the cyclic loading dilatometer method as described in Section 3.1.6.3. However, this method did not work for shell samples with no correlation being observed between the stress applied and the stress-induced strain as shown in Figure 73. In addition, the data proved unrepeatable showing a high degree of variance between runs. This may be due to the inhomogeneous nature of the multicomponent sample coupled with the variation in packing arrangement of stucco within the specimen and sample size. As such, the method was evaluated on more homogeneous slurry material without stucco present.

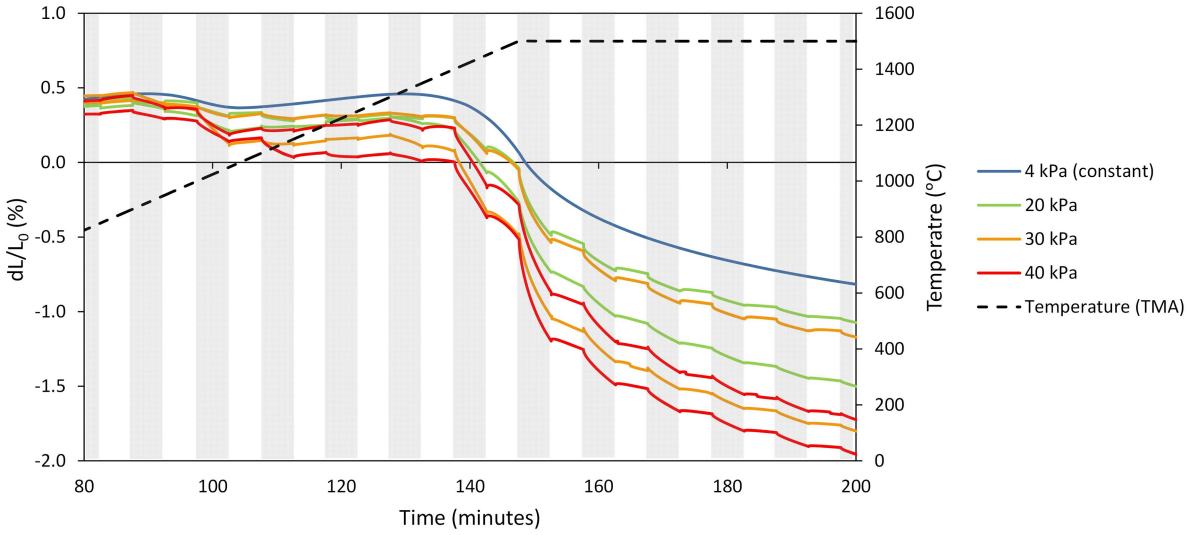



**Figure 73** – Cyclic loading dilatometry undertaken on sample Secondary (BD-$Al_2O_3$) with varied stresses applied under load. Shaded regions represent the period where loading takes place at the stated stress, outside this region a stress of 4 kPa is applied

The cyclic loading dilatometer analysis of sample Secondary (-) is shown in Figure 74. Once again it can be seen that there is no correlation between stress applied and the stress-induced strain.

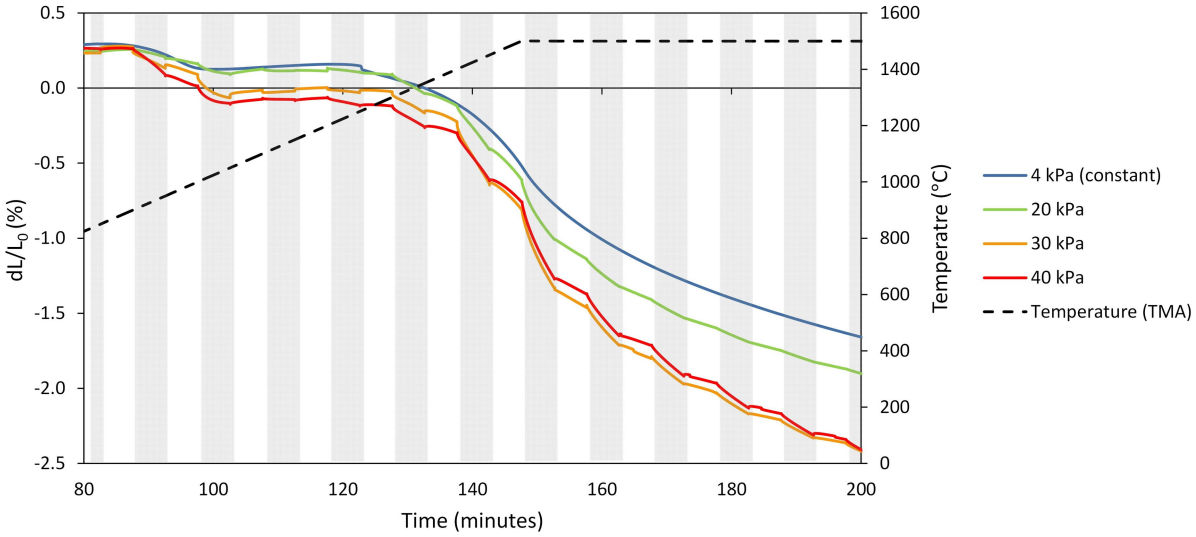



**Figure 74** – Cyclic loading dilatometry undertaken on sample Secondary (-) with varied stresses applied under load. Shaded regions represent the period where loading takes place at the stated stress, outside this region a stress of 4 kPa is applied.

It was therefore decided that this method could not be utilised to measure the viscosity ratio between layers. Subsequently, in order to progress the viscosity ratio was set equal to one for the entire firing cycle.

<u>Deflection from normal</u>

A positive deflection represents $\text{Section}_S$ contracting to a greater degree than $\text{Section}_P$ whereas a negative deflection represents $\text{Section}_P$ contracting to a greater degree than $\text{Section}_S$ as shown in Figure 75.

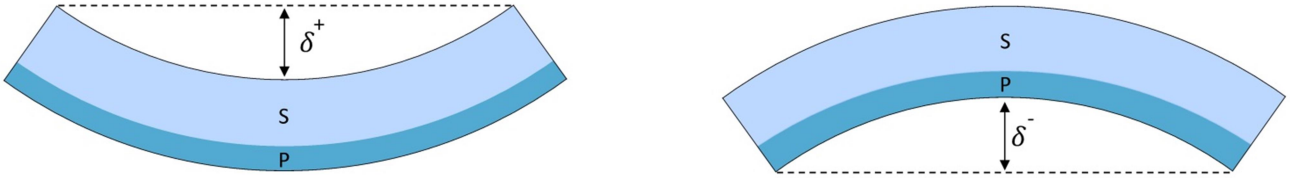



**Figure 75** – Positive deflection (left) and negative deflection (right)

The deflection from normal calculated from Equation 43 is expressed as a percentage of the original sample length ($L_0$) of 20 mm as shown by Equation 44. This is labelled normalised curvature.

$$Normalised\ curvature\ (\%) = \frac{\delta(mm)}{L_0(mm)} \times 100 \qquad \text{eq.44}$$

Predicted normalised curvature for shell samples

The curvature resulting from differential strain in $Section_P$ and $Section_S$ over the simulated casting cycle as calculated from the method outlined in this Section is displayed in Figure 76. Given that the thickness and viscosity ratios are assumed to be constant throughout the firing cycle, the curvature development is heavily dependent on the difference in strain between the specified $Section_P$ and $Section_S$ for a given sample. As such, the expansion/contraction of shell samples replicating $Section_P$ and $Section_S$ (as shown in Figure 68 in Section 5.3) explains the majority of the curvature predicted.

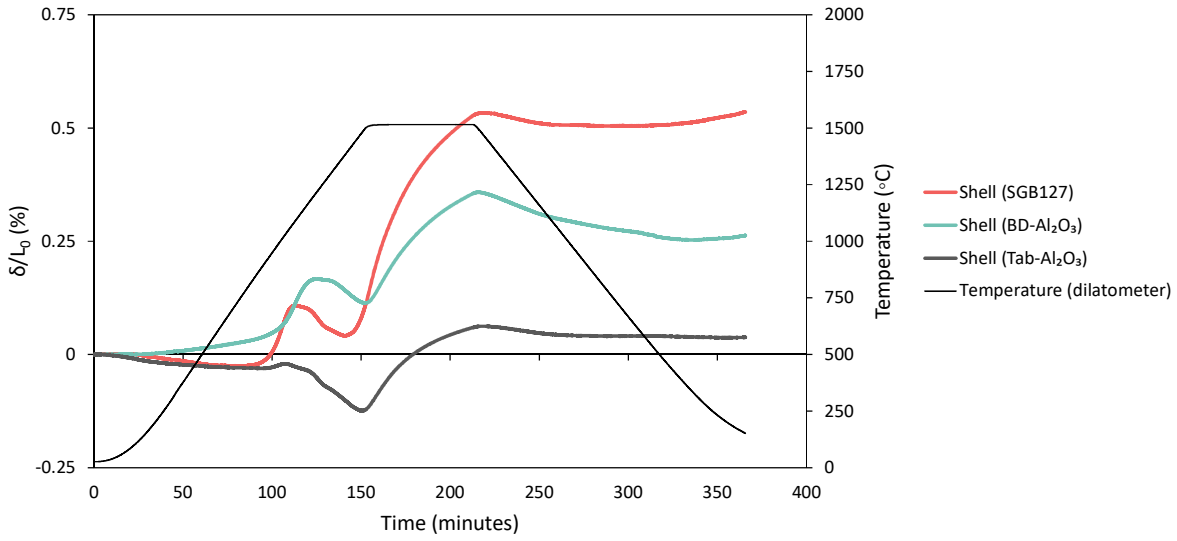



**Figure 76** – Normalised curvature predicted from thermal expansion/contraction of shell samples replicating $Section_P$ and $Section_S$ throughout the simulated casting cycle

Initially, curvature develops in each sample at a steady rate up until 700 ˚C due to different linear thermal expansion coefficients within each section. Above 700 ˚C the transition associated with silica binder sintering in the secondary layers causes greater shrinkage in sections containing porous stucco. This causes a rapid increase in positive curvature within Shell (BD-$Al_2O_3$) and Shell (SGB127) as $Section_S$ contracts to a greater degree than $Section_P$. Such behaviour is absent for Shell (Tab-$Al_2O_3$) as minimal shrinkage occurs in $Section_S$ within this region. As the shrinkage transition associated with silica binder nears completion in $Section_S$ the section begins to expand again as the thermal expansion of the constituent materials begins to outweigh the effect of the silica contraction. This causes the magnitude of positive curvature in Shell (BD-$Al_2O_3$) and Shell (SGB127) to decrease as $Section_S$ begins to expand as $Section_P$ displays contraction; subsequently a peak in normalised curvature can be seen in each shell at approximately 1200 ˚C and 1100 ˚C respectively. During the isothermal hold period the rate of contraction in $Section_S$ exceeds that of $Section_P$ for all shell samples resulting in positive curvature development. The rate of the curvature development is highest in Shell (BD-$Al_2O_3$) and Shell (SGB127) likely due to the high degree of porosity present whereas Shell (Tab-$Al_2O_3$) displays a slower rate of curvature development due to constraint from dimensionally stable refractory stucco in $Section_S$ restricting shrinkage in this layer. As particles coalesce and surface area reduces during the isothermal hold, the driving force for sintering reduces. As such, the rate of contraction in both $Section_P$ and $Section_S$ approaches 0 leading to the rate of curvature development forming an incomplete asymptote as both sections continue to display contraction until the end of the isothermal hold period. As the sample cools following the isothermal hold, both sections display similar rates of thermal contraction and thus minimal curvature is developed in this region. As a result of this behaviour, shells containing porous stucco display a greater degree of curvature following the firing cycle, the quantity of which is shown in Table 20.

**Table 20** – Normalised curvature following the complete simulated casting cycle predicted from thermal expansion/contraction of shell samples replicating $Section_P$ and $Section_S$

| **Complete shell** | **Normalised curvature predicted from thermal expansion/contraction of $Section_S$ and $Section_P$ (%)** |
|---|---|
| Shell (Tab-$Al_2O_3$) | 0.04 |
| Shell (BD-$Al_2O_3$) | 0.26 |
| Shell (SGB127) | 0.54 |

Camber development in investment casting moulds containing various slurry and stucco formulations has been studied by Leadbetter et al. [170]. However, it was concluded that deformation was not the result of differential shrinkage of layers because reversing the order of the layers gave a similar degree of deformation. It has also been demonstrated that raising the temperature of the molten alloy during casting produces greater deformation [171]. As such, it appears that typically, deformation in ceramic moulds occurs primarily due to creep. However, due to the drastic changes in material properties when substituting non-porous stucco for porous stucco in this work, the effect of differential thermal expansion/contraction between layers is more significant.

## 5.5 Predicting Stress

As explained by Cai et al. the maximum stress in a bi-layered ceramic is proportional to the change in strain rate between the layers [172]. This is described by Equations 45 and 46. These equations describe the maximum tensile stress in the section contracting fastest ($\sigma_{fast}^{max}$) is at the interface between the two sections and the maximum tensile stress in the section contracting slowest ($\sigma_{slow}^{max}$) is at the surface as shown in Figure 77. This stress varies linearly with thickness.

$$\sigma_{fast}^{max} = \left[\frac{a^2 b_e(4a+3)+1}{a^4 b_e^2 + 2ab_e(2a^2+3a+2)+1}\right]\eta_{fast}\Delta\dot{\varepsilon} \qquad \text{eq.45}$$

$\sigma_{fast}^{max}$ Maximum tensile stress in section contracting fastest (Pa)

$b_e$ Ratio of elastic modulus between layer 1 and 2 (-)

$\eta_{fast}$ Uniaxial viscosity of section contracting fastest (Pa s)

$\Delta\dot{\varepsilon}$ Change in strain rate ($s^{-1}$)

$$\sigma_{slow}^{max} = \left[\frac{a^4 b_e - a(3a-2)}{a^4 b_e^2 + 2ab_e(2a^2+3a+2)+1}\right]\eta_{slow}\Delta\dot{\varepsilon} \qquad \text{eq.46}$$

$\sigma_{slow}^{max}$ Maximum tensile stress in section contracting slowest (Pa)

$\eta_{slow}$ Uniaxial viscosity of section contracting slowest (Pa s)

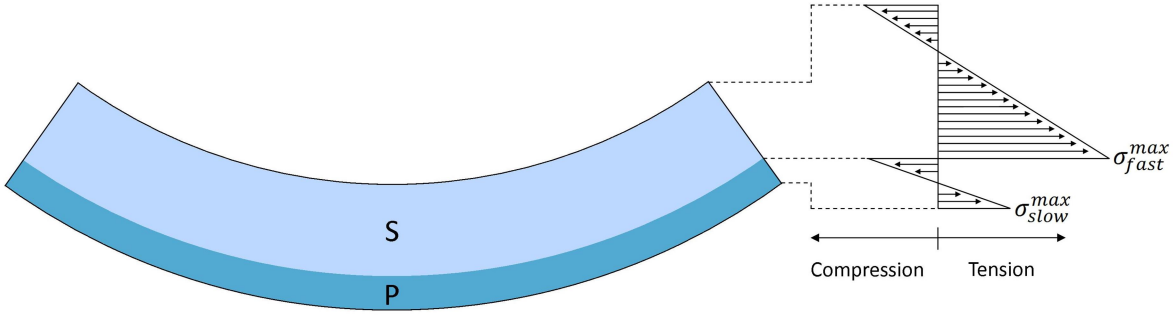



**Figure 77** – Stress distribution in a bi-layered ceramic resulting from Section$_S$ (S) contracting at a faster rate than Section$_P$ (P) causing a mismatch stress, the result of which produces curvature. Reproduced from [173]

Due to unsuccessful attempts at measuring $\eta_1$ and $\eta_2$ previously in Section 5.4 the exact magnitude of maximum stress could not be calculated for Section$_P$ or Section$_S$. However, due to the linear relationship between stress and mismatch strain rate (for a constant viscosity) it is possible to predict at what stage in the firing cycle the maximum stress will arise due to differential shrinkage rates between Section$_P$ and Section$_S$. This was undertaken by calculating the strain rate over 5 minute periods for each section and plotting the change in strain rate between Section$_P$ and Section$_S$ for each shell labelled in Table 17. It should be noted that the calculation was performed by subtracting the strain rate of Section$_S$ from the strain rate of Section$_P$, thus a negative mismatched strain rate is indicative of Section$_S$ shrinking at a faster rate than Section$_P$. This is shown in Figure 78.

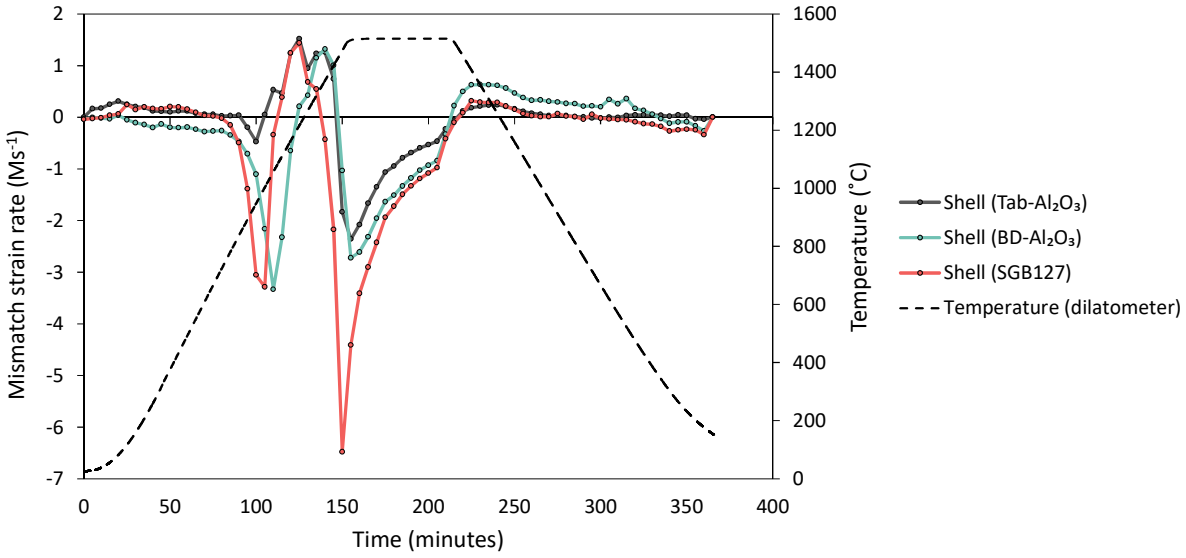



**Figure 78** – Mismatched strain rate between $Section_P$ and $Section_S$ of complete shell samples calculated from thermal expansion/contraction obtained by dilatometer

It can be seen that a peak in the magnitude of mismatched strain occurs at approximately 1000 ˚C for shells containing porous stucco and again at 1400 ˚C for all shell samples. This results from $Section_S$ shrinking at a greater rate than $Section_P$ during each period. As the magnitude of stress within each section is dependent on the viscosity of the section, the stress experienced in shells containing porous stucco at 1000 ˚C will likely be larger than at 1400 ˚C when the shell is less viscous at higher temperature [126]. This leads to shells containing porous stucco experiencing a high magnitude of stress in the early stages of the firing cycle which does not take place in Shell (Tab-$Al_2O_3$). As such, shells containing porous stucco are more likely to crack to relieve stress in comparison to Shell (Tab-$Al_2O_3$). The likelihood of failure is further increased for Shell (SGB127) which displays a strain rate mismatch approximately twice as large as Shell (Tab-$Al_2O_3$) and Shell (BD-$Al_2O_3$) at 1400 ˚C.

## 5.6 Measuring Flexural Deformation in-situ

Utilising the TMA in 3 point bend mode it was possible to measure the push rod displacement in real time (in-situ) over the simulated casting cycle. In this method the sample is held under a constant load with the push rod displacement being measured as it moves up and down throughout the simulated casting cycle as explained in Figure 79. Analysis was undertaken on complete shell samples in pre-fired condition reported on earlier in Chapter 4 as listed in Table 11. Each shell was analysed in both $Primary_{DOWN}$ and $Primary_{UP}$ orientation as shown in Figure 80 following the experimental method outlined in Section 3.1.6.4.

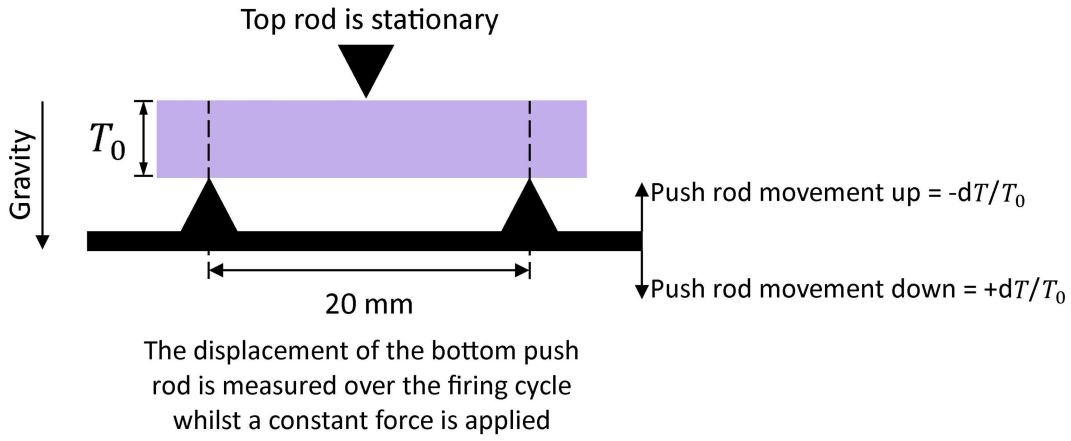



**Figure 79** – TMA schematic identifying isotropic thermal expansion results in push rod movement downwards (+d$T/T_0$) and isotropic thermal contraction results in push rod movement upwards (-d$T/T_0$) over a specified span length

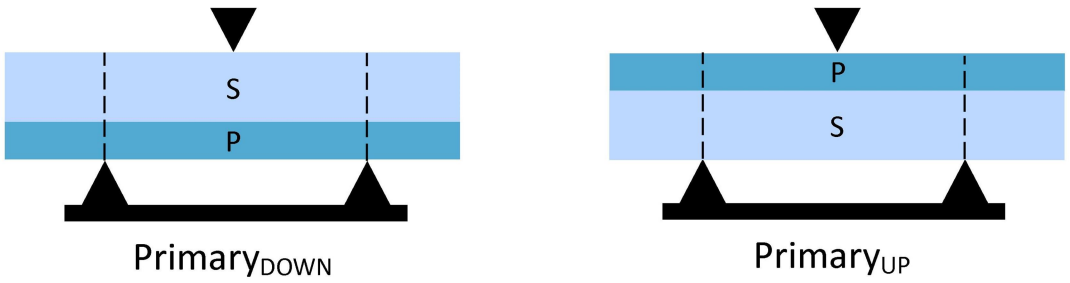



**Figure 80** – $Primary_{DOWN}$ (left) and $Primary_{UP}$ (right) orientations used for 3 point bend TMA labelled depending on orientation of $Section_P$ (P) and $Section_S$ (S)

It was proposed that the movement of the push rod in either $Primary_{DOWN}$ or $Primary_{UP}$ orientation is dependent on the following factors:

- Through thickness thermal expansion/contraction (ϕ)
- Creep resulting from gravity and load (ω)
- Curvature resulting from different thermal expansion/contraction between sections (δ)

Each factor varies in magnitude throughout the firing cycle with the effect of ϕ and δ producing an upward or downward push rod movement depending on the progression through the firing cycle. The effect of ω results in only push rod movement upwards as gravity and load act to bend the sample in the same direction.

Through thickness thermal expansion/contraction (ϕ)

It was assumed that the magnitude of ϕ is equal in both orientations as the sample will expand/contract volumetrically, thus the push rod will measure this movement equally in either orientation. Additionally, the direction of push rod movement resulting from ϕ will be the same in both orientations for the same reasons as above.

Creep resulting from gravity and load (ω)

Factors effecting creep in investment casting shells prepared from zircon filled colloidal silica slurryies with set dimensions over a given firing cycle have been identified as the following:

1. The concentration of oxides such as $Na_2O$, $K_2O$ and $Fe_2O_3$ which are present as stabilising agents within the water based silica sol and impurities from raw materials. Such species dissolve in silica at high temperature allowing softening to occur more rapidly due to a reduction in viscosity of the silica network [3, 21]

2. The grain size of polycrystalline materials has been identified as a parameter which influences creep induced strain as described by a universal form of creep equation shown in Equation 47 [109]. This equation describes the dependence of grain size when

subject to different mechanisms of creep identified by magnitude of $n_\sigma$ and $p$ for which a larger grain size produces a reduction in creep induced strain.

$$\dot{\varepsilon} = \frac{wkGb_J}{K\mathrm{T}}\left(\frac{b_J}{d_{grain}}\right)^p \left(\frac{\sigma}{G}\right)^{n_\sigma} \qquad \text{eq.47}$$

$\dot{\varepsilon}$ Strain rate in steady state period ($s^{-1}$)

$w$ Dimensionless constant (-)

$k$ Diffusion coefficient ($m^2\ s^{-1}$)

$G$ Shear modulus (Pa)

$b_J$ Burgers vector (m)

$K$ Boltzmann constant ($J\ K^{-1}$)

$\mathrm{T}$ Absolute temperature (K)

$d_{grain}$ Grain size (m)

$p$ Exponent of inverse grain size (-)

$\sigma$ Applied stress (Pa)

$n_\sigma$ Stress exponent (-)

3. The magnitude of stress acting on the sample as a result of sample weight and push rod force will influence the magnitude of creep as shown by Equation 47.

4. Porosity also influences the magnitude of creep as more porous structures experience a higher effective stress resulting from a reduced cross-sectional area. This has been shown in 50 vol% porous alumina beams displaying a creep rate 50 times greater than 5 vol% porous alumina beams [174].

Despite compositional variation existing between $\text{Section}_P$ and $\text{Section}_S$, the materials comprised within each section are similar. As such, variation in the concentration of oxides, grain size and porosity between sections were expected to insignificantly effect creep. As such, preference for creep in either $\text{Primary}_{UP}$ or $\text{Primary}_{DOWN}$ orientation (under identical load) should be absent as both sections were expected to behave similarly whether under compression or tension during 3 point bend loading. Therefore, it was assumed that the

magnitude of ω was also equal when testing in either $Primary_{UP}$ or $Primary_{DOWN}$ orientation. This results in push rod movement upwards in each orientation tested as the shell deforms in the direction of load at each contact point.

Deflection resulting from different thermal expansion between sections (δ)

It was also assumed that the magnitude of δ was equal in both orientations as $Section_P$ and $Section_S$ expand/contract independently of sample orientation. However, as $Section_P$ and $Section_S$ are rotated by changing the orientation from $Primary_{DOWN}$ to $Primary_{UP}$ the direction of push rod movement resulting from δ changes to give an opposite effect. This is the result of curvature developing to produce a concave surface on the section showing greatest contraction. Thus changing the sample orientation causes the direction of push rod movement resulting from δ to reverse.

Accumulating the magnitude and direction of each factor to calculate flexural deformation

Each factor is considered as non-interacting with the push rod movement being dependent exclusively on the three factors mentioned. This was justified by minimising the push rod force applied throughout analysis to allow each sample to sinter as freely as possible. As such, preference for enhanced sintering behaviour in a given section or orientation was limited, reducing the magnitude of interaction between factors.

Accumulating the contributing factors effecting the push rod movement and taking into account the sign of each depending on orientation, Equations 48 and 49 were proposed. These equations define the change in thickness recorded on the TMA as a function of ϕ, ω and δ at a given time throughout the firing cycle. The sign of $\delta_t$ is as stated to reflect the previous notation in Figure 75 of positive curvature resulting in push rod movement upward (-d$T/T_0$) in the $Primary_{DOWN}$ orientation or push rod movement downwards (+d$T/T_0$) in $Primary_{UP}$ orientation.

$$\underset{Time=t}{dT_{DOWN}} = \varphi_t + \omega_t - \delta_t \qquad \text{eq.48}$$

$dT_{DOWN}$ $_{Time=t}$ Change in thickness recorded on the TMA in Primary$_{DOWN}$ orientation at time $t$ resulting from push rod displacement (m)

$\varphi_t$ Push rod displacement resulting from through thickness expansion/contraction at time $t$ (m)

$\omega_t$ Push rod displacement resulting from creep at time $t$ (m)

$\delta_t$ Push rod displacement resulting from differential shrinkage of sections at time $t$ (m)

$$\underset{Time=t}{dT_{UP}} = \varphi_t + \omega_t + \delta_t \qquad \text{eq.49}$$

$dT_{UP}$ $_{Time=t}$ Change in thickness recorded on the TMA in Primary$_{UP}$ orientation at time $t$ resulting from push rod displacement (m)

As previously described, the magnitude of displacement for each contributing factor was expected to be equal in each orientation at a given time. As such, any variation in push rod displacement between Primary$_{UP}$ orientation and Primary$_{DOWN}$ orientation was expected to result from the contribution of $\delta_t$ as this is the only factor that changes sign when changing the orientation between Primary$_{UP}$ and Primary$_{DOWN}$. This can be shown by subtracting Equation 48 from Equation 49 to give Equation 50 which predicts any difference between the Primary$_{UP}$ and Primary$_{DOWN}$ trace for a given sample is the result of curvature.

$$\underset{Time=t}{dT_{UP}} - \underset{Time=t}{dT_{DOWN}} = 2\delta_t \qquad \text{eq.50}$$

The average push rod displacement as a percentage of $T_0$ for Shell (Tab-$Al_2O_3$), Shell (BD-$Al_2O_3$) and Shell (SGB127) in both Primary$_{UP}$ and Primary$_{DOWN}$ orientation is shown in Figure 81. Three samples were analysed per shell variant in each orientation.

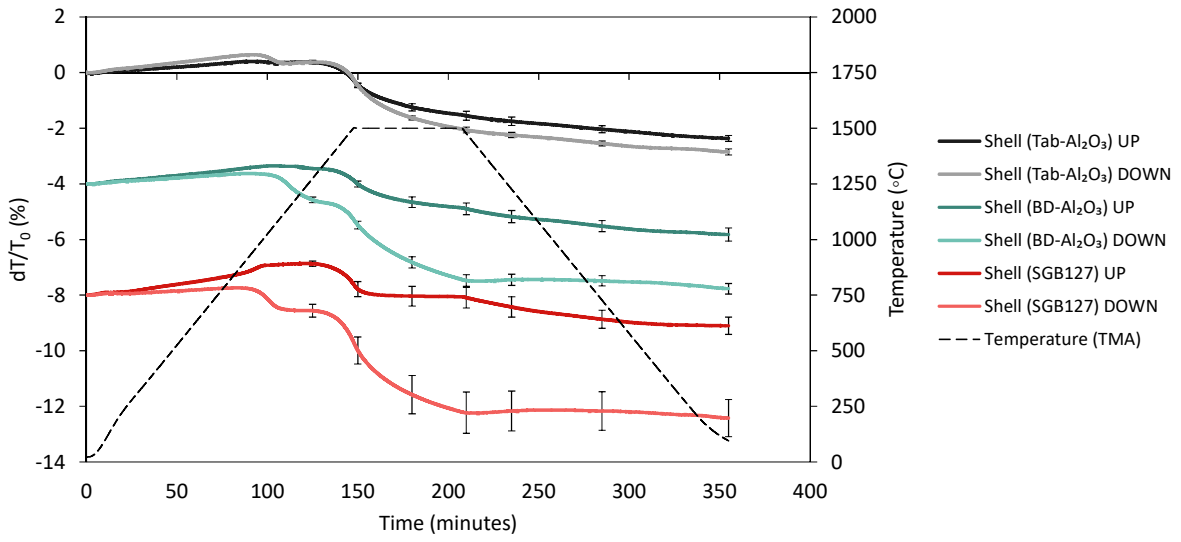



**Figure 81** – 3 point bend TMA of complete shells tested in $Primary_{UP}$ and $Primary_{DOWN}$ orientation throughout the simulated casting cycle. Each sample is separated by 4 % at the origin for clarification

It can be seen that the initial push rod movement between 25 – 700 °C varies slightly between $Primary_{UP}$ and $Primary_{DOWN}$ orientations as a result of curvature developing from different thermal expansion coefficients of $Section_P$ and $Section_S$. Additionally, over the entire firing cycle, shells containing porous stucco blends display a much greater deviation between $Primary_{UP}$ and $Primary_{DOWN}$ traces in comparison to Shell (Tab-$Al_2O_3$) containing only non-porous stucco. This is indicative of a greater magnitude of $\delta_t$ in shells containing porous stucco as both $\varphi_t$ and $\omega_t$ contributions are expected to be equal in each orientation and thus any deviation between the $Primary_{UP}$ and $Primary_{DOWN}$ traces are expected to be the result of the contribution of $\delta_t$. It should be noted that in both shells containing porous stucco the push rod movement in the $Primary_{UP}$ trace shows positive $dT/T_0$ until 1250 °C despite the push rod displaying negative $dT/T_0$ much earlier in the $Primary_{DOWN}$ trace. This was the result of curvature developing within the sample counteracting the effect of through thickness contraction. As such, the push rod shows minimal upwards movement due to the counteracting effects occurring in this period. Such effects can also be observed in the isothermal hold where the $Primary_{UP}$ trace displays a shallow gradient due to curvature counteracting the effect of through thickness contraction. The average push rod movement following the complete firing cycle for each shell variant in each orientation is given in Table 21.

**Table 21** – Average push rod movement of complete shell samples analysed by 3 point bend TMA in $Primary_{UP}$ and $Primary_{DOWN}$ orientation following the complete firing cycle

| | **$Primary_{UP}$ $dT/T_0$ (%)** | | **$Primary_{DOWN}$ $dT/T_0$ (%)** | |
|---|---|---|---|---|
| **Complete shell** | **Average** | **Standard deviation** | **Average** | **Standard deviation** |
| Shell (Tab-$Al_2O_3$) | -2.37 | 0.11 | -2.85 | 0.11 |
| Shell (BD-$Al_2O_3$) | -1.82 | 0.24 | -3.77 | 0.19 |
| Shell (SGB127) | -1.10 | 0.31 | -4.42 | 0.67 |

The push rod displacement values for each individual specimen were calculated throughout the simulated casting cycle using Equation 51. This equation multiplies the $dT/T_0$ value output from the TMA at a given time by the individual $T_0$ value obtained from sample dimensions measured by the TMA prior to firing. This process accounts for variability in $T_0$ values for each individual specimen.

$$\left(\frac{dT}{T_0}\right)_{Time=t} \times T_0 = dT \qquad \text{eq.51}$$

Inputting the average push rod displacement values for a given shell variant in either $Primary_{UP}$ or $Primary_{DOWN}$ orientation into Equation 50; the magnitude and sign of $\delta_t$ can be calculated independently at a given time, removing the effects of $\varphi_t$ and $\omega_t$. As $\delta_t$ equals $\delta$ at time $t$, Equation 44 can be utilised to express $\delta$ throughout the firing cycle as a percentage of the original sample length ($L_0$) which was equal to a constant 20 mm (the span length over which curvature was measured). As such, normalised curvature measured through this method can be compared directly to curvature predicted in Section 5.4 over the same span length.

Curvature values obtained by this method were compared to curvature values predicted from thermal expansion/contraction data of $Section_P$ and $Section_S$ from Section 5.4. As shown in Figure 82, it can be seen that overall, both methods predict a similar quantity of curvature for each shell sample with both instruments achieving analogous firing cycles.

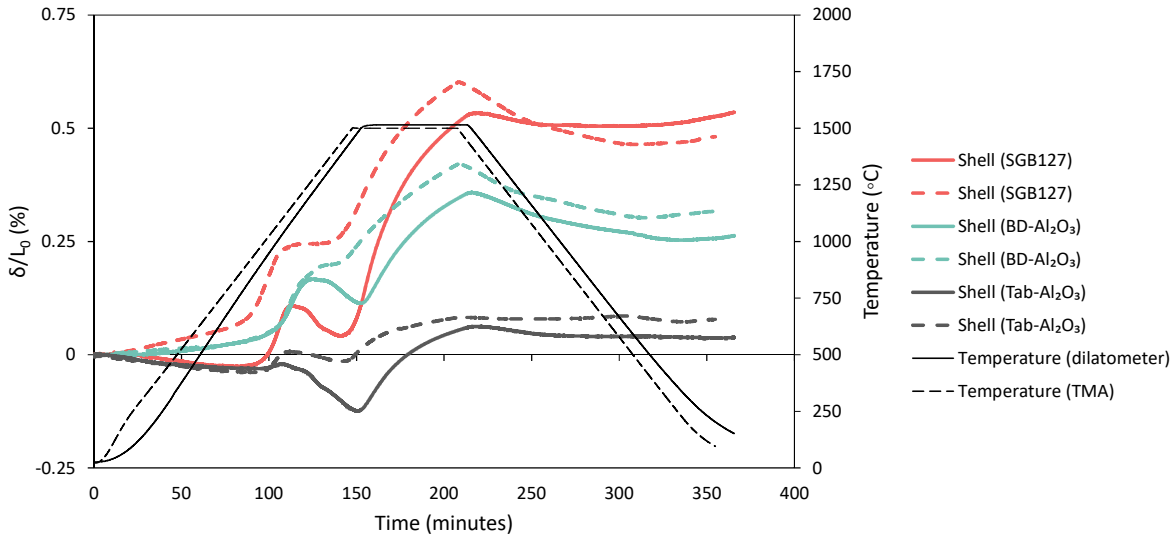



**Figure 82** – Normalised curvature predicted from thermal expansion/contraction of Section$_P$ and Section$_S$ analysed by dilatometer (full lines) compared to normalised curvature measured from 3 point bend TMA method (dashed lines) throughout the simulated casting cycle

As shown in Figure 82, the curvature measured for Shell (SGB127) via TMA method does not overlap with predicted curvature values in the region 25 – 700 °C. This was likely due to the unexpectedly high linear thermal expansion coefficient of section Secondary (SGB127) measured by linear dilatometer in Section 5.3. Excluding this sample it appears a high degree of overlap is present between both methods within the region 25 – 700 °C. As temperature increases above 700 °C the deviation between each method of analysis increases for the same sample which may be influenced by $\varphi_t$, $\omega_t$ or $\delta_t$ not being equal in each orientation tested. However, it is more likely that the curvature predicted from the dilatometer method is measuring the shrinkage freely without constraint from a bonded layer sintering at a different rate; amplified by the effect of force contracting the sample parallel to the layers. This is in contrast to the 3 point bend TMA method where sintering occurs in a constrained state as the section shrinking at a slower rate prevents sintering in the faster shrinking section with force applied perpendicular to the layers. This can explain the smoother trace observed for 3 point bend TMA method between 700 – 1500 °C where constraint between layers prevents curvature quickly changing from a positive gradient to negative gradient as predicted by linear dilatometer method. The quantity of normalised curvature calculated following the complete firing cycle is displayed in Table 22.

**Table 22** – Normalised curvature following the complete simulated casting cycle measured from 3 point bend TMA method for complete shell samples

| **Complete shell** | **Normalised curvature measured from 3 point bend TMA method (%)** |
|---|---|
| Shell (Tab-$Al_2O_3$) | 0.08 |
| Shell (BD-$Al_2O_3$) | 0.32 |
| Shell (SGB127) | 0.48 |

Overall, curvature development measured by 3 point bend TMA method concurs with results predicted using thermal expansion/contraction behaviour of samples representative of $Section_P$ and $Section_S$ for the same shell. This corroborates the hypothesis that curvature develops more dominantly in shells containing porous stucco in secondary layers due to differential expansion/contraction of shell sections.

## 5.7 3D Structured Light Analysis

Utilising 3D structured light analysis the dimensions of fine details in investment casting shells were measured to observe dimensional changes following the simulated casting cycle. Following the experimental procedure outlined in Section 3.1.6.5, shell samples approximately 100 x 120 x 5 mm were analysed before and after the simulated casting cycle. The dimensional change recorded for Shell (Tab-$Al_2O_3$), Shell (BD-$Al_2O_3$) and Shell (SGB127) is shown in Figure 83. It should be noted that in order to minimise the effect of creep due to gravity, samples were placed vertically in a furnace as shown previously in Figure 27. This allowed curvature to develop more freely without hindrance from the weight of the sample.

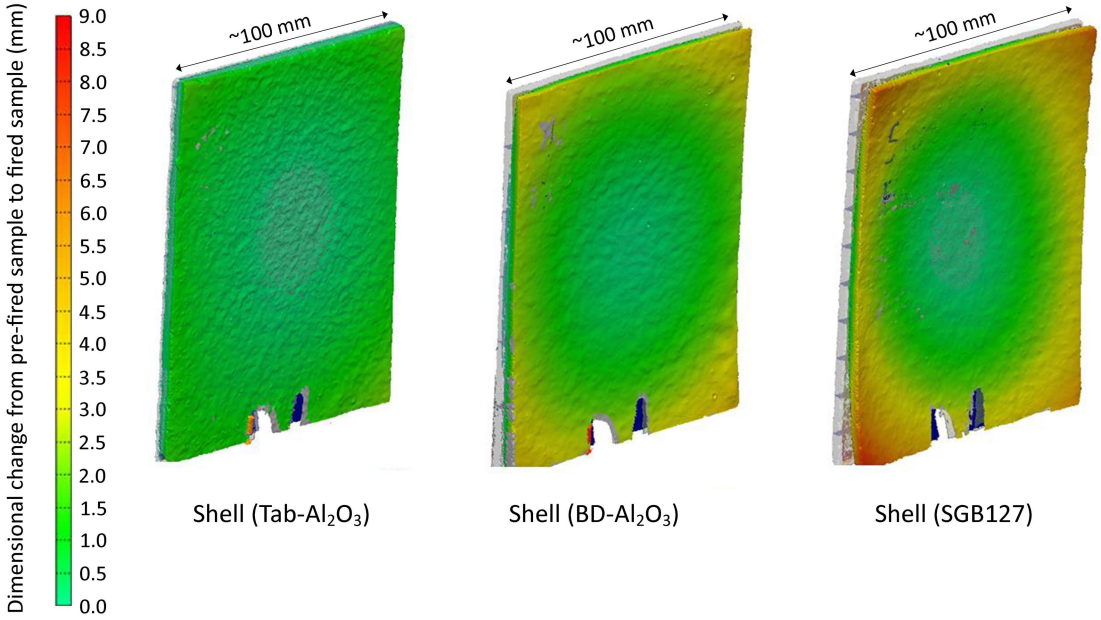



**Figure 83** – 3D structured light analysis showing dimensional change from pre-fired to fired condition

It can be seen that both shell samples containing porous stucco show more curvature in comparison to the shell sample containing non-porous stucco. In addition, it can be seen that curvature develops radially from the centre with greater dimensional change present on sections that are further away from this centre point. This occurs as curvature develops across the entire plane resulting from bi-axial shrinkage of $Section_P$ and $Section_S$. Corners are further away the from centre point and thus show the greatest dimensional change.

In order to quantify the magnitude of curvature, a cross-sectional area is taken through both the X and Y plane of each sample as shown in Figure 84.

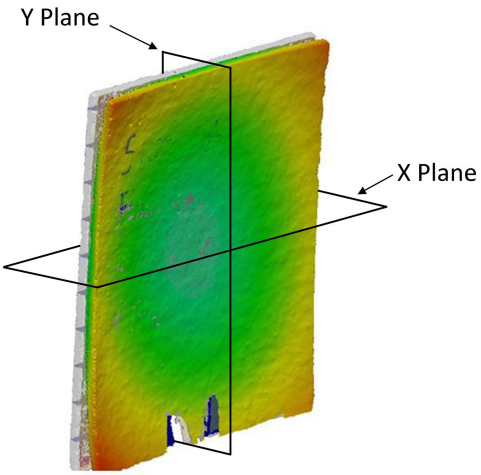



**Figure 84** – Defining X and Y plane for cross-section analysis as shown on sample Shell (SGB127)

An example of a cross-section analysis is given in Figure 85 displaying the original thickness in pre-fired condition ($T_0$), length of arc ($L_{arc}$) and deflection from normal resulting from differential expansion/contraction of sections ($\delta$).

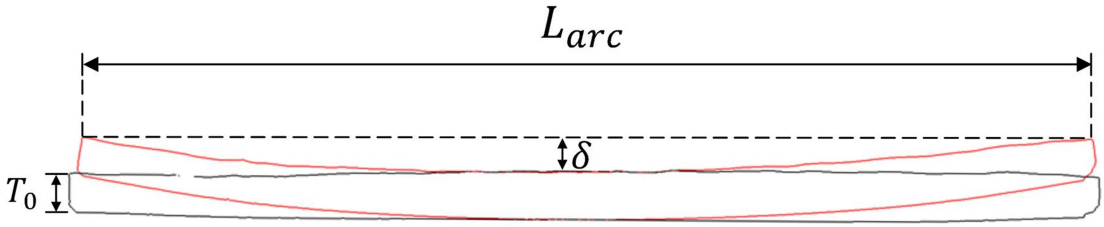



**Figure 85** – Cross-section analysis of Shell (SGB127) in X plane showing pre-fired cross-section in black and fired cross-section in red. Shown on the diagram is original thickness in pre-fired condition ($T_0$), length of arc ($L_{arc}$) and deflection from normal after firing ($\delta$)

The full list of dimensions measured in either the X or Y plane is given in Table 23. It can be seen that $T_0$ values for each shell broadly match values measured by SEM displayed in Table 19. However, it appears the shells containing porous stucco have a thinner nature in comparison to previous analysis. This may result from changes in slurry viscosity or variation in stucco deposition causing a change in thickness within each layer.

**Table 23** – Dimensional analysis of cross-sections in X and Y plane

| Complete shell | X plane | | | Y plane | | |
|---|---|---|---|---|---|---|
| | $L_{arc}$ (mm) | $T_0$ (mm) | $\delta$ (mm) | $L_{arc}$ (mm) | $T_0$ (mm) | $\delta$ (mm) |
| Shell (Tab-$Al_2O_3$) | 98.21 | 6.30 | 0.78 | 126.76 | 6.31 | 0.41 |
| Shell (BD-$Al_2O_3$) | 96.96 | 5.20 | 1.16 | 125.62 | 5.15 | 1.85 |
| Shell (SGB127) | 98.20 | 4.61 | 3.11 | 124.93 | 4.57 | 3.40 |

As $\delta$ was measured over a different arc length for each sample in plane X and Y this cannot be directly compared to previous methods in Sections 5.4 and 5.6 where analysis was conducted over a span of 20 mm. As such, the deflection from normal over 20 mm is calculated from $\delta$ values for the specified $L_{arc}$ value. This was undertaken by calculating the radius of curvature ($\rho$) for each individual sample in either X or Y plane using Equation 43 and inputting the specified $L_{arc}$ and $\delta$ values from Table 23. Equation 43 was then used to calculate the unknown deflection from normal over an arc length of 20 mm using the calculated radius of curvature ($\rho$) which is equal for both arc lengths. This process is illustrated in Figure 86.

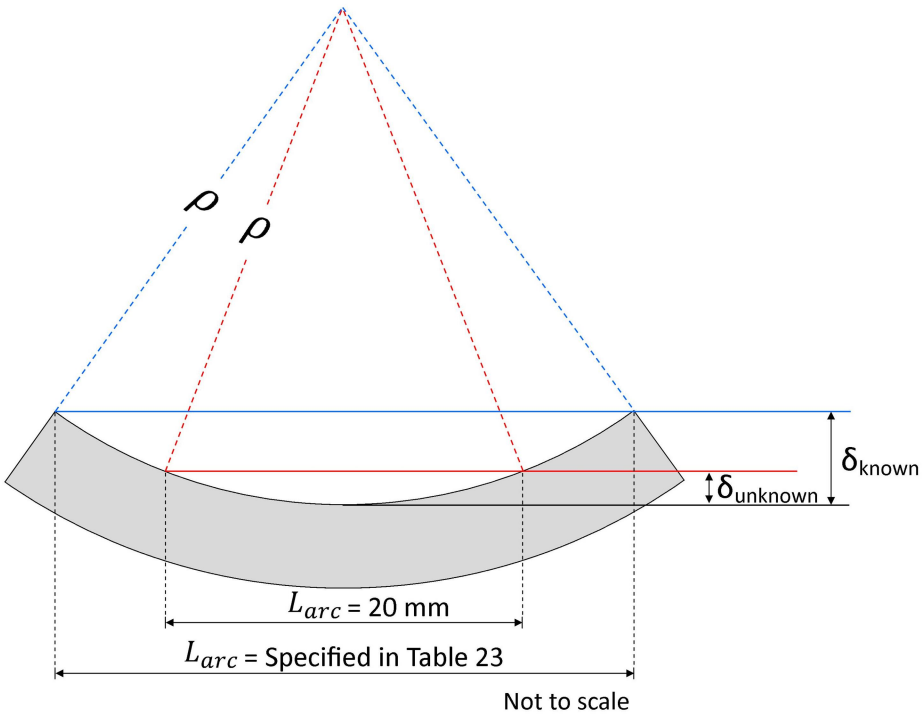



**Figure 86** – Diagram illustrating the unknown deflection from normal for an arc length equal to 20 mm ($\delta_{unknown}$) calculated from deflection for a known arc length ($\delta_{known}$)

Utilising Equation 44 the deflection from normal over a 20 mm arc length was calculated as a percentage of $L_0$ by approximating $L_0$ to $L_{arc}$ (20 mm). This expresses the deflection as normalised curvature to match previous notation in Sections 5.4 and 5.6. These results are displayed in Table 24 using the same curvature notation as shown in Figure 75. It can be seen that high variability in curvature between X and Y planes exists for each shell variant with a systematically higher curvature calculated in the X plane. This may result from curvature developing more freely in the X plane as the Y plane is constricted due to gravity or as a result of influence from curvature developing in the Y plane.

**Table 24** – Normalised curvature following the complete firing cycle measured by 3D structured light imaging method for complete shell samples

| Complete shell | Normalised curvature measured by 3D structured light imaging (%) | | |
|---|---|---|---|
| | X plane | Y plane | Average |
| Shell (Tab-$Al_2O_3$) | 0.16 | 0.05 | 0.11 |
| Shell (BD-$Al_2O_3$) | 0.25 | 0.23 | 0.24 |
| Shell (SGB127) | 0.64 | 0.44 | 0.54 |

## 5.8 Comparison between Methods

The flexural deformation characterised by all three methods is displayed in Figure 87. It can be seen that each method predicts/measures a similar magnitude of curvature following the simulated casting cycle giving comparable results for each shell variant. As such, it is without a doubt that curvature developing in shells containing porous stucco results from differential thermal expansion/contraction of shell sections. However, analysis cannot explain the consistently higher curvature recorded for Shell (SGB127) in comparison to Shell (BD-$Al_2O_3$). One explanation for this phenomenon is that the lower volume of SGB127 stucco deposited on the slurry (as measured in Section 4.3.1) produces a higher ratio of slurry to stucco in comparison to Shell (BD-$Al_2O_3$). Subsequently the lower concentration of stucco in $Section_S$ in Shell (SGB127) allows shrinkage to occur more freely than Shell (BD-$Al_2O_3$) leading to the difference in curvature observed for each sample.

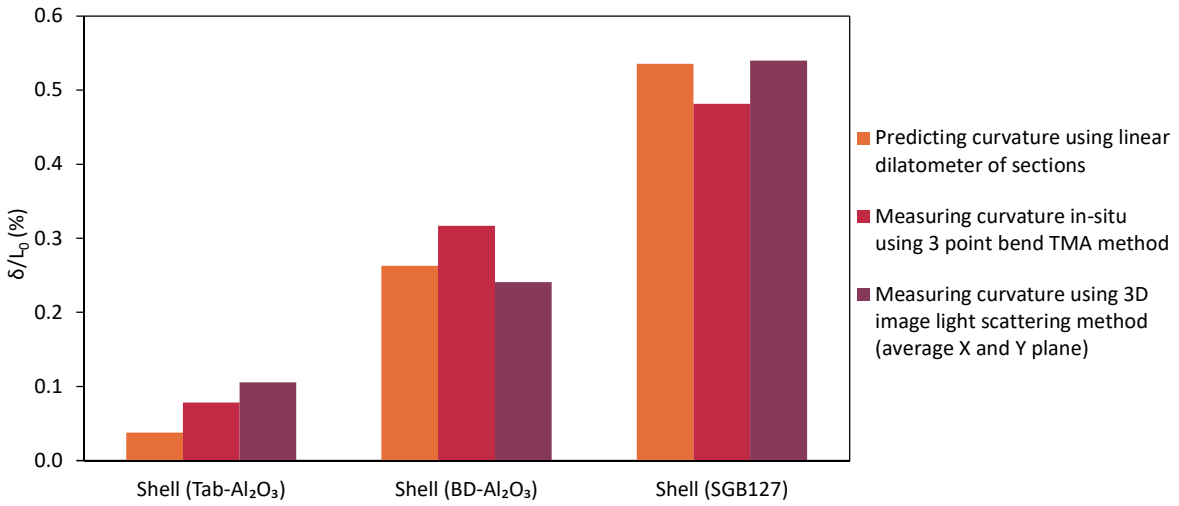



**Figure 87** – Normalised curvature following the complete simulated casting cycle characterised by three methods

## 5.9 Effect of Flexural Deformation on Casting

The high degree of deformation observed in shells containing porous stucco will produce dimensional changes within the shell as the shell is fired. Assuming that the shell remains whole throughout the firing cycle, the cast component will possess significant dimensional differences in comparison to the original wax pattern as a result. This occurs as the alloy cools and solidifies within the deformed shell retaining the shape of the deformed mould. This effect is amplified over longer distances as described by Equation 43 where the magnitude of $\delta$ is proportional to $L_{arc}$ squared for a given radius of curvature. This produces greater dimensional change on larger components.

In addition, the shell may also crack as a result of excessive deformation. This effect is expected to have the greatest impact in edge regions of the shell as the formation of concave surfaces along the walls result in tensile stress developing on the outside edge and compressive stress on the inside edge as shown in Figure 88. Such stresses are expected to increase in magnitude as the curvature increases during the firing cycle and the edge must deform to a greater degree to remain bonded to both walls. If a high magnitude of stress is exerted on the edge, failure will occur through cracking or delamination to relieve stress. Failure occurring early in the firing cycle will result in the shell continuing to deform as the firing cycle progresses leading to opening of initially hairline fractures to produce large

cavities in the shell. Such behaviour is shown in Figure 89 where extreme cracking and deformation can be observed indicative of fracture early in the firing cycle as predicted in Section 5.5. It should be noted that no such defects were observed in Shell (Tab-$Al_2O_3$).

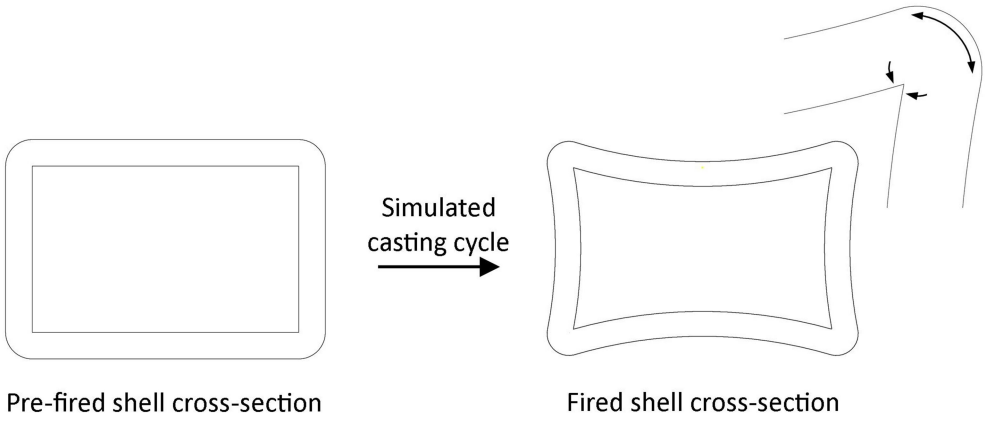



**Figure 88** – Cross-section of pre-fired shell exhibiting curvature following the simulated casting cycle with a magnified image showing development of tensile and compressive stresses concentrated in the edge regions




**Figure 89** – Examples of failure in Shell (BD-$Al_2O_3$) following the simulated casting cycle indicative of fracture early in the firing cycle

## 5.10 Conclusions

The flexural deformation resulting from differential thermal expansion/contraction of shell sections has been characterised by three complimentary methods. Each method has provided evidence that porous stucco sintering in the early stages of the firing cycle produces a highly porous, shrinkage prone structure as the stucco particles shrink away from the slurry matrix. This effect was likely amplified due to the presence of voids distributed throughout the shell prior to firing and a greater volumetric ratio of slurry to stucco in shells containing porous stucco. In contrast, shells containing only non-porous stucco inhibit shrinkage due to the presence of multiple planes of refractory particles which cannot easily slide past each other during the firing cycle. As such, the application of monolithic porous stucco in secondary layers leads to curvature development as $Section_S$ shrinks to a greater degree than $Section_P$. As a result of this finding it was imperative that the water absorbing stucco remain dimensionally stable in the firing process or measures be taken to prevent excess shrinkage in the layers containing porous stucco to avoid shell deformation and cracking. These solutions are explored in Chapter 6.

# 6. Solutions to Flexural Deformation

## 6.1 Introduction

In this Chapter, two solutions are proposed to counteract the flexural deformation observed when applying monolithic porous stucco in the secondary layers of investment casting shells whilst maintaining the surface finish properties offered by the presence of primary layers. The first solution looks to encapsulate mesoporous alumina within a sintered macroporous α-$Al_2O_3$ framework to produce a material capable of absorbing water at room temperature, but remain dimensionally stable at high temperature. The second solution looks to apply non-porous stucco on the final layer of the shell. Both solutions were evaluated for curvature development using techniques developed in Chapter 5 to assess if porous stucco can be incorporated into the shell without causing excessive flexural deformation.

## 6.2 Composite Stucco

The drive for a thermally stable, porous material leads to the conclusion a composite structure combining the high temperature stability of densified α-$Al_2O_3$ with the water absorbing capabilities of mesoporous alumina is a feasible solution. The described material is shown in Figure 90 displaying an α-$Al_2O_3$ framework with interconnected porosity saturated with mesoporous $Al_2O_3$ within the pore volume of the α-$Al_2O_3$ framework. Complexity arises in producing this material as the α-$Al_2O_3$ framework must be sintered prior to the addition of the mesoporous alumina to prevent the collapse of the mesoporous structure at high temperature. Additionally, all external mesoporous alumina should be kept to a minimum to prevent volumetric shrinkage at high temperature.

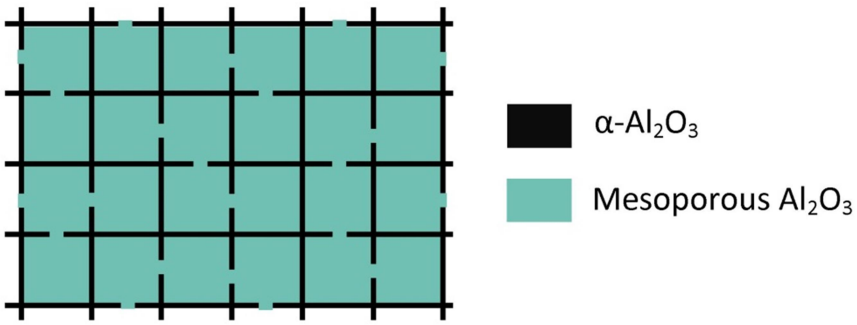



**Figure 90** – Cross-section of the proposed composite material displaying interconnected porosity throughout the structure

### 6.2.1 Synthesis of α-$Al_2O_3$ Framework

The procedure for synthesising the α-$Al_2O_3$ framework (detailed in Section 3.2.6) was designed around a burnout and sintering process as proposed by Gregorova et al. utilising wheat flour and alumina powder [81]. The schematic for the procedure is given in Figure 91. Procedure milling times, filler ratios and firing cycles were tailored to produce a highly porous material which displayed minimal shrinkage throughout the simulated casting cycle with sufficient mechanical strength to endure handling without fracture. Following completion of the synthesis route the material is denoted αFrame.

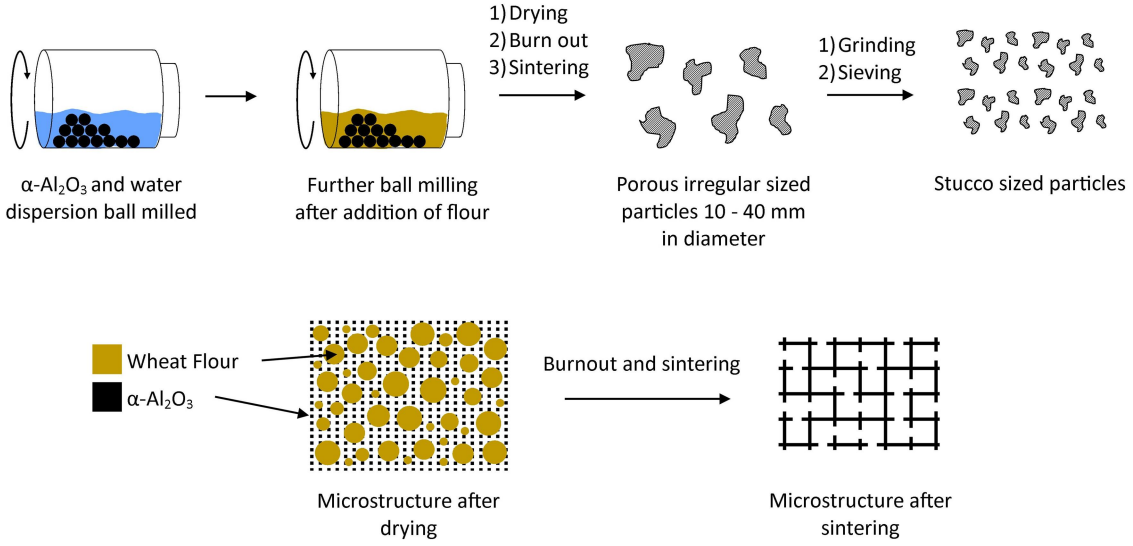



**Figure 91** – Synthesis route for α-$Al_2O_3$ framework denoted αFrame

### 6.2.2 Characterisation of α-$Al_2O_3$ Framework

#### 6.2.2.1 Scanning Electron Microscopy (SEM)

SEM analysis of the αFrame particles is displayed in Figures 92, 93 and 94. It can be seen that the structure is highly porous, attaining a range of interconnected pore sizes throughout the material, producing a structure inhomogeneous in nature. This may be the result of flour particles agglomerating which form large holes in the structure once burnt out. At higher magnification particle-particle necking can be observed between primary α-$Al_2O_3$ grains with each grain displaying a rounded nature. This occurs as grains minimise surface energy by forming contacts between neighbouring particles and reducing surface area at high temperature.

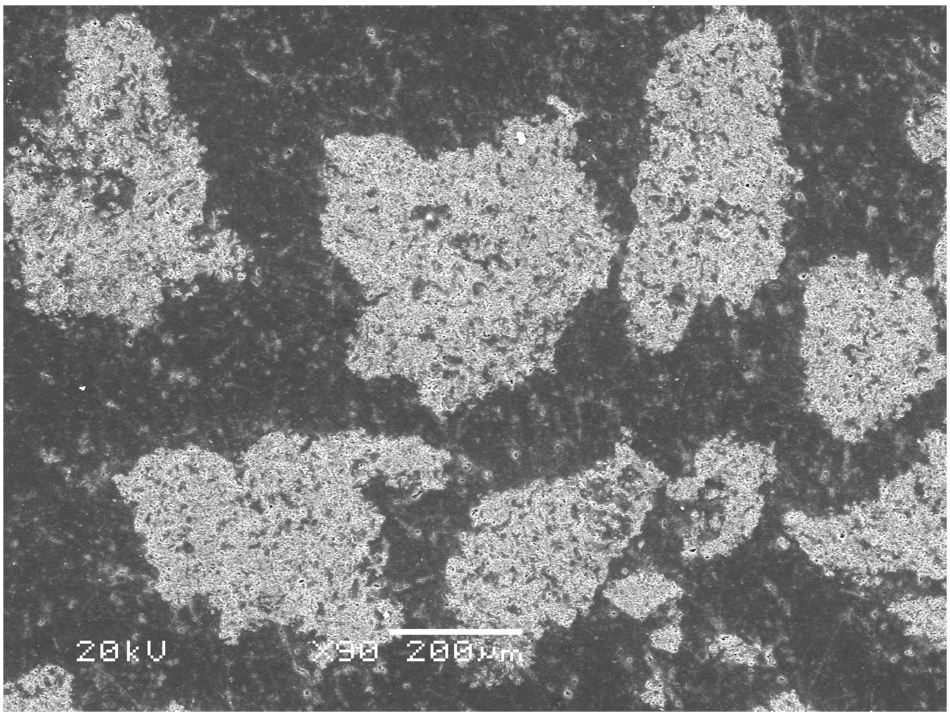



**Figure 92** – SEM image of αFrame particles at 90X magnification showing porosity in the grains and the angular nature of the particles resulting from the grinding process

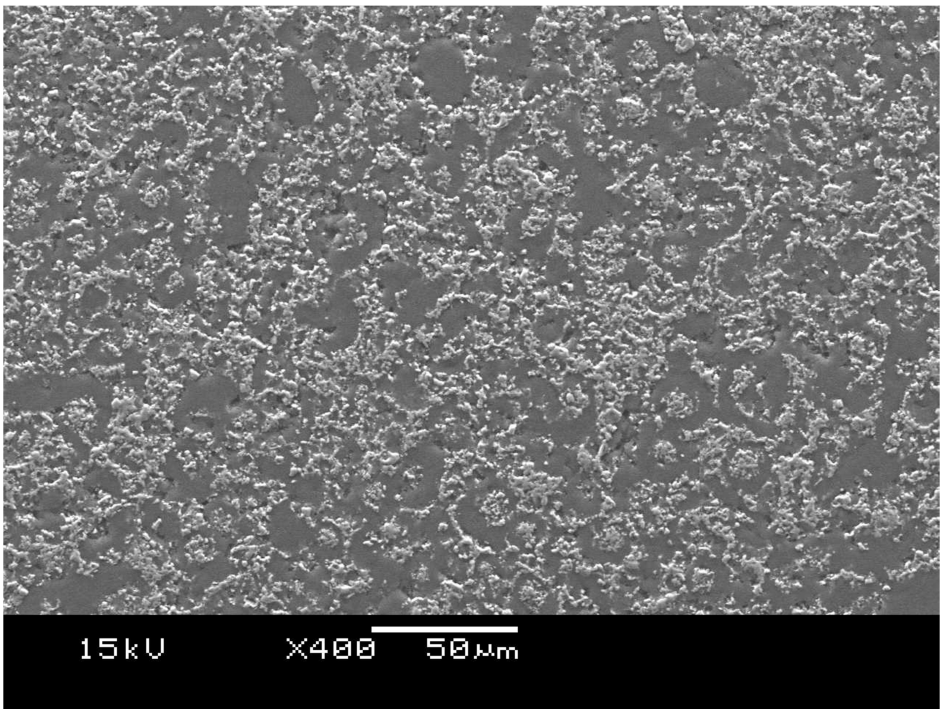



**Figure 93** – SEM image of αFrame particle at 400X magnification

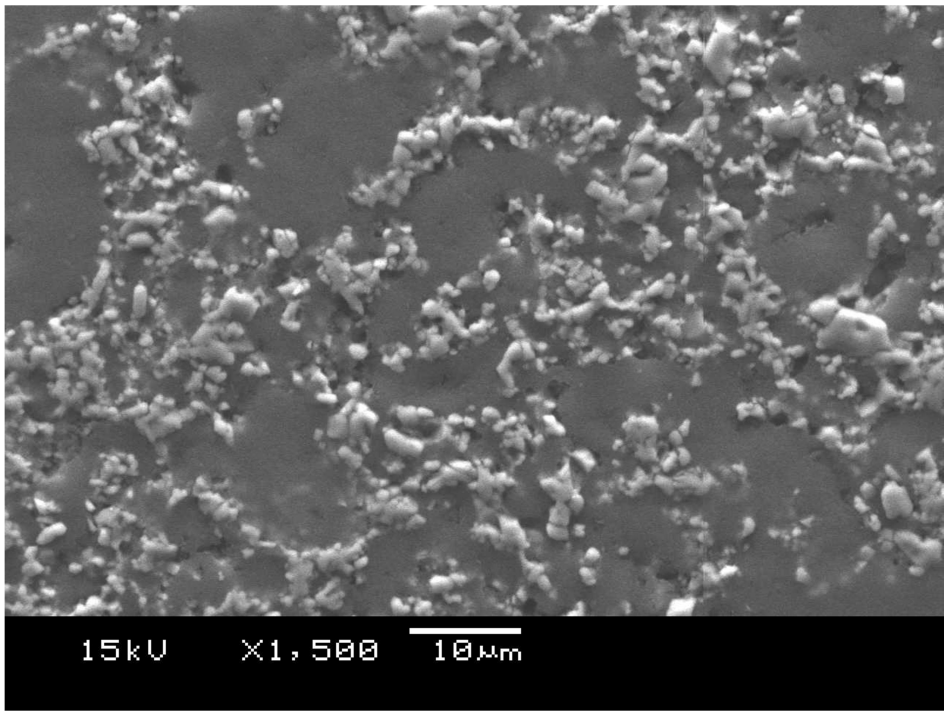



**Figure 94** – SEM image of αFrame particle at 1500X magnification showing particle-particle necking

6.2.2.2 Archimedes' Porosity

Archimedes' porosity was carried out on αFrame material taken before the grinding step, approximately 10 – 40 mm in diameter. A total of three repeat analyses were conducted using the procedure outlined in Section 3.1.1.8. Using this method the bulk density, true density and porosity of the material were characterised. The results are shown in Table 25.

**Table 25** – Bulk density, true density and porosity of αFrame material calculated by Archimedes method

| | **Bulk density ($g\ cm^{-3}$)** | | **True density ($g\ cm^{-3}$)** | | **Porosity ($cm^3_{pore}\ cm^{-3}_{bulk}$)** | |
|---|---|---|---|---|---|---|
| **Sample** | **Average** | **Standard deviation** | **Average** | **Standard deviation** | **Average** | **Standard deviation** |
| αFrame | 1.86 | 0.18 | 3.89 | 0.17 | 0.52 | 0.03 |

As shown in Table 25, the method has accurately calculated the true density of α-$Al_2O_3$ in comparison to literature sources of 3.98 g $cm^{-3}$ [134]. It was also found that a porosity of approximately 50 vol% was attained for αFrame, producing a reasonable pore volume to fill with water absorbing, mesoporous alumina in later stages.

### 6.2.3 Synthesis of α-$Al_2O_3$ Framework Composite

The procedure required to saturate the internal structure of the αFrame material with mesoporous alumina involves impregnating the macroporous αFrame material with alumina sol. The impregnated material was then dried and subsequently fired to transform the boehmite phase to mesoporous alumina. However, as drying takes place only a small volume of dried alumina sol deposits within the structure as a large volume of liquid evaporates. To maximise the volume of dried alumina sol deposited in the αFrame structure a high solids loading, low viscosity alumina sol was required. For this reason a commercial peptized boehmite sol (Remasol A20) was used. To further increase the volume of boehmite in the αFrame structure, repeated impregnation and drying steps were performed prior to phase transformation. Once the framework has been vacuum impregnated and dried a given number of times firing was conducted at 700 °C to transform the dried alumina sol into mesoporous alumina. The mesoporous alumina is denoted $BD^{I}$-$Al_2O_3$ due to similarities in composition and properties to the material BD-$Al_2O_3$. The αFrame material impregnated and dried n number of times is denoted αFrame-$Impreg_n$ following the firing procedure to transform the dried alumina sol into $BD^{I}$-$Al_2O_3$. The schematic for the material synthesis route is shown in Figure 95 visualising the synthesis procedure outlined in Section 3.2.6.

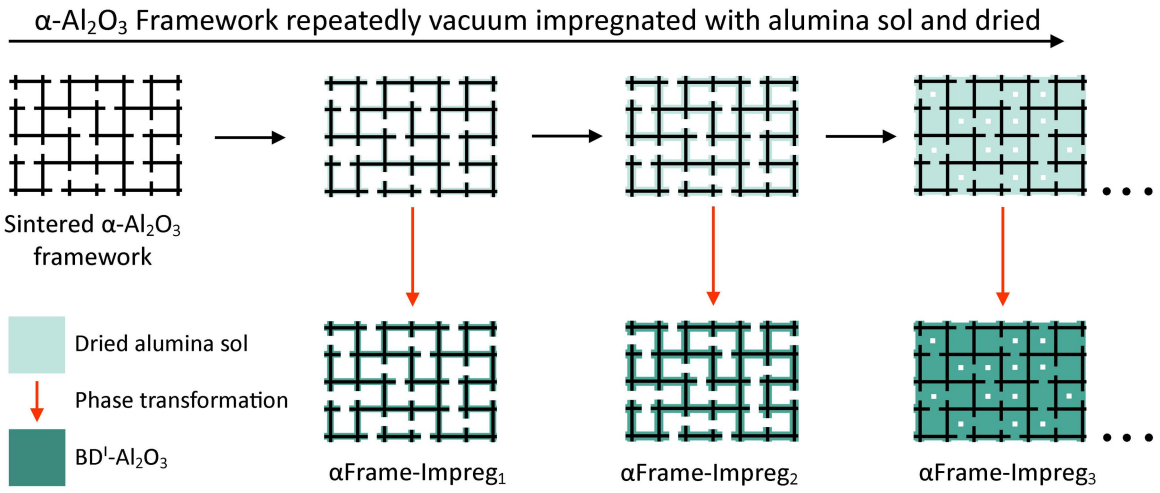



**Figure 95** – Schematic of synthesis route for production of α-$Al_2O_3$ framework composite

6.2.3.1 Formulation and Process Optimisation

To determine the optimum number of vacuum impregnation and drying steps required to saturate the pores within the αFrame material with mesoporous alumina, nitrogen adsorption analysis was implemented. Utilising this technique the surface area and pore volume of composite materials can be determined to characterise the weight and volume fractions of each component. The surface area and pore volume for composite materials and their isolated constituents is shown in Table 26 and 27 respectively. Both composite and isolated materials containing $BD^{I}$-$Al_2O_3$ were fired in identical firing cycles as described in Section 3.2.6. All materials were collected between 200 – 600 µm sieves before analysis was completed with each sample analysed a total of three times. It should be noted that pore volume as measured by the BJH method can only measure pores with a diameter 2 – 50 nm and as such pore volume as characterised by this technique excludes macropore volume.

**Table 26** – Average surface area of composite materials and their constituent materials analysed by nitrogen adsorption

| Sample | Number of vacuum impregnation steps | Surface area ($m^2$ $g^{-1}$) | |
|---|---|---|---|
| | | Average | Standard deviation |
| αFrame | - | 0.65 | 0.02 |
| $BD^{I}$-$Al_2O_3$ | - | 156.86 | 0.78 |
| αFrame-$Impreg_1$ | 1 | 16.71 | 1.11 |
| αFrame-$Impreg_2$ | 2 | 25.00 | 0.46 |
| αFrame-$Impreg_3$ | 3 | 32.06 | 1.13 |
| αFrame-$Impreg_4$ | 4 | 38.45 | 0.57 |
| αFrame-$Impreg_5$ | 5 | 40.62 | 0.56 |
| αFrame-$Impreg_6$ | 6 | 43.13 | 0.97 |
| αFrame-$Impreg_7$ | 7 | 44.03 | 1.04 |
| αFrame-$Impreg_8$ | 8 | 44.40 | 1.11 |

**Table 27** – Average pore volume of composite materials and their constituent materials analysed by nitrogen adsorption

| Sample | Number of vacuum impregnation steps | Pore volume ($cm^3\ g^{-1}$) | |
|---|---|---|---|
| | | Average | Standard deviation |
| αFrame | - | 0.0012 | 0.00004 |
| $BD^I$-$Al_2O_3$ | - | 0.3906 | 0.0039 |
| αFrame-$Impreg_1$ | 1 | 0.0483 | 0.0029 |
| αFrame-$Impreg_2$ | 2 | 0.0735 | 0.0021 |
| αFrame-$Impreg_3$ | 3 | 0.0917 | 0.0032 |
| αFrame-$Impreg_4$ | 4 | 0.1085 | 0.0016 |
| αFrame-$Impreg_5$ | 5 | 0.1185 | 0.0015 |
| αFrame-$Impreg_6$ | 6 | 0.1246 | 0.0017 |
| αFrame-$Impreg_7$ | 7 | 0.1260 | 0.0017 |
| αFrame-$Impreg_8$ | 8 | 0.1297 | 0.0045 |

Using data in Tables 26 and 27 the unknown mass fraction of a given composite material was calculated assuming the two components were in the same state in the composite material as analysed independently and thus did not interact. This was highly probable as seeding peptized boehmite with α-$Al_2O_3$ does not aid in the phase transition to α-$Al_2O_3$ until temperatures above 1100 ˚C [175]. Thus, firing to 700 ˚C to phase transform boehmite into mesoporous alumina is unlikely to catalyse the collapse of pores. The unknown mass fraction of a given component was calculated by assuming the surface area or pore volume of the composite material resulted from the weighted mass fraction of each component as shown by Equations 52 and 55. Combining Equations 52 and 53 gives Equation 54 from which the mass fraction of $BD^I$-$Al_2O_3$ can be calculated using surface area data. Combining Equations 55 and 53 gives Equation 56 from which the mass fraction of $BD^I$-$Al_2O_3$ can be calculated using pore volume data. Using either surface area or pore volume data the mass fraction of $BD^I$-$Al_2O_3$ was calculated for each composite material. This is shown in Table 29.

$$S_{Composite} = \left(S_{BD^I-Al_2O_3} \times F_{mass(BD^I-Al_2O_3)}\right) + \left(S_{\alpha Frame} \times F_{mass(\alpha Frame)}\right) \quad \text{eq.52}$$

$$F_{mass(\alpha Frame)} + F_{mass(BD^I-Al_2O_3)} = 1 \quad \text{eq.53}$$

$$F_{mass(BD^I-Al_2O_3)} = \frac{S_{Composite} - S_{\alpha Frame}}{S_{BD^I-Al_2O_3} - S_{\alpha Frame}} \quad \text{eq.54}$$

| | |
|---|---|
| $S_{Composite}$ | Surface area of composite material ($m^2\ g^{-1}$) |
| $S_{BD^I-Al_2O_3}$ | Surface area of BD$^I$-$Al_2O_3$ ($m^2\ g^{-1}$) |
| $F_{mass(BD^I-Al_2O_3)}$ | Mass fraction of BD$^I$-$Al_2O_3$ (-) |
| $S_{\alpha Frame}$ | Surface area of αFrame ($m^2\ g^{-1}$) |
| $F_{mass(\alpha Frame)}$ | Mass fraction of αFrame (-) |

$$P_{Composite} = \left(P_{BD^I-Al_2O_3} \times F_{mass(BD^I-Al_2O_3)}\right) + \left(P_{\alpha Frame} \times F_{mass(\alpha Frame)}\right) \quad \text{eq.55}$$

$$F_{mass(BD^I-Al_2O_3)} = \frac{P_{Composite} - P_{\alpha Frame}}{P_{BD^I-Al_2O_3} - P_{\alpha Frame}} \quad \text{eq.56}$$

| | |
|---|---|
| $P_{Composite}$ | Pore volume of composite material ($cm^3\ g^{-1}$) |
| $P_{BD^I-Al_2O_3}$ | Pore volume of BD$^I$-$Al_2O_3$ ($cm^3\ g^{-1}$) |
| $P_{\alpha Frame}$ | Pore volume of αFrame ($cm^3\ g^{-1}$) |

To calculate the volume fraction of BD$^I$-$Al_2O_3$ with respect to the entire volume of the composite material (comprising BD$^I$-$Al_2O_3$, α-$Al_2O_3$ and empty macropore volume), Equation 57 was proposed.

$$F_{vol(BD^I-Al_2O_3)} = \frac{Volume\ of BD^I - Al_2O_3}{Bulk\ volume\ of\ composite} = \frac{\left(\frac{F_{mass(BD^I-Al_2O_3)}}{\rho_{BD^I-Al_2O_3}}\right)}{\left(\frac{F_{mass(\alpha Frame)}}{\rho_{\alpha Frame}}\right)} \quad \text{eq.57}$$

| | |
|---|---|
| $F_{vol(BD^I-Al_2O_3)}$ | Volume fraction BD$^I$-$Al_2O_3$ (-) |
| $\rho_{BD^I-Al_2O_3}$ | Bulk density of BD$^I$-$Al_2O_3$ ($g\ cm^{-3}$) |
| $\rho_{\alpha Frame}$ | Bulk density of αFrame ($g\ cm^{-3}$) |

This calculation utilised the bulk density of BD$^{I}$-$Al_2O_3$ ($\rho_{BD^{I}-Al_2O_3}$) as displayed in Table 28, calculated from Equation 31 using the pore volume of BD$^{I}$-$Al_2O_3$ from Table 27 and the true density of BD$^{I}$-$Al_2O_3$ measured by helium pycnometer from Table 28. In addition the bulk density of αFrame ($\rho_{\alpha Frame}$) was required which is displayed in Table 25 as calculated by Archimedes' method. Using these values, the volume fraction of BD$^{I}$-$Al_2O_3$ was calculated for each composite material utilising Equation 57. This information is displayed in Table 29.

**Table 28** – True density of BD$^{I}$-$Al_2O_3$ calculated from helium pycnometer analysis and bulk density of BD$^{I}$-$Al_2O_3$ calculated from helium pycnometer and nitrogen adsorption data

| | True density (g cm$^{-3}$) | | |
|---|---|---|---|
| **Sample** | **Average** | **Standard deviation** | **Bulk density (g cm$^{-3}$)** |
| BD$^{I}$-$Al_2O_3$ | 3.45 | 0.01 | 1.47 |

Using the volumetric porosity of αFrame material (equal to 0.52 as calculated in Section 6.2.2.2) the volume fraction of pores saturated with BD$^{I}$-$Al_2O_3$ was calculated using Equation 58. This equation assumes that if the volume fraction of BD$^{I}$-$Al_2O_3$ is equal to the volume fraction of pores within the αFrame material, the pores are 100 % saturated. The volume fraction of pores within the αFrame structure saturated with BD$^{I}$-$Al_2O_3$ ($\tau$) for each composite material is displayed in Table 29. This is displayed graphically in Figure 96.

$$\tau = \frac{Volume\ fraction\ of\ BD^{I} - Al_2O_3}{Volume\ fraction\ of\ pores\ in\ \alpha Frame} = \frac{F_{vol(BD^{I}-Al_2O_3)}}{F_{vol(pore)}} \qquad \text{eq.58}$$

$\tau$ Volume fraction of pores in αFrame saturated with BD$^{I}$-$Al_2O_3$ (-)

$F_{vol(pore)}$ Volume fraction of pores in αFrame (-)

**Table 29** – Mass and volume fractions of BD$^{I}$-$Al_2O_3$ in composite materials following a given number of vacuum impregnation steps calculated from surface area or pore volume of each material with the accompanying percentage saturation of pores in each material

| | Calculated from surface area | | | Calculated from pore volume | | |
|---|---|---|---|---|---|---|
| **Sample** | $F_{mass(BD^I-Al_2O_3)}$ | $F_{vol(BD^I-Al_2O_3)}$ | $\tau$ (%) | $F_{mass(BD^I-Al_2O_3)}$ | $F_{vol(BD^I-Al_2O_3)}$ | $\tau$ (%) |
| αFrame-Impreg$_1$ | 0.10 | 0.15 | 28 | 0.12 | 0.17 | 33 |
| αFrame-Impreg$_2$ | 0.16 | 0.23 | 45 | 0.19 | 0.29 | 56 |
| αFrame-Impreg$_3$ | 0.20 | 0.32 | 61 | 0.23 | 0.38 | 74 |
| αFrame-Impreg$_4$ | 0.24 | 0.40 | 78 | 0.28 | 0.48 | 93 |
| αFrame-Impreg$_5$ | 0.26 | 0.44 | 84 | 0.30 | 0.55 | 105 |
| αFrame-Impreg$_6$ | 0.27 | 0.47 | 91 | 0.32 | 0.59 | 113 |
| αFrame-Impreg$_7$ | 0.27 | 0.49 | 94 | 0.31 | 0.60 | 115 |
| αFrame-Impreg$_8$ | 0.28 | 0.49 | 95 | 0.33 | 0.62 | 120 |

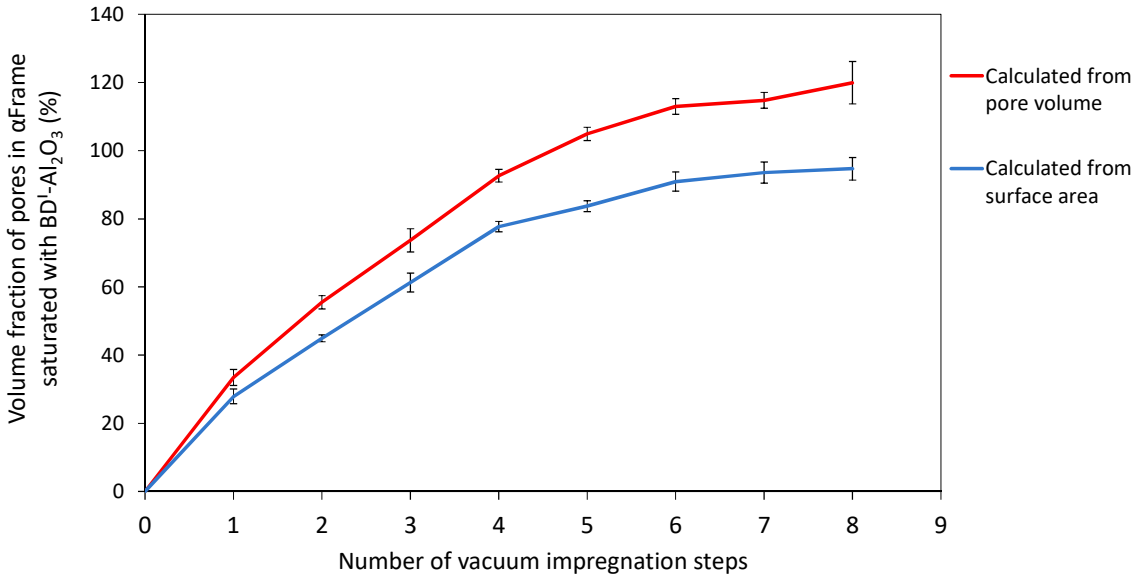



**Figure 96** – Volume fraction of pores in αFrame saturated with BD$^{I}$-$Al_2O_3$ ($\tau$) following a given number of vacuum impregnation steps calculated from surface area or pore volume data

As shown in Figure 96, the quantity of $BD^{I}$-$Al_2O_3$ within the αFrame structure increases with successive vacuum impregnation steps as calculated via surface area or pore volume. With each additional step, the quantity of alumina sol impregnated decreases as the free pore volume inside the αFrame material reduces after each successive step. It can also be seen that calculating saturation ($\tau$) via pore volume data systematically predicts a greater volume of $BD^{I}$-$Al_2O_3$ within the αFrame structure than calculation via surface area data. The reason for this occurring may result from structural changes taking place within the $BD^{I}$-$Al_2O_3$ component when in close proximity to α-$Al_2O_3$ framework upon firing. As such, the $BD^{I}$-$Al_2O_3$ component likely possesses a higher pore volume or lower surface area in the composite material in comparison to the material analysed independently.

It can also be observed that as the number of steps increases a plateau is reached whereby a greater number of vacuum impregnation steps appear to yield little benefit. Additionally, evidence is present that external $BD^{I}$-$Al_2O_3$ exists, causing the saturation of pores to read greater than 100 vol% when calculated via pore volume method. This likely arises from poor draining of excess alumina sol following the vacuum impregnation process, leaving liquid sol present between particles; this then dries outside the αFrame structure. External $BD^{I}$-$Al_2O_3$ will result in significant shrinkage upon firing at casting temperatures and thus will lead to flexural deformation in shells containing this material in secondary layers as explained in Chapter 5. In order to counteract this, a mild grinding step was implemented on αFrame material vacuum impregnated and dried 8 times prior to phase transition to remove the external coverage of dried alumina sol. This was carried out by rubbing the particles together by hand in a fume cupboard and removing fines with a 200 μm sieve prior to phase transition (procedure detailed in Section 3.2.6). After implementing this additional cleaning step the material is denoted αFrame-$Impreg_8$-Clean following the phase transition of the dried alumina sol. The difference in external coverage of $BD^{I}$-$Al_2O_3$ can be seen from SEM analysis of αFrame-$Impreg_8$-Clean in comparison to αFrame-$Impreg_8$, this is shown in Figures 97 and 98.

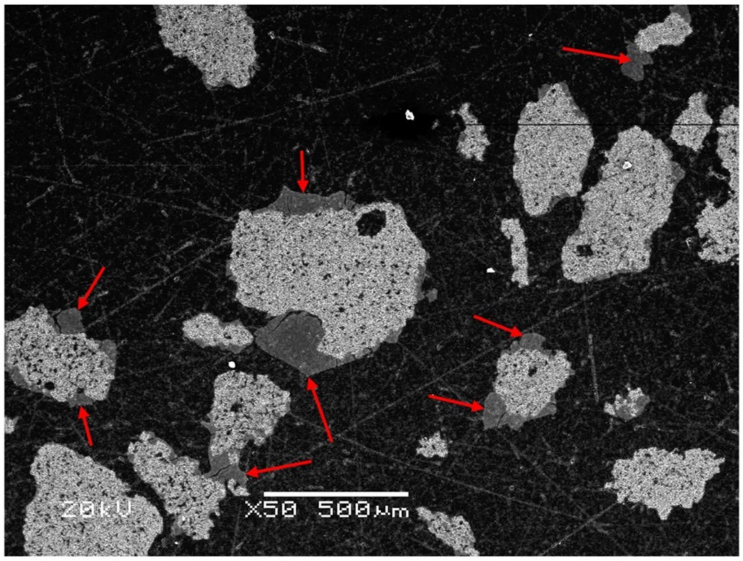



**Figure 97** – SEM image of αFrame-Impreg$_8$ particles showing external coverage of BD$^{I}$-$Al_2O_3$ as highlighted by red arrows

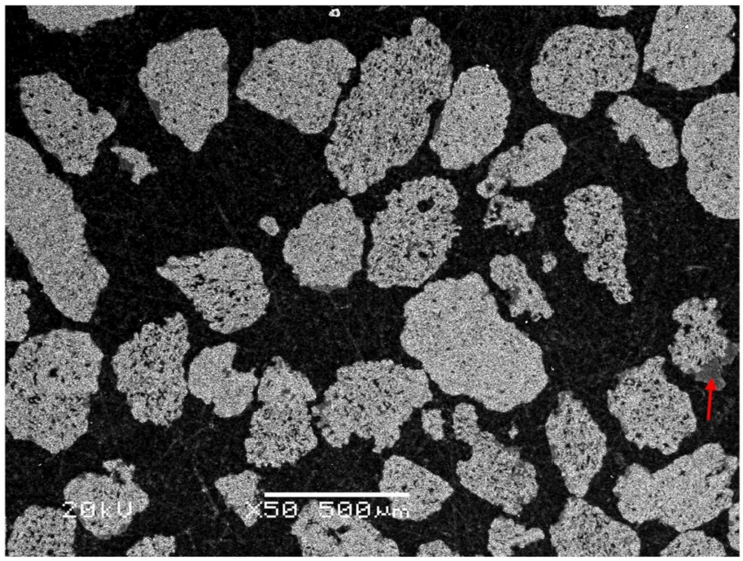



**Figure 98** – αFrame-Impreg$_8$-Clean particles showing minimal external coverage of BD$^{I}$-$Al_2O_3$ as highlighted by the red arrow

The αFrame-Impreg$_8$-Clean material was analysed using nitrogen adsorption to attain surface area and pore volume data for three repeat analyses, this is displayed in Table 30. Using Equations 54 and 56 the mass fraction of BD$^I$-$Al_2O_3$ was calculated using either surface area or pore volume data. The corresponding volume fraction was then calculated from Equation 57. Using this value the volume fraction of pores in αFrame saturated with BD$^I$-$Al_2O_3$ ($\tau$) was calculated from Equation 58. The mass fraction, volume fraction and percentage saturation are displayed in Table 31. The calculated volume fraction of pores in αFrame saturated with BD$^I$-$Al_2O_3$ ($\tau$) for αFrame-Impreg$_8$ and αFrame-Impreg$_8$-Clean is displayed graphically in Figure 99 as calculated by either pore volume of surface area data. This emphasises the effect of removing the external BD$^I$-$Al_2O_3$.

**Table 30** – Average pore volume and surface area of αFrame-Impreg$_8$-Clean analysed by nitrogen adsorption

| | **Surface area ($m^2\ g^{-1}$)** | | **Pore volume ($cm^3\ g^{-1}$)** | |
|---|---|---|---|---|
| **Sample** | **Average** | **Standard deviation** | **Average** | **Standard deviation** |
| αFrame-Impreg$_8$-Clean | 35.04 | 0.93 | 0.0986 | 0.0023 |

**Table 31** – Mass and volume fractions of BD$^I$-$Al_2O_3$ in αFrame-Impreg$_8$-Clean calculated from surface area or pore volume of each material with the accompanying saturation of pores in the material

| | **Calculated from surface area** | | | **Calculated from pore volume** | | |
|---|---|---|---|---|---|---|
| **Sample** | $F_{mass(BD^I-Al_2O_3)}$ | $F_{vol(BD^I-Al_2O_3)}$ | $\tau$ (%) | $F_{mass(BD^I-Al_2O_3)}$ | $F_{vol(BD^I-Al_2O_3)}$ | $\tau$ (%) |
| αFrame-Impreg$_8$-Clean | 0.22 | 0.36 | 69 | 0.25 | 0.42 | 81 |

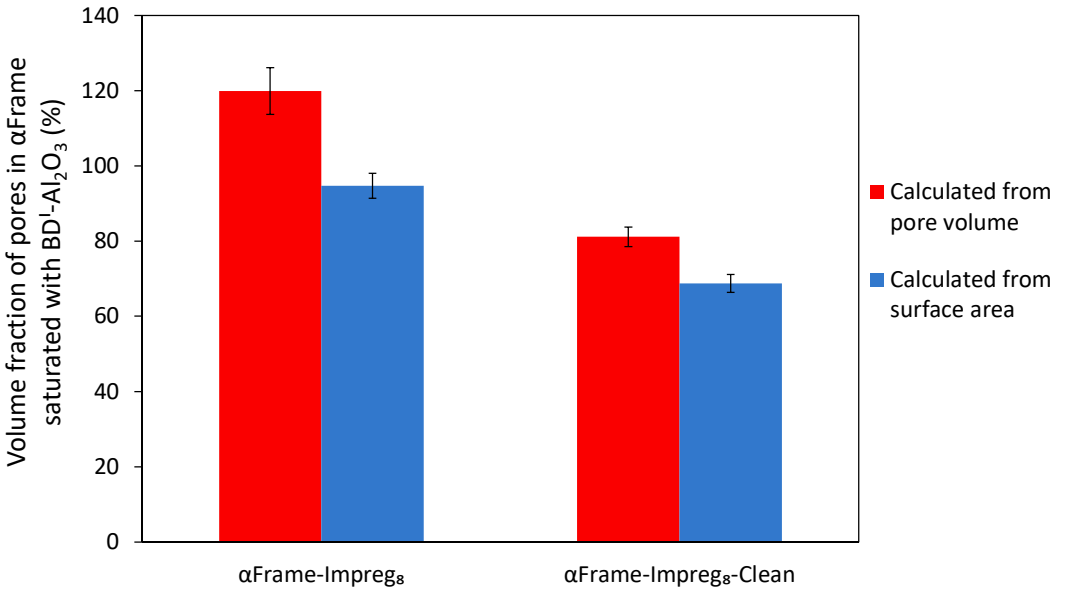



**Figure 99** – Volume fraction of αFrame saturated with BD$^{I}$-$Al_2O_3$ ($\tau$) for αFrame-Impreg$_8$ and αFrame-Impreg$_8$-Clean calculated from surface area or pore volume data

As shown in Figure 99, the removal of external BD$^{I}$-$Al_2O_3$ has reduced the calculated pore volume of αFrame saturated with BD$^{I}$-$Al_2O_3$ ($\tau$) to a more realistic value. This shows that a significant proportion of BD$^{I}$-$Al_2O_3$ was present on the surface of the αFrame material and following its removal a saturation of between 69 – 81 % was calculated.

In order to determine the optimised process conditions to produce a stucco material that can adsorb the highest quantity of water and remain dimensionally stable throughout the simulated casting cycle a number of considerations were taking into account:

1. Increasing the number of vacuum impregnation and drying steps yields less BD$^{I}$-$Al_2O_3$ deposited within the αFrame structure per action taken.
2. External BD$^{I}$-$Al_2O_3$ deposits during the process of vacuum impregnation which is expected to produce large volumetric shrinkage upon firing.
3. The material will be used to prove the concept that water absorbing particles can be implemented as stucco without affecting the dimensional stability of the shell.

Therefore, it was decided that the αFrame-Impreg$_8$-Clean material had a sufficiently high volume fraction of BD$^l$-$Al_2O_3$ and that further vacuum impregnation steps would not yield a significantly higher water absorption capacity. Also the cleaning step was necessary to remove external BD$^l$-$Al_2O_3$ and reduce volumetric shrinkage to a minimum. In addition this material produces a stucco material less than 100 $m^2 g^{-1}$ and thus below the value specified in patent US 2011/0232857 A1 [67]. As such, composite porous stucco can be implemented into the shell without infringing on this patent.

Once the optimised conditions had been established, the synthesis of αFrame-Impreg$_8$-Clean was scaled up to produce sufficient quantities to manufacture investment casting shells implementing the material as stucco in secondary layers.

### 6.2.4 Characterisation of α-$Al_2O_3$ Framework Composite

6.2.4.1 X-ray Diffraction (XRD)

X-ray diffraction was carried out on BD$^l$-$Al_2O_3$, αFrame and αFrame-Impreg$_8$-Clean to characterise the crystalline phases present in each material using Table 6 to identify each phase. As shown in Figure 100, BD$^l$-$Al_2O_3$ displays identical peaks to BD-$Al_2O_3$ displayed previously in Figure 28, as such the same conclusions can be made that BD$^l$-$Al_2O_3$ is composed primarily of γ-$Al_2O_3$. αFrame displays peaks only associated with α-$Al_2O_3$. αFrame-Impreg$_8$-Clean displays peaks matching both α-$Al_2O_3$ and γ-$Al_2O_3$. However, the γ-$Al_2O_3$ peaks are suppressed in intensity due to the higher degree of crystallinity exhibited by the α-$Al_2O_3$ phase [176].

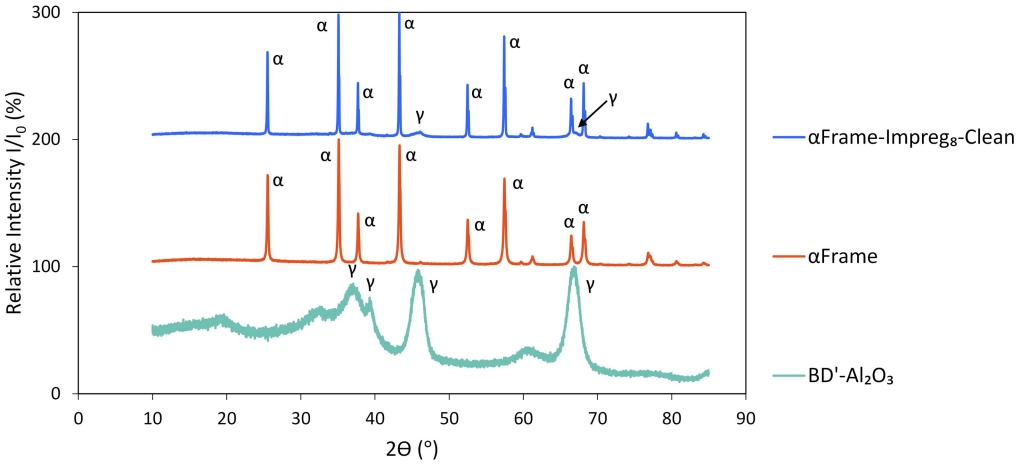



**Figure 100** – XRD traces with labels identifying main peaks for each phase (γ = γ-$Al_2O_3$ and α = α-$Al_2O_3$). The intensity is shifted by 1 for each sample for clarification

6.2.4.2 Nitrogen Adsorption

The pore size distribution of αFrame-Impreg$_8$-Clean and BD$^I$-$Al_2O_3$ is shown in Figure 101 as calculated by the BJH method. It can be seen that the average pore size varies between the two materials as quantified in Table 32. This may explain the variation in the calculated volume fraction of BD$^I$-$Al_2O_3$ when using either surface area or pore volume data in Section 6.2.3.1 as the BD$^I$-$Al_2O_3$ component of the composite stucco analysed independently attains a slightly different pore structure in comparison to the BD$^I$-$Al_2O_3$ component within the composite stucco.

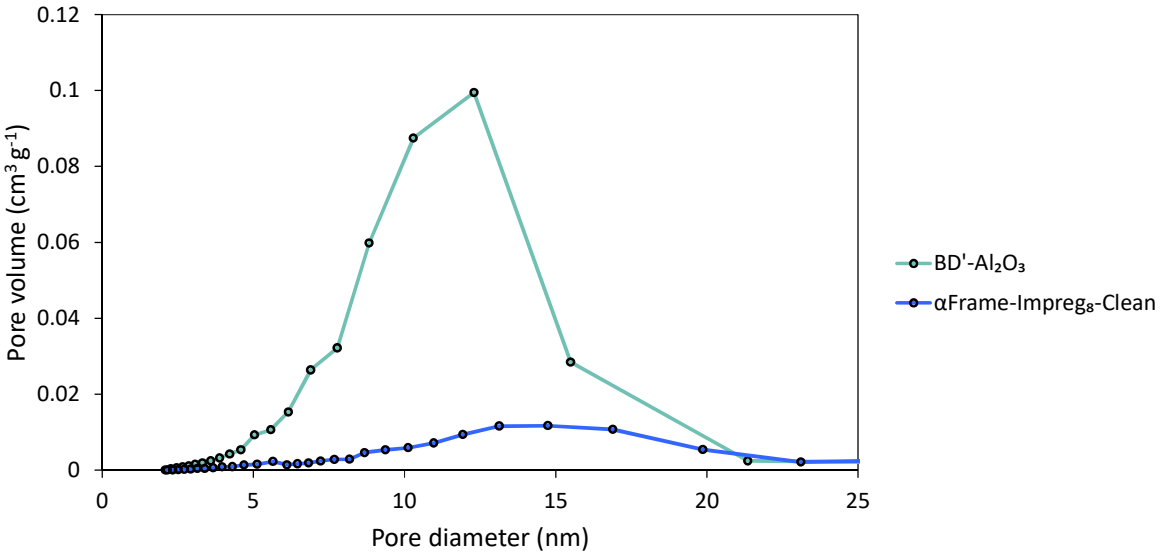



**Figure 101** – Representative example of incremental pore volume calculated by BJH method plotted against pore diameter for αFrame-Impreg$_8$-Clean and BD$^I$-$Al_2O_3$

**Table 32** – Surface and pore characteristics of composite stucco and mesoporous component of composite stucco obtained by nitrogen adsorption

| Material | Pore diameter (nm) | |
|---|---|---|
| | Average | Standard deviation |
| BD$^I$-$Al_2O_3$ | 8.60 | 0.09 |
| αFrame-Impreg$_8$-Clean | 10.27 | 0.05 |

6.2.4.3 Analysis of Internal Structure

The internal structure of αFrame-Impreg$_4$ and αFrame-Impreg$_8$ was analysed via SEM as shown in Figures 102 and 103 respectively. The αFrame component can be seen in white whereas the BD$^I$-$Al_2O_3$ component can be seen as dark grey. The black areas are filled with epoxy resin and therefore represent empty pore volume. The BD$^I$-$Al_2O_3$ can be seen to deposit on the surface of the αFrame and fill pore volume within the structure. A greater pore volume can be seen in αFrame-Impreg$_4$ in comparison to αFrame-Impreg$_8$ resulting from a lower concentration of BD$^I$-$Al_2O_3$ in the αFrame structure.

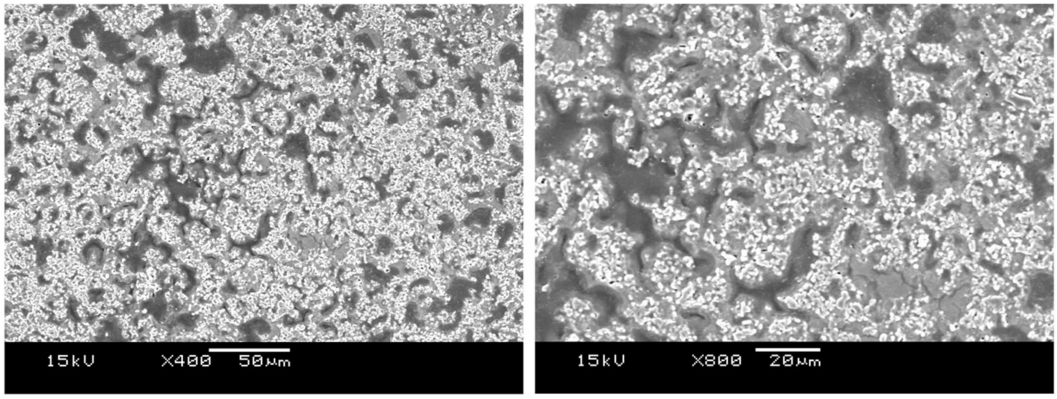



**Figure 102** – SEM image of internal structure of αFrame-Impreg$_4$ at 400X magnification (left) and 800X magnification (right)

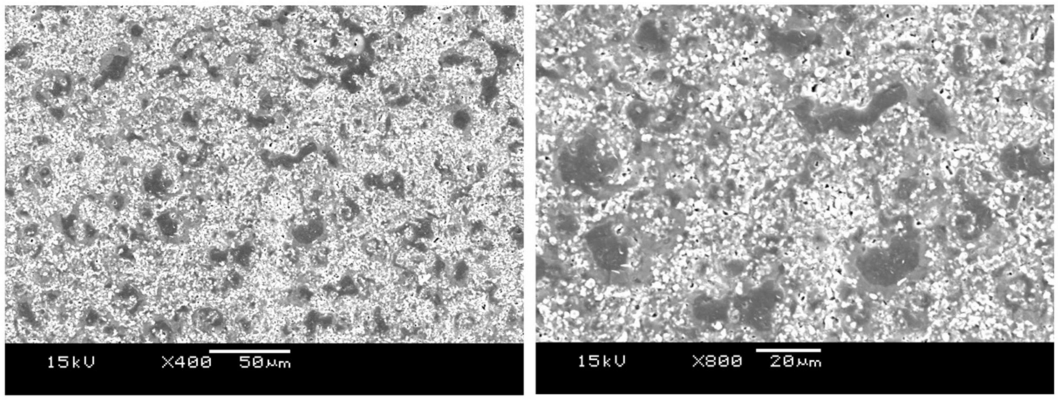



**Figure 103** – SEM image of internal structure of αFrame-Impreg$_8$ at 400X magnification (left) and 800X magnification (right)

6.2.4.4 Dynamic Vapour Sorption (DVS)

Dynamic vapour sorption was used to assess the sorption of water onto the accessible surfaces of αFrame-Impreg$_8$-Clean stucco over a broad range of humidity environments; this is shown in Figure 104. It can be seen that the material exhibits a reversible isotherm which can be identified as type IV with a H2 hysteresis loop, similar to BD-$Al_2O_3$ as shown in Section 4.2.5. This was expected as both materials contain boehmite derived alumina fired under an identical firing cycle. As such, the mechanism of water sorption was likely to be identical to BD-$Al_2O_3$.

Presuming the shell room accurately maintains a $R_H$ of 50 % and that pores are saturated at 90 % $R_H$ it is found that αFrame-Impreg$_8$-Clean is 10 % saturated in the shell room environment. Assuming the stucco reaches saturation when deposited onto the slurry, pores within αFrame-Impreg$_8$-Clean will remain 12 % saturated as the shell is dried at 50 % $R_H$. As such, αFrame-Impreg$_8$-Clean stucco displays similar properties to BD-$Al_2O_3$ remaining mostly unsaturated during handling to leave a large quantity of free pore volume available to absorb water when in contact with the slurry.

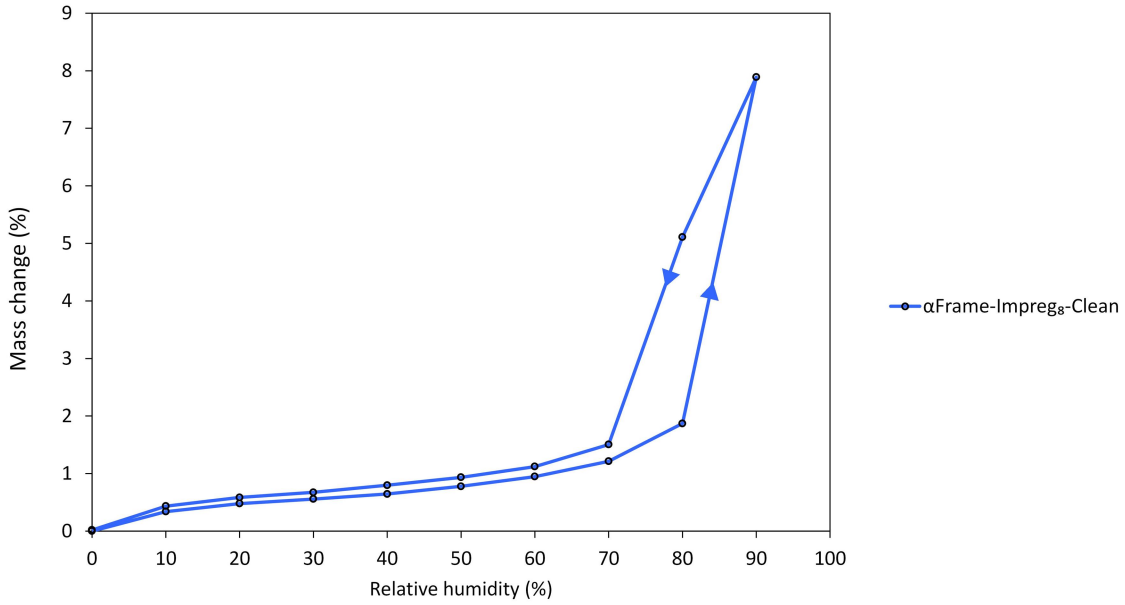



**Figure 104** – Dynamic vapour sorption plot for αFrame-Impreg$_8$-Clean material

6.2.4.5 Thermomechanical Analysis (TMA)

As described in Chapter 5, the large volumetric contraction of porous stucco in secondary layers has been identified as the cause of flexural deformation upon firing. As such, the linear expansion/contraction of both the αFrame and αFrame-Impreg$_8$-Clean was measured throughout the simulated casting cycle. Samples representative of αFrame were prepared from flakes of αFrame taken before the grinding process and cut into cylinders approximately 5 mm in length and 6 mm in diameter. Samples representative of αFrame-Impreg$_8$-Clean were prepared by vacuum impregnating and drying the αFrame cylinders 8 times before cleaning the sample to remove external dried alumina and firing to phase transform the dried alumina sol to BD$^{I}$-$Al_2O_3$. The average expansion/contraction of both αFrame and αFrame-Impreg$_8$-Clean materials throughout the simulated casting cycle is shown in Figure 105 alongside previous data reproduced from Section 4.2.6 for BD-$Al_2O_3$ for comparison. Three analyses were conducted per sample. The average linear shrinkage following the complete firing cycle is displayed in Table 33 for each material.

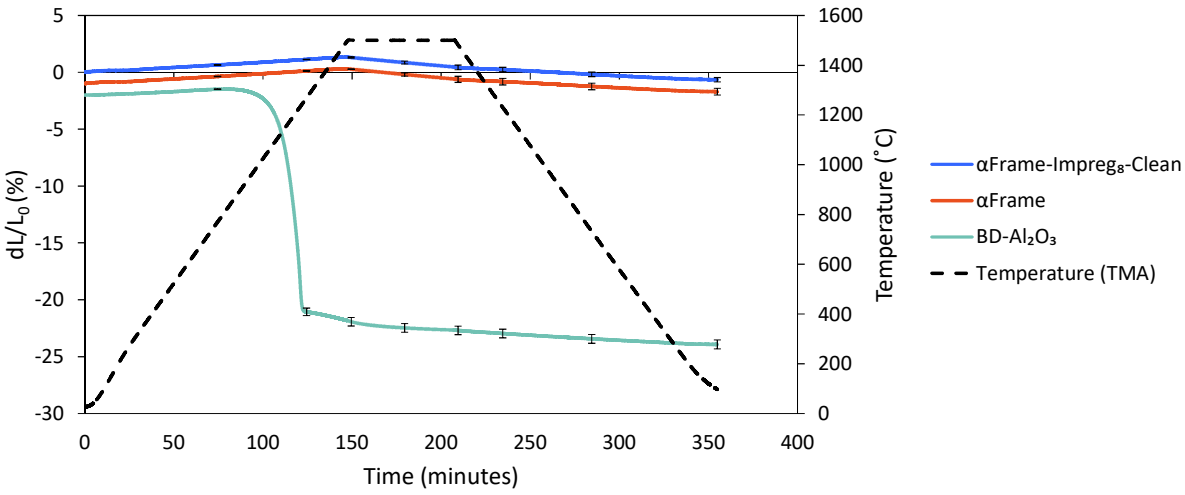



**Figure 105** – Expansion/contraction of αFrame-Impreg$_8$-Clean, αFrame and BD-$Al_2O_3$ throughout the simulated casting cycle conducted by TMA. Samples are separated by 1 % for clarification

**Table 33** – Linear shrinkage of αFrame-Impreg$_8$-Clean, αFrame and BD-$Al_2O_3$ following the simulated casting cycle measured by TMA

| Sample | Linear shrinkage (%) | |
|---|---|---|
| | **Average** | **Standard deviation** |
| αFrame-Impreg$_8$-Clean | 0.64 | 0.19 |
| αFrame | 0.70 | 0.29 |
| BD-$Al_2O_3$ | 23.9 | 0.39 |

It can be seen that both αFrame and αFrame-Impreg$_8$-Clean materials exhibit a minor quantity of shrinkage, substantially lower than BD-$Al_2O_3$. It was also observed that the impregnation process has no measureable effect on the magnitude of shrinkage, with αFrame-Impreg$_8$-Clean and αFrame displaying analogous thermal expansion/contraction profiles over the simulated casting cycle. As such, a porous ceramic displaying water absorbing capabilities with minimal shrinkage has successfully been synthesised.

6.2.4.6 Particle Size Distribution (PSD)

The particle size distribution of αFrame and αFrame-Impreg$_8$-Clean were analysed via aero dispersion method and compared to Tab-$Al_2O_3$ data reproduced from Section 4.2.2, this is shown in Figure 106. It can be seen that αFrame and αFrame-Impreg$_8$-Clean stucco traces overlap showing no significant difference in PSD. This implies minimal external coverage of $BD^I$-$Al_2O_3$ was present on αFrame-Impreg$_8$-Clean particles due to similarities in average particle diameter. Additionally, the PSD of αFrame-Impreg$_8$-Clean and Tab-$Al_2O_3$ are very similar, thus the synthesis procedure has successfully produced a porous stucco with a similar average grain size to the standard material. In addition, the aero dispersion technique has worked successfully for αFrame and αFrame-Impreg$_8$-Clean material unlike the results observed for BD-$Al_2O_3$ and SGB127 in Section 4.2.2 which showed signs of disintegrating during analysis. As such it can be concluded that both αFrame and αFrame-Impreg$_8$-Clean display a greater resistance to abrasion in comparison to BD-$Al_2O_3$ and SGB127.

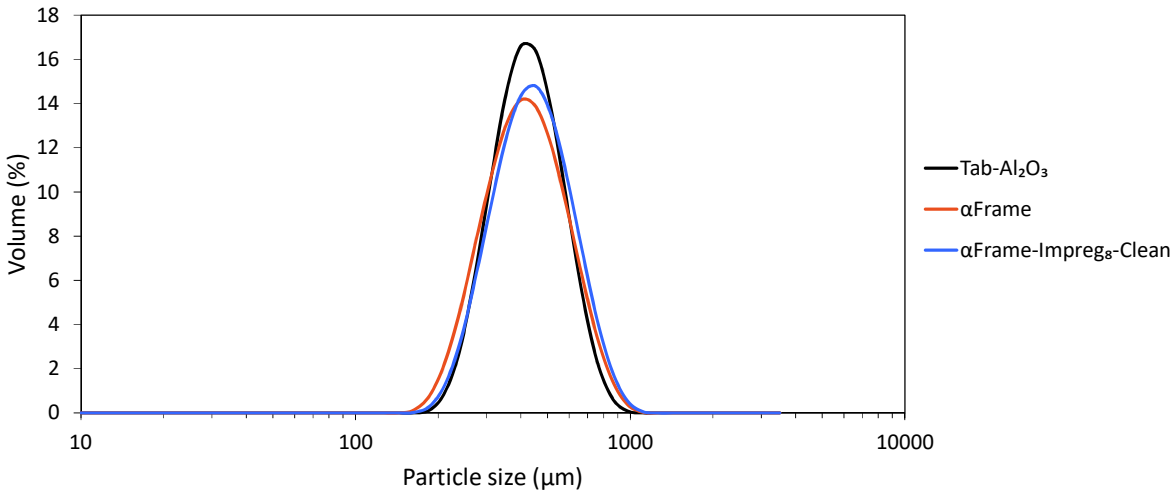



**Figure 106** – Particle size distribution of stucco grains analysed under aero dispersion method

6.2.4.7 Particle Density and Porosity

To calculate the bulk density of αFrame-Impreg$_8$-Clean the unsaturated pore volume of the αFrame material needs to be taken into consideration. As such, Equation 59 was proposed to calculate the bulk density of such particles. As the volume percentage of pores in αFrame saturated with BD$^{I}$-$Al_2O_3$ ($\tau$) has been calculated to equal 69 % using surface area data and 81 % using pore volume data in Section 6.2.3.1 an average of both values (75 %) was taken to calculate the bulk density. The bulk density of BD$^{I}$-$Al_2O_3$ ($\rho_{BD^{I}-Al_2O_3}$) was taken as 1.47 g cm$^{-3}$ as calculated in Section 6.2.3.1, volume fraction of pores in αFrame ($F_{vol(pore)}$) was taken as 0.52 as calculated in Section 6.2.2.2, therefore the volume fraction of solid in αFrame ($F_{vol(\alpha Frame)}$) was equal to 0.48. The true density of αFrame ($\rho_{\alpha Frame}$) was measured by helium pycnometer as shown in Table 34. Inputting these values into Equation 59 the bulk density of αFrame-Impreg$_8$-Clean was calculated to equal 2.49 g cm$^{-3}$.

$$Bulk\ Density\ (g\ cm^{-3}) = \left(F_{vol(pore)} \times \tau \times \rho_{BD^{I}-Al_2O_3}\right) + \left(F_{vol(\alpha Frame)} \times \rho_{\alpha Frame}\right) \quad \text{eq.59}$$

**Table 34** – True density of αFrame attained by helium pycnometer method

| Sample | True density (g $cm^{-3}$) | |
|---|---|---|
| | **Average** | **Standard deviation** |
| αFrame | 3.99 | 0.0008 |

Utilising the true density of BD$^{I}$-$Al_2O_3$ from Section 6.2.3.1 (3.45 g $cm^{-3}$) and porosity of BD$^{I}$$Al_2O_3$ from Section 6.2.3.1 (0.39 $cm^3$ $g^{-1}$) Equation 35 was used to calculate the volumetric porosity of BD$^{I}$-$Al_2O_3$ as 0.57 $cm^3_{pore}$ $cm^{-3}_{bulk}$ .

The pore volume contained within the BD$^{I}$-$Al_2O_3$ component of αFrame-Impreg$_8$-Clean was calculated by taking the volume fraction of pores in αFrame ($F_{vol(pore)}$) as 0.52, the volume of pores saturated with BD$^{I}$-$Al_2O_3$ ($\tau$) as 75 % and the volumetric porosity of BD$^{I}$-$Al_2O_3$ as 0.57 $cm^3_{pore}$ $cm^{-3}_{bulk}$ . Using these values the pore volume contained within αFrame-Impreg$_8$-Clean material was calculated to equal 0.22 $cm^3_{pore}$ $cm^{-3}_{bulk}$ .

### 6.2.5 Shell Build

6.2.5.1 Analysing Surface Coverage after Stucco Deposition

Using the bulk density values of αFrame-Impreg$_8$-Clean and Tab-$Al_2O_3$ from Sections 6.2.4.7 and 4.2.4 respectively the surface coverage of blended stucco formulations were recorded. Surface coverage images were taken on a wax pattern of dimensions 130 x 100 x 20 mm following the application of P (Fused-$Al_2O_3$)$_2$ and P+1 (Fused-$Al_2O_3$)$_2$ layers. The partially completed shell was then dipped in Secondary slurry and after draining the required stucco blend was applied. The surface coverage for 20, 40, 60, 80 and 100 vol% αFrame-Impreg$_8$-Clean stucco blended with Tab-$Al_2O_3$ stucco for the remaining vol% is given in Figure 107 after drying for a minimum of two hours.

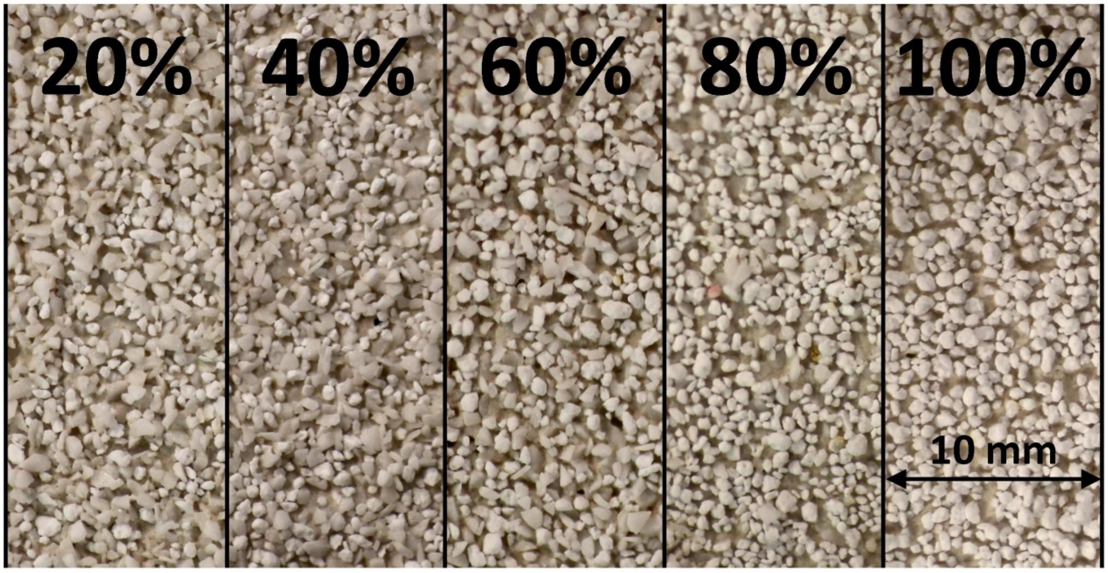



**Figure 107** – Surface coverage of αFrame-Impreg$_8$-Clean stucco blends deposited onto Secondary slurry

It can be seen that an acceptable coverage of stucco was produced over the full range of concentrations tested. In addition, a high level of adhesion was produced between the stucco and slurry surface displaying an adhesion rating of 3 for all concentrations tested using the description of adhesion listed in Table 9 within Section 4.3.1. This may be the result of the reduced mesopore volume of αFrame-Impreg$_8$-Clean in comparison to monolithic porous stucco materials; thus particles have a reduced capacity to absorb water comparatively. Alternatively, the convoluted pathway water takes upon capillary action within αFrame-Impreg$_8$-Clean material may lead to a low absorption rate allowing particles to embed in slurry before it begins to thicken. Given that an acceptable level of adhesion and surface coverage was produced using 100 vol% αFrame-Impreg$_8$-Clean stucco, shells were built using this concentration in secondary layers to maximise the drying potential. The full shell build is given in Table 35 using notation from Section 3.1.3 to label each layer.

**Table 35** – Composition of shell containing αFrame-Impreg$_8$-Clean stucco labelled Shell (αFrame-I$_8$-C)

| Complete shell identifier | Layer composition in order of application | Number of layers |
|---|---|---|
| Shell (αFrame-I$_8$-C) | P (FusedAl)$_2$ | 1 |
| | P+1 (FusedAl)$_2$ | 1 |
| | S (100 αFrame-Impreg$_8$-Clean)$_2$ | 5 |
| | Seal (Secondary) | 1 |

### 6.2.6 Shell Characterisation

6.2.6.1 Scanning Electron Microscopy (SEM)

SEM analysis was conducted on Shell (αFrame-I$_8$-C) in both pre-fired and fired condition as shown in Figure 108. Analysis was conducted on shell cross-sections taken at 15X magnification and αFrame-Impreg$_8$-Clean particles embedded in the shell at 150X magnification. The slurry in each layer is identified using notation outlined in Section 4.4.1.

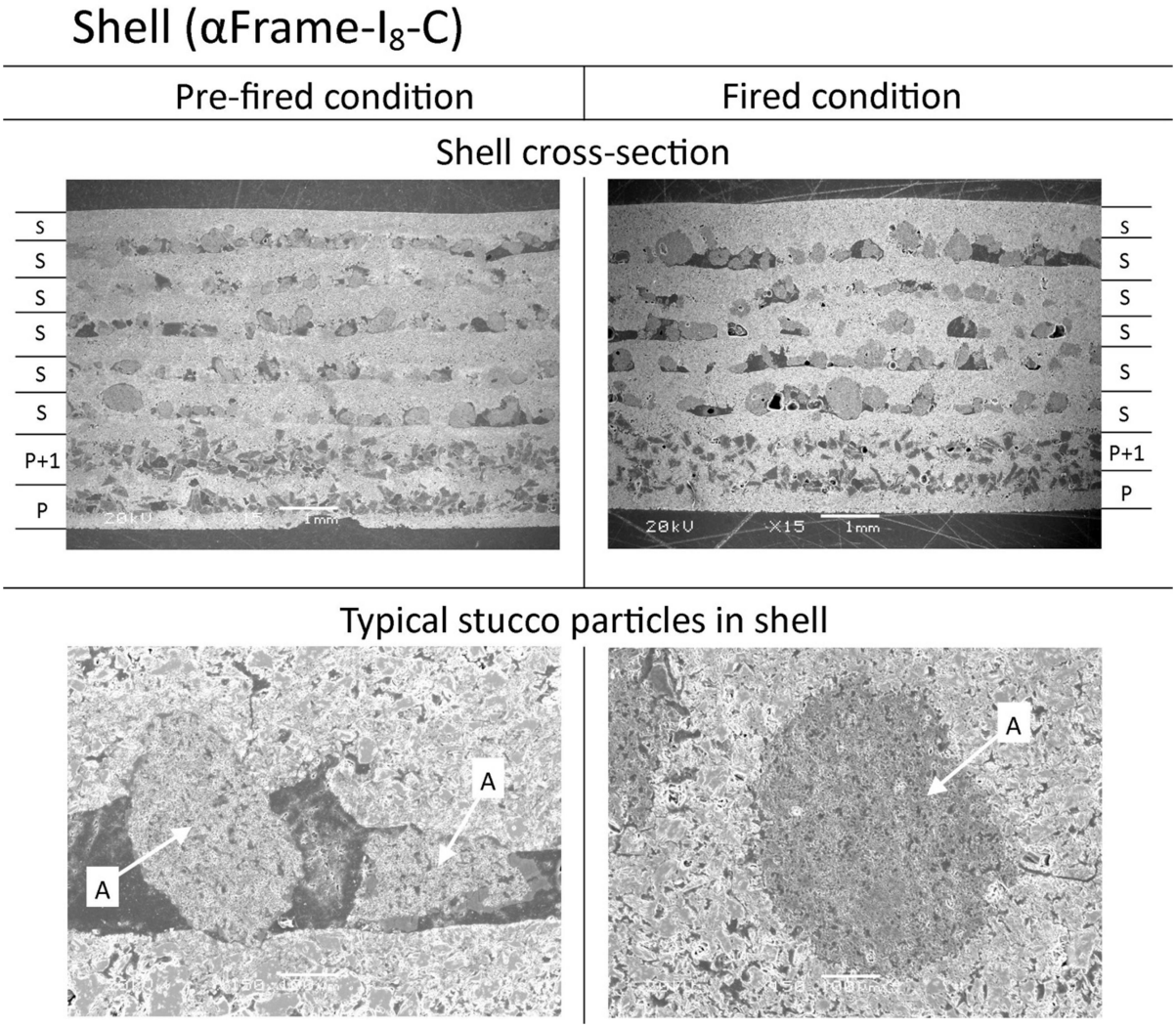



**Figure 108** – SEM analysis of Shell (αFrame-$I_8$-C) displaying the shell cross-section with slurry applied in each layer identified. Typical stucco particles are shown at greater magnification. A = Individual αFrame-Impreg$_8$-Clean particles

As shown in Figure 108, Shell (αFrame-$I_8$-C) displays similar characteristics to Shell (BD-$Al_2O_3$) and Shell (SGB127) in Section 4.4.1 whereby poor adhesion can be seen between the stucco and slurry matrix in pre-fired condition. In addition, a high volumetric slurry to stucco ratio is observed in secondary layers. This likely arises through mechanisms discussed in Sections 4.3.2 and 4.4.1 respectively whereby slurry dries before penetrating between embedded grains or as a result of air being displaced with water upon absorption. However, unlike Shell (BD-$Al_2O_3$) and Shell (SGB127) the stucco in Shell (αFrame-$I_8$-C) remains dimensionally stable after firing and does not shrink away from the slurry matrix.

6.2.6.2 Mechanical Strength

The mechanical strength of Shell (αFrame-$I_8$-C) in green, pre-fired and fired condition was measured using 3 point bend flexural strength analysis and compared to a new sample of Shell (Tab-$Al_2O_3$) using the same slurries for each shell. These results are displayed in Figure 109.

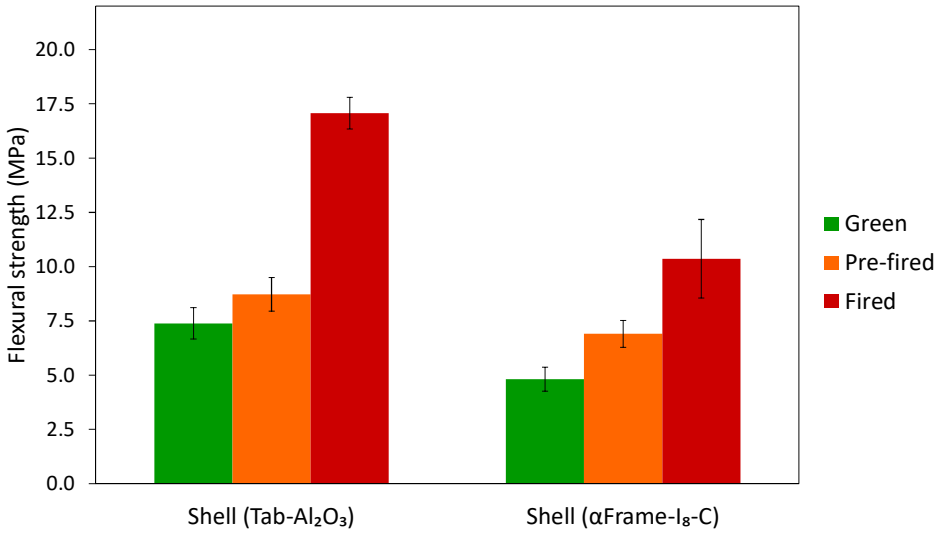



**Figure 109** – Flexural strength of Shell (Tab-$Al_2O_3$) and Shell (αFrame-$I_8$-C) in green, pre-fired and fired condition tested in ambient conditions

As shown in Figure 109, Shell (αFrame-$I_8$-C) displays a reduction in green and pre-fired strength of 35 % and 20 % respectively in comparison to Shell (Tab-$Al_2O_3$). This was similar to results obtained for Shell (BD-$Al_2O_3$) in Section 4.4.3 in which the weakness was attributed to porosity generated within the shell. As identified in Section 6.2.6.1, porosity in Shell (αFrame-$I_8$-C) was thought to arise through the same mechanism as in Shell (BD-$Al_2O_3$), as such the reduction in strength for both shell systems in green and pre-fired condition was expected to be the same.

It was also observed that Shell (αFrame-$I_8$-C) attains a reduction in fired strength of 40 % in comparison to Shell (Tab-$Al_2O_3$). This contrasts to Shell (BD-$Al_2O_3$) and Shell (SGB127) which displayed an increased fired strength previously in Section 4.4.3. This was likely due to the αFrame-Impreg$_8$-Clean particles remaining stable in the firing process preventing the enhanced densification of the shell network observed when using BD-$Al_2O_3$ and SGB127 stucco. As such, the shell was weakened due to the presence of porosity without the effect of enhanced densification.

6.2.6.3 Thermal Expansion/Contraction of Shell Layers

Following the procedure outlined in Section 5.3, shell samples were produced representative of $Section_S$ in Shell (αFrame-$I_8$-C) and analysed via dilatometer method. The composition of this sample is displayed in Table 36 using notation from Section 3.1.3 to label each layer. The thermal expansion/contraction of the sample tested throughout the simulated casting cycle is shown in Figure 110 in comparison to sample Secondary (Tab-$Al_2O_3$) and Secondary (BD-$Al_2O_3$) using data reproduced from Section 5.3. The linear shrinkage, linear coefficient of thermal expansion and sintering onset temperatures are shown in Tables 37 and 38. A magnified image of the thermal expansion/contraction of Secondary (αFrame-$I_8$-C) is shown in Appendix 1.

**Table 36** – Composition of shell replicating $Section_S$ of Shell (α-Frame-$I_8$-C)

| Sample identifier | Layer composition in order of application | Number of layers |
|---|---|---|
| Secondary (αFrame-$I_8$-C) | S (100 αFrame-$Impreg_8$-Clean)$_2$ | 7 |
| | Seal (Secondary) | 1 |

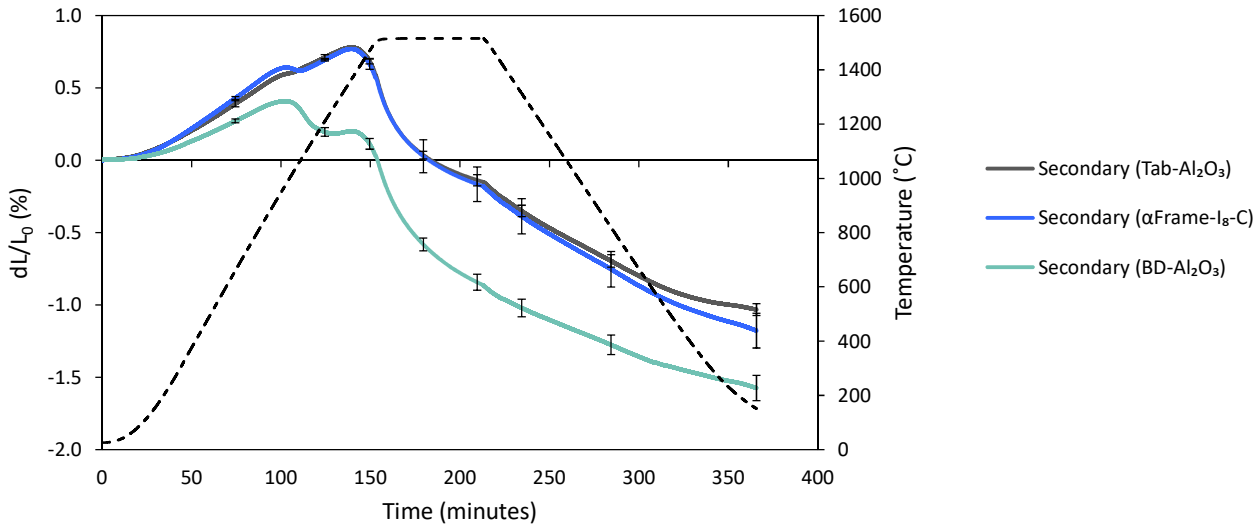



**Figure 110** – Expansion/contraction of shell samples replicating $Section_S$ analysed throughout the simulated casting cycle conducted by dilatometer analysis

**Table 37** – Linear shrinkage of shell samples following the simulated casting cycle and thermal expansion coefficients measured from 50 – 700 ˚C by dilatometer analysis

| Sample | Linear shrinkage (%) | | Linear thermal expansion coefficient from 50 – 700 ˚C ($10^{-6}$ $K^{-1}$) | |
|---|---|---|---|---|
| | Average | Standard deviation | Average | Standard deviation |
| Secondary (αFrame-$I_8$-C) | 1.17 | 0.120 | 6.75 | 0.11 |
| Secondary (Tab-$Al_2O_3$) | 1.03 | 0.041 | 6.39 | 0.14 |
| Secondary (BD-$Al_2O_3$) | 1.57 | 0.086 | 4.61 | 0.21 |

**Table 38** – First and second sintering onset temperatures for shell samples conducted by dilatometer analysis

| Sample | First sintering onset temperature (˚C) | | Second sintering onset temperature (˚C) | |
|---|---|---|---|---|
| | Average | Standard deviation | Average | Standard deviation |
| Secondary (αFrame-$I_8$-C) | 894 | 8.8 | 1339 | 8.8 |
| Secondary (Tab-$Al_2O_3$) | 902 | 3.1 | 1310 | 20.9 |
| Secondary (BD-$Al_2O_3$) | 895 | 11.3 | 1370 | 9.4 |

As shown in Figure 110, the thermal expansion/contraction trace of Secondary (αFrame-$I_8$-C) is similar to Secondary (Tab-$Al_2O_3$) in most aspects. It appears the dimensional stability of the αFrame-Impreg$_8$-Clean material at high temperature (as shown by TMA in Section 6.2.4.5) has prevented the shell densifying in a similar manner to Secondary (BD-$Al_2O_3$) where particle contraction leads to enhanced densification of the shell matrix as explained in Figure 69 previously. Given that the thermal expansion/contraction trace of Secondary (αFrame-$I_8$-C) is similar to that of Secondary (Tab-$Al_2O_3$) despite large pores and high slurry content observed in Shell (αFrame-$I_8$-C) shows that the dimensional stability of the stucco particles is the main driving factor in the expansion/contraction behaviour of the shell.

Overall, this result shows that water absorbing stucco can be incorporated into the shell without detrimentally affecting the magnitude of shrinkage of Section$_S$. As such, a comparable degree of curvature was expected to be developed in Shell (αFrame-$I_8$-C) and Shell (Tab-$Al_2O_3$) due to the similar sintering profiles in each Section$_S$.

6.2.6.4 Predicting Flexural Deformation

Following the procedure outlined in Section 5.4 the normalised curvature was predicted for Shell (αFrame-$I_8$-C) using the expansion/contraction trace of sample Primary (Fused-$Al_2O_3$) reproduced from Section 5.4 and sample Secondary (αFrame-$I_8$-C) from Section 6.2.6.3 to replicate $Section_P$ and $Section_S$ respectively for the complete shell. As outlined in Section 5.4, the radius of curvature was calculated from Equation 39 using the change in strain between Primary (Fused-$Al_2O_3$) and Secondary (αFrame-$I_8$-C) and assuming a viscosity ratio of one throughout the firing cycle. The thickness ratio used in the equation was calculated from three SEM images of Shell (αFrame-$I_8$-C) from which the average thickness of $Section_P$ and $Section_S$ were measured, the results of which are displayed in Tables 39 and 40. The deflection from normal was then calculated using Equation 43 and displayed as a percentage of the original sample length of 20 mm to give normalised curvature using Equation 44. Figure 111 shows the normalised curvature for Shell (αFrame-$I_8$-C) using the method outlined above in comparison to Shell (Tab-$Al_2O_3$) and Shell (BD-$Al_2O_3$) using data reproduced from Section 5.4.

**Table 39** – Average thickness for $Section_P$ and $Section_S$ measured by SEM analysis

| **Complete shell** | **Average $Section_P$ thickness (mm)** | **Standard deviation** | **Average $Section_S$ thickness (mm)** | **Standard deviation** |
|---|---|---|---|---|
| Shell (αFrame-$I_8$-C) | 1.72 | 0.083 | 4.65 | 0.211 |

**Table 40** – Average original thickness ($T_0$) and thickness ratio ($a$) for each shell

| **Complete shell** | **Average thickness (mm)** | **Thickness ratio (-)** |
|---|---|---|
| Shell (αFrame-$I_8$-C) | 6.37 | 0.370 |

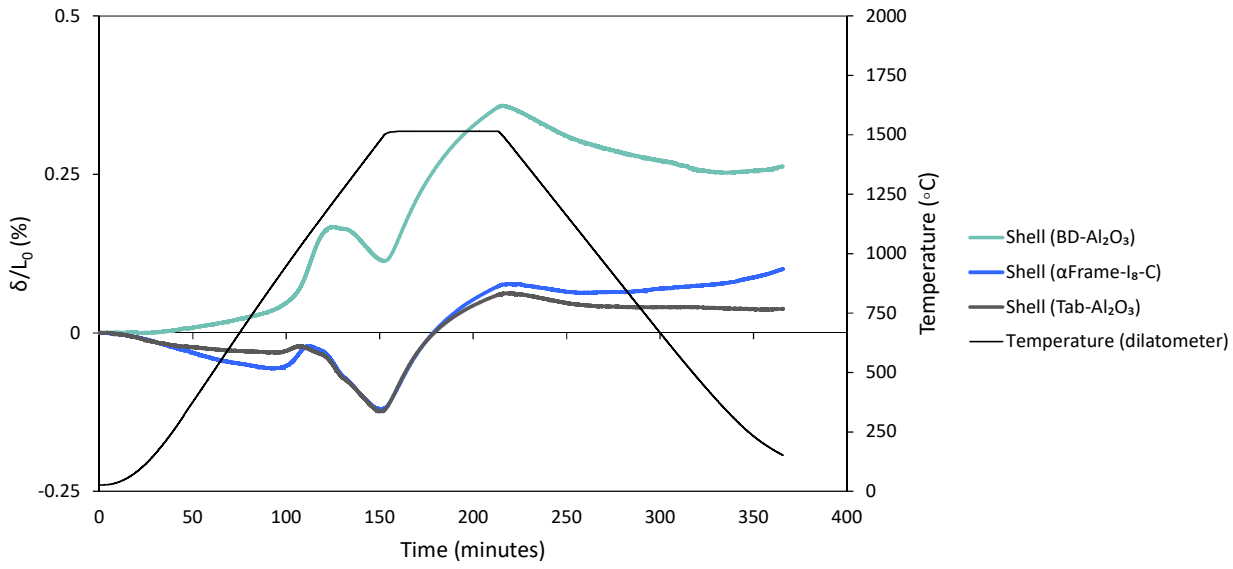



**Figure 111** – Normalised curvature predicted from thermal expansion/contraction of shell samples replicating $Section_P$ and $Section_S$ throughout the simulated casting cycle

As shown in Figure 111, the predicted normalised curvature of Shell (α-Frame-$I_8$-C) is remarkably similar to Shell (Tab-$Al_2O_3$). As such, a comparable degree of curvature was predicated following the complete firing cycle, significantly less than Shell (BD-$Al_2O_3$). As such, the development of α-Frame-$Impreg_8$-Clean stucco has provided evidence that water absorbing stucco can be used in the shell whilst attaining the same level of flexural deformation as non-porous stucco in Shell (Tab-$Al_2O_3$). The normalised curvature for each sample following the complete simulated casting cycle is shown in Table 41.

**Table 41** – Normalised curvature following the complete simulated casting cycle predicted from thermal expansion/contraction of shell samples replicating $Section_P$ and $Section_S$

| **Complete shell** | **Normalised curvature predicted from thermal expansion/contraction of $Section_s$ and $Section_P$ (%)** |
|---|---|
| Shell (αFrame-$I_8$-C) | 0.11 |
| Shell (Tab-$Al_2O_3$) | 0.04 |
| Shell (BD-$Al_2O_3$) | 0.26 |

6.2.6.5 Measuring Flexural Deformation in-situ

Using the method developed in Section 5.6, Shell (αFrame-$I_8$-C) was evaluated for flexural deformation throughout the simulated casting cycle using 3 point bend TMA. The average push rod displacement as a percentage of $T_0$ for Shell (αFrame-$I_8$-C) in either $Primary_{UP}$ or $Primary_{DOWN}$ orientation is shown in Figure 112 alongside Shell (Tab-$Al_2O_3$) and Shell (BD-$Al_2O_3$) for comparison using data reproduced from Section 5.6. Each shell was analysed three times in each orientation. The average push rod displacement for each shell variant in each orientation following the complete firing cycle is shown in Table 42.

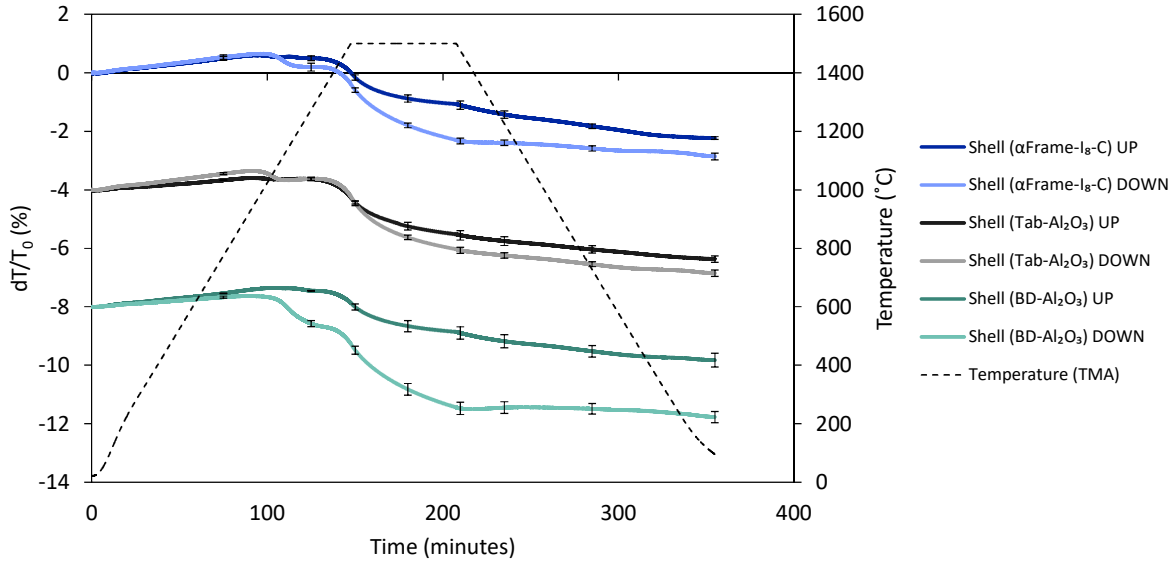



**Figure 112** – 3 point bend TMA of complete shells tested in $Primary_{UP}$ and $Primary_{DOWN}$ orientation throughout the firing cycle. Each sample is separated by 4 % at the origin for clarification

**Table 42** – Average push rod movement of complete shell samples analysed by 3 point bend TMA in $Primary_{UP}$ and $Primary_{DOWN}$ orientation following the simulated casting cycle

| | **$Primary_{UP}$ $dT/T_0$(%)** | | **$Primary_{DOWN}$ $dT/T_0$ (%)** | |
|---|---|---|---|---|
| **Complete Shell** | **Average** | **Standard deviation** | **Average** | **Standard deviation** |
| Shell (αFrame-$I_8$-C) | -2.23 | 0.05 | -2.86 | 0.12 |
| Shell (Tab-$Al_2O_3$) | -2.37 | 0.11 | -2.85 | 0.11 |
| Shell (BD-$Al_2O_3$) | -1.82 | 0.24 | -3.77 | 0.19 |

It can be seen that Shell (αFrame-$I_8$-C) displays a fair degree of separation between $Primary_{UP}$ and $Primary_{DOWN}$ orientation, however, this minimises during the cooling period. As such, curvature is expected to develop during the isothermal hold period and decrease towards the end of the firing cycle. This shows the αFrame-$Impreg_8$-Clean stucco acts to prevent curvature development, but not as efficiently as Tab-$Al_2O_3$.

Carrying out the procedure detailed in Section 5.6, the deflection from normal over a 20 mm span (normalised curvature) was calculated using push rod displacement values output from the TMA for each individual Shell (αFrame-$I_8$-C) specimen throughout the simulated firing cycle. The calculated normalised curvature for Shell (αFrame-$I_8$-C) is shown in Figure 113 combined with previous data reproduced from Section 5.6 for Shell (Tab-$Al_2O_3$) and Shell (BD-$Al_2O_3$) for comparison. The average normalised curvature following the complete simulated casting cycle is displayed in Table 43.

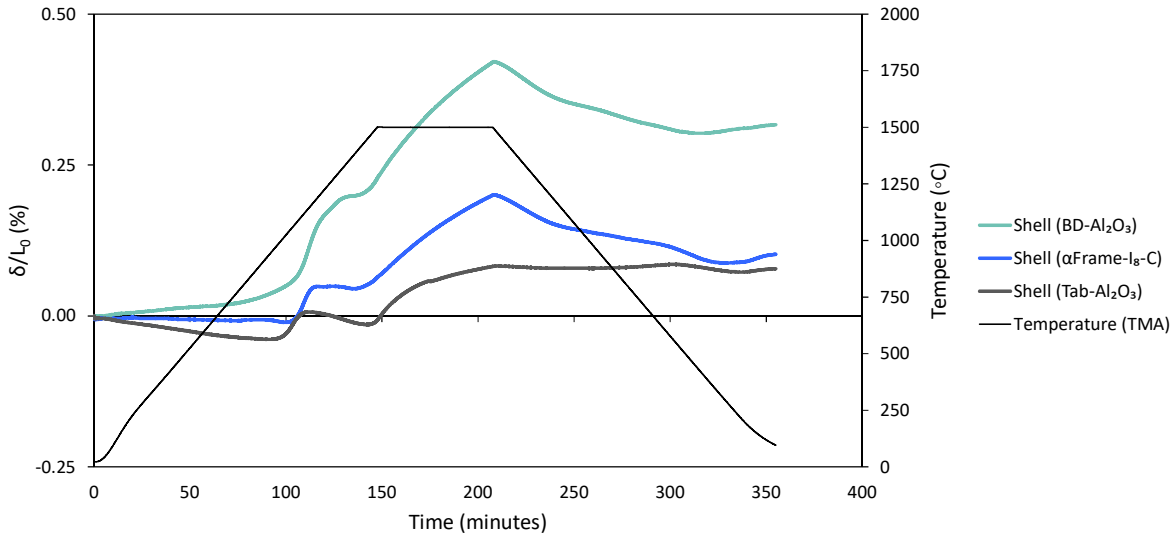



**Figure 113** – Normalised curvature measured from 3 point bend TMA method throughout the simulated casting cycle

**Table 43** – Normalised curvature following the complete simulated casting cycle measured from 3 point bend TMA method for complete shell samples

| Complete shell | Normalised curvature measured from 3 point bend TMA method (%) |
|---|---|
| Shell (αFrame-$I_8$-C) | 0.10 |
| Shell (Tab-$Al_2O_3$) | 0.08 |
| Shell (BD-$Al_2O_3$) | 0.32 |

It can be observed that the normalised curvature following the complete firing cycle is similar for Shell (αFrame-$I_8$-C) and Shell (Tab-$Al_2O_3$). However, the pathway through which this is achieved is considerably different. This contrasts with analysis conducted in Section 6.2.6.4 where the normalised curvature for Shell (αFrame-$I_8$-C) matched the normalised curvature of Shell (Tab-$Al_2O_3$) throughout the majority of the firing cycle. As the samples in both methods were prepared from the same batch of stucco it is unlikely that batch to batch variation was the cause. Additionally, all slurrys were in specification when used and no contamination could be observed in SEM analysis.

Therefore a feasible explanation as to why this method measures more curvature development in Shell (αFrame-$I_8$-C) in comparison to Shell (Tab-$Al_2O_3$) may be the result of the direction of force applied during each analysis technique. As the method in Section 6.2.6.4 measures the shrinkage parallel to layer formation by applying force in this direction, the analysis is measuring the propensity for the shell to resist contraction under compression in this plane. As both Tab-$Al_2O_3$ and αFrame-Impreg$_8$-Clean particles remain dimensionally stable at high temperature, a similar degree of shrinkage was measured for both shell samples as particles remain in contact throughout the firing cycle as explained in Figure 69. However, despite both particles preventing contraction of the shell under compression, the application of force perpendicular to the layer formation, combined with constraint from an additional section (as carried out in 3 point bend TMA method) may result in different sintering behaviour in Section$_S$. Consequently, Shell (αFrame-$I_8$-C) displays a greater degree of curvature development in comparison to Shell (Tab-$Al_2O_3$) when characterised by TMA.

To conclude, the conflicting evidence for curvature development in shells containing αFrame-Impreg$_8$-Clean stucco leads to the conclusion that the stucco effectively reduces curvature in comparison to its monolithic counterpart (BD-$Al_2O_3$). However, curvature may develop to a greater degree than using the standard Tab-$Al_2O_3$ stucco.

6.2.6.6 Reduced Drying Times

The effectiveness of αFrame-Impreg$_8$-Clean stucco at reducing drying times between Secondary slurry dips during shell manufacture was recorded to compare to earlier results in Section 4.4.5 using Tab-$Al_2O_3$ stucco. Shells were manufactured on a wax pattern of dimensions 130 x 100 x 20 mm applying P (Fused-$Al_2O_3$)$_2$ and P+1 (Fused-$Al_2O_3$)$_2$ layers (notation described in Section 3.1.3) before applying five secondary layers and a seal coat at either 2, 1.5, 1.25, 1, 0.75 or 0.5 hours drying time between dips. Once shell manufacture was complete the shells were left to dry for 24 hours before recording the surface.

The effect of reducing drying times between Secondary slurry dips for shells containing 100 vol% αFrame-Impreg$_8$-Clean stucco in secondary layers is shown in Figure 114, this can be compared to shells containing 100 vol% Tab-$Al_2O_3$ stucco in Figure 59. It was observed that cracks became visible on the surface after drying times were reduced below 1.25 hours, producing a reduction in drying time of 37.5 % without failure.

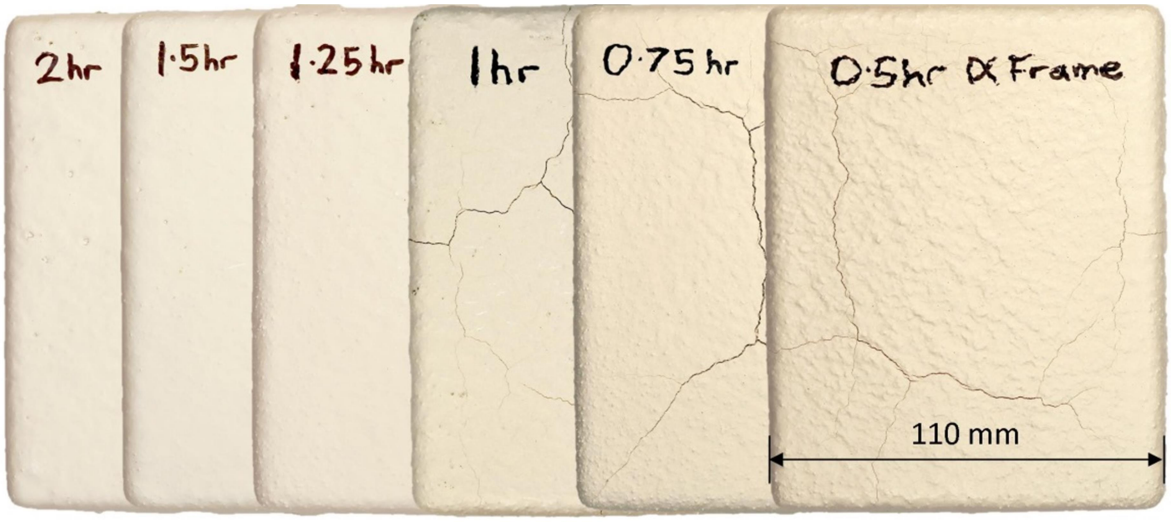



**Figure 114** – Shells containing 100 vol% αFrame-Impreg$_8$-Clean in secondary layers showing the formation of cracks when reducing the drying time between Secondary slurry dips from 2 hours to 0.5 hours. Reducing the drying time between dips below 1.25 hours causes failure

The shells which remained whole after reducing the drying time were taken for flexural strength testing in the green state as shown in Figure 115. These results are compared against data for shells containing 100 vol% Tab-$Al_2O_3$ stucco in secondary layers reproduced from Section 4.4.5.1.

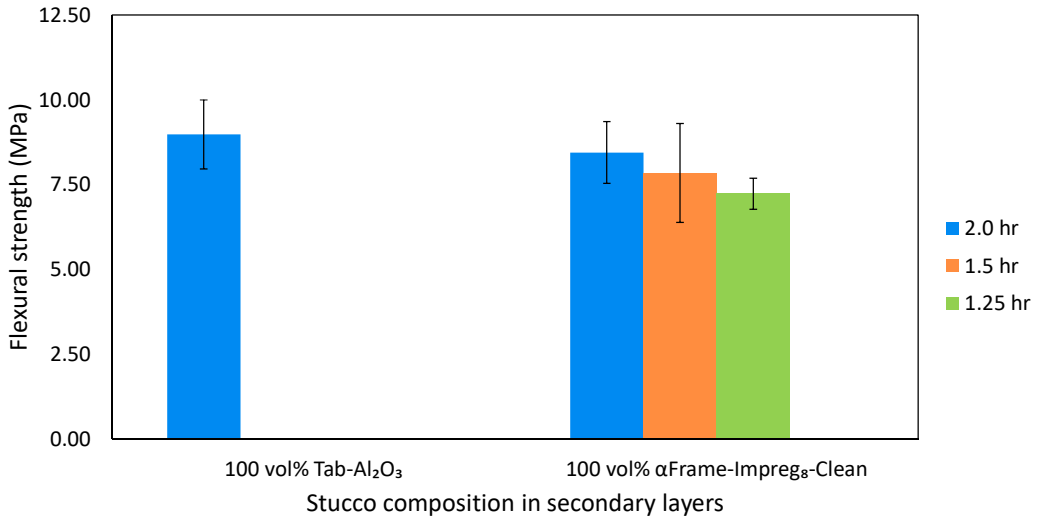



**Figure 115** – Flexural strength of shell bars in green state after varying the drying time in secondary layers tested in ambient condition

It can be seen that despite reducing the drying times, only minor reductions in green strength were observed. As such, the green strength is acceptable for all samples that remained whole following the reduced drying period.

### 6.2.7 Closing Comments

By optimising the formulation and processing parameters, the synthesis of a composite ceramic material displaying both water absorption properties and dimensional stability at high temperature has been successfully conducted. Utilising this material as stucco in the investment casting process has proven composite stucco materials can prevent enhanced shrinkage in the slurry matrix and thus significantly reduce the flexural deformation observed in comparison to utilising monolithic porous stucco. However, the synthesis of composite stucco is time consuming and burdensome.

Overall, the use of composite stucco is an effective yet taxing method to accelerate the drying of investment casting shells without causing excessive flexural deformation however, compromise to flexural strength ensues.

## 6.3 Introduction of the Tertiary Layer

Another method evaluated to counteract the flexural deformation of shells containing porous stucco in the secondary layers was to introduce a tertiary layer containing non-porous stucco as shown in Figure 116. This additional section (labelled $Section_T$) prevents the enhanced contraction of the $Section_S$ by shrinking to a similar degree as $Section_P$. This however leads to tensile stress development in $Section_S$ resulting from constraint during sintering. As a result, cracks and porosity can be introduced into $Section_S$ if the stress is not adequately accommodated [177]. Additionally, the introduction of a layer containing non-porous stucco will inevitably require a longer drying procedure in comparison to a mould utilising purely porous stucco. However, it is possible a reduction in drying time can be made in comparison to a mould utilising purely non-porous stucco.

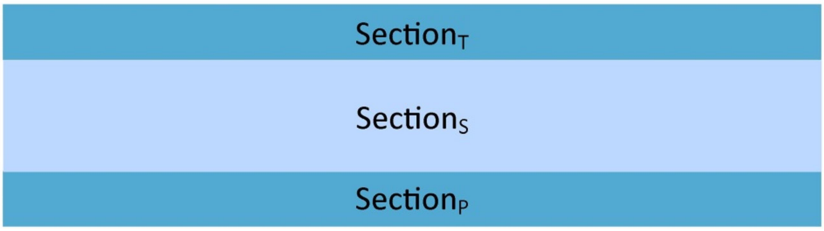



**Figure 116** – Shell composed of a primary section ($Section_P$), secondary section ($Section_S$) and tertiary section ($Section_T$)

### 6.3.1 Shell Build

Two shell systems were built containing an additional tertiary section to counteract flexural deformation observed in Shell (BD-$Al_2O_3$). The composition of each shell labelled Shell (Tert Tab-$Al_2O_3$) and Shell (Tert Fused-$Al_2O_3$) is given in Table 44 using the notation from Section 3.1.3 to label each layer.

**Table 44** – Composition of shells containing a tertiary section labelled Shell (Tert Tab-$Al_2O_3$) and Shell (Tert Fused-$Al_2O_3$)

| Complete shell identifier | Layer composition in order of application | Number of layers |
|---|---|---|
| Shell (Tert Tab-$Al_2O_3$) | P $(FusedAl)_2$ | 1 |
| | P+1 $(FusedAl)_2$ | 1 |
| | S (60 BD-$Al_2O_3)_2$ | 4 |
| | S (Tab-$Al_2O_3)_2$ | 1 |
| | Seal (Secondary) | 1 |
| Shell (Tert Fused-$Al_2O_3$) | P $(FusedAl)_2$ | 1 |
| | P+1 $(FusedAl)_2$ | 1 |
| | S (60 BD-$Al_2O_3)_2$ | 4 |
| | P+1 $(FusedAl)_2$ | 1 |
| | P $(FusedAl)_2$ | 1 |
| | Seal (Primary+1) | 1 |

### 6.3.2 Shell Characterisation

6.3.2.1 Scanning Electron Microscopy (SEM)

SEM analysis was undertaken on Shell (Tert Tab-$Al_2O_3$) and Shell (Tert Fused-$Al_2O_3$) in both pre-fired and fired condition as shown in Figures 117 and 118 respectively. It can be seen that the presence of transverse cracks are prevalent in both structures following the firing process. This likely results from $Section_S$ contracting under constraint from $Section_P$ and $Section_T$ [177]. The slurry in each layer is identified using notation outlined in Section 4.4.1.

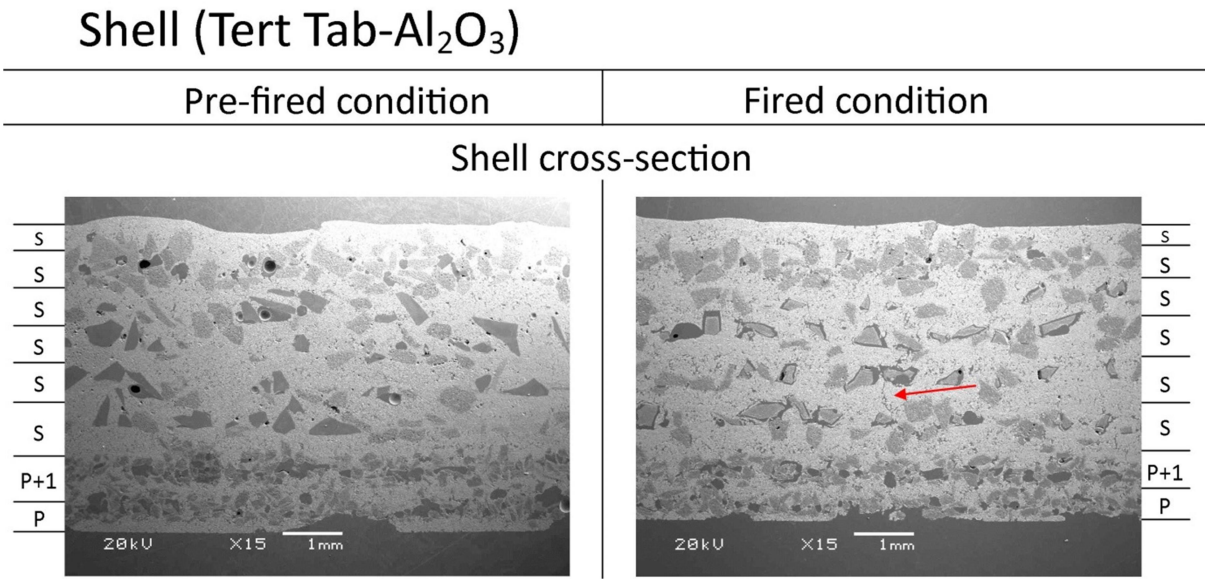



**Figure 117** – SEM analysis of Shell (Tert Tab-$Al_2O_3$) displaying the shell cross-section with slurry applied in each layer identified. The red arrow identifies a transverse crack

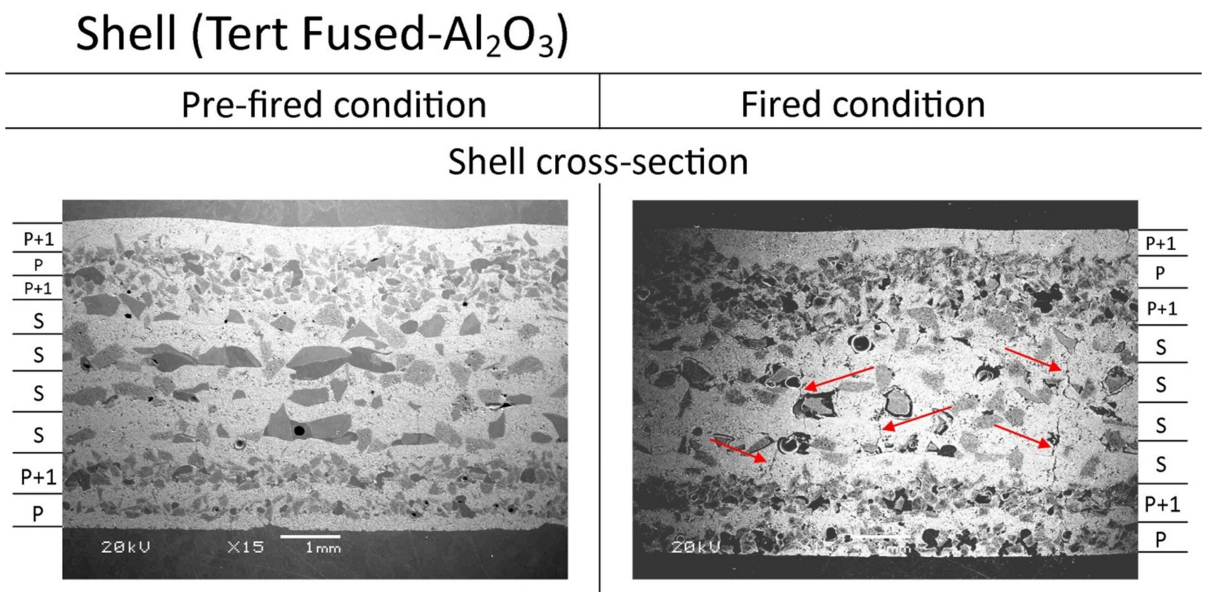



**Figure 118** – SEM analysis of Shell (Tert Fused-$Al_2O_3$) displaying the shell cross-section with slurry applied in each layer identified. The red arrows identify transverse cracks

6.3.2.2 Mechanical Strength

The mechanical strength of Shell (Tert Tab-$Al_2O_3$) and Shell (Tert Fused-$Al_2O_3$) in green, pre-fired and fired condition is shown in Figure 119 in comparison to Shell (Tab-$Al_2O_3$) using data reproduced from Section 6.2.6.2.

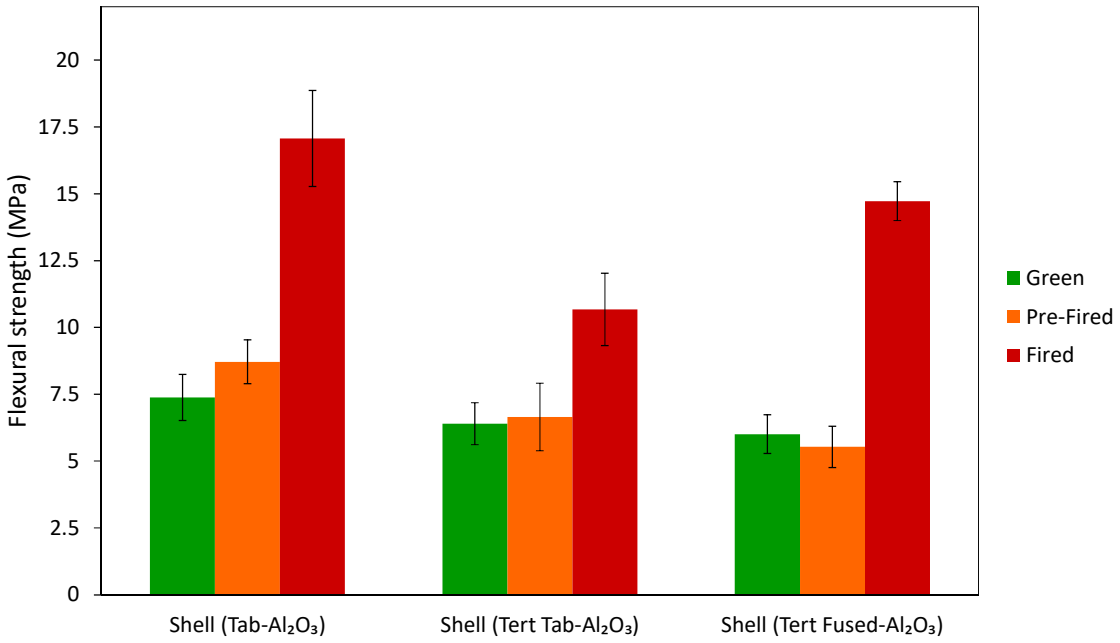



**Figure 119** – Flexural strength measured by 3 point bend loading on shell samples containing a tertiary section in comparison to the standard shell

As shown in Figure 119, Shell (Tert Tab-$Al_2O_3$) and Shell (Tert Fused-$Al_2O_3$) attain a reduced green strength in comparison to Shell (Tab-$Al_2O_3$) equal to 13 % and 19 % respectively; in addition, a reduction in pre-fired strength was also observed equal to 23 % and 36 % respectively. This was hypothesised to result from the same mechanism effecting Shell (BD-$Al_2O_3$) whereby porosity generated within the shell leads to a reduced load bearing area and subsequently failure at lower pressures. The fired strength of Shell (Tert Tab-$Al_2O_3$) and Shell (Tert Fused-$Al_2O_3$) was also reduced in comparison to Shell (Tab-$Al_2O_3$), attaining a reduction of 37 % and 14 % respectively. This was likely the result of the high concentration of transverse cracks as observed by SEM in Section 6.3.2.1. These cracks are an inherent weakness in the material and propagate when under load.

6.3.2.3 Measuring Flexural Deformation in-situ

As the method developed in Section 5.4 can only be used to predict curvature for asymmetric shell systems the curvature of shells containing a tertiary section was measured using the method developed in Section 5.6 using 3 point bend TMA. Using this method the average push rod displacement as a percentage of $T_0$ for Shell (Tert Tab-$Al_2O_3$) and Shell (Tert Fused-$Al_2O_3$) in either $Primary_{UP}$ or $Primary_{Down}$ orientation is shown in Figure 120; this is shown alongside Shell (Tab-$Al_2O_3$) and Shell (BD-$Al_2O_3$) for comparison using data reproduced from Section 5.6. Each shell was analysed three times in each orientation. The average push rod displacement for each shell variant in each orientation following the complete simulated casting cycle is shown in Table 45.

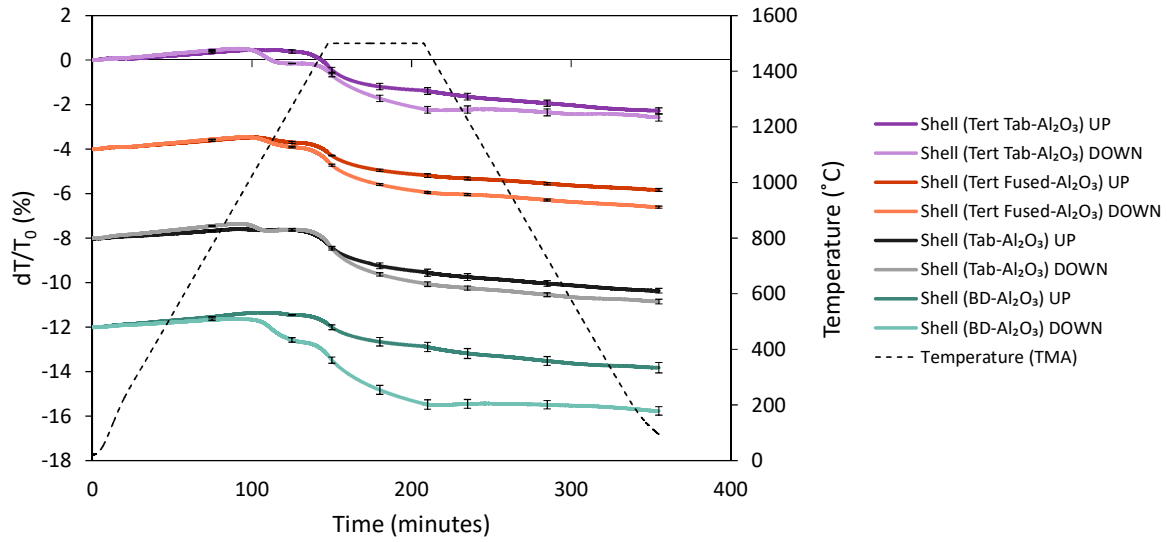



**Figure 120** – 3 point bend TMA of shells containing a tertiary section in both $Primary_{UP}$ and $Primary_{DOWN}$ orientation in comparison to Shell (Tab-$Al_2O_3$) and Shell (BD-$Al_2O_3$) throughout the simulated casting cycle. Samples are separated by 4 % for clarification

**Table 45** – Average push rod movement of complete shell samples analysed by 3 point bend TMA in $Primary_{UP}$ and $Primary_{DOWN}$ orientation following the simulated casting cycle

| | **$Primary_{UP}$ $dT/T_0$ (%)** | | **$Primary_{DOWN}$ $dT/T_0$ (%)** | |
|---|---|---|---|---|
| **Complete Shell** | **Average** | **Standard deviation** | **Average** | **Standard deviation** |
| Shell (Tert Tab-$Al_2O_3$) | -2.28 | 0.13 | -2.58 | 0.16 |
| Shell (Tert Fused-$Al_2O_3$) | -1.84 | 0.06 | -2.61 | 0.05 |
| Shell (Tab-$Al_2O_3$) | -2.37 | 0.11 | -2.85 | 0.11 |
| Shell (BD-$Al_2O_3$) | -1.82 | 0.24 | -3.77 | 0.19 |

It was observed that shells incorporating a tertiary section display a similar degree of push rod movement in both orientations resulting in a similar degree of flexural deformation as the sample Shell (Tab-$Al_2O_3$). As such, the addition of a tertiary section has effectively reduced the flexural deformation producing a trace more characteristic of Shell (Tab-$Al_2O_3$) than Shell (BD-$Al_2O_3$).

Carrying out the procedure detailed in Section 5.6, the deflection from normal over a 20 mm span (normalised curvature) was calculated using push rod displacement values output from the TMA for each individual Shell (Tert Tab-$Al_2O_3$) or Shell (Tert Fused-$Al_2O_3$) specimen throughout the simulated firing cycle. The calculated normalised curvature for both Shell (Tert Tab-$Al_2O_3$) and Shell (Tert Fused-$Al_2O_3$) is shown in Figure 121 combined with previous data reproduced from Section 5.6 for Shell (Tab-$Al_2O_3$) and Shell (BD-$Al_2O_3$) for comparison. The average normalised curvature following the complete firing cycle is displayed in Table 46.

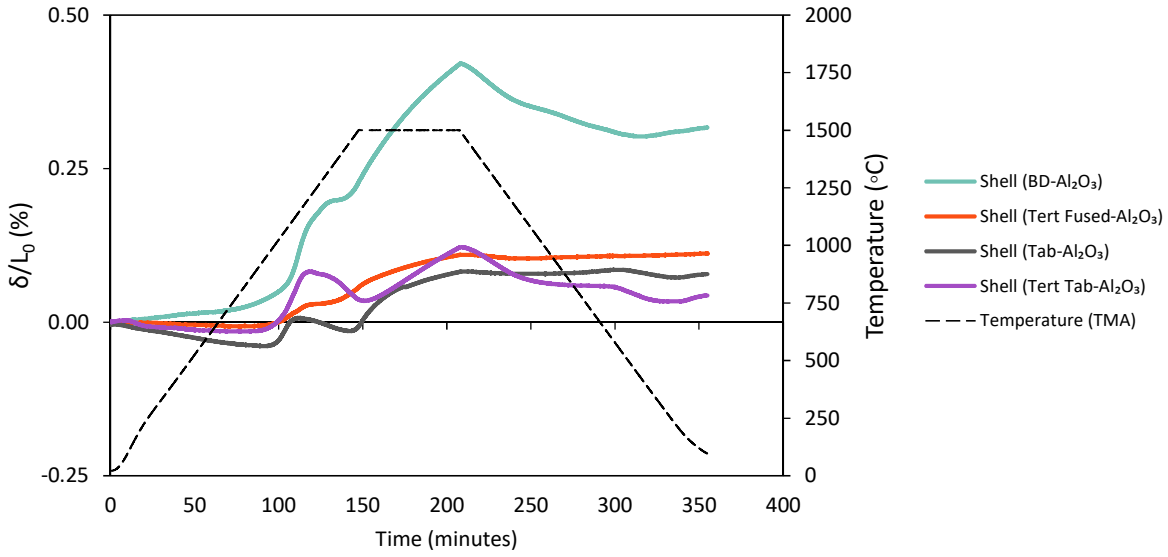



**Figure 121** – Normalised curvature measured from 3 point bend TMA method throughout the simulated casting cycle

**Table 46** – Normalised curvature following the complete simulated casting cycle measured from 3 point bend TMA method for complete shell samples

| Complete shell | Normalised curvature measured from 3 point bend TMA method (%) |
|---|---|
| Shell (Tert Tab-$Al_2O_3$) | 0.04 |
| Shell (Tert Fused-$Al_2O_3$) | 0.11 |
| Shell (Tab-$Al_2O_3$) | 0.08 |
| Shell (BD-$Al_2O_3$) | 0.32 |

It can be seen that the curvature profiles for both samples utilising a $Section_T$ show a greatly reduced flexural deformation in comparison to the Shell (BD-$Al_2O_3$) across the entire firing cycle. This demonstrates that the addition of a tertiary section has prevented excessive flexural deformation, producing a shell capable of casting components with less dimensional variation upon firing. It was also observed that despite the apparent symmetry of the sample Shell (Tert Fused-$Al_2O_3$), flexural deformation still arises. This was likely the result of the initial P $(FusedAl)_2$ layer deposited on the smooth wax pattern producing a flat plane of stucco in comparison to the latter P $(FusedAl)_2$ layer which was deposited onto a rougher shell surface. As a result of this, the Fused-$Al_2O_3$ particles in the tertiary section may be able to rearrange more freely producing the positive curvature recorded.

### 6.3.3 Closing Comments

The use of a tertiary section to reduce flexural deformation in shells containing monolithic porous stucco in the secondary section has proven to be successful. The additional section offers a fast and easy approach to reduce flexural deformation using readily available materials. Through this method a reduction in drying time in the secondary section can be achieved without excessive flexural deformation occurring however, compromise in flexural strength ensues.

## 6.4 Conclusions

Two solutions were proposed to incorporate water absorbent porous stucco into investment casting moulds without causing flexural deformation upon firing. The first solution considered a water absorbent porous material that remained dimensionally stable at casting temperature to use as stucco. This solution aimed to reduce the of differential thermal expansion/contraction between $Section_S$ and $Section_P$ for the shell system. The second solution considered a tertiary layer which constrained shrinkage within $Section_S$. This solution aimed to limit the magnitude of sintering in $Section_S$ by constraining sintering with the use of a layer expanding/contracting at a similar rate to $Section_P$. Both solutions were successful in reducing the magnitude of flexural deformation in comparison to use of monolithic porous stucco in secondary layers. However, a significant reduction in flexural strength was observed for each solution in comparison to the standard shell system in green, pre-fired and fired condition. Further optimisation for each solution may produce flexural strength results similar to the standard formulation.

# 7. Drying Behaviour

## 7.1 Introduction

In this Chapter the mechanism of accelerated drying is investigated to understand the process through which a reduction in drying time is achieved during shell build when utilising porous stucco in comparison to non-porous stucco. This was undertaken by measuring the moisture content of the system (slurry and stucco) when drying was conducted by recording weight loss over time. Alternatively, the moisture content of the slurry was measured independently from the stucco when drying was conducted by using a slurry which changes colour with moisture content. The combination of these two methods aimed to differentiate between dewatering of the slurry due to evaporation and dewatering of the slurry due to transport of liquid from the slurry to the porous stucco.

## 7.2 Monitoring Weight Loss

### 7.2.1 Introduction

The evaporation of water from a surface coated in slurry and stucco was measured by recording weight loss over a 6 hour period. As the slurry dries, the weight loss plateaus and a dry weight is determined. The percentage of moisture lost at a given time was then calculated as a percentage of the difference between the original weight and the dry weight. The rate of evaporation was also calculated over time and as a percentage of remaining moisture content to determine the mechanism through which water is transported to the surface. This was undertaken for both non porous and porous stucco blends deposited onto Secondary slurry.

Weight loss was measured as described in Section 3.1.5.1 utilising a rectangular wax pattern of dimensions 130 x 100 x 20 mm in two conditions. One condition in which slurry and stucco were applied directly to the wax pattern and another condition in which slurry and stucco were applied to a wax pattern coated in dried layers. The details of each drying experiment are given in Table 47, three repeat analyses were conducted for each experiment.

**Table 47** – Classification of each drying experiment labelled depending on the condition of the wax pattern dipped in slurry and the stucco composition applied

| Drying experiment label | Layers on wax before slurry application | Slurry applied | Stucco applied |
|---|---|---|---|
| Condition 1 – Tab-$Al_2O_3$ | None | Secondary | 100 vol% Tab-$Al_2O_3$ |
| Condition 1 – BD-$Al_2O_3$ Blend | None | Secondary | 60 vol% BD-$Al_2O_3$ 40 vol% Tab-$Al_2O_3$ |
| Condition 2 – Tab-$Al_2O_3$ | P (Fused-$Al_2O_3$)$_2$ P+1 (Fused-$Al_2O_3$)$_2$ | Secondary | 100 vol% Tab-$Al_2O_3$ |
| Condition 2 – BD-$Al_2O_3$ Blend | P (Fused-$Al_2O_3$)$_2$ P+1 (Fused-$Al_2O_3$)$_2$ | Secondary | 60 vol% BD-$Al_2O_3$ 40 vol% Tab-$Al_2O_3$ |

### 7.2.2 Recording Weight Loss

The recorded weight loss over time for each drying experiment labelled in Table 47 is shown in Figure 122. It can be seen a high level of variation occurs for each experiment. This was likely due to variation in the volume of slurry deposited between samples which subsequently resulted in variation to the quantity of moisture lost.

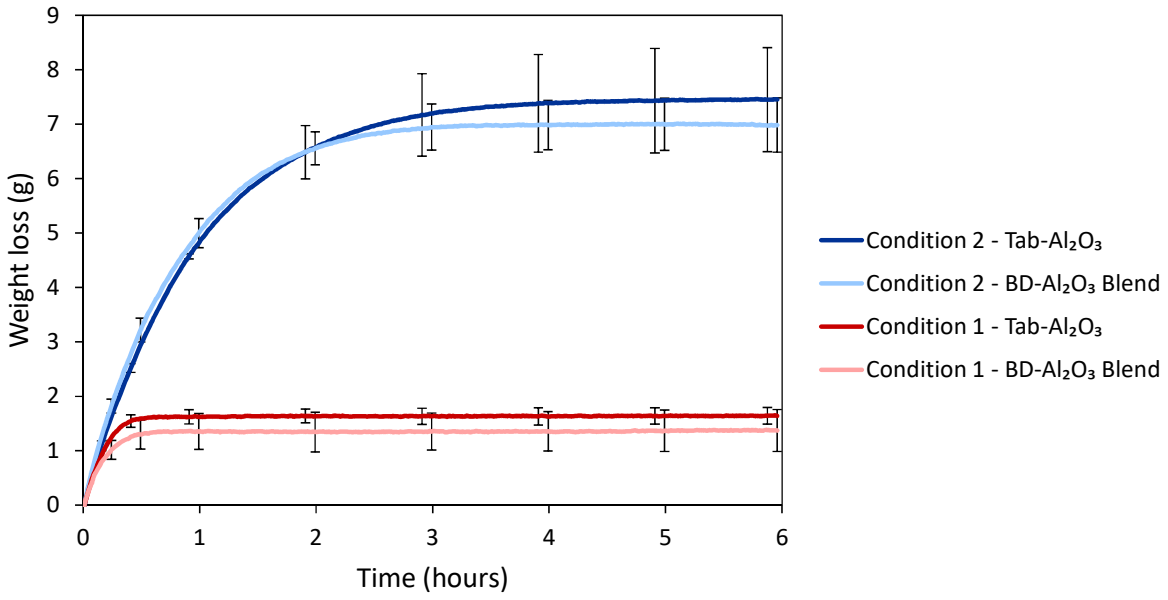



**Figure 122** – Recorded weight loss over time for drying experiments conducted on samples coated in slurry and stucco

For each drying experiment the sample was defined as 100 % dry after 6 hours, at which time a change in weight loss less than ±0.01g was measured over the previous 10 minutes. The quantity of weight loss after the 6 hour period for each drying experiment is listed in Table 48.

**Table 48** – Average weight loss for each drying experiment after 6 hours

| Drying experiment label | Weight loss (g) | |
|---|---|---|
| | **Average** | **Standard deviation** |
| Condition 1 - Tab-$Al_2O_3$ | 1.64 | 0.14 |
| Condition 1 - BD-$Al_2O_3$ Blend | 1.37 | 0.39 |
| Condition 2 - Tab-$Al_2O_3$ | 7.45 | 0.94 |
| Condition 2 - BD-$Al_2O_3$ Blend | 6.98 | 0.47 |

It can be seen that the average weight loss varies drastically between conditions 1 and 2, this results from previously dried layers absorbing water when redipped, leading to greater magnitudes of weight loss when drying occurs. However, the variation in average weight loss for a given condition with different stucco composition is negligible due to the overlap in standard deviation. As such, it was not possible to accurately conclude the effect of varying stucco composition on weight loss. However, a reduction in overall weight loss when applying porous stucco appears present in both conditions. This may be the result of strongly bound water retained within the structure of BD-$Al_2O_3$ stucco following drying leading to a reduction in the quantity of water evaporated. However, as shown by DVS in Section 4.2.5, only a small mass increase of 0.5 % occurs following saturation followed by drying in an environment stabilized at 50 % $R_H$. Utilising the mass of stucco deposited onto a partially built shell surrounding a wax pattern identical in dimensions to measuring weight loss measurements (Section 4.3.2) and assuming an accurate 60 vol% concentration of BD-$Al_2O_3$ was deposited, it was calculated that approximately 5.84 g of BD-$Al_2O_3$ was deposited. Therefore, the expected amount of water retained in the BD-$Al_2O_3$ stucco is 0.03 g assuming a 0.5 % weight increase. This is an insignificant amount in comparison to the large discrepancies observed when applying porous stucco in comparison to non-porous stucco for each condition. Therefore, enhanced accuracy and repeatability of drying experiments would be required to further quantify if this effect is indeed real or the result of error.

### 7.2.3 Mass Balance

Utilising the calculated volume of BD-$Al_2O_3$ stucco blend deposited onto a partially built shell surrounding a wax of dimensions 130 x 100 x 100 mm (Section 4.3.2) and the porosity of BD-$Al_2O_3$ (Section 4.2.4); the pore volume contained within this layer of stucco can be calculated from Equation 60. This volume can then be compared against the weight loss measured in Section 7.2.2 for a partially built shell surrounding an identically sized wax pattern to calculate the volume of liquid the porous stucco could absorb if all pore volume had the capacity to absorb water from the slurry assuming 1 g of $H_2O$ is equal to 1 $cm^3$. Equation 60 assumes the following:

-The porous stucco was dehydrated to the same degree in which porosity measurements were taken

-The concentration of porous stucco in porous stucco blends was accurately represented when depositing stucco onto slurry

$$\begin{matrix}Total\\ pore\\ volume\\ (cm^3_{pore})\end{matrix} = \begin{matrix}Stucco\\ volume\\ deposited\\ (cm^3_{bulk})\end{matrix} \times \begin{matrix}Porosity\ of\\ porous\ stucco\\ (cm^3_{pore}\ cm^{-3}_{bulk})\end{matrix} \times \begin{matrix}Volume\ ratio\\ of\ porous\ stucco\\ (-)\end{matrix} \qquad \text{eq.60}$$

It was calculated from Equation 60 that for the specified wax pattern size the total pore volume present within the BD-$Al_2O_3$ stucco blend was 2.37 $cm^3$. Assuming all pore volume has the capacity to absorb water from the slurry and weight loss measurements conducted with 100 vol% Tab-$Al_2O_3$ stucco in Section 7.2.2 represent the true quantity of water present in the slurry; depositing a layer of 60 vol% BD-$Al_2O_3$ stucco has the capacity to absorb 145 % of the volume of water present in condition 1 or 32 % of the water volume present in condition 2. However, the available pore volume will reduce as water is adsorbed onto the BD-$Al_2O_3$ structure depending on the $R_H$ of the environment as shown by DVS in Section 4.2.5. To conclude, the porous stucco has a limited capacity to absorb water from the slurry and thus as more layers are built, a lower percentage of total water can be absorbed due to previously dried layers absorbing water upon redipping.

### 7.2.4 Percentage Weight Loss

Utilising the average total weight loss recorded for each drying experiment in Table 48 the average percentage weight loss over time was calculated for each drying experiment. This was undertaken by displaying the average weight loss at a given time (displayed in Figure 122) as a percentage of the total weight loss (Table 48). This is displayed in Figure 123.

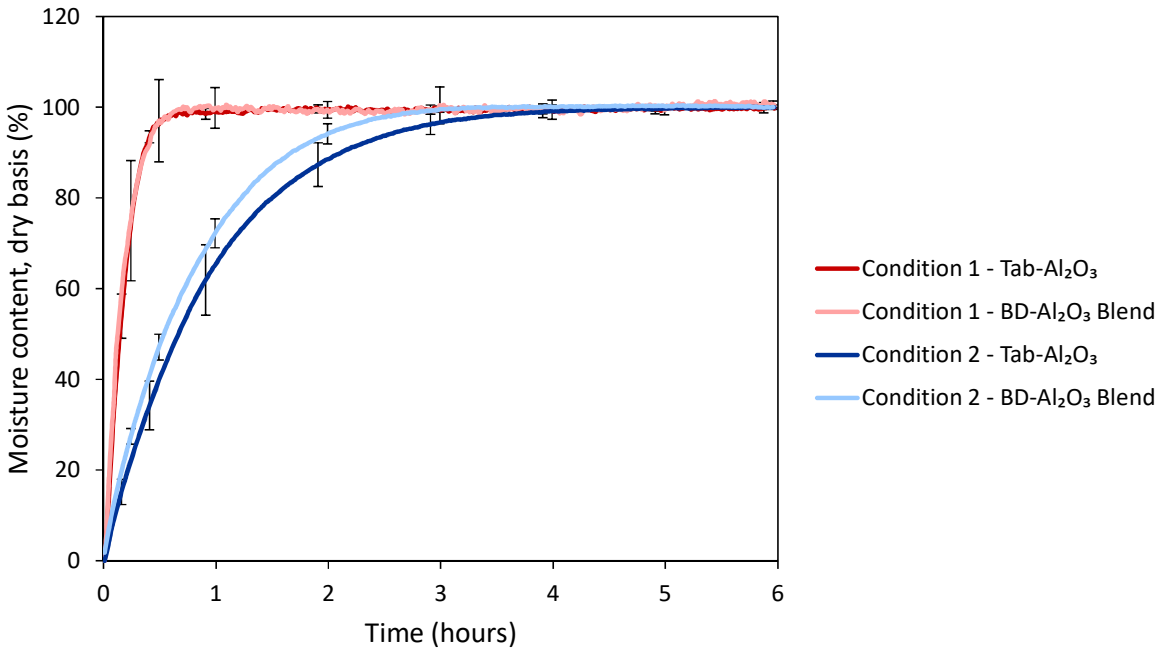



**Figure 123** – Percentage weight loss over time for drying experiments conducted on samples coated in slurry and stucco

As shown in Figure 123, condition 1 attains complete dryness earlier than condition 2. This was the result of a smaller volume of water being evaporated over the same area for condition 1, thus less time was required to reach a specific moisture content. Once again, standard deviations bars overlap for a given condition, preventing accurate interpretation for different stucco compositions.

### 7.2.4 Rate of Weight Loss

The average rate of weight loss over 60 second periods for each drying experiment is shown plotted against time in Figure 124 and plotted against moisture content in Figure 125. It can

be seen that negative rates of evaporation are calculated towards later stages of drying. This occurs as the variation in weight as a result of error exceeds the change in weight resulting from evaporation.

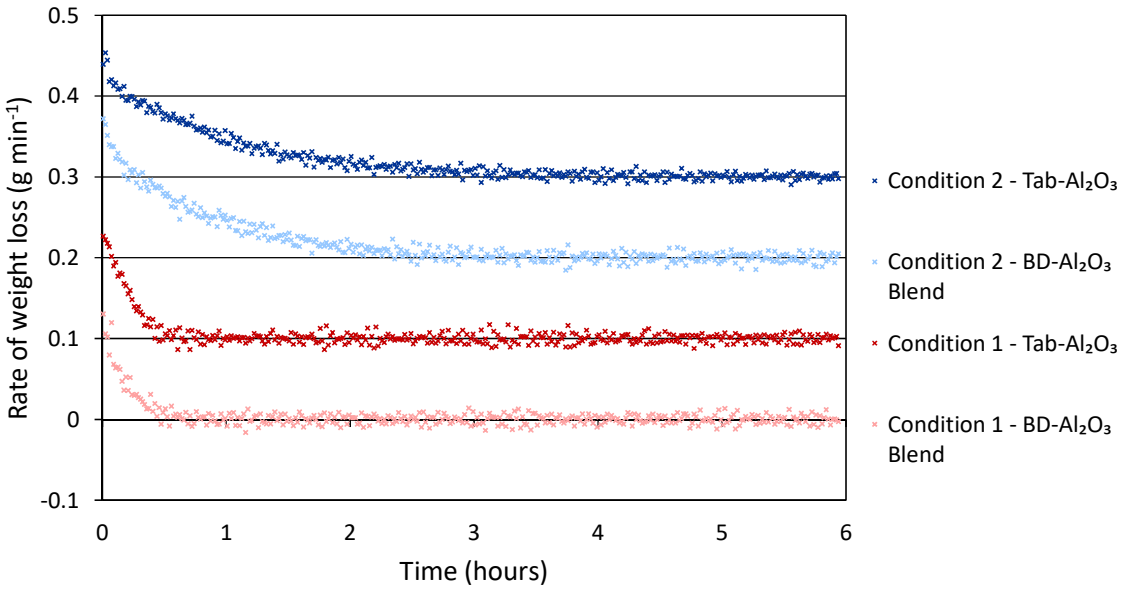



**Figure 124** – Rate of weight loss against time for drying experiments conducted on samples coated in slurry and stucco. Samples are separated by 0.1 g $min^{-1}$ at the origin for clarification

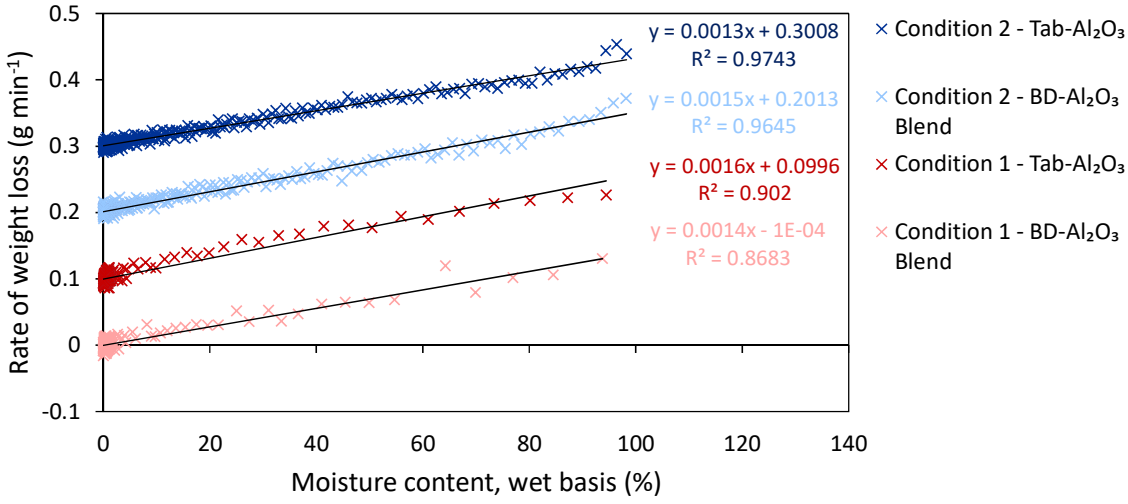



**Figure 125** – Rate of weight loss against moisture content for drying experiments conducted on samples coated in slurry and stucco. Samples are separated by 0.1 g $min^{-1}$ at the origin for clarification

The rate of weight loss for each drying experiment follows first order kinetics with respect to moisture content, similar to the FRP1 in Figure 6 (b). This behaviour is indicative of capillary controlled mass transfer resulting from liquid flowing to the surface from the bulk as a result of capillary action [40]. During this period it is recognised that the liquid is in a funicular state as the meniscus of the larger pores has begun receding into the bulk [36] and the rate of moisture loss decreases linearly with moisture content. The rate determining step for moisture loss during capillary controlled mass transfer is the evaporation of liquid from the surface. The hypothesis that moisture loss of investment casting slurries is controlled by capillary controlled mass transfer is supported by studies on similar investment casting slurries showing external factors such as $R_H$ [29], temperature [62] and air speed [37] vary the rate of moisture loss.

The absence of an equilibration period indicates that the temperature reduction resulting from the latent heat of evaporation equilibrates quickly or that the minor temperature change does not significantly affect the rate of evaporation. In addition, the absence of a CRP indicates that the slurry has transitioned from an initially fluid state during dipping to a rigid state once weight loss measurements begin in the drying chamber.

Furthermore, the presence of a FRP2 cannot be seen, a characteristic which is typically observed in most drying mediums, however, often not present when observing thin granular beds [41] or colloidal suspensions [43]. The absence of this period indicates that the slurry can maintain transport of liquid to the surface by capillary action until completely dry. Therefore, the rate limiting step of water loss is never limited by diffusion of liquid from the bulk to the surface, even in thicker samples (condition 2). Alternatively, the depression of the rate of moisture loss as the FRP2 occurs is too small to measure and thus cannot be observed.

It can also be seen that at any given time for a given condition the rate of weight loss is approximately equal when depositing porous or non-porous stucco compositions. This was unexpected as the transfer of water from the slurry to the porous stucco would expectedly result in a reduction in rate of evaporation at the slurry surface. This would occur because a reduction in moisture content reduces the rate of evaporation within FRP1. To explain this phenomenon two mechanisms are evaluated:

1) Water is not transferred from the slurry to the porous stucco and evaporation takes place in an identical manner to applying non-porous stucco. This mechanism is unlikely as it has been shown that drying times have successfully been reduced when applying porous stucco (as shown in Section 4.4.5.1 and 6.2.6.6). Therefore it is highly likely that porous particles are absorbing water when deposited onto the slurry surface.

2) Liquid is absorbed by the porous stucco however; the rate of weight loss remains equal to application of non-porous stucco as water evaporates from the porous stucco surface to account for the reduction in rate of evaporation at the slurry surface. This mechanism appears plausible and thus is explored further.

A schematic for the proposed mechanism is shown in Figure 126 accounting for evaporation occurring at both the slurry and stucco surface assuming the porous stucco particles absorb water from the slurry due to the narrower pore size. Non-porous particles remain inert and do not absorb water. The mechanism is split to accommodate a pathway in which porous particles become saturated or remain unsaturated when contacting the slurry surface.

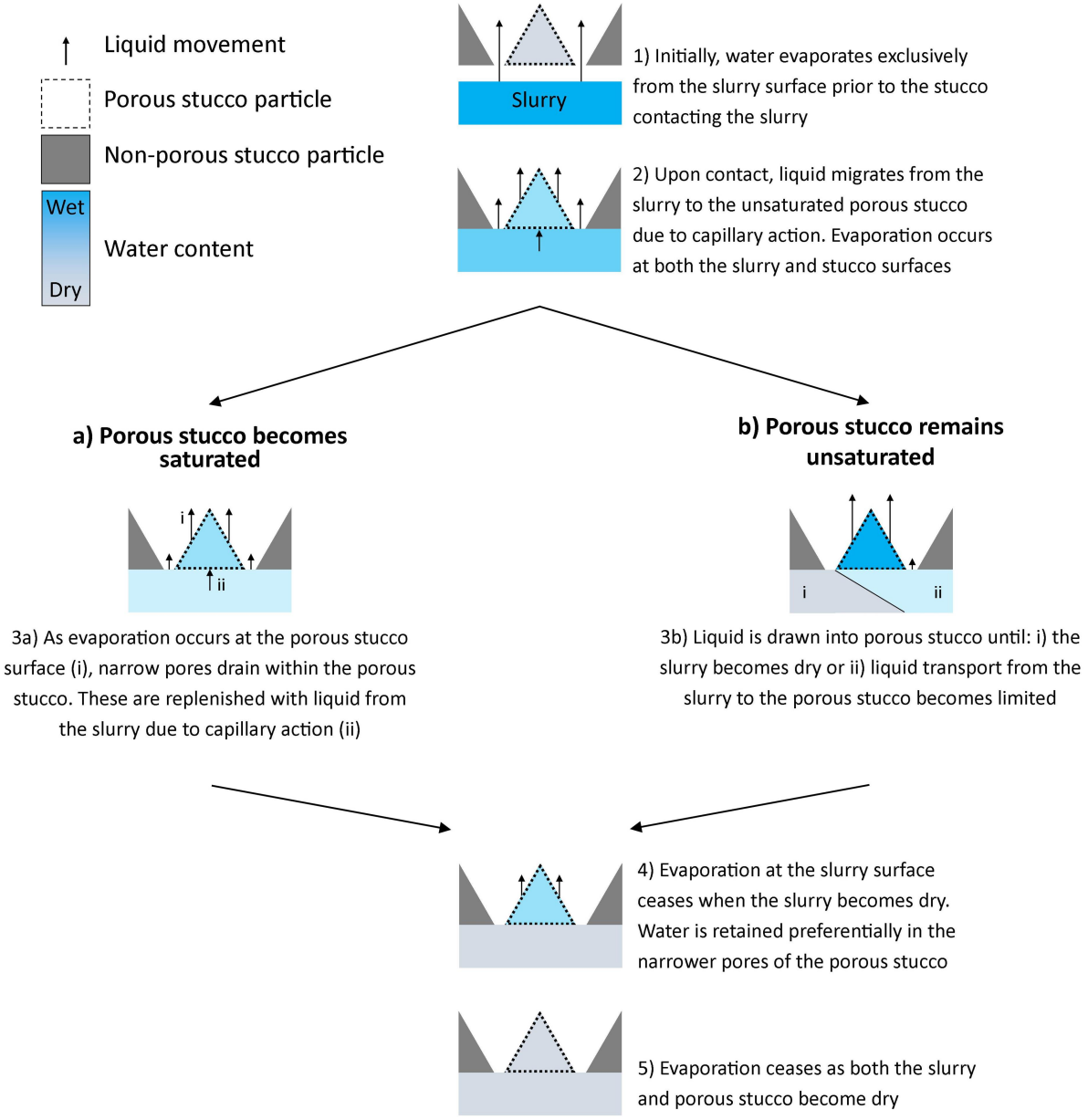



**Figure 126** – Schematic proposed to describe the evaporation of liquid from both the slurry and porous stucco surfaces throughout the drying period upon contact

It would be expected that the water transferred from the slurry to the BD-$Al_2O_3$ particles desorbs at a different rate to the slurry, thus a difference in the rate of weight loss would be expected when applying porous stucco in comparison to non-porous stucco. This would be predicted to occur due to the different material properties and pore structure of the slurry in comparison to the BD-$Al_2O_3$ particles. In addition, the system containing porous stucco

has a larger surface area through which evaporation can occur as water can evaporate from both the slurry and stucco surface. However, the rate of weight loss for a given condition remains equal for both stucco compositions. It may therefore be a coincidence that the cumulative rate of evaporation from the slurry and BD-$Al_2O_3$ particles (when depositing BD-$Al_2O_3$ stucco blends) is equal to the rate of evaporation from the slurry (when depositing non-porous stucco). This hypothesis is expressed visually in Figure 127 using terms from Equations 61 and 62 to describe the rate of moisture loss in a system containing porous stucco or non-porous stucco.

$$R_{NP(system)} = R_{NP(slurry)} \quad \text{eq.61}$$

$R_{NP(system)}$ Rate of moisture loss from system containing only non-porous stucco (kg $m^{-2}$ $s^{-1}$)

$R_{NP(slurry)}$ Rate of moisture loss resulting from evaporation at slurry-air interface in system containing only non-porous stucco (kg $m^{-2}$ $s^{-1}$)

$$R_{P(system)} = R_{P(slurry)} + R_{P(BD-Al_2O_3)} \quad \text{eq.62}$$

$R_{P(system)}$ Rate of moisture loss in system containing porous stucco (kg $m^{-2}$ $s^{-1}$)

$R_{P(slurry)}$ Rate of moisture loss resulting from evaporation at slurry-air interface in system containing porous stucco (kg $m^{-2}$ $s^{-1}$)

$R_{P(BD-Al_2O_3)}$ Rate of moisture loss resulting from evaporation at BD-$Al_2O_3$-air interface in system containing porous stucco (kg $m^{-2}$ $s^{-1}$)

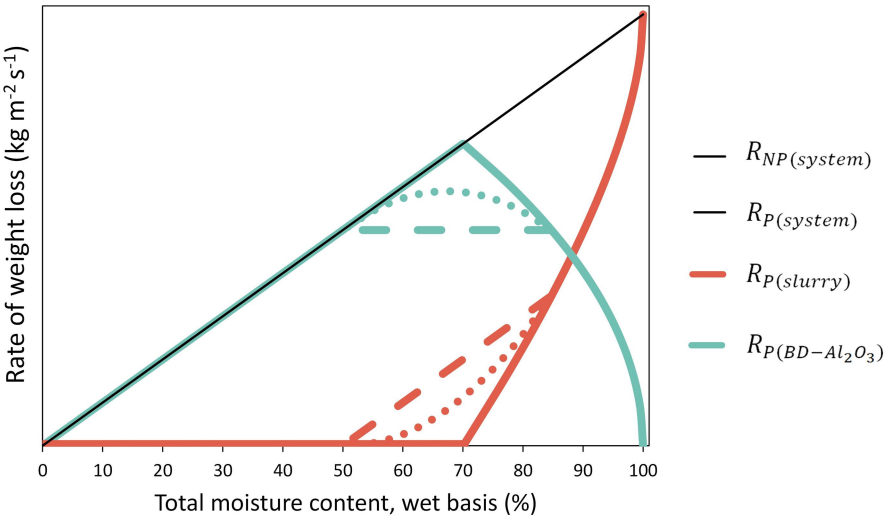



**Figure 127** – Example of possible mechanisms in which the rate of evaporation in the system remains equal when applying porous or non-porous stucco despite porous stucco absorbing water from the slurry. Full lines represent the porous stucco absorbing water until the slurry is completely dry. Dotted lines represent the porous stucco absorbing until liquid transport becomes limited. Dashed lines represent the porous stucco absorbing water until becoming saturated, a constant rate of evaporation occurs at the stucco surface as pores in the porous stucco are replenished with liquid from the slurry as evaporation takes place until the slurry is completely dry

As hypothesised in Figure 127, the transfer of water from the slurry to the porous stucco results in evaporation occurring at both slurry and BD-$Al_2O_3$ surfaces. Evaporation occurring at the BD-$Al_2O_3$ surface accounts for the reduction in rate of evaporation at the slurry surface; this produces an equal rate of evaporation in a system containing porous or non-porous stucco. Such behaviour explains how the rate of evaporation can be equal when depositing porous and non-porous stucco despite transfer of water from the slurry to the porous stucco. Additionally, the transfer of water from the slurry to the BD-$Al_2O_3$ particles explains the reduction in drying time required before the next layer can be applied when depositing porous stucco. This occurs because the slurry attains a lower moisture content at a given time in comparison to depositing non-porous stucco. Furthermore, water transferred from the slurry to the porous stucco reduces the amount of time until the slurry attains complete dryness as less time is required to evaporate the remaining water retained in the slurry.

## 7.3 Monitoring Colour Change

### 7.3.1 Introduction

In attempts to differentiate between water evaporated from the slurry and water absorbed by the porous stucco; an experiment was designed to quantify the moisture content of the slurry utilising a colour indicating colloidal silica binder. The Ransom and Randolph Primecote binder with ReDip$^{TM}$ indicator contains a fluorescein dye which changes colour as it transitions from wet to dry. This property was exploited to measure the moisture content of the slurry independently from the porous stucco. As detailed in Section 3.1.5.2, the method measures the average colour of an image taken through a clear beaker recording pictures at minute intervals with the aid of a box and rubber seal to prevent excess light and glare.

### 7.3.2 Method

Following the procedure outlined in Section 3.1.5.2 a glass beaker was dipped into Indicating slurry and coated with the required stucco before placing the coated beaker inside a box. A typical image taken from the inside of the glass beaker is shown in Figure 128. The image displays slurry coated on the outside of the beaker which obscures direct line of sight to the stucco coated on the surface of the slurry. The slurry is observed to have a yellow hue which diminishes in intensity as drying progresses as a result of the fluorescein dye.

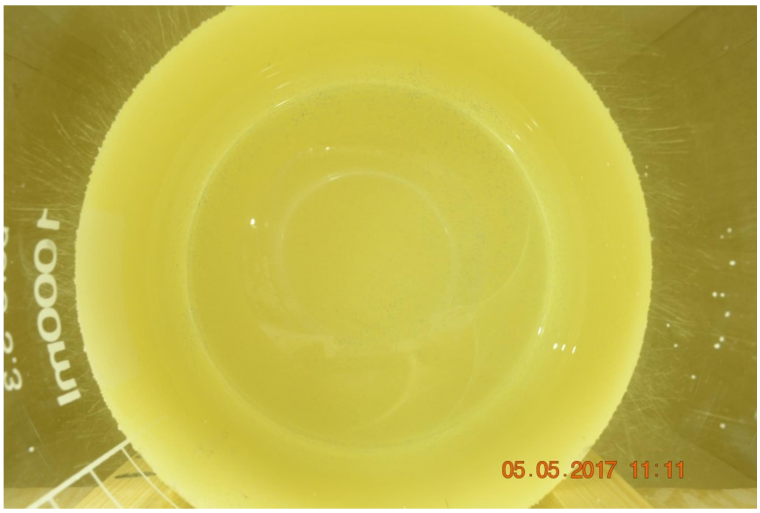



**Figure 128** – Typical image recorded during experiment of a glass beaker coated in Indicating slurry and Tab-$Al_2O_3$ stucco at the initial point of the drying

Capturing images at minute intervals and measuring the average colour component value for red, blue and green in each image, the progression of colour over time was recorded. This is shown in Figure 129 for slurry coated in 100 vol% Tab-$Al_2O_3$ stucco. It can be seen that both red and green component values vary slightly over time, whereas the blue component follows a transition which eventually plateaus, indicating that the slurry is dry. In industry this colour transition can be useful to determine when the outer coat is dry and the next layer of slurry can be added to the mould.

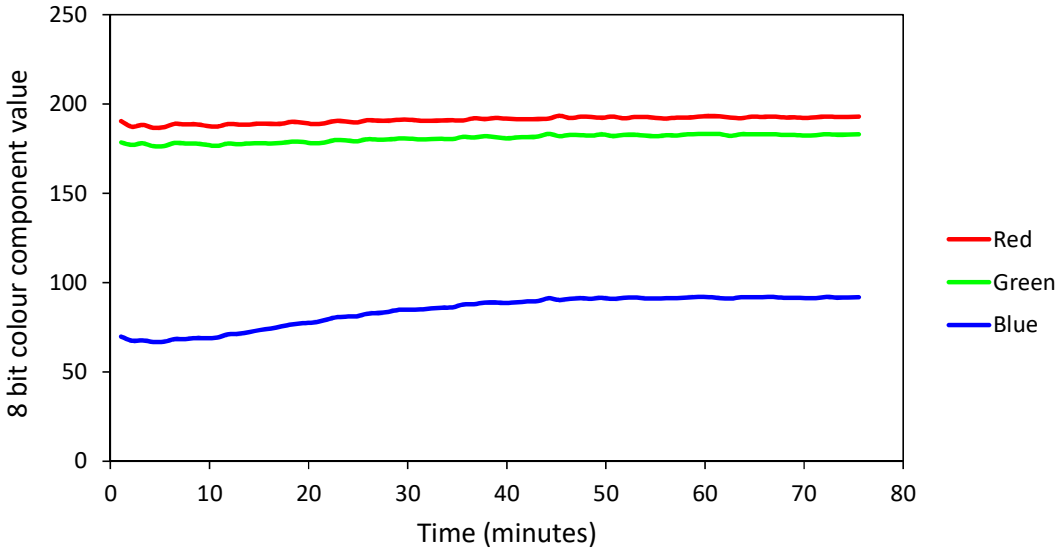



**Figure 129** – Average red, blue or green colour component values over time for images taken of a glass beaker coated in Indicating slurry and Tab-$Al_2O_3$ stucco

The time taken for the slurry to dry was identified by calculating the gradient of blue colour component values over 10 consecutive minutes using the least mean squared fit method. The shortest length of time required for the following 10 consecutive blue colour component values to attain a gradient of less than 0.1 $min^{-1}$ is defined as the length of time taken for the slurry to dry. This gradient was chosen as the maximum gradient a previously dried sample could achieve due to variability in 10 minutes was observed to be 0.1 $min^{-1}$ over an hour period. As such, if the gradient drops below this value the resulting variation in colour is likely to be the result of error; therefore the sample is defined as dry.

The moisture content of the slurry is identified using the blue colour component values between the minimum value and subsequent values prior to when the slurry is defined as dry. The moisture content of the slurry is defined as 0 % dry at the minimum blue colour component value. The moisture content of the slurry is defined as 100 % dry at the average blue colour component value over the 10 minute period in which the gradient is less than 0.1 $min^{-1}$. The moisture content at a given time can then be calculated by expressing the blue colour component value as a percentage of the total difference between the blue colour component values at 0 % and 100 % dry. This process is shown in Figure 130.

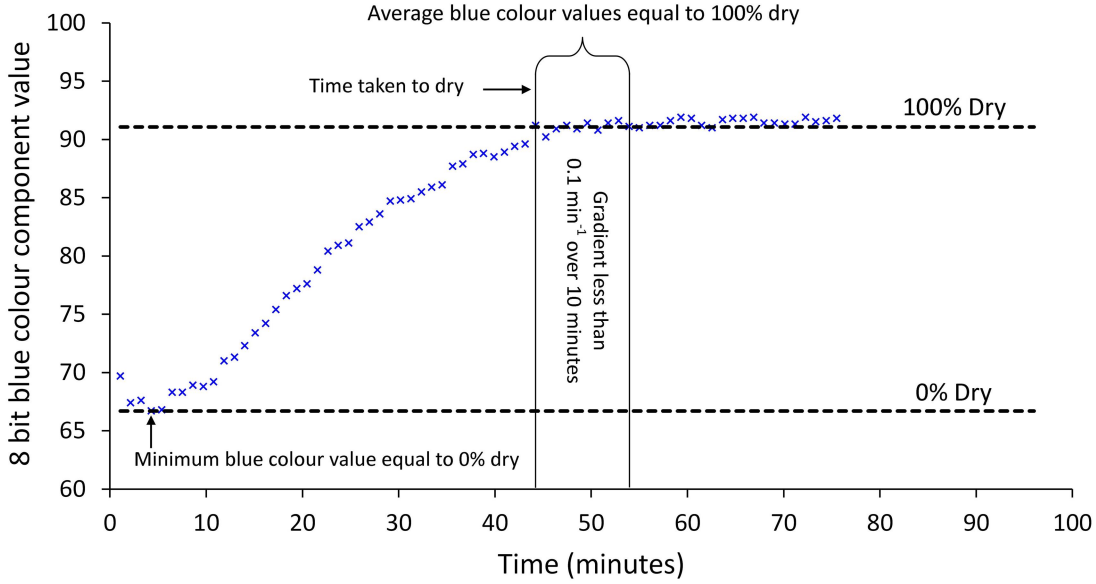



**Figure 130** – Annotated diagram of blue colour component values over time for images taken of a glass beaker coated in Indicating slurry and Tab-$Al_2O_3$ stucco. The time taken to dry is identified in addition to the blue colour component values equal to 0 % and 100 % dry

A range of stucco compositions were tested to compare the effectiveness of each material at absorbing water from the slurry. The composition of each stucco blend is shown in Table 49. Each stucco composition was analysed three times with each experiment running for approximately 1 hour.

**Table 49** – Identifying labels for various stucco compositions

| Stucco composition label | Stucco composition |
|---|---|
| Tab-$Al_2O_3$ | 100 vol% Tab-$Al_2O_3$ |
| BD-$Al_2O_3$ Blend | 60 vol% BD-$Al_2O_3$<br>40 vol% Tab-$Al_2O_3$ |
| SGB127 Blend | 60 vol% SGB127<br>40 vol% Tab-$Al_2O_3$ |
| αFrame-Impreg$_8$-Clean Blend | 60 vol% αFrame-Impreg$_8$-Clean<br>40 vol% Tab-$Al_2O_3$ |

### 7.3.3 Results

Following the method outlined in Section 7.3.2, a representative plot of slurry moisture content progression is given in Figure 131 for each stucco composition listed in Table 49.

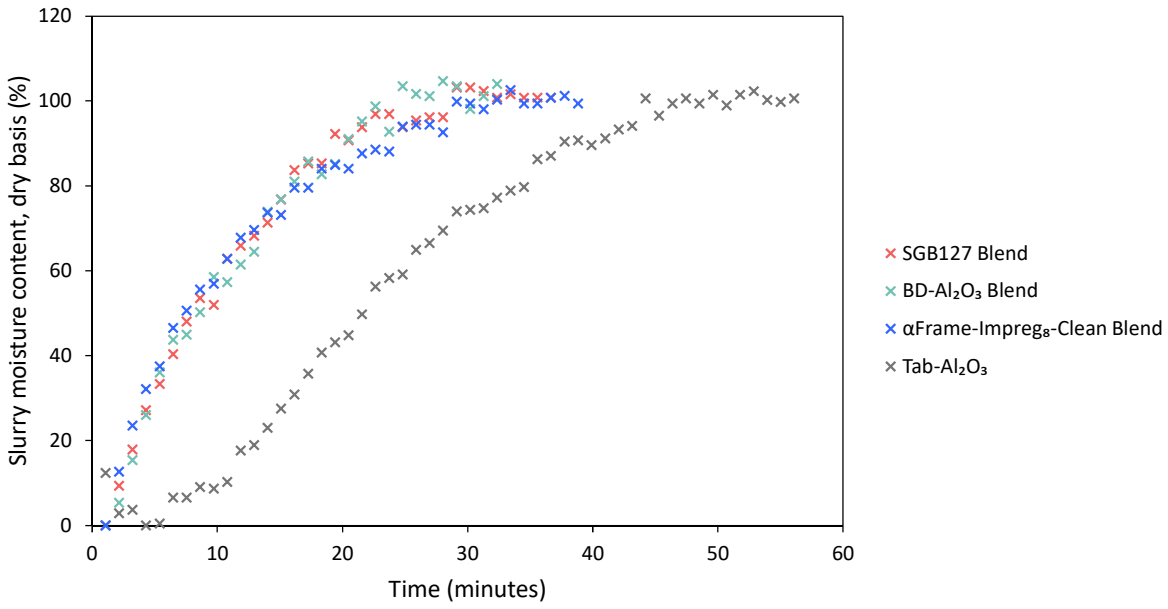



**Figure 131** – Typical examples of moisture content progression over time when applying different stucco compositions. Each plot displays the recorded moisture content until the sample is determined to be dry in addition to the 10 minutes proceeding this.

Accumulating the three repeat analyses per stucco composition, the moisture content at 10 minute intervals is displayed in Figure 132. This shows the variability in moisture content measured for the three repeat analyses conducted for each stucco composition. The time

taken to dry the slurry as defined in Section 7.3.2 is displayed in Figure 133 for each stucco composition.

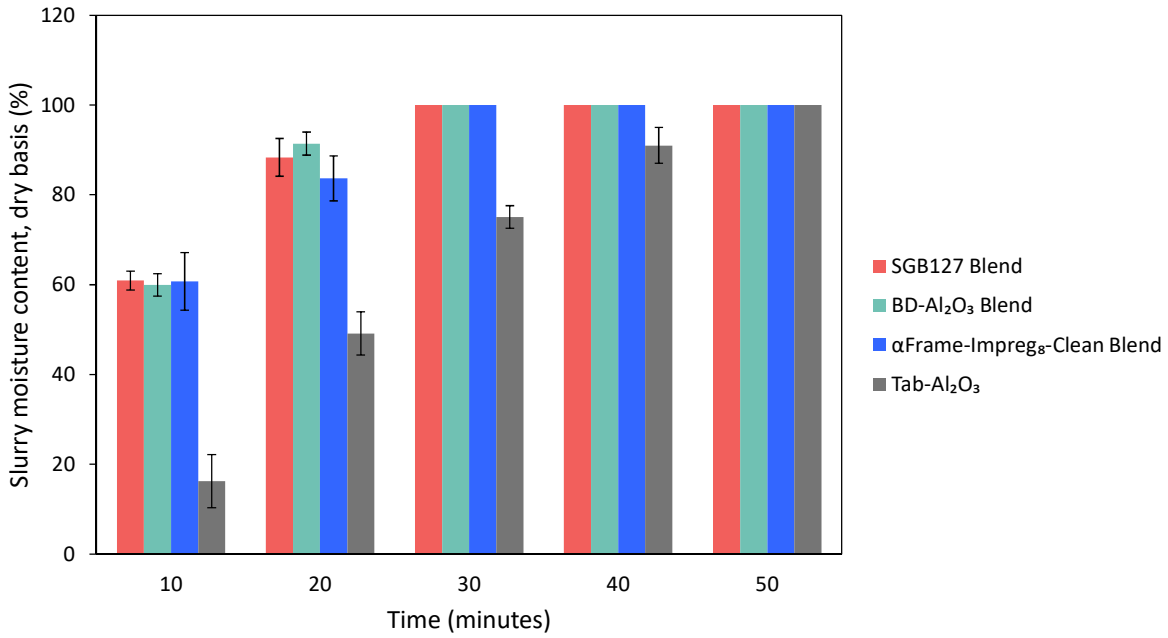



**Figure 132** – Moisture content at 10 minute intervals when applying different stucco compositions. Once all 3 repeat analyses per stucco composition have been identified as dry the moisture content is taken as 100 % dry with no variability.

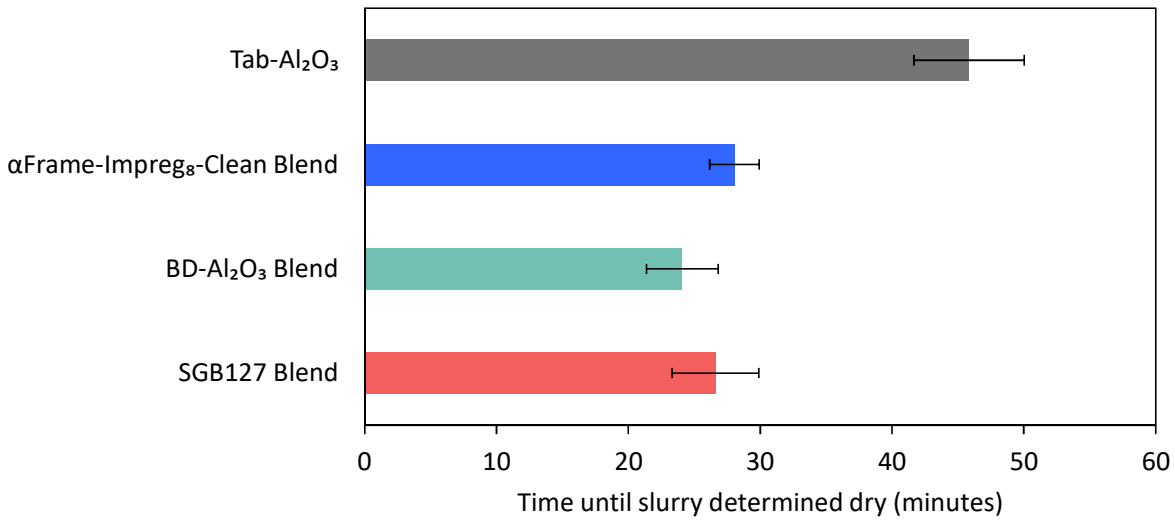



**Figure 133** – Time taken for each stucco composition to dry the Indicating slurry

Analysing Figures 131 and 132, it can be seen that the replacement of Tab-$Al_2O_3$ stucco with porous stucco has altered the mechanism through which water is removed from the slurry. Slurry coated in porous stucco consistently displays a lower moisture content at any given time in comparison to slurry coated in Tab-$Al_2O_3$ stucco. Additionally, slurry coated in porous stucco reaches a consistent average blue colour component value over 10 consecutive minutes more quickly, leading to the shell being identified as dry significantly earlier than slurry coated in Tab-$Al_2O_3$ as shown in Figure 133.

Further analysis of moisture content progression for slurry coated in Tab-$Al_2O_3$ stucco (Figure 131) reveals the image with the lowest average blue colour component value is located approximately 5 minutes after starting the drying experiment. This phenomenon was observed for all repeats carried out on slurry coated with Tab-$Al_2O_3$, but not observed when porous stucco was used. It was hypothesised that the reason this phenomenon only occurs when depositing Tab-$Al_2O_3$ results from slurry continuing to wet the glass surface or alternatively the reduction of bubbles at the glass-slurry interface. This would result in successively greater areas of slurry in the image, lowering the average blue colour component value. This effect continues until the slurry becomes viscous and stops spreading out or the liquid meniscus reaches the slurry-glass interface, causing the average blue colour component value to increase as the slurry visible to the camera begins to dry and change colour.

The reason this lag period was absent when applying porous stucco can be explained by the porous stucco absorbing water upon contact as proposed in Figure 126. This causes the slurry to become viscous before the first image is taken, preventing the slurry from wetting the glass surface further. Additionally, as a result of the accelerated drying process the liquid meniscus reaches the slurry-glass interface before the first image is taken. This results in the first image of slurry coated in porous stucco attaining the lowest average blue colour value.

This hypothesis leads to the conclusion that the porous stucco quickly absorbs water from the slurry upon contact. As a result of this, by the time the first image was taken the slurry has become partially dewatered despite this image attaining the lowest average blue colour component value of the set of images. Consequently, the magnitude of difference between the minimum blue colour component value and the blue colour component value defined as 100 % dry is smaller when applying porous stucco than applying non-porous stucco as

shown in Figure 134. Subsequently, the calculated moisture content is slightly inaccurate when applying porous stucco compositions due to colour change occurring before the first image being taken. This could be resolved by taking images in quicker succession by producing a light box that accommodates more light whilst still removing glare and shadowing.

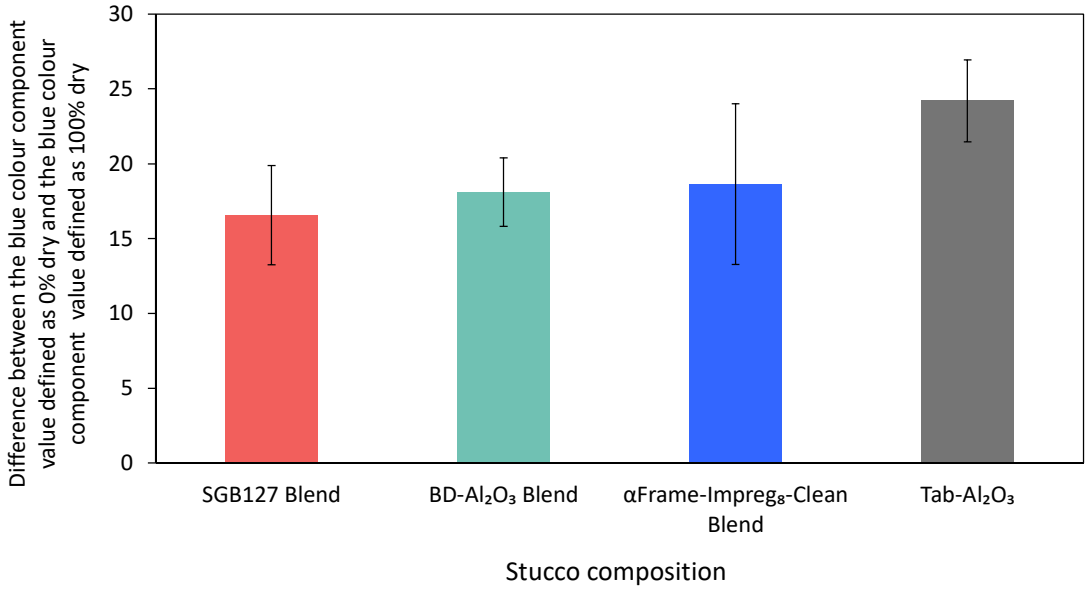



**Figure 134** – Difference between the blue colour component value defined as 0 % dry and the blue colour component value defined as 100 % dry when applying different stucco compositions to Indicating slurry

It can also be seen that irrespective of which porous stucco material is used, the same moisture content progression occurs as shown in Figure 132. This was unexpected as BD-$Al_2O_3$, SGB127 and αFrame-$Impreg_8$-Clean contain drastically different quantities of pore volume as calculated by BJH method (0.59, 0.37 and 0.22 $cm^3_{pore}$ $cm^{-3}_{bulk}$ respectively). As such, if each porous material absorbed water into the entire available pore volume upon contact with the slurry, variation in the moisture content progression of the slurry would be observed as a result of variation in the volume of water absorbed by each material. This behaviour appears to contradict results observed in Section 4.3.1 whereby a greater vol% of porous stucco dried the slurry surface more quickly resulting in a poor surface coverage and adhesion. However, these two observations cannot be compared directly as the

experimental method monitoring colour change measures the moisture content within the bulk not at the slurry-air interface. As such it would be useful to monitor the colour change of Indicating slurry using different concentrations of porous stucco blends to see if this effects the moisture content progression significantly.

Given that the pore volume of the porous stucco does not appear to correlate with drying behaviour it was hypothesised a rate limiting step prevents water being absorbed by the porous stucco despite unsaturated pore volume being available. Possible mechanisms limiting the transport of water from the slurry to the stucco which exclude the stucco particles becoming saturated include:

1) Formation of a discontinuous pathway between the slurry and the porous stucco as the drying front recedes into the bulk and the diffusion of water through the bulk limits water transport to the slurry-air interface.

As shown in Section 7.2.4, the application of porous stucco onto a slurry composed of colloidal silica and zircon powder follow kinetics which are indicative of capillary flow of liquid from the bulk to the surface for the entire drying period. Assuming that the Indicating slurry applied in this Section follows the same drying kinetics as Section 7.2.4 (due to the similarities in composition) water is expected to be transported to the surface by capillary action; thus the drying front never recedes into the bulk. Therefore, it is expected a continuous pathway is maintained between the slurry and the stucco for the entire drying period and the diffusion of water from the bulk to the surface does not occur.

2) Solids dispersed in the slurry block pores in the porous stucco, preventing additional transport of water from the slurry to the porous stucco.

This hypothesis was proposed as it has been shown that fine particles are preferentially transported to the mould interface during slip casting of bimodal distributions of silicon carbide [153]. As such, in a synonymous scenario of porous stucco absorbing water from a dispersion of fine silica particles and coarse zircon particles, the fine silica particles may block pores at the surface of the porous stucco. However, articles referring to slip casting of

colloidal $Y_2O_3$ [178] and $Al_2O_3$ [179] nanoparticles have been published inferring porous moulds are not typically blocked by nanoparticle dispersions.

3) As water is transferred from the slurry to the porous stucco, the narrowest unsaturated pore in the porous stucco becomes larger than the widest saturated pore in the slurry matrix as water is rearranged to fill the narrowest pores available in each material. This causes the suction potential of each material to equalise and water is no longer transferred from the slurry network to the porous stucco.

As shown previously in Tables 7 and 32, the average pore size of SGB127 is much smaller than BD-$Al_2O_3$ and αFrame-Impreg$_8$-Clean. This infers that if each stucco material is fully dried, SGB127 will attain a higher suction potential than BD-$Al_2O_3$ or αFrame-Impreg$_8$-Clean. As such, SGB127 will be capable of absorbing water from narrower pores within the slurry matrix than BD-$Al_2O_3$ or αFrame-Impreg$_8$-Clean. Subsequently, it would be expected that SGB127 material would be capable of absorbing a greater quantity of water from the slurry than BD-$Al_2O_3$ and αFrame-Impreg$_8$-Clean before attaining the same suction potential as the slurry matrix (assuming a sufficient pore volume is available). This, however, was not observed and all porous stucco materials dry the Indicating slurry in the same manor. Thus it was concluded that the equalisation of suction potentials in the slurry and stucco does not limit water absorption into the porous stucco. It is, however, possible that the $R_H$ of the atmosphere fills narrow pores present in SGB127 material as shown in Section 4.2.5. This may result in all porous stucco materials absorbing an equal quantity of water before the suction potentials equalise, thus producing a similar slurry moisture content progression for each porous material analysed.

4) The rate of water transport from the slurry matrix to the porous stucco.

It is possible liquid transport from the slurry to the porous stucco is slow, resulting in a large fraction of water evaporating from the slurry surface as opposed to migrating to the porous stucco. Assuming that water is transferred from the slurry to the porous stucco at an equal rate for each material, this may explain the similar slurry moisture content progression

when depositing each porous material. However, due to the large variation in pore size and porosity for each material it would be expected water is transferred from the slurry to the porous stucco at different rates for each material.

Irrespective of the mechanism responsible for limiting the porous stucco absorbing water from the slurry, this experiment has shown a greater quantity of mesopore volume does not necessarily equate to a faster drying time as initially hypothesised. As a result of this behaviour, it may be possible to reduce the concentration of porous stucco when depositing porous stucco blends or alternatively reduce the quantity of impregnation steps required to synthesise a composite stucco material whilst still achieving optimum drying performance.

## 7.4 Conclusions

The drying behaviour of investment casting slurries coated in porous and non-porous stucco has been conducted. Recording weight loss over time, it was observed that the rate of moisture loss follows first order kinetics with respect to moisture content throughout the entire drying period indicative of a continuous FRP1. This suggests capillary action is drawing water from the bulk to the surface until the slurry is completely dry. In addition, it was also observed that deposition of porous stucco blends yielded the same rate of weight loss as deposition of non-porous stucco. It was therefore concluded that moisture evaporates from both the slurry and porous stucco when porous stucco was deposited. This accounts for the equal rate of evaporation observed when using porous or non-porous stucco compositions despite the expected reduction in evaporation rate at the slurry surface resulting from water transferring from the slurry to the porous stucco.

Utilising a fluorescein dye in the colloidal silica binder, the moisture content of the slurry was measured independently from the stucco. This experiment provided evidence that the porous stucco quickly absorbs water from the slurry upon deposition. However, the porosity of each porous material made little difference to the rate at which the slurry dried. This was explained by the presence of a rate limiting step restricting water transport from the slurry to the porous stucco. The possible mechanisms preventing the utilisation of the entire pore volume are discussed. However, identifying the exact cause is difficult with the limited range of techniques used.

# 8. Conclusions and Future Work

## 8.1 Summary of Conclusions

The viability of accelerating production of investment casting moulds by contact-sorption drying has been studied by replacing traditional refractory ceramic materials with porous water absorbing materials as stucco. This process was specifically developed for accelerating the drying in the secondary layers, whilst preserving the surface finish of the mould achieved by the unmodified primary layers. It was initially observed that the complete replacement of traditional ceramic materials with porous ceramic materials produced to an unacceptable surface coverage with minimal adhesion between the stucco particles and the slurry. Subsequently, blends of each material were trialled and it was found that a 60:40 volume ratio of porous to non-porous stucco produced an acceptable surface coverage and adhesion. Implementing this formulation produced a 50 % reduction in drying time in comparison to use of traditional non-porous stucco within secondary layers. However, shells built utilising porous stucco blends caused a reduction in green and pre-fired strength in addition to an increased fired strength when compared to shells utilising traditional non-porous stucco. Moreover, flexural deformation was observed in shells containing porous stucco upon firing to casting temperatures. This resulted in dimensional changes to the mould and failure due to fracture.

The flexural deformation observed upon firing shells containing porous stucco was investigated further by producing shell samples representative of either $Section_S$ or $Section_P$ for a complete shell. Dilatometer analysis concluded that samples representative of $Section_S$ containing porous stucco contracted to a greater degree in the firing cycle than samples containing only non-porous stucco. Using this data, it was calculated that shells containing porous stucco in secondary layers produce substantial flexural deformation due to the greater magnitude of shrinkage in $Section_S$ in comparison to $Section_P$. A supplementary technique was developed using 3 point bend TMA to measure the flexural deformation of complete shell samples which closely matched the results calculated from dilatometer analysis of samples representative of $Section_S$ and $Section_P$. In addition, a 3$^{rd}$ technique was developed to measure the dimensional change of the shell before and after firing. All three techniques measured a greater flexural deformation when utilising porous stucco in

comparison to non-porous stucco in secondary layers. It was therefore concluded that as the porous stucco particles begin to contract during firing, the slurry matrix becomes less constrained as a result of breakage in the continuity of particles in contact throughout each layer. This produces a greater magnitude of contraction in a slurry matrix containing porous stucco in comparison to a slurry matrix containing non-porous stucco.

In order to i) maintain the surface finish provided by $Section_P$; ii) incorporate porous stucco within $Section_S$ and iii) counteract the flexural deformation observed; two possible solutions were evaluated. The first solution involved synthesis of a composite ceramic which attained the water absorbing properties of the porous stucco, but the dimensional stability of the non-porous stucco. This was achieved by producing a macroporous $\alpha$-$Al_2O_3$ framework and impregnating the structure with peptized boehmite which was subsequently converted to a mesoporous phase of alumina. Utilising this composite ceramic material as stucco successfully reduced the magnitude of flexural deformation upon firing when compared to monolithic porous stucco. In addition, a 37.5 % reduction in drying time was achieved in comparison to use of traditional non-porous stucco within secondary layers. An alternative solution was also investigated to reduce the flexural deformation upon firing involving the use of a tertiary section containing non-porous stucco. This solution also successfully reduced the magnitude of flexural deformation upon firing in comparison to use of monolithic porous stucco without use of a tertiary section. As such, both techniques offer a solution to incorporate water absorbing stucco into the shell whilst maintaining an acceptable degree of dimensional stability but compromise on flexural strength. In addition, this work has highlighted the influence of stucco composition on the dimensional properties of the shell mould. It is therefore envisaged that techniques developed within this work can be used to test compatibility of stucco variants within the shell system in the future.

The mechanism of accelerated drying was investigated by recording weight loss of slurry with either porous or non-porous stucco compositions deposited on the surface. This work concluded that a continuous FRP1 was observed throughout the drying schedule indicative of capillary action drawing water from the bulk to the surface for both porous and non-porous stucco compositions. As the rate of weight loss recorded for a system containing porous or non-porous stucco was equal for a given condition, it was proposed water evaporates from both the slurry and porous stucco following transfer of liquid from the

slurry to the porous stucco. Utilising a colour changing dye to measure the moisture content of the slurry independently from the stucco concluded that variation in stucco composition affects the mechanism of water removal from the slurry. However, for each porous stucco material analysed, a similar progression of moisture content over time was observed. This lead to the hypothesis that a rate limiting step occurs which restricts the utilisation of the full pore volume available.

To summarise, the utilisation of porous stucco to accelerate the drying of investment casting moulds works successfully, but presents many challenges. These challenges arise due to the drastic changes in material properties when substituting non-porous stucco with porous stucco which subsequently cause detrimental changes to the integral properties of the mould. However, it has been demonstrated that by understanding the mechanism through which each defect occurs, solutions can be implemented which produce a mould more characteristic of a mould comprising non-porous stucco. To successfully implement a process utilising this technology that reduces lead time whilst maintaining the quality of the cast component, further process and material optimisation is required. However, the techniques developed in this work; combined with the greater depth of knowledge attained on the influence of stucco properties on the mould structure and behaviour will be foundational in the successful implementation of this technology into industry.

## 8.2 Future Work

In the pursuit of optimising the drying process of investment casting shells with porous stucco, it is important to understand in more detail the mechanism limiting the use of the full pore volume. Understanding this mechanism may allow materials to be developed capable of absorbing a larger portion of the liquid present in the slurry or alternatively find a minimum pore volume a given material must attain to absorb the maximum amount of water from the slurry. This will allow a material to be developed which absorbs the largest quantity of water from the slurry (thus reducing the drying time to a minimum) while considering the cost and time consumption of producing such material. To achieve this, an accurate and reliable method of measuring water transport from the slurry to the stucco is required. A possible technique which fulfils these criteria is magnetic resonance imaging (MRI) which has proven successful in analysing water transport in porous mediums [180] in

addition to evaporation in porous substrates [181]. Implementation of such a technique would add invaluable information in the discussion of transport of water from the slurry to the stucco and the evaporation from each material.

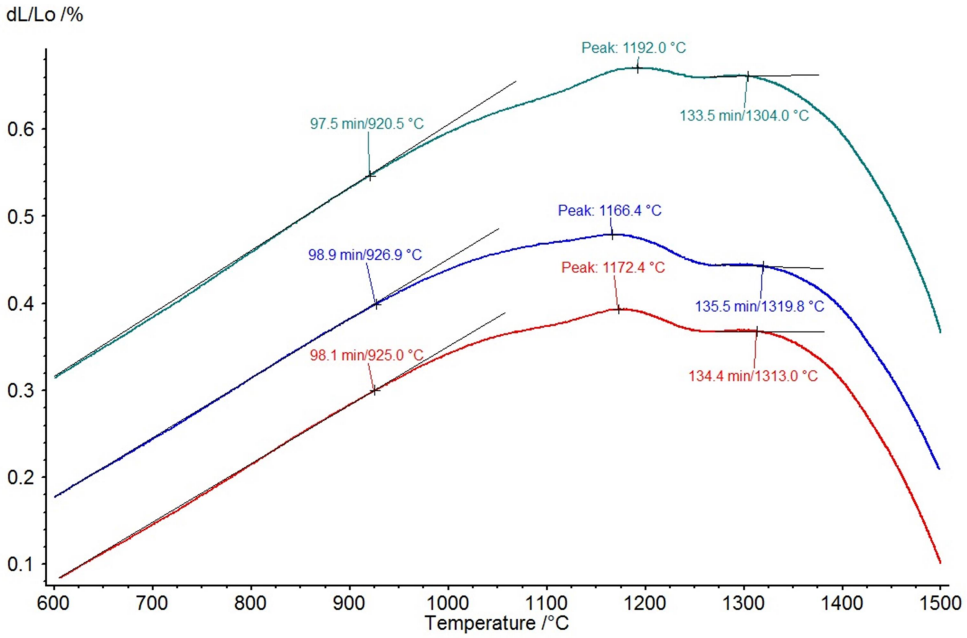
To minimise flexural deformation resulting from varying expansion/contraction behaviour in $Section_S$ containing porous stucco and $Section_P$ containing only non-porous stucco, it may be beneficial to develop a shell utilising porous stucco in both $Section_P$ and $Section_S$ to remove incompatibility issues. This solution offers a pathway to utilise simple monolithic porous stucco without flexural deformation occurring if the sintering behaviour of both sections can be matched. It is possible the composition of the primary layers are determined to be integral to the properties and/or surface finish of the mould and must remain unmodified. In such a case, utilising composite stucco exhibiting dimensional stability at high temperature and water absorbing properties in secondary layers may work more effectively at maintaining the properties of the shell. Utilising composite stucco in any shell formulation requires a synthesis route which is both economic and scalable as the previously described batch processing route for producing α-Frame-$Impreg_8$-Clean material utilises a very manual and time consuming procedure.

Any new shell formulation containing porous stucco should be evaluated via Weibull statistics following extensive mechanical analysis after exposure to various temperature profiles. This will determine how the likelihood of failure compares to other traditional systems at a given stress. In addition, new shell formulations containing porous stucco should be subject to creep testing before conducting casting trials. This is required to evaluate if the modification of the shell structure resulting from the introduction of porous stucco has produced a material more susceptible to creep in comparison to a shell containing only non-porous stucco. Creep tests on shell bars should be completed on formulations proven to solve the issue of flexural deformation as the two effects will compete to deform the shell simultaneously, causing problematic interpretation of results.

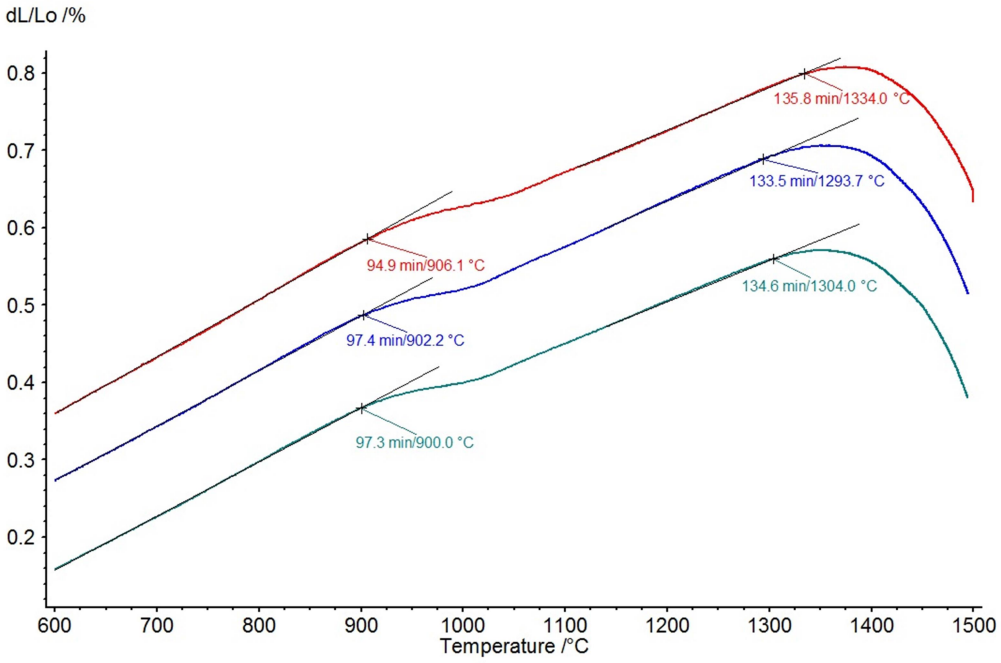
Providing that creep analysis demonstrates that an equal magnitude of deformation is attained under load with shells containing porous and non-porous stucco, casting trials can be completed. Small scale casting trials will investigate the dimensional accuracy, crystal structure and surface finish of cast components to compare against components cast from the standard shell system. This information will be used to examine the practicality of

implementing this technology in industry by evaluating if the accelerated production of the mould produces a cast component equal in quality to the standard process.

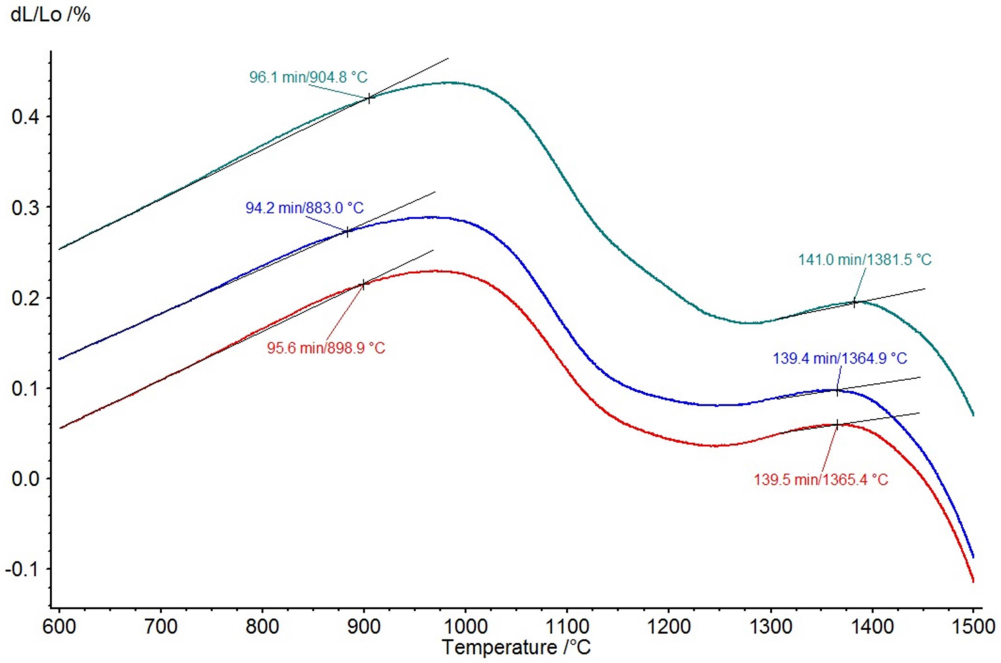
# 9. Appendices



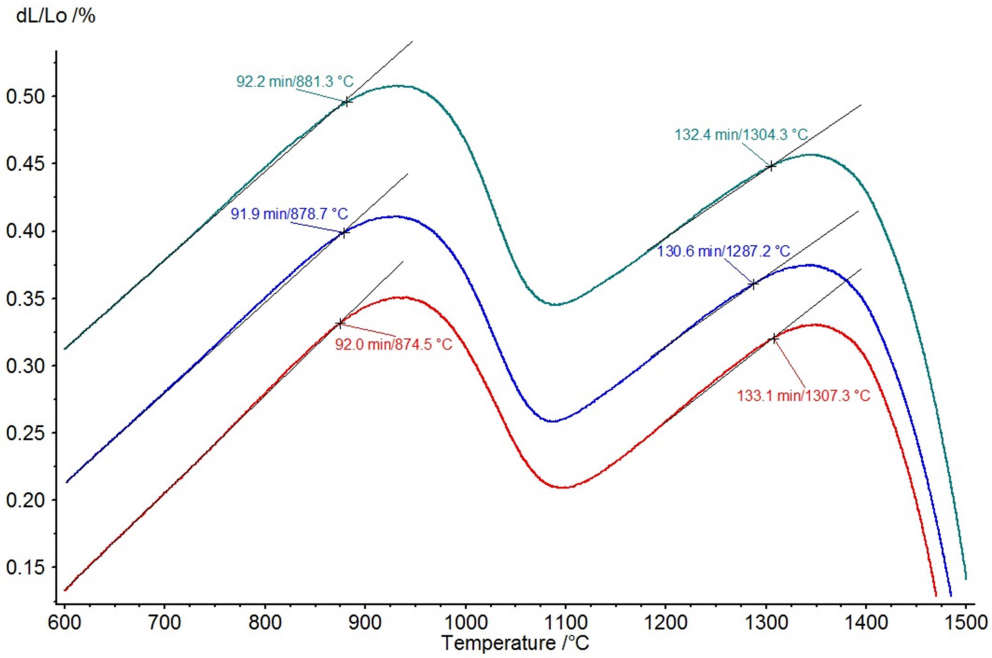

**Appendix 1a** – Magnified image of each repeat sintering profile for sample Primary (Fused-$Al_2O_3$) analysed by dilatometer. Samples are separated by 0.1 % at origin for clarification



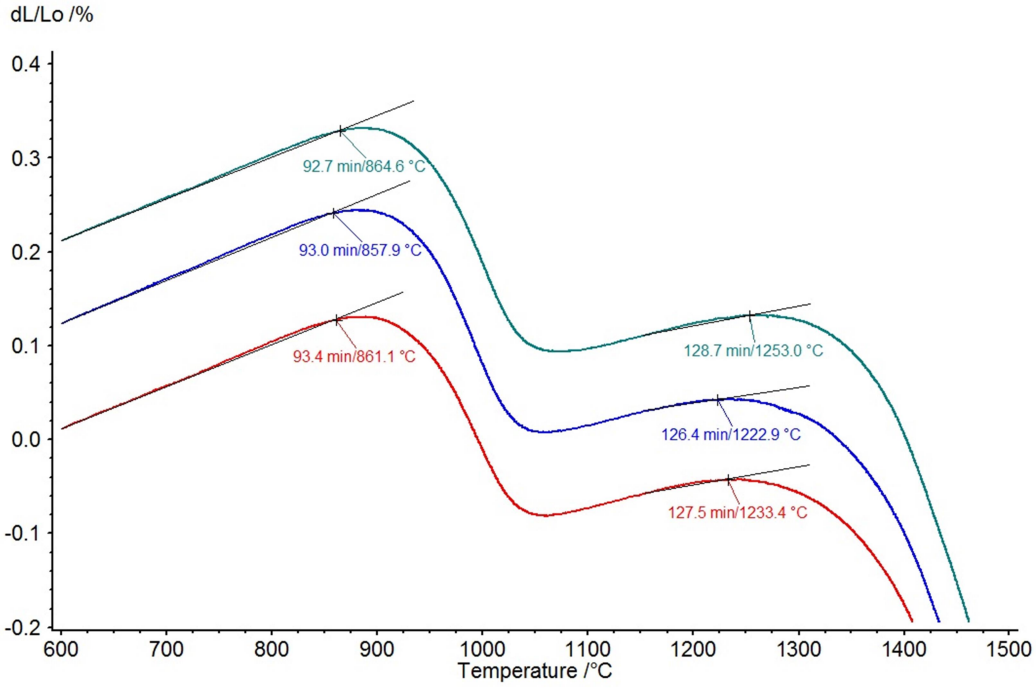

**Appendix 1b** – Magnified image of each repeat sintering profile for sample Secondary (Tab-$Al_2O_3$) analysed by dilatometer. Samples are separated by 0.1 % at origin for clarification



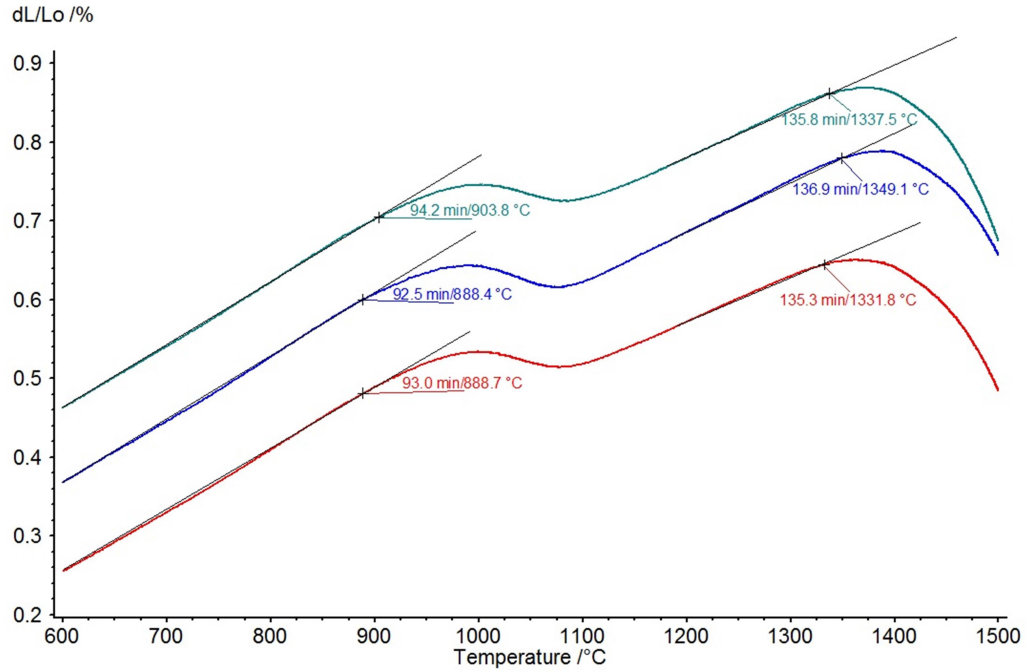

**Appendix 1c** – Magnified image of each repeat sintering profile for sample Secondary (BD-$Al_2O_3$) analysed by dilatometer. Samples are separated by 0.1 % at origin for clarification




**Appendix 1d** – Magnified image of each repeat sintering profile for sample Secondary (SGB127) analysed by dilatometer. Samples are separated by 0.1 % at origin for clarification




**Appendix 1e** – Magnified image of each repeat sintering profile for sample Secondary (-) analysed by dilatometer. Samples are separated by 0.1 % at origin for clarification




**Appendix 1f** – Magnified image of each repeat sintering profile for sample Secondary (αFrame-$I_8$-C) analysed by dilatometer. Samples are separated by 0.1 % at origin for clarification

# 10. References

[1] T. M. Pollock and S. Tin, “Nickel-based superalloys for advanced turbine engines: Chemistry, microstructure, and properties,” *Journal of Propulsion and Power,* vol. 22, pp. 361-374, 2006.

[2] Rolls Royce plc, The Jet Engine, Wiley-Blackwell, 1996.

[3] P. R. Beeley and M. F. Smart, Investment Casting, Taylor & Francis Group, 1995.

[4] S. Pattanik, D. B. Karunakar and P. K. Jha, “Developments in investment casting process - A review,” *Journal of Materials Processing Technology,* vol. 212, pp. 2332-2348, 2012.

[5] M. Jolly and G. Dooley, “Advancing current materials and methods in the investment casting of cobalt prosthesis,” in *Japan Foundry Society, Inc.*, 2012.

[6] S. Jones, Improved Sol Based Ceramic Moulds For Use in Investment Casting, University of Birmingham, 1993.

[7] M. Leadbetter, G. L. Knowles, P. Savage and H. T. Bidwell, “Control of primary coating and its relation to surface Finish,” in *9th Bicta Conference on Investment Casting*, 1969.

[8] K. L. Murty, S. Gollapudi, K. Ramaswamy, M. D. Mathew and I. Charit, “Chapter 3 - Creep deformation of materials in light water reactors (LWRs),” in *Materials Ageing and Degradation in Light Water Reactors*, Woodhead Publishing, 2013, pp. 81-148.

[9] J. Belan, Study of Advanced Materials for Aircraft Jet Engines Using Quantitative Metallography, IntechOpen, 2012.

[10] D. Ma, “Novel casting processe for single-crystal turbine blades of superalloys,” *Frontiers of Mechanical Engineering,* vol. 13, pp. 3-16, 2018.

[11] M. Gell, D. N. Duhl and A. F. Giamei, “The development of single crystal superalloy turbine blades,” in *Superalloys Conference (Fourth International Symposium)*, 1980.

[12] G. Halsey, “Some factors influencing the dewaxing of ceramic shell moulds,” in *10th Bicta Conference on Investment Casting*, 1970.

[13] J. Hockin, “Dimensional variations in invesment castings,” in *9th Bicta Conference on Investment Casting*, 1968.

[14] C. Panwisawas, H. N. Mathur, B. W. Broomfield, D. Patman and C. M. F. Rae, “Prediction of recrystallisation in single crystal nickel-based superalloys during

investment casting," *MATEC Web of Conferences,* vol. 14, 2014.

[15] E. D. E. R. Hyde, A. Seyfaee, F. Neville and R. Moreno-Atanasio, "Colloidal silica particle synthesis and future industrial manufacturing pathways: A review," *Industrial & Engineering Chemistry Research,* vol. 55, no. 33, pp. 8891-8913, 2016.

[16] I. A. Rahman and V. Padavettan, "Synthesis of silica nanoparticles by sol-gel: Size dependent properties, surface modification, and applications in silica-polymer nanocomposites — A review," *Journal of Nanomaterials,* vol. 8, pp. 1-15, 2012.

[17] C. J. Brinker and G. W. Scherer, "Sol-Gel Science," in *Sintering*, Acedemic Press Limited, 1990, pp. 675-742.

[18] R. K. Iler, The Chemistry of Silica, Wiley-Interscience, 1979.

[19] T. Cosgrove, Colloid Science: Principles, Methods and Applications, 2nd Edition, Wiley, 2010.

[20] E. J. W. Verwey and J. T. G. Overbeek, Theory of the stability of lyphobic colloids, vol. 51, Elsevier Publishing Company, 1948, p. 631–636.

[21] R. Hyde, P. A. Withey, S. Jones and P. M. Marquis, "Hot distortion mechanisms of moulds for investment casting," in *23rd Bicta Conference on Investment Casting*.

[22] J. M. Hanchar and P. W. O. Hoskin, Zircon, Mineralogical Society of America, 2003.

[23] P. J. Wilson, S. Blackburn, R. W. Greenwood, B. Prajapti and K. Smalley, "The role of zircon particle size distribution, surface area and contamination on the properties of silica-zircon ceramic materials," *Journal of the European Ceramic Society,* vol. 31, pp. 1849-1855, 2011.

[24] R. C. Dante, Handbook of Friction Materials and their Applications, Woodhead Publishing, 2016.

[25] M. Awaad and S. H. Kenawy, "Sintering of zircon: the role of additives," *British Ceramic Transactions,* vol. 102, no. 2, pp. 69-72, 2003.

[26] M. Madono, "Alumina raw materials for the refractory industry," *CN-Refractories,* vol. 6, no. 3, pp. 54-63, 1999.

[27] G. Buchel, X. Liu, A. Buhr and J. Dutton, "Review of tabular alumina as high performance refractory material," *International Ceramic Review,* pp. 6-12, 2007.

[28] R. Prasad, "Progress in Investment Castings," in *Science and Technology of Casting Processes*, Intech, 2012, pp. 25-72.

[29] S. P. Leyland and I. S. Smith, "Implementation of a water based shell mould investment casting process," in *23rd Bicta Conference on Investment Casting*, 1997.

[30] C. Yuan and S. Jones, “Investigation of fibre modified ceramic moulds for investment casting,” *Journal of the European Ceramic Society,* vol. 23, pp. 399-407, 2003.

[31] M. J. Nadolski and Z. Konopka, “The investigation of properties of investment casting moulds reinforced with ceramic fibre,” *Archives of Foundry Engineering,* vol. 7, pp. 127-130, 2007.

[32] F. Wang, F. Li, B. He and B. Sun, “Microstructure and strength of needle coke modified ceramic casting molds,” *Ceramics International,* vol. 40, pp. 479-486, 2013.

[33] R. K. Dwivedi, “Drying behaviour of alumina gels,” *Journal of Materials Science Letters,* vol. 5, no. 4, pp. 373-376, 1986.

[34] R. W. Ford, Ceramics Drying, Pergamon, 1986.

[35] C. J. Geankoplis, “Drying of Process Materials,” in *Transport Processes and Separation Process Principles*, 4th Edition ed., Prentice Hall, 2003, pp. 559-624.

[36] G. W. Scherer, “Theory of drying,” *Journal of American Ceramic Society,* vol. 73, no. 1, pp. 3-14, 1990.

[37] S. Leyland and S. Jones, “The effect of varying the intercoat drying time upon the rate of moisture removal from the investment casting shell mould,” in *22nd Bicta Conference on Investment Casting*, 1995.

[38] R. H. Perry and D. W. Green, “Solid Drying Fundamentals,” in *Perry's Chemical Engineering Handbook*, 7th Edition ed., McGraw-Hill Professional, 1997, pp. 997-1032.

[39] Y. H. Hui, C. Clary, M. M. Farid, O. O. Fasina, A. Noomhorm and J. Welti-Chanes, Food Drying Science and Technology - Microbiology, Chemistry, Applications, DEStech Publications, 2008.

[40] N. H. Ceaglske and O. A. Hougen, “Drying granular solids,” *Industrial & Engineering Chemistry,* vol. 29, no. 7, pp. 805-813, 1937.

[41] J. F. Pearse, T. R. Oliver and D. M. Newitt, “The mechanism of the drying of solids Part I,” *Transactions of the Institutetution of Chemical Engineers,* vol. 27, pp. 1-8, 1949.

[42] K. T. Sherwood, “The drying Of solids - Part I,” *Industrial and Engineering Chemistry,* vol. 21, no. 1, pp. 12-16, 1929.

[43] K. N. P. Kumar, V. Zaspalis, K. Keizer and A. Burggraaf, “Drying process in the formation of sol-gel-derived TiO2 ceramic membrane,” *Journal of Non-Crystalline Solids,* vol. 147, no. 1, pp. 375-381, 1992.

[44] G. Pajonk, “Drying methods preserving the texural properties of gels,” *Journal de Physique Colloques,* vol. 50, no. 1, pp. 13-22, 1989.

[45] H. Darcy, Les fontaines publiques de la ville de Dijon: exposition et application, 1856: Victor Dalmont.

[46] E. W. Comings, “Contributions of T.K. Sherwood and associates to the field of drying, (Part 2),” *Drying Technology,* vol. 2, no. 1, p. 117–148, 1983.

[47] T. Young, “III. An essay on the cohesion of fluids,” *Philosophical transactions of the Royal Society of London,* vol. 95, pp. 65-87, 1805.

[48] P. S. Laplace, Traite de Mechanique Celeste Supplements au Livre X, Paris: De l'imprimerie de Crapelet, 1805.

[49] T. Metzger and E. Tsotsas, “Network models for capillary porous media: application to drying technology,” *Drying,* vol. 82, no. 6, pp. 869-879, 2010.

[50] T. Metzger, A. Irawan and E. Tsotsas, “Isothermal drying of pore networks: Influence of friction for different pore structures,” *Drying Technology,* vol. 25, no. 1, pp. 49-57, 2007.

[51] J. Hager, M. Hermansson and R. Wimmerstedt, “Modelling steam drying of a single porous ceramic sphere: experiments and simulations,” *Chemical Engineering Science,* vol. 52, no. 8, pp. 1253-1264, 1997.

[52] T. Metzger and E. Tsotsas, “Influence of pore size distribution on drying kinetics: A simple capillary model,” *Drying Technology,* vol. 23, no. 9-11, pp. 1797-1809, 2005.

[53] J. B. Laurindo and M. Prat, “Numerical and experimental network study of evaporation in capillary porous media. Drying rates,” *Chemical Engineering Science,* vol. 53, no. 12, pp. 2257-2269, 1998.

[54] T. Kudra and A. S. Mujumdar, Advanced Drying Technologies, CRC Press, 2001.

[55] M. J. V. Rensburg, M. L. Roux, Q. P. Campbell and E. S. Peters, “Moisture transport during contact sorption drying,” *International Journal of Coal Preparation and Utilization,* pp. 1-16, 2018.

[56] S. L. Sturton, W. K. Bilanski and D. R. Menzies, “Moisture exchange between corn and the desiccant bentonite in an intimate mixture,” *Canadian Agricultural Engineering,* vol. 25, no. 1, pp. 139-141, 1983.

[57] A. Tadayyon and G. A. Hill, “Contact-sorption drying of penicillium bilaii in a fluidized bed dryer,” *Journal of Chemical Technology & Biotechnology: International Research in Process, Environmental and Clean Technology,* vol. 68, no. 3, pp. 277-282, 1997.

[58] J. H. D. Hampton, “Experimental and Theoretical Studies of the Filtration of Ceramic Studies,” PhD Thesis, McGill University, 1991.

[59] F. M. Tiller and C.-D. Tsai, "Theory of filtration of ceramics: I: Slip casting," *Journal of American Ceramic Society,* vol. 69, no. 12, pp. 882-887, 1986.

[60] D. S. Adcock and I. C. McDowall, "The mechanism of filter pressing and slip casting," *Journal of the American Ceramic Society,* vol. 40, no. 10, pp. 355-360, 1957.

[61] B. K. Chakrabarti, "Drying conditions and their effect on ceramic shell investment casting process," *Materials and Science Technology,* vol. 18, pp. 935-940, 2002.

[62] G. Halsey, "Drying of ceramic shell moulds," in *8th Bicta Conference on Investment Casting*, 1968.

[63] M. Kugelgen, "From 7 days to 7 hours - Investment casting parts within the shortest time," in *68th Worls Foundry Congress*, 2008.

[64] S. Jones, "Improved Investment Casting Process". European Patent EP 1 708 838 B1, 07 February 2007.

[65] S. Jones, "Investment Casting Process". United States of America Patent US 7,594,529,B2, 29 September 2009.

[66] E. Karadag and D. Saratdin, "Swelling of superabsorbent acrylamide/sodium acrylate hydrogels prepared using multifunctional crosslinkers," *Turkish Journal of Chemistry,* vol. 26, no. 6, pp. 863-875, 2002.

[67] D. S. McGuire, "Investment Casting Shell Incorporating Desiccant Material". United States of America Patent US 2011/0232857 A1, 29 September 2011.

[68] A. Pierre and C. Matthieu, "Surface and porosity of nanocrystalline boehmite xerogels," *Journal of Colloid and Interface Science,* vol. 290, no. 1, pp. 208-219, 2005.

[69] S. M. Kim, Y. J. J. W. Bae, H. S. Potdar and K. W. Jun, "Synthesis and characterization of a highly active alumina catalyst for methanol dehydration to dimethyl ether," *Applied Catalysis A: General,* vol. 348, no. 1, pp. 113-120, 2008.

[70] X. Zheng, T. Ge and R. Wang, "Recent progress on desiccant materials for solid desiccant cooling," *Energy,* vol. 74, pp. 280-294, 2014.

[71] K. V. Wong and A. Hernandez, "A review of additive manufacturing," *ISRN Mechanical Engineering,* pp. 1-10, 2012.

[72] C. J. Bae and J. W. Halloran, "Integrally cored ceramic mold fabricated by ceramic stereolithography," *Applied Ceramic Technology,* vol. 8, no. 6, pp. 1255-1262, 2011.

[73] H. Wu, D. Li, Y. Tang, N. Guo, F. Cui and B. Sun, "Rpaid casting of hollow turbine blades using integral ceramic moulds," *Proceedings of the Institution of Mechanical Engineers. Part B: Journal of Engineering Manufacture,* vol. 223, no. 6, pp. 695-702,

2009.

[74] A. Gahler and J. G. Heinrich, “Direct laser sintering of Al2O3 dental ceramic components by layer-wise slurry deposition,” *The American Ceramic Society,* vol. 89, no. 10, pp. 3076-3080, 2006.

[75] F. Klocke and C. Ader, “Direct laser sintering of ceramics,” *International Solid Freeform Fabrication Symposium,* 2003.

[76] J. Rouquerol, D. Avnir, C. W. Fairbridge, D. H. Everett, J. M. Haynes, N. Pernicone, J. D. F. Ramsay, K. S. W. Sing and K. K. Unger, “Recommendations for the characterization of porous solids (technical report),” *Pure and Applied Chemistry,* vol. 66, no. 8, p. 1739–1758, 1994.

[77] T. Ohji and M. Fukushima, “Macro-porous ceramics: processing and properties,” *International Materials Reviews,* vol. 57, no. 2, pp. 115-131, 2012.

[78] A. R. Studart, U. T. Gonzenbach, E. Tervoort and L. J. Gauckler, “Processing routes to macroporous ceramics: A review,” *Journal of the American Ceramic Society,* vol. 89, no. 6, pp. 1771-1789, 2006.

[79] E. Hammel, O. L. R. Ighodaro and O. I. Okoli, “Processing and properties of advanced porous ceramics: An application based review,” *Ceramics International,* vol. 40, no. 10, pp. 15351-15370, 2014.

[80] C. R. Rambo, T. Andrade, T. Fey, H. Sieber, A. E. Martinelli and P. Greil, “Microcellular Al2O3 ceramics from wood for filter applications,” *Journal of the American Ceramic Society,* vol. 91, no. 3, pp. 852-859, 2008.

[81] E. Gregorová, W. Pabst, Z. Zivcová, I. Sedlárová and S. Holíková, “Porous alumina ceramics prepared with wheat flour,” *Journal of the European Ceramic Society,* vol. 30, no. 14, pp. 2871-2880, 2010.

[82] R. M. Pasquarelli, J. J. Rosário, L. Rath and G. A. Schneider, “High temperature behavior of monodisperse porosity in alumina films,” *Journal of the European Ceramic Society,* vol. 35, no. 14, pp. 3917-3926, 2015.

[83] G. Zhang, J. Yang and T. Ohji, “Fabrication of porous ceramics with unidirectionally aligned continuous pores,” *Journal of the American Ceramic Society,* vol. 84, no. 6, pp. 1395-1397, 2001.

[84] Z. Yang and Y. S. Lin, “Sol-gel synthesis of silicalite/γ-alumina granules,” *Industrial Engineering Chemistry Research,* vol. 39, no. 12, pp. 4944-4948, 2000.

[85] K. Wefers and C. Misra, Oxides and hydrides of aluminium, Alcoa Research Laboratories, 1972.

[86] J. T. Kloprogge, H. D. Ruan and R. L. Frost, "Thermal decomposition of bauxite minerals: infrared emission spectroscopy of gibbsite, boehmite and diaspore," *Journal of Materials Science,* vol. 37, no. 6, pp. 1121-1129, 2002.

[87] C. Rodriguez-Navarro, E. Ruiz-Agudo, A. Luque, A. B. Rodriguez-Navarro and M. Ortega-Huertas, "Thermal decomposition of calcite: Mechanisms of formation and textural evolution of CaO nanocrystals," *American Mineralogist,* vol. 94, no. 4, p. 578–593, 2009.

[88] L. Guo, H. Arafune and N. Teramae, "Synthesis of mesoporous metal oxide by the thermal decomposition of oxalate precursor," *Langmuir,* vol. 29, no. 13, pp. 4404-4412, 2013.

[89] K. Okada, "Selective leaching for the preparation of functional porous ceramics," *International Journal of the Society of Materials Engineering for Resources,* vol. 8, no. 2, pp. 50-54, 2000.

[90] P. Kim, Y. Kim, H. Kim, I. K. Song and J. Yi, "Synthesis and characterization of mesoporous alumina for use as a catalyst support in the hydrodechlorination of 1,2-dichloropropane: effect of preparation condition of mesoporous alumina," *Journal of Molecular Catalysis A: Chemical,* vol. 219, no. 1, pp. 87-95, 2004.

[91] H. A. Ali, A. Chughtai and A. Sattar, "Synthesis of quality silica gel; Optimization of parameters," *Journal of Faculty of Engineering & Technology,* vol. 16, no. 1, pp. 19-32, 2010.

[92] Z. A. Alothman, "A review: Fundamental aspects of silicate mesoporous materials," *Materials,* vol. 5, no. 12, pp. 2874-2902, 2012.

[93] P. S. Santos, H. S. Santos and S. P. Toledo, "Standard transition aluminas. Electron microscopy studies," *Materials Research,* vol. 3, no. 4, pp. 104-114, 2000.

[94] Z. Holkova, L. Pach, D. Lath and J. Kristin, "Relation among the aggregation of boehmite particles in sols, microstructure of gels, and crystallization of corundum," *Chemical Papers,* vol. 58, no. 3, pp. 149-154, 2004.

[95] B. E. Yoldas, "Alumina gels that form porous transparent Al2O3," *Journal of Material Science,* vol. 10, no. 11, pp. 1856-1860 , 1975.

[96] R. I. Zakharchenya, "Influence of peptization on the properties of alumina produced from boehmite sols," *Journal of Sol-Gel Science and Technology,* vol. 6, no. 2, pp. 179-186, 1996.

[97] B. Gaweł, K. Gaweł and G. Øye, "Sol-gel synthesis of non-silica monolithic materials," *Materials,* vol. 3, no. 4, pp. 2815-2833, 2010.

[98] F. Karouia, M. Boualleg, M. Digne and P. Alphonse, "Control of the texural properties

of nanocrystalline boehmite (γ-AlOOH) regarding its peptization ability," *Powder Technology,* vol. 237, pp. 602-609, 2013.

[99] M. Rahaman, Ceramic Processing and Sintering, CRC Press, 2003.

[100] S. Sakka, Handbook of sol-gel science and technology. 3. Applications of sol gel, Springer Science & Business Media, 2005.

[101] E. Morgado, Y. L. Lam, S. M. C. Menezes and L. F. Nazar, "Characterization of petpetized boehmite systems: An 27Al nuclear magnetic resonance study," *Journal of Colloid and Interface Science,* vol. 176, no. 2, pp. 432-441, 1995.

[102] S. Somiya, F. Aldinger, R. Spriggs, K. Uchino, K. Koumoto and M. Kaneno, "Sintering of ceramics," in *Handbook of Advanced Ceramics*, Academic Press, 2003, pp. 187-264.

[103] R. M. German, "Coarsening in sintering: Grain shape sistribution, grain size distribution, and grain growth kinetics in solid-pore systems," *Critical Reviews in Solid State Material Science,* vol. 35, no. 4, pp. 263-305, 2010.

[104] J. R. Moon, "Sintering of metal powders," *Powder Metallurgy International,* vol. 3, no. 4, pp. 194-199, 1971.

[105] R. M. German, P. Suri and S. J. Park, "Review: liquid phase sintering," *Journal of Material Science,* vol. 44, no. 1, pp. 1-39, 2009.

[106] T. M. Shaw, "Liquid redistribution during liquid-phase sintering," *Journal of the American Ceramic Society,* vol. 69, no. 1, pp. 27-34, 1986.

[107] K. J. Buschow, R. W. Cahn, M. C. Flemings, B. Ilschner, E. J. Kramer and S. Mahajan, "Laminates: Physical and Mechanical Behavior to Lumber: Laminated Veneer," in *Encyclopedia of Materials - Science and Technology, Volumes 1-11*, Elsevier, 2001, pp. 4597-4609.

[108] H. Djohari, J. I. Martinez-Herrera and J. J. Derby, "Transport mechanisms and densification during sintering: I. Viscous flow versus vacancy diffusion," *Chemical Engineering Science,* vol. 64, no. 1, pp. 3799-3808, 2009.

[109] R. W. Cannon and T. G. Langdon, "Creep of ceramics: Part 1 mechanical characteristics," *Journal of Material Science,* vol. 18, no. 1, pp. 1-50, 1983.

[110] R. W. Cannon and T. G. Langdon, "Creep of ceramics: Part 2 an examination of flow mechanisms," *Journal of Materials Science,* vol. 23, no. 1, pp. 1-20, 1988.

[111] G. Mie, "Beiträge zur Optik trüber medien, speziell kolloidaler metallösungen," *Annalen der Physik,* vol. 330, no. 3, pp. 377-445, 1908.

[112] J. R. Rumble, CRC Handbook of Chemistry and Physics, 99th Edition: CRC Press, 2018.

[113] S. Brunauer, P. H. Emmett and E. Teller, “Adsorption of gasses in multimolecular layers,” *Journal of American Chemical Society,* vol. 30, no. 2, pp. 309-319, 1938.

[114] E. P. Barrett, L. G. Joyner and P. P. Halenda, “The determination of pore volume and area distributions in porous substances. I. Computations from nitrogen isotherms,” *Journal of the American Chemical Society,* vol. 73, no. 1, p. 373–380, 1951.

[115] G. Leofanti, M. Padovan, G. Tozzola and B. Venturelli, “Surface area and pore texture of catalysts,” *Catalysis Today,* vol. 41, no. 1, pp. 207-219, 1998.

[116] S. Storck, H. Bretinger and W. F. Maier, “Characterization of micro- and mesoporous solids by physisorption methods and pore-size analysis,” *Applied Catalysis A: General,* vol. 174, no. 1, pp. 137-146, 1998.

[117] W. D. Harkins and G. Jura, “Surfaces of solids. XIII. A vapor adsorption method for the determination of the area of a solid without the assumption of a molecular area, and the areas occupied by nitrogen and other molecules on the surface of a solid,” *Journal of the American Chemical Society,* vol. 66, no. 8, p. 1366–1373, 1944.

[118] J. H. de-Boer, B. C. Lippens, B. G. Linsen, J. C. P. Broekhoff, A. v. d. Heuvel and T. J. Osinga, “The t-curve of multimolecular N2-adsorption,” *Journal of Colloid and Interfacial Science,* vol. 21, no. 4, pp. 405-414, 1966.

[119] M. Thommes, K. Kaneko, A. V. Neimark, J. P. Olivier, F. Rodriguez-Reinoso, J. Rouquerol and K. S. Sing, “Physisorption of gases, with special reference to the evaluation of surface area and pore size distribution (IUPAC Technical Report),” *Pure and Applied Chemistry,* vol. 87, no. 9-10, pp. 1051-1069, 2015.

[120] ASTM C373 - 14, “Standard Test Method for Water Absorption, Bulk Density, Apparent Porosity, and Apparent Specific Gravity of Fired Whiteware Products, Ceramic Tiles, and Glass Tiles,” PA, West Conshohocken, 2014.

[121] ASTM D1200-10, “Standard Test Method for Viscosity by Ford Viscosity Cup,” PA, West Conshohocken, 2018.

[122] S. P. Leyland, “Drying characteristics of investment casting water based shell mould systems,” in *23rd Bicta Conference on Investment Casting*, 1997.

[123] M. F. Ashby and D. Jones, Engineering Materials 1 (Fourth Edition), Butterworth-Heinemann, 2011.

[124] V. L. Richards, R. V. Wolf and G. Connin, “Four point bend testing to characterise the strength of ceramic mold shells,” in *49th ICI Technical Conference*, Orlando , Florida, 2001.

[125] R. Hyde, S. Leyland and P. W. S. Jones, “Evaluation of the mechanical properties of investment casting shells,” in *22nd Bicta Conference on Investment Casting*, 1995.

[126] P. Z. Cai, G. L. Messing and D. L. Green, "Determination of the mechanical response of sintering compacts by cyclic loading dilatometry," *Journal of the American Ceramic Society,* vol. 80, no. 2, pp. 445-452, 1997.

[127] D. Ravi and D. J. Green, "Sintering stresses and distortion produced by densifying differences in bi-layer structures," *Journal of the European Ceramic Society,* vol. 26, no. 1-2, pp. 17-25, 2006.

[128] D. Mishra, S. Anand, R. P. and R. Das, "Hydrothermal preparation and characterization of boehmites," *Materials Letters,* vol. 42, no. 1-2, pp. 38-45, 2000.

[129] R. Bleta, P. Alphonse, L. Pin, M. Gressier and M. Menu, "An efficient route to aqueousphase synthesis of nanocrystalline y-Al2O3 with high porosity: From stable boehmite colloids to large pore mesoporous alumina," *Journal of Colloid and Interface Science,* vol. 367, no. 1, pp. 120-128, 2012.

[130] G. Paglia, C. E. Buckley, T. J. Udovic, A. L. Rohl, F. Jones, C. F. Maitland and J. Connolly, "Boehmite derived y-alumina system. 2. Considerations of hydrogen and surface effects," *Chemistry of Materials,* vol. 16, pp. 1914-1923, 2004.

[131] A. C. V. Coelho, G. A. S. Santos, H. S. Santos and P. K. Kiyohara, "Specific surface area and structures of aluminas from fibrillar pseudoboehmite," *Matéria (Rio de Janeiro),* vol. 13, no. 2, pp. 329-341, 2008.

[132] K. A. Cychosz, R. Guillet-Nicolas, J. Garcia-Martinez and M. Thommes, "Recent advances in the textural characterization of hierarchically structured nanoporous materials," *Chemical Society Reviews,* vol. 46, no. 2, pp. 389-414, 2017.

[133] K. Miyazawa and S. Inagaki, "Control of the microporosity within the pore walls of ordered mesoporous silica SBA-15," *Chemical Communications,* vol. 21, pp. 2121-2122, 2000.

[134] W. Gitzen, Alumina as a ceramic material, The American Ceramic Society, 1970.

[135] C. Brinker, G. Scherer and E. Roth, " Sol -> Gel -> Glass : II. Physical and structrual evolution during constant heating rate experiments," *Journal of Non-Crystalline Solids,* vol. 72, no. 2-3 , pp. 345-368, 1985.

[136] K. Kotoh, M. Enoeda and T. Matsui, "A multilayer model for adsorption of water on activated alumina in relation to adsorption potential," *Journal of Chemical Engineering of Japan,* vol. 26, no. 4, pp. 355-360, 1993.

[137] A. M. Ribeiro, T. P. Sauer, C. A. Grande, R. F. P. M. Moreira, J. M. Loureiro and A. E. Rodrigues, "Adsorption equilibrium and kinetics of water vapor on different adsorbents," *Industrial & Engineering Chemistry Research,* vol. 47, no. 18, pp. 7019-7026, 2008.

[138] H. Naono, R. Fujiwara and M. Yagi, "Determination of physisorbed and chemisorbed waters on silica gel and porous silica glass by means of desorption isotherms of water vapor," *Journal of Colloid and Interface Science,* vol. 76, no. 1, pp. 74-82, 1980.

[139] K. Bodisova, L. Pach and V. Kovar, "Sintering of transient Al2O3 phases in monolithic gels," *Ceramics− Silikaty,* vol. 49, no. 4, pp. 263-268, 2005.

[140] P. A. Badkar and J. E. Bailey, "The mechanism of simultaneous sintering and phase transformation in alumina," *Journal of materials science,* vol. 11, no. 10, pp. 1794-1806, 1976.

[141] F. W. Dynys and J. W. Halloran, "Alpha alumina formation in alum-derived gamma alumina," *Journal of the American Ceramic Society,* vol. 65, no. 9, pp. 442-448, 1984.

[142] J. Ahn, J. Park and H.-W. Lee, "Effect of compact structures on the phase transition, subsequent densification and microstructure evolution during sintering of ultrafine gamma alumina powder," *NanoStructured Materials,* vol. 11, no. 1, pp. 133-140, 1999.

[143] H. Murata, D. E. Meyers, F. Kirkbir, S. R. Chaudhuri and A. Sarkar, "Drying and sintering of bulk silica gels," *Journal of Sol-Gel Science and Technology,* vol. 8, no. 1-3, pp. 297-402, 1997.

[144] G. W. Scherer, "Stress in leached phase-separated glass," *The American Ceramic Society,* vol. 68, no. 8, pp. 419-426, 1985.

[145] I. Chuang and G. E. Maciel, "Probing hydrogen bonding and the local environment of silanols on silica surfaces via nuclear spin cross polarization dynamics," *Journal of the American Chemical Society,* vol. 118, no. 2, pp. 401-406, 1996.

[146] C. J. Brinker, E. P. Roth, G. W. Scherer and D. R. Tallant, "Structural evolution during the gel to glass conversion," *Journal of Non-Crystalline Solids,* vol. 71, no. 1-3, pp. 171-185, 1985.

[147] G. L. Humphrey and E. G. King, "Heats of formation of quartz and cristobalite," *Journal of the American Chemical Society,* vol. 74, no. 8, pp. 2041-2042, 1952.

[148] S. B. Holmquist, "Conversion of quartz to tridymite," *Journal of the American Ceramic Society,* vol. 44, no. 2, pp. 82-86, 1961.

[149] P. Wilson, Investigating the formulation of silica-based ceramic core materials for investment casting, EngD Thesis, University of Birmingham, 2011.

[150] K. Akiyama, "X-Ray studies of silica," *Waseda Applied Chemical Society Bulletin,* vol. 17, no. 1, pp. 21-25, 1940.

[151] R. C. Breneman and J. W. Halloran, "Kinetics of cristobalite formation in sintered silica," *Journal of the American Ceramic Society,* vol. 97, no. 4, p. 2272–2278, 2014.

[152] A. J. Perrotta, D. K. Grubbs, E. S. Martin and N. R. Dando, "Chemical stability of beta-cristobalite," *Journal American Ceramic Society,* vol. 72, no. 3, pp. 441-447, 1989.

[153] J. M. F. Ferreira, "Role of the clogging effect in the slip casting process," *Journal of European Ceramic Society,* vol. 18, no. 9, pp. 1161-1169, 1998.

[154] S. Jones, A. Cendrovich, M. Jolly, J. Gebelin, K. Lewis and I. Al-Dawery, "Boilerclave thermal profiles and the effect of moisture upon ceramic shells during the steam de-wax process," in *50th Technical Conference & Expo 2002*, 2002.

[155] N. Savchenko, I. Sevostyanova, T. Sablina, L. Gömze and S. Kulkov, "The influence of porosity on the elasticity and strength of alumina and zirconia ceramics," *AIP Conference Proceedings,* vol. 1623, no. 1, pp. 547-550, 2014.

[156] J. Eom, Y. Kim and S. Raju, "Processing and properties of macroporous silicon carbide ceramics: A review," *Journal of Asian Ceramic Societies,* vol. 1, no. 3, pp. 220-242, 2013.

[157] J. Meng, T. Jin, X. Sun and Z. Hu, "Surface recrystallization of a single crystal nickel-base superalloy," *International Journal of Minerals, Metallurgy and Materials,* vol. 18, no. 2, pp. 197-202, 2011.

[158] C. Panwisawas, J. C. Gebelin and R. C. Reed, "Analysis of the mechanical deformation arising from investment casting of directionally solidified nickel-based superalloys," *Materials Science and Technology,* vol. 29, no. 7, pp. 843-853, 2013.

[159] D. Hardy and D. J. Green, "Mechanical properties of a partially sintered alumina," *Journal of the European Ceramic Society,* vol. 15, no. 8, pp. 769-775, 1995.

[160] C. J. Brinker and S. P. Mukherjee, "Conversion of monolithic gels to glasses in a multicomponent silicate glass system," *Journal of Materials Science,* vol. 16, no. 7, pp. 1980-1988, 1981.

[161] E. Ringdalen and M. Tangstad, "Softening and melting of SiO2, an important parameter for reactions with quartz in Si Production," in *Advances in Molten Slags, Fluxes, and Salts: Proceedings of the 10th International Conference on Molten Slags, Fluxes and Salts 2016*, 2016.

[162] J. O. Bockris, J. D. Mackenzie and J. A. Kitchener, "Viscous flow in silica and binary liquid silicates," *Transactions of the Faraday Society,* vol. 51, pp. 1734-1748, 1955.

[163] A. A. Wereszczak, K. Breder, M. K. Ferber, T. P. Kirkland, E. A. Payzant and C. J. Rawn, "Dimensional changes and creep of silica core ceramics used in investment casting of superalloys," *Journal of Material Science,* vol. 37, no. 19, pp. 4235-4245, 2002.

[164] O. Sudre and F. F. Lange, "Effect of inclusions on densification: I, Microstructural development in an Al2O3 matrix containing a high volume fraction of ZrO2 inclusions,"

*Jounrnal of American Ceramic Society,* vol. 75, no. 3, pp. 519-524, 1992.

[165] Y. Nurishi and J. A. Pask, "Sintering of α-Al2O3 - amorphous silica compacts," *Ceramics International,* vol. 8, no. 2, pp. 57-59, 1982.

[166] I. Zaplatynsky, "Devitrification and shrinkage behavior of silica fibers," NASA Technical Document D-6891, 1972.

[167] M. Anseau, E. D. Rupo and F. Cambier, "Thermal expansion o f zircon-alumina materials prepared by reaction sintering," *Journal of Material Science,* vol. 16, no. 3, pp. 825-828, 1981.

[168] P. Z. Cai, D. J. Green and G. L. Messing, "Constrained densification of alumina/zirconia hybrid laminates, I: Experimental observations of processing defects," *Journal of the American Ceramic Society,* vol. 80, no. 8, pp. 1929-1939, 1997.

[169] S. Timoshenko, "Analysis of bi-metal thermostats," *Journal of the Optical Society of America,* vol. 11, no. 3, pp. 233-255, 1925.

[170] M. Leadbetter, "A method of testing hot deformation of ceramic shell moulds," in *14th Bicta Conference on Investment Casting*, 1977.

[171] J. D. Snow, "How the shell affects casting dimentions," in *22nd Bicta Conference on Investment Casting*, 1995.

[172] P. Z. Cai, D. J. Green and G. L. Messing, "Constrained densification of alumina/zirconia hybrid laminates, II: Viscoelastic stress computation," *Journal of the American Ceramic Society,* vol. 80, no. 8, pp. 1940-1948, 1997.

[173] J. B. Ollagnier, O. Guullon and J. Rodel, "Constrained Sintering of a Glass Ceramic Composite: I. Asymmetric Laminate," *Journal of the American Ceramic Society,* vol. 93, no. 1, pp. 74-81, 2010.

[174] M. Bengisu, Engineering Ceramics, Springer-Verlag Berlin Heidelberg, 2001.

[175] E. Prouzet, D. Fargeot and J. F. Baumard, "Sintering of boehmite-derived transition alumina seeded with corundum," *Journal of Materials Science Letters,* vol. 9, no. 1, p. 779–781, 1990.

[176] B. Sathyaseelan, I. Baskaran and K. Sivakumar, "Phase transition behvaiour of nanocrystalline Al2O3 powders," *Soft Nanoscience Letters,* vol. 3, no. 4, pp. 69-74, 2013.

[177] Z. Liang and S. Blackburn, "Analysis of crack developments during processing of laminated ceramic tubes," *Journal of Material Science,* vol. 37, no. 19, pp. 4227-4233, 2002.

[178] D. Hou, Z. Yanchun, S. Xudong, L. Xiaodong and L. Shaohong, “Preparation of transparent Y2O3 ceramic by slip casting and vacuum sintering,” *Journal of Rare Earths,* vol. 30, no. 1, pp. 57-62, 2012.

[179] M. Gholami and Z. Khakpour, “Manufacturing of new potential plaster molds for slip casting of alumina,” *Journal of the Australian Ceramic Society,* pp. 1-5, 2018.

[180] K. Ogawa, T. Matsuka, S. Hirai and K. Okazaki, “Three-dimensional velocity measurement of complex interstitial flows through water-saturated porous media by the tagging method in the MRI technique,” *Measurement and Science Technology,* vol. 12, no. 2, pp. 172-180, 2001.

[181] N. Reis, R. Griffiths, M. Mantle, L. Gladden and J. Santos, “MRI investigation of the evaporation of embedded liquid droplets from porous surfaces under different drying regimes,” *International Journal of Heat and Mass Transfer,* vol. 49, no. 5, pp. 951-961, 2006.